Low luminosity elliptical galaxies

Halliday, Claire

Low Luminosity Elliptical Galaxies

Claire Halliday

A thesis submitted to the University of Durham
in accordance with the regulations for
admittance to the Degree of Doctor of Philosophy.

Department of Physics
University of Durham
September 1998

The copyright of this thesis rests with the author. No quotation from it should be published without the written consent of the author an information derived from it should be acknowledged.

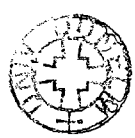

Abstract

Long-slit spectra for the photometric axes of a sample of 14 elliptical galaxies, predominantly low-luminosity ellipticals, in the Virgo cluster and in nearby groups, are studied to investigate the galaxy kinematical structure and stellar evolutionary history.

To determine the galaxy kinematical structure, the shape of the line-of-sight velocity distribution (hereafter LOSVD) is measured using the Fourier Correlation Quotient method of Bender (1990), adopting the parametrisation of the LOSVD due to van der Marel and Franx (1993). This parametrisation enables the asymmetrical and symmetrical deviations of the LOSVD from a Gaussian function to be measured by the amplitudes H_3 and H_4 of the Gauss-Hermite series respectively. Rotation, velocity dispersion (σ), H_3 and H_4 are determined as a function of radius for both the major and minor axes of our sample. To summarise, LOSVD asymmetries were measured for the major axes of 12 galaxies which in the majority of cases have been interpreted as evidence for central disk-like components; evidence of both radial and tangential anisotropy were found from the measurement of H_4; central decreases in σ are measured for 3 galaxies, which is interpreted as evidence that they have undergone some form of merger or interaction. On the basis of their measurements, galaxies are classified into 3 classes: types 1, 2 and 3. "Type 1" galaxies show strong evidence for both disk and bulge components and have the greatest measured values of H_3 for our sample. Galaxies of "type 2" show strong evidence for embedded disk components and most (3 of 4) are measured to have central decreases in σ. "Type 3" galaxies have kinematically-decoupled cores. Other galaxies, not classified, are NGC 3379 and NGC 4468.

Measurements of the line-strength indices Mg_b, Mg_2, Hβ, Fe5270, Fe5335 and $< Fe >$ are determined as a function of radius for all spectra and established to the Lick/IDS scale. The relations Mg'_b–Mg_2, $Mg'_b - log(\sigma)$, Mg_b– <Fe> and Hβ–[Mg_b <Fe>] are then studied. The Mg'_b–Mg_2 relation of Wegner et al. (1998) and the calibrations of Worthey (1994) are compared with measurements here: this is used as a check of our calibration of Mg'_b and Mg_2. Measurements in the $Mg'_b - log(\sigma)$ plane are considered separately for each galaxy and compared with the central relation of Colless et al. (1998). Measurements for most galaxies are found to be in good agreement with this relation. Measurements of Mg_b and <Fe> are similarly considered for each galaxy and compared with the predictions of the models of Worthey (1994). For the majority of galaxies, measurements are clearly offset from the Mg_b– <Fe> model grid of Worthey (1994), representing an $[\frac{Mg}{Fe}]$ overabundance. This is an important result which shows that the $[\frac{Mg}{Fe}]$ *overabundance detected previously for the giant ellipticals similarly exists for ellipticals of the low luminosities studied here.* For most galaxies this overabundance is found to be a constant function of radius. For the "type 2" galaxy NGC 3605, and NGC 4468, measurements are consistent with solar abundance ratios. Finally, measurements of Hβ and [Mg_b <Fe>] are compared with the models of Worthey (1994) to distinguish gradients in both age and metallicity. For all galaxies, gradients in metallicity are found with metallicity decreasing as a function of radius. For 5 galaxies (NGC 4564, NGC 3377, NGC 4478, NGC 4339 and NGC 3605) age gradients are also detected, with the galaxy centre shown to be younger than the surrounding galaxy.

Interpreting these results together, different formation scenarios are proposed for the different galaxy types. For galaxies of "type 1", formation by homogenous, dissipational collapse is proposed. Galaxies of "type 2" show evidence for a less homogenous evolutionary history involving dissipationless collapse. No conclusive scenario is proposed for galaxies of "type 3".

Preface

The work described in this thesis was undertaken between 1994 and 1998 whilst the author was a research student under the supervision of Professor Roger L. Davies in the Department of Physics at the University of Durham. This work has not been submitted for any other degree at the University of Durham or at any other University.

The majority of the work contained in this thesis is the authors own. Results presented in chapters 3 and 4 were obtained using the **FCQ** program and **MIDAS** routines written by Ralf Bender and Roberto Saglia. Measurements presented in chapters 5 and 6 were obtained using programs written by Glenn Baggley and Harald Kuntschner.

Acknowledgements

I thank my supervisor Roger L. Davies for his time, inspiration and encouragement thoughout my PhD and for introducing me to this fascinating field of research. His enthusiasm has made a considerable impression on this thesis and was a key factor in helping me to take it to completion. I thank Harald Kuntschner, Glenn Baggley and Roberto Saglia for their considerable help, advice and for providing computer software to allow me to complete a large proportion of my research. I also thank our collaborators Mark Birkinshaw and Ralf Bender for their help and support. I gratefully acknowledge the support of a PPARC studentship and the use of Starlink facilities.

I have been very fortunate in friends and colleagues during my time in Durham and their genuine friendliness have made this a very memorable time. I thank you all. I give a special thankyou to Eric Bell, Harald Kuntschner, Katherine Gunn and Fiona Hoyle for their careful reading of draft chapters of this thesis.

My most sincere thanks I reserve for my parents for their love, encouragement and support throughout my life. Their marvellous example in life is a continuing source of inspiration. Thank you David, my brother, for always convincing me to look on the bright side! I remember the love of my late Gran with very special fondness. I finally thank my Aunty Rhona and late Uncle Gifford for their love and for their keen interest in my career.

Contents

Chapter 1

Introduction

Elliptical galaxies are important components in our study of the nearby Universe. They are found to exist principally within clusters of galaxies and comprise approximately 20% of observable galaxies classified in magnitude limited catalogues.

The discovery of the true nature of ellipticals can be traced to the work of Sir William Herschel. Herschel, together with his son John, compiled an extensive set of observations of so-called "nebulae". He believed that these systems could be distinguished into two classes, genuinely gaseous gas clouds (e.g. planetary nebulae, nebulae as known to this day), and unresolved external stellar systems similar to our own Galaxy. The confirmation of the extragalactic nature of these ellipticals however, had to await the spectroscopic observations by Hubble (1936).

In 1944, Baade resolved the populations of Local Group galaxies and the nearby ellipticals NGC 147 and NGC 185 (Baade, 1944a,b). Baade differentiated the stars he detected into two distinct groups, older red giants found mainly in the bulge and halo components of elliptical and spiral galaxies, and younger, blue supergiants located within the spiral arms, and on this basis postulated the existence of two different stellar populations, a scheme which has proven to be a successful tool in the study of galaxy evolution.

1.1 Formation

Until the 1970's, elliptical galaxies were widely believed to be old, coeval populations of stars formed dissipationally in a rapid, single burst of star formation some 15 Gyr ago, a view adopted by the early models (Larson, 1969, 1974a,b, 1975). Observational support for formation by dissipational collapse remains considerable to this day. The tightness of the colour-magnitude relation has been interpreted as representing early formation of the bulk of stars within ellipticals (Bower et al., 1992; Kodama and Arimoto, 1997), although some residual star formation has been shown to be consistent with the observed observational scatter (Bower et al., 1998). Similarly the small spread in the relation found between central measurements of both the Mg spectral index and velocity dispersion, σ, (Burstein et al., 1988; Bender et al., 1993; Ziegler and Bender, 1997), has been quantified as representing a combined variation in both age and metallicity of the order of 15% RMS (Bender et al., 1993), placing lower limits on the possible ages of the stellar populations dominating

the light of ellipticals. Measurements of chemical abundance gradients using spectral line-strength indices have until recently been almost exclusively interpreted as gradients in metallicity (section 1.2.3); such gradients are predicted by dissipational collapse models.

By the 1980's controversial evidence for the existence of a younger, intermediate population of stars began to emerge from population synthesis studies, suggesting ellipticals had suffered a more recent burst of star formation (e.g. for M32, O'Connell (1980)). Detection of features such as kinematically-decoupled cores, shells and ripples and boxy isophote shapes now present strong evidence that ellipticals have not only had complex histories but that merging has had an important influence on their evolution (for a recent review see Schweizer (1998)). This is consistent with hierarchical clustering model descriptions for the evolution of the Universe such as CDM (e.g. Cole et al. (1994); Kauffmann (1996)).

To reconcile these conflicting scenarios and explain the smooth variation of their kinematical properties with galaxy mass, Bender et al. (1992) proposed that "dynamically hot galaxies" (i.e. both giant and compact ellipticals and bulges) of increasing mass form from the increasingly less gaseous mergers of smaller systems. This scenario, although not inconsistent with the $Mg - \sigma$ relation (Bender et al., 1993), suggests that systems of low luminosity could be the building blocks of more luminous systems, i.e. that *merging* was an important part of the evolution of ellipticals.

1.2 Stellar Populations

To this day, observations of the populations of the majority of elliptical galaxies remains confined to the study of their unresolved integrated light. In the decades following Baade's pioneering observations, it was realised that an important obstacle in the study of elliptical galaxy evolution were the conflicting effects of age and metallicity on the observable properties of their light (Osterbrock, 1995). This problem, now commonly known as the "age-metallicity degeneracy" has recently been approached by the use of more carefully defined stellar population indicators based on absorption line-strength indices (e.g. Worthey (1994); Kuntschner and Davies (1998)).

1.2.1 Population Synthesis Models

The development of models to describe the evolutionary history of ellipticals can be traced to the early work of Whipple (1935). Early attempts to study the stellar populations using broad-band colours were troubled by the degenerate effects of different ages and metallicity. The development of stellar evolutionary synthesis models have recently enabled an accurate comparison of ages of the composite stellar populations of ellipticals (e.g. Worthey (1994)).

A wide range of stellar population models are now available (e.g. Bruzual and Charlot (1993), Worthey (1994), Weiss et al. (1995), Kodama and Arimoto (1997)). In general modern models are based on either or both of two principles, evolutionary and population synthesis. Evolutionary synthesis models attempt to reproduce the observable properties of the integrated galaxy population by assuming particular stellar isochrones. Population synthesis by contrast involves fitting a combination of stellar spectra for the measured galaxy spectrum and is in general based on far fewer physical constraints. The models of Worthey (1994) are adopted in this thesis and employ a

combination of both techniques.

1.2.2 The Lick project

With the ultimate aim of investigating the stellar populations of ellipticals and globular clusters, an important development in recent years has been the project started in the 1970's at UCO/Lick Observatory. A key step in this work has been the development of single-burst stellar population models (Worthey, 1994). The development of these models has involved the calibrations of 21 carefully defined spectral line-strength indices as a function of metallicity (i.e. $[\frac{Fe}{H}]$), stellar temperature (i.e. given by $V-K$), and surface gravity for a sample of 460 Galactic stars (Faber et al., 1985; Gorgas et al., 1993; Worthey et al., 1994). These stellar observations and observations of 381 galaxies and 38 globular clusters (see Trager et al. (1998)), were completed between 1972 and 1984 using the red-sensitive IDS and Cassegrain Spectrograph on the 3m Shane Telescope at Lick Obervatory. The wavelength range 4000-6200Å was chosen since the G and K-type stars which dominate the light for this range were able to be more readily calibrated, both theoretically and empirically.

In his thesis work Worthey (1994) quantified the relative age and metallicity sensitivity of the different Lick line-strength indices. He found that while many of the commonly used broadband colours were degenerate in age and metallicity, the Balmer absorption index Hβ for example is predominantly age-sensitive and the metal lines (e.g. Fe5270, Fe5335) have varying sensitivities to metallicity. Using his population models he showed that the "age-metallicity degeneracy" could be broken by using a combination of predominantly more age or metallicity sensitive Lick indices. This was demonstrated by González (1993) in his thesis who presented measurements of line-strengths for his sample of 41 ellipticals lying mainly in the field or in small groups. By comparison with the models of Worthey (1994) his measurements suggested that the stellar populations of ellipticals have a spread in age. Care however is required in interpreting such results since the integrated light of a galaxy is the *luminosity-weighted* sum of the different stellar population components. It has been shown, for example, that the younger luminosity-weighted ages for ellipticals studied by González (1993) could be attributed to the presence of a minority younger component, with, for example, 20% by mass of a 2 Gyr disk population superimposed on an older stellar population of 12 Gyr explaining his measurements (de Jong and Davies, 1997). Furthermore, the Hβ measurements of González (1993) have been questioned by Carrasco et al. (1996) who have shown that his correction for Hβ emission is unlikely to be secure.

1.2.3 Colours and Line-Strengths Gradients

The study of the stellar population gradients of galaxies dates back to the measurement of colour gradients by de Vaucouleurs (1961) who observed galaxies to become bluer when increasingly large photometric apertures was used. To enable a more precise investigation of the integrated galaxy light, the use of spectral line-strength features has been adopted. The most generally accepted line-strength definitions are those of UCO/Lick Observatory, the standard adopted in this thesis. Many authors have published measurements of line-strength gradients established to the Lick standard, particular for the Mg_2 feature (e.g. Thomsen (1989), Gorgas et al. (1990), Boroson and Thompson (1991), Carollo et al. (1993), Fisher et al. (1995), Fisher et al. (1996)). As in the earlier studies of

colour gradients, these studies have interpreted gradients in line-strength features as gradients in metallicity, with metallicity predominantly decreasing outwards from the galaxy centre.

1.3 Central Disk Populations

There is increasing observational evidence for the existence of disk populations at the centres of number of ellipticals. The ground-based detections of central disks by e.g. Nieto et al. (1991), have since been followed by detections of yet smaller nuclear disks using HST (e.g. van den Bosch et al. (1994) and Lauer et al. (1995)). These embedded disks are in general of higher surface brightness than the disks of spirals and S0s, supporting the idea that they represent part of a continuous sequence of disk components (Scorza and van den Bosch, 1998). Being supported by their rotation, nuclear disks have been used to constrain the intrinsic shape and mass distribution of the host elliptical galaxy (van den Bosch et al., 1994). Their detection using photometry however has been shown to be strongly dependent on their inclination to the line-of-sight (Rix and White, 1990), such that disks that are sufficiently face-on may not be distinguished from the surrounding bulge component. Nuclear disks have also been detected for a high fraction of ellipticals containing *kinematically-decoupled cores* (hereafter KDCs) (Carollo et al., 1997).

1.4 Isophote shapes

The isophote shapes of ellipticals are very close approximations to perfect ellipses. Deviations from elliptical isophotes can however provide an important insight into galaxy evolution. The most significant of measured deviations for ellipticals, of typically less than 1% in radius, are parametrised by the $cos(i\Theta)$ terms of the following fit for isophote shape, by Fourier series expansion:

$$I(\Theta) = \sum_{i=1}^{4} C_i cos(i\Theta) + \sum_{i=1}^{4} S_i sin(i\Theta) \tag{1.1}$$

Measurements of $C4 < 0$ represent extensions at skew angles to the galaxy principal axes, and $C4 > 0$, extensions in the direction of the galaxy major axis; these represent measurements of "boxiness" and "diskiness" respectively. "Disky" isophotes have been interpreted as evidence for an embedded disk in some ellipticals; predictions of N-body simulations suggest that "boxy" isophotes are evidence that ellipticals have been produced by merging (e.g. Binney and Petrou (1985), Barnes (1992)). Correlations between isophote shape and kinematics (e.g. $\frac{v}{\sigma}$) provide evidence for two distinct classes of elliptical: "disky", low-luminosity and more rotationally-supported, and "boxy", luminous and more anisotropic (Bender et al., 1989).

1.5 Kinematics

Until the 1970's, ellipticals were believed to be coeval populations of stars, their shapes fully supported by rotation and their properties generally consistent with formation by dissipative collapse. Rotation curves of luminous ellipticals however were found not to be consistent with simple isotropic rotator models (Bertola and Capaccioli, 1975; Illingworth, 1977) but could in fact be more accurately described by anisotropic models (Binney, 1978). On the realisation that the ellipticals were not in general supported by rotation, the assumption of axisymmetry was also investigated (Binney, 1978). It was realised that detection of minor axis rotation was a key observational indicator that ellipticals were not axisymmetric but instead triaxial.

1.5.1 Measurement of Kinematics

The rigorous measurement of the kinematics of ellipticals was not possible until the 1970's when both advances in the quality of spectroscopic data and the introduction of Fourier Transform techniques enabled the reliable measurement of both velocity and velocity dispersion. Before then, a range of different methods had generated largely discrepant results, these methods depending on the highly subjective eyeball comparison of the position and width of individual galaxy spectral lines with those of stellar spectra. Initially introduced by Brault and White (1971) and developed by Simkin (1974) and Sargent et al. (1977), the Fourier analysis method established itself as a robust and efficient means of determining galaxy kinematics which has remained the basis of many modern techniques.

A central assumption of the early Fourier techniques developed in the 1970's was that the galaxy *line-of-sight velocity distribution* (hereafter LOSVD) could be accurately approximated as a Gaussian function, an assumption which is now known to be inaccurate. It is now recognised that a more robust measurement of the galaxy kinematical structure requires the recovery and analysis of the *shape* of the LOSVD itself. Methods employed today, e.g. the Fourier Correlation-Quotient method of Bender (1990) and the Fourier-fitting method of Rix and White (1992), now involve more general parametrisations of the LOSVD to detect and measure deviations from a Gaussian distribution, as e.g. the parametrisation due to van der Marel and Franx (1993).

1.5.2 Dynamical Modelling

A key difficulty in early attempts to model the mass distribution of ellipticals were the degenerate effects of mass-to-light ratio and velocity dispersion anisotropy on the measured kinematics (Binney and Mamon, 1982). This was a particular problem in determining the central mass density (e.g. Dressler and Richstone (1988)). Developments both in the measurement of the LOSVD and dynamical modelling now enable the velocity dispersion anisotropy of a galaxy to be constrained as a function of radius (Gerhard, 1993; Rix et al., 1997; Gerhard et al., 1998). Such advances now enable the accurate modelling of the dynamical structure of ellipticals (see de Zeeuw (1997) for a recent review).

1.5.3 Kinematically-decoupled cores

Key observational support that ellipticals have experienced merging in their past is the detection of *kinematically-decoupled cores* (hereafter KDCs) within a significant fraction of ellipticals studied to date. The nature of this phenomenon is still a very active area of research. In chapter 4 of this thesis, observational evidence for embedded disk components in a significant number of galaxies is presented. Two galaxies observed are classic examples of KDCs.

The first case of a kinematically-decoupled core (hereafter KDC) was NGC 5813 detected by Efstathiou et al. (1982). These systems are characterised by decoupled velocity and velocity dispersion (σ) profiles and measured asymmetries of the LOSVD. These asymmetries have been shown to be consistent with the presence of a rapidly rotating disk component of low σ and slowly rotating bulge of greater σ (Franx and Illingworth (1988)). A number of very different kinematical properties have been detected: cores have been found to rotate in a similar direction, at a skew angle or to be completely counter-rotating with respect to the main bulge population.

Various competing scenarios exist to explain the KDC phenomenon: these include the accretion of a gas-rich secondary galaxy (Kormendy, 1984; Franx and Illingworth, 1988; Balcells and Quinn, 1990) and the detection of triaxial orbits (Statler, 1991). Spiral-spiral equal-mass mergers produce counter-rotating central gas disks although more advanced modelling of the gas in these simulations is required. Scenarios not involving full mergers have also been proposed e.g. the models of Hau and Thomson (1994).

Recent studies of HST surface photometry of ellipticals containing KDCs have identified no distinctive characteristics for these objects compared to "normal" elliptical galaxies (e.g. Forbes et al. (1995) and Carollo et al. (1997)). This suggests that any interaction is not associated with significantly enhanced star formation, or with significant enrichment of material by the interacting galaxy.

1.6 Motivation for Thesis Research

Elliptical galaxies, believed until the 1970's to have formed as the result of isolated, dissipational collapse, are now known to have had considerably more complex star formation histories. The discovery that the lower luminosity ellipticals have different kinematical properties (Davies et al., 1983), and the finding by Bender et al. (1989) that diskiness is more predominant in low-luminosity ellipticals, offer strong evidence for the existence of two distinct families of ellipticals.

Recent advances in both observational capabilities and in the analysis of the LOSVD now enable the measurement of the LOSVD shape to the resolution comparable to the velocity dispersion of ellipticals of low-luminosity. This has provided a powerful tool with which to study the underlying kinematical structure of these galaxies. The lower velocity broadening in these objects enables the higher-orders of the LOSVD to be more accurately measured than for more luminous ellipticals. Low-luminosity ellipticals are isotropic rotators (Davies et al., 1983) which implies that the modelling of their dynamical structure will be less complex than for the giant ellipticals, which are anisotropic.

By comparison with stellar population models it has been shown that the light element

abundances of the more luminous metal-rich giant ellipticals, most notably as measured by the Mg line-strength index, are overabundant relative to Fe when compared with ratios calibrated for the solar neighbourhood. Early measurements for less-luminous compact ellipticals suggested that this so-called "$[\frac{Mg}{Fe}]$ overabundance" may not persist to lower luminosity (Worthey et al., 1992) and that their metallicities were closer to being solar. An important aim of this thesis is to address this issue for our sample of low-luminosity ellipticals. If these early findings are found to hold, the stellar populations of these objects can be accurately studied with available models without the limitations inherent in the study of the giant ellipticals.

The main objectives of this thesis are the measurement of the kinematical structure and stellar evolutionary histories of a sample of nearby low-luminosity ellipticals.

Chapter 2

Observations and Reduction

To achieve our scientific aims, high quality long-slit spectra taken at high spectral resolution were acquired. In this Chapter I describe the observations made and data obtained for this project, and the steps involved in its reduction.

In summary, long-slit spectra were obtained for the principal photometric axes of our galaxy sample. Stellar spectra were taken to enable us to measure the galaxy kinematics. To perform a series of calibration steps, additional frames were taken during each night of observations. Bias & flat-field frames were taken at the beginning & end of each night. HeNe+Ar calibration frames were taken both before & after each galaxy exposure to geometrically rectify our spectra and to check for any geometrical instabilities occurring during each galaxy exposure. To determine galaxy kinematics reduction steps in addition to the above were required.

2.1 Observations

2.1.1 Galaxy Sample

The galaxy sample studied here consists almost entirely of low-luminosity ellipticals (hereafter LLEs). Evidence has grown steadily over the past 15 years that LLEs may be very different both in their kinematical behaviour and their stellar populations to more luminous ellipticals (Davies et al., 1983; Nieto and Bender, 1990).

An original sample of 17 galaxies classified as ellipticals, was selected from the Virgo catalog of Bingelli et al. (1985) to be complete for the absolute magnitude range $-20 \leq M_B \leq -17$ and to have a wide range of different structural properties i.e. levels of diskiness and boxiness.

9 galaxies of this original sample were observed during our observations. Other low-luminosity ellipticals (NGC 2778, NGC 5582, NGC 3377, NGC 3605, NGC 3608) were observed when Virgo was not observable due to cloudy & windy conditions. The well studied luminous elliptical NGC 3379 was observed to enable consistency checks to be made with the measurements of other authors. Our observed sample is given in Table 2.1 which lists values for apparent magnitude B_T, the effective radius in arcsecs (R_e) and optical heliocentric redshift, cz_{helio}, all taken from the

Third Reference Catalogue (i.e. de Vaucouleurs et al. (1991), hereafter RC3). Values of absolute magnitude were calculated by assuming either a distance for each galaxy or by using its value of redshift (see Table 2.1).

Name	Type	B_T	R_e	cz_{helio}	M_B	Virgo?
NGC 2778	E	13.35	15.74	2019	-19.68	n
NGC 3377	E5+	11.24	34.45	692	-18.87	n
NGC 3379	E0	10.24	35.25	889	-19.87	n
NGC 3605	E4+	13.13	21.24	649	-17.44	n
NGC 3608	E2	11.70	33.66	1205	-20.21	n
NGC 4239	E	13.70	15.39	921	-17.32	y
NGC 4339	E0	12.26	32.15	1281	-18.76	y
NGC 4387	E	13.01	15.74	561	-18.01	y
NGC 4458	E0+	12.93	26.13	668	-18.09	y
NGC 4464	S?	13.46	7.54	1255	-17.56	y
NGC 4467	E2	14.77	10.64	1474	-16.25	y
NGC 4468	S0?	13.58	27.36	895	-17.44	y
NGC 4478	E2	12.36	13.40	1382	-18.66	y
NGC 4551	E	12.97	13.10	1189	-18.05	y
NGC 4564	E6	12.05	19.82	1119	-18.97	y
NGC 5582	E	12.48	32.89	1332	-19.65	n

Table 2.1: Observed galaxy sample. Values of B_T, R_e and cz_{helio} were taken from the RC3. B_T is given in magnitudes, R_e in arcseconds and cz_{helio} in km s^{-1} The galaxy Hubble type, also taken from the RC3, is given in column 2: E-elliptical, S-spiral, S0-lenticular, +-intermediate (i.e. between elliptical and S0), ?-doubtful classification. To calculate the absolute magnitude (M_B), a distance of 16.0 Mpc was assumed for identified members of the Virgo cluster (Davies et al., 1987). Column 6 indicates whether each galaxy is a member of the Virgo cluster (n-no, y-yes). For NGC 3379 and NGC 3377, members of the Leo-I group (Ferguson and Sandage, 1990), a distance of 10.5 Mpc was assumed. For all remaining galaxies M_B was calculated using the value of stated redshift (cz_{helio}) and by assuming H_o=50km s^{-1}Mpc^{-1}. Galaxies taken from Bingelli et al. (1985) to define our original sample, but unable to be observed were NGC 4168, NGC 4261, NGC 4360, NGC 4486A, NGC 4515, IC 3653, NGC 4623, NGC 4660.

2.1.2 Stellar Sample

To determine the kinematical properties of each galaxy, a range of 3-8 different template stars were observed during each night. Our sample was compiled from lists used to determine galaxy kinematics, supplied by R. L. Davies. A complete listing of all stars observed is given in Table 2.2. Template stars were chosen to be mainly of K and G stellar type, stellar types believed to be the main contributor to the integrated light of elliptical galaxies. This choice reduces the effect of template-mismatching although for the method adopted here (i.e. the FCQ method of Bender (1990)) this is not as critical as for earlier methods.

Star	RA (J2000)	Dec (J2000)	V (magn.)	Stellar type
BD+362495	14h28m16.44s	+36°11′48.″8	6.10	K0 III
BD+502146	15h08m19.46s	+50°03′18.″7	6.39	K0 III
HD 52071	07h00m57.99s	+27°09′25.″5	7.12	K2 III
HD 56224	07h17m15.61s	+26°21′49.″9	7.25	K1 III
HD 56823	07h18m35.08s	−00°39′45.″0	10.10	A2
HD 58683	07h27m49.01s	+27°17′38.″5	7.37	K0
HD 71597	08h28m14.49s	+00°14′38.″8	7.31	K2 III
HD 85990	09h55m34.98s	−01°07′31.″6	7.98	K0 III
HD 134585	15h05m46.54s	+71°52′56.″6	7.44	K2
HD 143393	15h59m05.61s	+29°25′56.″9	7.10	K2 III
HD 172401	18h39m39.64s	+08°43′58.″6	6.99	K0 III
HD 184275	19h32m56.49s	+21°27′22.″4	7.83	K1 III
HR 2478	06h43m59.25s	+13°13′43.″3	4.49	K1 III
HR 2503	06h47m19.85s	+08°02′14.″5	4.77	K4 III
HR 2697	07h11m08.42s	+30°14′45.″2	4.42	K2 III
HR 2701	07h10m13.63s	−04°14′24.″4	4.92	K0 III
HR 3369	08h33m00.27s	+24°05′07.″4	6.36	G9 III
HR 4932	13h02m11.45s	+10°57′32.″1	2.83	G8 III
HR 5270	14h02m32.41s	+09°41′13.″9	6.20	F8 IV

Table 2.2: Stellar templates observed. RA, Dec, V magnitude and stellar type for all templates were taken from the SIMBAD Astronomical Database maintained by the CDS, Strasbourg. RA and Dec are given in Julian 2000 coordinates.

2.1.3 Description of Observations

Long-slit spectroscopic data were taken to study our galaxy sample using the Blue Channel Spectrograph at the Multiple Mirror Telescope, Arizona, U.S.A., during 5-7 March and 15-17 May 1994, and 22-26 February 1995. Seeing was typically 0.5-2.0 arcsec. The CCD chip of the Blue Channel Spectrograph was replaced between the observing runs of May 1994 and February 1995; two different CCDs were therefore used to obtain our data and the properties of both are outlined in Table 2.3.

A wavelength range of ~4555-6045Å was chosen to be centred on the Mg_b and a range of Fe Lick/IDS-defined spectral features. Velocity dispersions of as low as 60km s^{-1} have been measured for LLEs. To accurately determine such low values of σ, a high spectral resolution, ~1.5Å FWHM, was required. For this purpose a spectrographic grating of 1200 g/mm and a slit width of 1 arcsec were chosen. A slit length of 180 arcsecs was selected to study line-strengths and kinematics as a function of radius for each galaxy.

Vignetting occurred towards the edges of both the rows and columns of the CCD array. No correction for this effect in the direction of rows, i.e. in the direction of the dispersion axis of each frame, was made; the most affected regions (i.e. columns of the array) were later removed from further analysis (see figure 2.2 and section 2.2.5). To remove badly affected regions in the direction of the spectrograph slit, the array was "windowed" to produce frames corresponding to columns 1-3072 and rows 281-880 for the Blue Channel 1994 CCD (hereafter BC94), and rows 181-820 for the Blue Channel 1995 (BC95) CCD. A resolution element in the spatial direction was rebinned to 2 pixels to produce a spatial scale of 0.6 arcsec $pixel^{-1}$. A measure of the bias level for each frame was provided within an *overscan strip*: this consisted of 20 columns which were added to the edge of the frame to produce a final frame of dimensions 3092x300 pixels for the BC94 CCD and 3092x320 pixels for the BC95 CCD.

A log of all galaxy observations made is given in Table 2.4 which includes values of RA and Dec at which observations were actually made, the position angle of each observation, the exposure time in seconds and the CCD detector used to obtain the observation (BC94 = Blue Channel 1994, BC95 = Blue Channel 1995). Data for the galaxies NGC 4467 and NGC 4239 were of poor signal-to-noise and results for these objects will not be presented in this thesis.

Property	Blue Channel 1994	Blue Channel 1995
Dimensions	3072 x 1024	3072 x 1024
Pixel Size	15μm x 15μm	15μm x 15μm
Readout Noise	8e^{-1}	7.5e^{-1}
Gain	1.6e^{-1}/ADU	1.5e^{-1}/ADU
Cosmetics	20-30 bad columns	$\sim$ 4 bad columns
Spatial Scale	0.3″ †	0.3″ †

† *Unbinned pixel*

Table 2.3: Properties of the Blue Channel Spectrograph CCDs

Date	Name	RA (obs.)	Dec (obs.)	PA (deg.)	Exp.(s)	Detector
05.03.94	NGC 3605	11h14m07.9s	+18°17′34″.3	290 min	3600	BC94
05.03.94	NGC 3605	11h14m09.2s	+18°17′39″.4	200 maj	3600	BC94
05.03.94	NGC 4387	12h23m09.9s	+13°05′19″.2	322 maj	3600	BC94
05.03.94	NGC 4387	12h23m10.2s	+13°05′17″.1	52 min	3600	BC94
05.03.94	NGC 4564	12h33m56.0s	+11°42′46″.3	135 min	3600	BC94
05.03.94	NGC 4468	12h26m59.5s	+14°19′25″.7	155 min	3600	BC94
06.03.94	NGC 3608	11h14m21.3s	+18°25′20″.4	351 min	3600	BC94
06.03.94	NGC 2778	09h09m19.0s	+35°14′01″.8	225 maj	3600	BC94
06.03.94	NGC 2778	09h09m18.7s	+35°13′59″.2	135 min	3600	BC94
06.03.94	NGC 5582	14h18m41.3s	+39°55′17″.7	205 maj	3600	BC94
15.05.94	NGC 4564	12h33m55.8s	+11°42′51″.8	45 maj	3600	BC94
15.05.94	NGC 4468	12h26m59.6s	+14°19′28″.4	65 maj	3600	BC94
15.05.94	NGC 4464	12h26m49.2s	+08°25′56″.1	95 min	3600	BC94
15.05.94	NGC 4464	12h26m49.2s	+08°25′55″.9	5 maj	3600	BC94
15.05.94	NGC 5582	14h18m41.6s	+39°55′15″.8	295 min	4200	BC94
16.05.94	NGC 3608	11h14m21.5s	+18°25′18″.7	81 maj	3600	BC94
22.02.95	NGC 4467	12h26m58.2s	+08°16′03″.1	41 maj	3600	BC95
22.02.95	NGC 4467	12h26m57.9s	+08°15′53″.8	131 min	3600	BC95
23.02.95	NGC 3379	10h45m11.9s	+12°50′43″.5	71 maj	600	BC95
23.02.95	NGC 3379	10h45m11.4s	+12°50′47″.0	161 min	600	BC95
23.02.95	NGC 3377	10h45m03.9s	+14°14′59″.6	42 maj	1800	BC95
23.02.95	NGC 3377	10h45m03.4s	+14°14′58″.9	312 min	1800	BC95
23.02.95	NGC 4551	12h33m07.0s	+12°32′16″.9	70 maj	3600	BC95
23.02.95	NGC 4551	12h33m06.5s	+12°32′19″.6	340 min	3600	BC95
23.02.95	NGC 4458	12h26m25.7s	+13°31′03″.2	5 maj	3600	BC95
23.02.95	NGC 4458	12h26m25.7s	+13°31′03″.2	95 min	3600	BC95
23.02.95	NGC 4478	12h27m45.4s	+12°36′12″.7	145 maj	3600	BC95
24.02.95	NGC 4478	12h27m46.4s	+12°36′17″.7	55 min	3600	BC95
24.02.95	NGC 4339	12h21m02.6s	+06°21′33″.0	20 maj	2700	BC95
24.02.95	NGC 4339	12h21m02.7s	+06°21′26″.0	110 min	2700	BC95
24.02.95	NGC 4239	12h14m42.6s	+16°48′24″.4	115 maj	5400	BC95

Table 2.4: Actual observed galaxy sample. The date of each observation is given in column 1. Columns 3 & 4 list the actual RA and Dec for which each observation was obtained. Column 5 gives the position angle of the observation with sense North through East; positions corresponding to the major (maj) and minor (min) axes are indicated. Column 6 lists the exposure time in seconds and column 7 indicates the CCD detector used to obtain each observation (BC94 = Blue Channel 1994, BC95 = Blue Channel 1995).

Two different types of stellar observation were made: *"trailed"* and *"rocked"*. "Trailed" spectra were obtained by placing the stellar image at the end of the slit and trailing the stellar image along the length of the slit with the telescope slightly de-focussed. The measurement of galaxy kinematics is simplified greatly where the instrumental broadening can be assumed to be similar for both galaxy and stellar template spectra. This is a central assumption of the FCQ method used here and to help ensure this was accurate, a second type of stellar observation, a "rocked" stellar frame, was taken for each star observed: a "rocked" spectrum was created by trailing the stellar image *across* the slit at regular intervals (10-20 arcsecs) along the slit length. This ensured that the slit was identically illuminated by both the stellar and galaxy images.

In the afternoon before each night of observations most of the necessary calibration observations were made.

A stack, ~16-49 frames taken consecutively, of *zero-second* exposures of the bias level were obtained. On the first night of each observing run the optimal focus setting for the entire CCD array was decided. A series of comparison lamp spectra were taken for a range of different focus settings. The IRAF task **specrcor** was used to measure the point-spread function for a range of identified spectral lines at different positions along the slit length of each frame. The focus setting adopted was a compromise between achieving the sharpest and most uniform focus for all positions within the CCD array.

Dark exposures of 1 hour duration were taken for each observing run. These were used to decide whether a dark correction was necessary. Such long exposures also enabled significant light leaks to be identified. The mean pixel intensity for dark frames taken during all observations made, was found to very low, $\sim 4 \pm 2ADU$. It was therefore decided that a correction for dark signal should *not* be made for all nights of observation. It should be noted however that the dark current signal was removed during the sky subtraction.

To perform flat-fielding a series of flat-field exposures of an incandescent lamp were obtained. To simulate the night sky illumination in the flat-field correction and to correct for the variations in the width of the slit along its length, exposures of the twilight night sky were made in the evening before or morning after the main galaxy and stellar observations of each night.

To enable a wavelength calibration and geometrical rectification of the object CCD frames (i.e. stellar and galaxy frames) to be performed, exposures of standard arc lamp spectra were obtained. For our wavelength range a combination of *He-Ar* and *Neon* comparison lamp sources was chosen to provide the largest number of strong regularly-spaced spectral lines. These sources were observed simultaneously during all comparison lamp exposures. Comparison exposures were taken for each stellar and galaxy exposure. For the longer galaxy frame exposures a comparison exposure of 2-5 minutes was taken both *before and after* the exposure; this enabled the effect of any gradual shifting in the instrumental set-up to be detected and a more accurate geometrical correction to be made for the galaxy frame. For a given star, a single comparison exposure of ~2-4 minutes was obtained for *both* the 'rocked' and 'trailed' exposures for that star where these were taken consecutively. Time-permitting a stack (5-20) of comparison lamp frames were taken for each night: when median-combined these provided a high signal-to-noise reference spectrum to complete the wavelength calibration of all comparison lamp frames.

2.2 Reduction

Before any accurate scientific measurements may be derived, spectral frames must undergo a series of processes to remove effects other than those produced by the objects under study. To achieve our scientific objectives the following steps were performed: subtraction of the bias level (2.2.1), trimming of the CCD frame (2.2.2), correction for bad-pixel columns (2.2.3), removal of cosmic ray hits (2.2.4), flat-fielding (2.2.5), wavelength calibration (2.2.6) and geometrical rectification (2.2.7), subtraction of the background sky signal (2.2.8) and correction for chromatic focus variations (2.2.9). All steps were completed separately for each night of observation.

The bulk of all reduction steps described were performed using IRAF (Image Reduction and Analysis Facility). To complete the measurement of galaxy kinematics, steps were required in addition to those outlined above; these steps were performed using both IRAF and the MIDAS image processing package of ESO and will be described in section (2.2.10).

2.2.1 Bias Subtraction

Subtracting the bias signal for each pixel involved two steps: the mean level of bias for each CCD frame was subtracted by the *overscan correction*; the typical pixel-to-pixel variation in the bias was then removed by subtracting a median-combined *bias* frame.

The Analogue-to-Digital Convertor (ADC) of the CCD was unable to handle electronic signal corresponding to negative values, e.g. a signal for negative value of -5 may typically be converted by the ADC to a very large positive number, e.g. 2^8-5. This problem can seriously affect for example measurement of the RMS spread in pixel intensity across the array. To prevent this a pedestal value called the *bias level* was added to the signal for each pixel. This helped to ensure that signals corresponding to positive values only were handled by the ADC. To subsequently subtract this bias level a bias subtraction was performed.

A precise measure of the value and of the row-to-row variation in the bias level for each observation was measured using signal stored within an *overscan strip* situated at the edge of each CCD frame. To *overscan correct* a given frame the average profile for all columns within the overscan strip was determined to produce a single column profile for each frame. A best-fit polynomial was found for this profile, typically a 9^{th} order legendre function, and then subtracted from the profiles of each column across the CCD frame. An example of a fit to the overscan region is given in figure 2.1. The overscan correction was applied to all CCD frames including the zero-second exposures taken to complete the bias correction. The overscan strip was finally trimmed from each frame.

The overscan correction subtracted a mean measure of the bias level in the direction of the columns of each frame and therefore did not account for variation in bias between columns. To remove a typical pixel-to-pixel representation of the bias level, a stack of zero-second exposure bias frames were taken for each night of observation: these exposures read the bias and no other signal for each pixel. All bias frames were *median-combined* to reduce the uncertainty in the bias signal level. This selected the median of all signal values for each pixel (or mean of the two central values where the number of bias frames is even); this was preferred to taking the average because of the problem of very high signal values associated with cosmetic defects. The median-combined bias

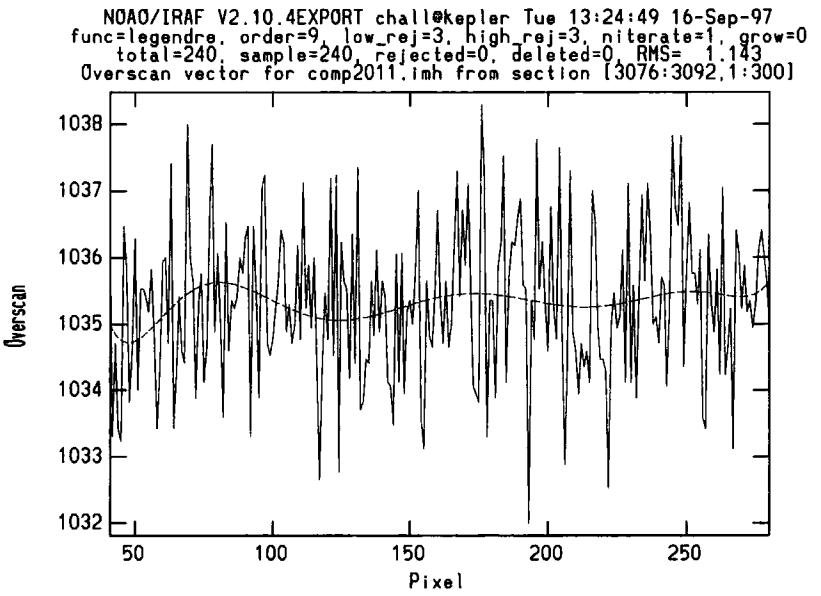

Figure 2.1: An example of a typical overscan correction level and its fitted function. The axis of ordinates (y-axis) is given in pixel intensity units.

frame was then subtracted from all CCD exposures taken for that night.

2.2.2 Trimming of CCD Frames

Although the CCD array was "windowed" at the telescope, evidence of vignetting was still found in the final CCD frames. The most affected areas were decided by studying the intensity profiles of a selection of frames, i.e. sky flat-field frames, stellar ("trailed") frames and galaxy frames. After the overscan correction and before subtraction of the median-combined zero-second exposure frame, all CCD frames were typically trimmed to an area of 3072 by 240 pixels by removing 30-40 pixel rows from both edges of each frame.

2.2.3 Removal of Bad Pixel Areas

To locate bad pixel areas a range of CCD frames were displayed, i.e. the median-combined bias and flat-field frames and different object frames. The dynamic range of the display was changed and bad pixel areas were identified as those of high contrast in intensity compared to neighbouring pixels. These areas were bad pixel columns (typically 1-3 columns), or regions of charge traps or unresponsive pixels at the edges of the CCD frame. Selected bad pixel areas were interpolated over within object, flat-field and dark frames using the IRAF **fixpix** routine. Small clusters of very unresponsive pixels were later removed by **lineclean** during steps to remove cosmic rays (section 2.2.4).

2.2.4 Removal of Cosmic Ray Hits

During exposures to obtain galaxy spectra, typically 1 hour, ~200 cosmic ray hits were detected by the CCD array. These varied in both shape and size, from occupying small 3x3 pixel areas to larger extended features of 20 pixels in length. The intensity for all pixels affected by hits was saturated. Some smaller areas of cosmic ray hits were detected during the stellar exposures which were treated using the IRAF task **cosmicrays**. For the galaxy frames and stellar frames where cosmic ray hits were unsuccessfully removed using **cosmicrays**, the **lineclean** was used instead as described below. These steps were performed after all main reduction steps besides geometrical rectification and sky subtraction had been completed.

To remove cosmic ray hits from the galaxy frames the IRAF routine **lineclean** was applied. This routine removed cosmic rays hits by fitting a function to each row of the CCD frame and replacing pixel values occurring outside particular sigma rejection levels by the value of the fitted function. To decide parameters for this routine a function was fit interactively for various rows within both the stellar and galaxy frames. A high order, typically 20^{th} order, legendre function was fit for each row. This followed the continuum for both stars and galaxies. The low and high rejection sigmas (σ_r) for each fit were chosen to ensure that no recognised spectral features in either the galaxy or stellar spectra were rejected from the fitted relation and subsequently interpolated by **lineclean**. For the galaxy frames low and high σ_r's of 16 and 4 respectively were chosen. This choice did not remove all cosmic rays hits but was decided as a compromise between removing cosmic rays and preventing any spectral features of the galaxy spectra itself from being affected. For stellar frames where cosmic rays had not been successfully removed by **cosmicrays**, particular care was taken to ensure that the sharper stellar lines were not mistaken for the cosmic ray hits. In this case low and high σ_r's of 16 and 8 respectively were chosen.

2.2.5 Flat-Fielding Corrections

Corrections for variations in pixel sensitivity across the CCD array were made by *"flat-fielding"* all frames. Different flat-field frames were taken for each night as described in section 2.1.3. All lamp and sky flat frames obtained were median-combined to produce single lamp and sky flat-field correction frames respectively for each night of observations. The flat-field correction was performed in a number of steps, the ultimate aim of which was to produce a single flat-field frame whose pixel-to-pixel spatial variations would depend solely on the sensitivity of the CCD frame.

A *"response"* frame was created from the median-combined lamp flat-field frame. To remove the smooth shape of the tungsten lamp spectral energy distribution from this frame a 50^{th} order cubic spline function was fitted to the averaged pixel intensity profile for all rows as shown for example in figure 2.2. This best-fit function was divided into each row of the median-combined lamp flat-field frame.

In figure 2.2 it is clear that there is a sharp decrease in the level of illumination for columns ~1-280 and ~2860-3072. This was similarly observed for other flat-field calibration frames, for all nights of observations. After a full data reduction, sharp decreases in the spectral continuum level of both the stellar and galaxy frames still existed for these columns, which were found to correspond to the spectral absorption features C4668 (centred at ~4677Å) and NaD (at ~5893Å)

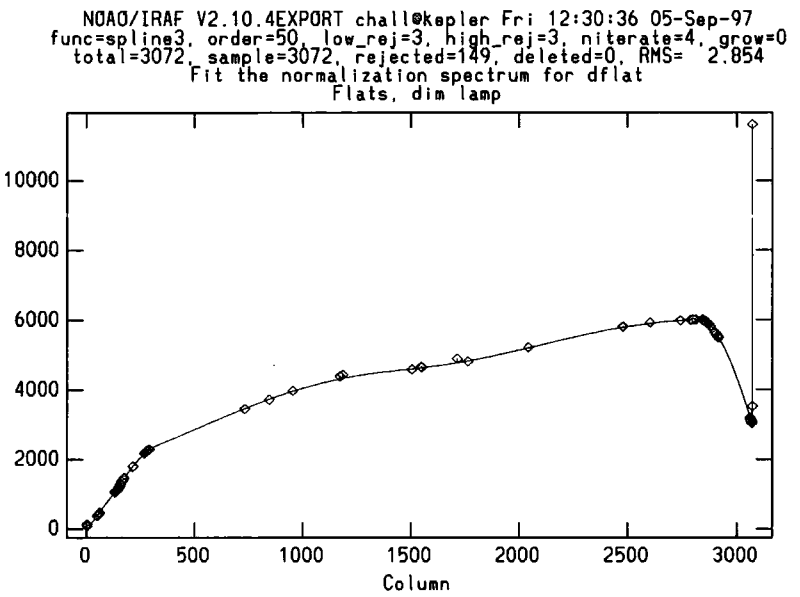

Figure 2.2: The fitted function for the averaged pixel intensity profile for all rows of the median-combined dome-flat frame. The sharp discontinuity corresponding to column 3072 is due to an uncorrected bad pixel column. The axis of ordinates is given in pixel intensity units.

of the Lick/IDS line-strength system. The measurements of both indices as a result, were found to be badly affected. It was decided that both the C4668 & NaD spectral features be omitted from later stages of analysis, and indeed that all subsequent analysis be restricted to the wavelength range corresponding to the columns ~280-2860.

The CCD array was illuminated differently by the tungsten lamp and the actual night sky. To take this effect into account and to correct for variations in the width of the spectroscopic slit with length, an illumination correction ("illumination") frame was created. The median-combined sky flat frame was divided by the newly-created "response" frame to correct for spatial variations in CCD sensitivity. Pixels along the dispersion axis of the resultant frame were divided into 20 different bins to create an "illumination" frame using the IRAF task **illumination**. A 11^{th} order legendre function was then fitted to the averaged profiles for columns of each bin with a low and high rejection clipping of 2σ (see figure 2.3).

To create a final normalised flat-field frame the "response" frame was then multiplied by the "illumination" frame to correct for differences in illumination of the CCD frame. This produced a frame whose pixel-to-pixel intensity variations represented changes both in the CCD sensitivity and in the level of illumination across the CCD array. All galaxy, stellar and comparison lamp frames were flat-fielded by dividing each by this final flat-field frame. A final check was made to ensure all bad pixel areas had been successfully removed by either **fixpix** or by flat-fielding. Any remaining features were treated by **fixpix** as described in section 2.2.3.

2.2.6 Wavelength Calibration

An important prerequisite to the analysis of spectral data is the definition of an accurate wavelength calibration. Since the data presented here are long-slit spectra, this calibration was performed for

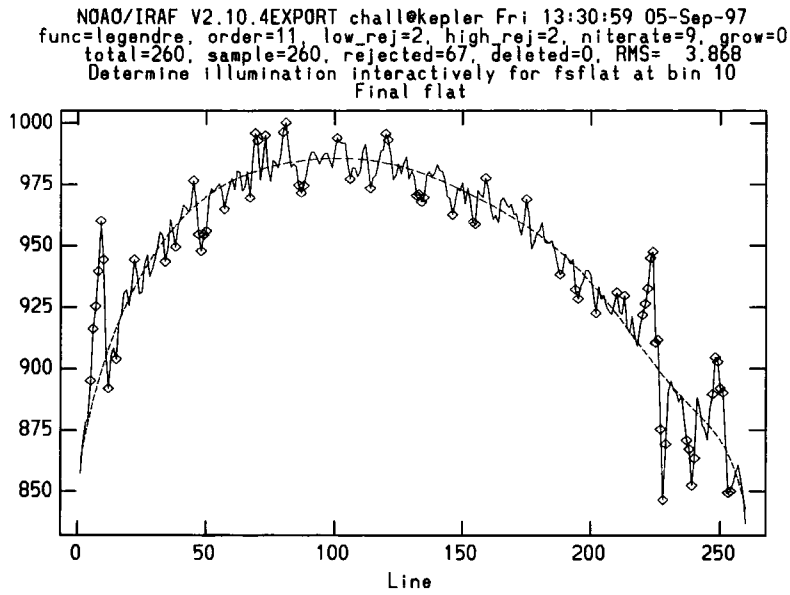

Figure 2.3: Fitted function for a single aperture of "response-corrected" median-combined sky flat frame to derive illumination-correction frame. The axis of ordinates is given in pixel intensity units.

different positions along the direction of the spectrograph slit. This was necessary because light passing through a spectrograph system suffers distortion (e.g. S-distortion) such that its subsequent position on a CCD detector need not necessarily be a linear function of its wavelength.

A wavelength calibration was completed using the HeNe+Ar comparison lamp exposures obtained for each object frame as described in section 2.1.3. The concept was to relate the positions of spectral lines across each calibration frame to specific values of wavelength. Where available a "best" comparison frame, i.e. one for which spectral lines could most easily be identified, was chosen: this was usually the comparison frame of the longest exposure time or where a stack of comparison lamp frames had been obtained, the median-combined frame of this stack. This was then used to help identify similar features in the other comparison lamp spectra where identification proved difficult. Spectral lines were "identified" for an aperture, i.e. 10 rows, centred on the middle row of this frame, using the IRAF task **identify**: a few of the stronger spectral lines were marked interactively and a first guess value of wavelength was entered for each; this value was compared against a list of wavelengths for known features of the HeNe+Ar lamp spectrum; where a value, subject to certain criteria, was found to closely match the value entered it was taken to be the feature wavelength. This procedure defined a preliminary calibration function of pixel column number against wavelength. This was typically fitted using a 4^{th} order legendre polynomial. This basic calibration was used to "identify" other features within the aperture spectrum. A check was made by "zooming" into the identified features: any very asymmetric or very weak line was removed from the calibration fit. A 9^{th} order legendre polynomial was finally fitted for all identified features. An example of the non-linear component of such a fit is given in figure 2.4.

Using **reidentify**, the calibration function determined for the middle aperture of each comparison frame was applied to similarly identify spectral features within apertures of similar size covering all rows of the frame. The wavelength calibration was completed for all apertures to a typical RMS uncertainty of $\sim$0.05Å.

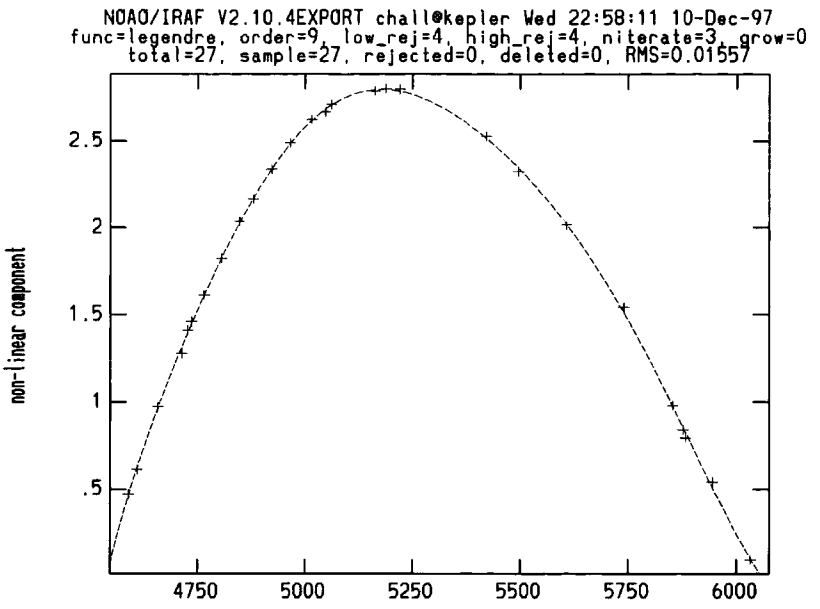

Figure 2.4: Non-linear component of the best-fit function for a single aperture centred on the middle row within a HeNe+Ar comparison lamp frame, relating the pixel columns of identified spectral features to their wavelengths. The axis of abscissas (x-axis) corresponds to the value of wavelength assigned to each identified feature in angstroms.

2.2.7 Geometrical Rectification

In later analysis it was critical that the object frame spectra be perfectly aligned with both the rows and columns of each frame, i.e. that each column of the CCD frame correspond to a unique value of wavelength for all rows and that spectra for all positions along the slit length be aligned in the direction of the CCD rows. To ensure that this could be accurately assumed a geometrical rectification of each object frame was performed. An important stage towards achieving the first requirement, alignment of spectral lines with the columns of each frame, was completion of the wavelength calibration as described in section 2.2.6 above. To achieve the second requirement, alignment with rows, the positions of strips of spectra within "rocked" spectra were traced across the dispersion axis. Using **identify** and **reidentify** and applying a similar procedure to that adopted for the wavelength calibration, the positions of peaks corresponding to the centres of the stellar images were identified for apertures spaced at regular intervals of 50 columns along the dispersion axis. Examples of the typical peaks identified within a single aperture are given in figure 2.5.

To perform the geometrical alignment, "distortion" maps were created using the IRAF task **fitcoords** by fitting a three-dimensional surface to the positions of spectral features identified across each calibration frame and to the positions of the strips of spectra within the rocked stellar frames. Fits were obtained separately for each comparison frame and for the "rocked" frames a single fit was made for the positions of apertures for all frames: for both cases a 12th order polynomial was fitted to the positions in the dispersion direction and a 6th order polynomial in the direction of the spectroscopic slit. During the wavelength calibration of the comparison frames, spectral features had occasionally been identified for only a small fraction of the length of the slit; these corresponded to typically very weak and/or misidentified spectral lines. Where such features

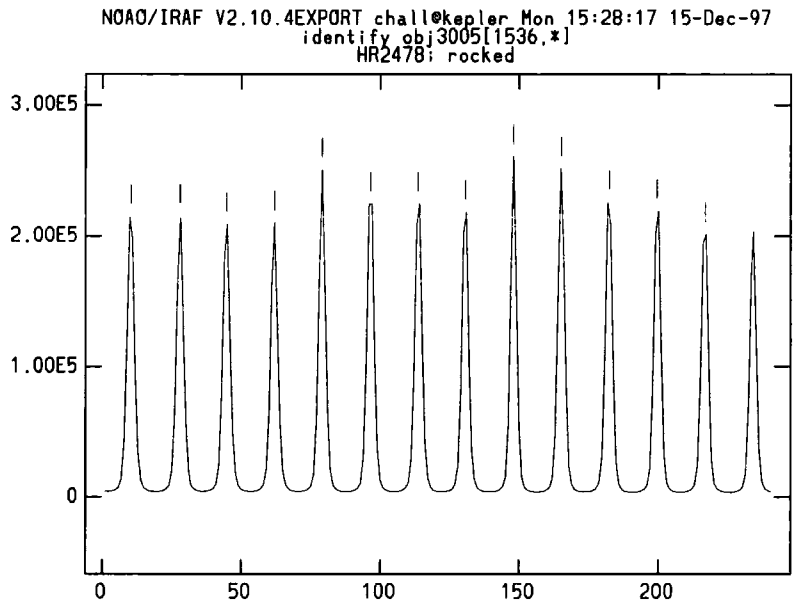

Figure 2.5: Example of peaks identified within "rocked" stellar frames to align the object frame spectra with the rows of the CCD array. The axis of abscissas corresponds to the CCD row number. The axis of ordinates is given in pixel intensity units.

deviated significantly from the fitted function, they were removed from the fit. All fits were made to a typical accuracy of $\leq$0.2 pixels RMS. Examples of fits for a comparison lamp spectrum and for the "rocked" stellar frames are given in figures 2.6 and 2.7 respectively.

In all described above and in section 2.2.6, no actual rebinning of pixels of the object frames took place. The geometrical rectification for each object frame was finally performed by the IRAF routine **transform** using the fits obtained by **fitcoords** for the respective comparison lamp spectra for each spectrum and the "rocked" stellar frames. Pixels across the object frame were rebinned to match functions relating wavelength to different pixel positions, as given by the distortion maps, as closely as possible. Pixels in the direction of the dispersion axis of each frame were rebinned to a linear wavelength scale.

2.2.8 Sky Background Subtraction

Sky subtraction was performed for the galaxy, and stellar "rocked" frames where possible, using the IRAF task **background**. A linear fit was made to the background sky level by selecting rows judged to contain the sky signal alone. For galaxy frames typically 20-30 rows (~12-18 arcsecs) were chosen at the edge of each frame. For "rocked" spectra the sky level was interpolated where possible between regions of sky at both edges of the array. No sky background was subtracted from the "trailed" stellar spectra. A sky signal of typically 15-50 ADU counts was subtracted for each pixel of the galaxy frames. An example of a fit for the sky level for a single column is given in figure 2.8.

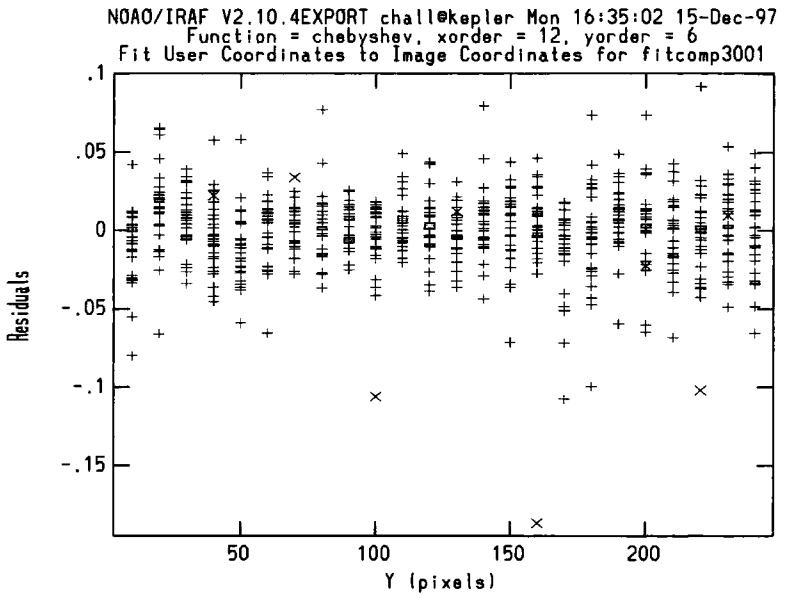

Figure 2.6: Fit for a comparison lamp frame by **fitcoords**. The axis of abscissas corresponds to the rows of the CCD frame and the axis of ordinates to residuals from the surface fitted for the positions of the spectral lines of the comparison frame in pixel intensity units.

2.2.9 Corrections for Focus Variations Along Dispersion Axes

The spectroscopic data presented here was found to be affected by chromatic focus variations across the CCD array. This effect has been found for similar data by González (1993), Davies et al. (1993) and Mehlert (1998). For our galaxy spectra such variations caused the image profile width measured in the spatial direction to vary systematically with wavelength. Uncorrected this affected our measurements of line-strengths and kinematics as functions of radius, particularly for spectra taken using the BC94 chip. A correction similar to a method adopted by Mehlert (1998) was applied using a procedure written by H. Kuntschner, which I adapted. This involved measuring the variation of the width of the galaxy profile by fitting a Gaussian function for apertures at regular intervals across the dispersion axis of each frame.

Before measurement of the galaxy profile, a step was included to correct for any distortion unsuccessfully removed during the basic data reduction. The position of the galaxy centre was traced using the IRAF task **apall** and a legendre polynomial of order 4-40 was fitted to the function of column pixel to galaxy centre. The spectra were then rebinned such that the galaxy centre was perfectly aligned with a single pixel row. The dispersion axis was divided into a series of apertures. Apertures were defined to be a maximum of ~10-20 columns across the dispersion axis of the spectral frame. All columns within each aperture were summed and the average column profile for each aperture was found. A Gaussian function of width σ was then fitted for this averaged profile; only a restricted number of pixel rows were considered in this fit (usually taken to be ~11 rows centred on the galaxy centre), the chosen number of rows being slightly dependent on the shape of the galaxy profile.

A polynomial or cubic spline function was then fitted to the function of column aperture pixel and the measured standard deviation σ_G of the best-fit Gaussian function for each aperture.

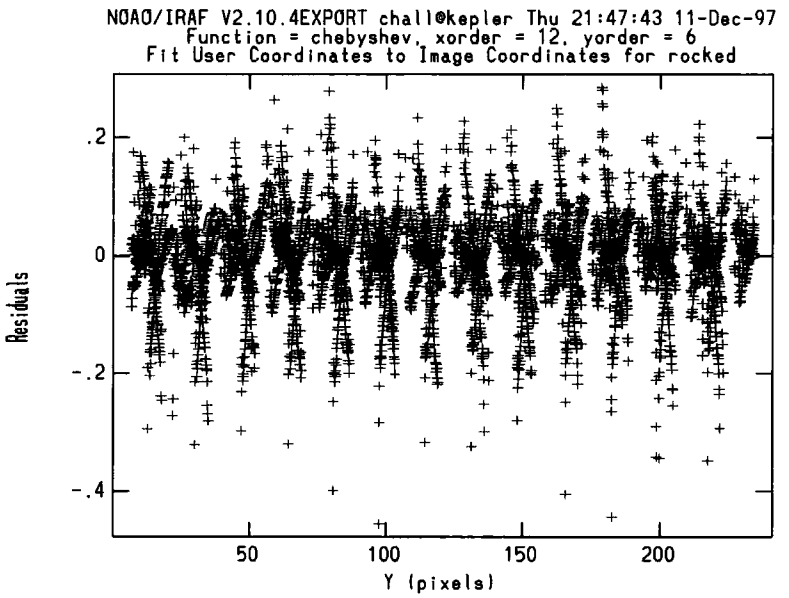

Figure 2.7: Fit by **fitcoords** for *all* "rocked" stellar frames to complete geometrical rectification in the direction of length of the spectroscopic slit. The axes of abscissas and ordinates are as in figure 2.6.

An example plot of both the measurements and the fitted function is given in figure 2.9. The greatest value of σ_G, σ_{MAX}, was chosen interactively using this plot; this was taken to be the maximum measured value for the wavelength range of interest. Since no spectral information was to be derived for wavelengths corresponding to columns ~1-200 and ~2860-3072, measured values of σ_G for these columns were not considered in deciding the maximum value of σ_G. To correct for focus variations, the galaxy pixel intensity profile for each pixel column was then smoothed by a Gaussian function of width σ_{cor} given by,

$$\sigma_{cor}{}^2 = \sigma_{MAX}{}^2 - \sigma_{bf}{}^2 \tag{2.1}$$

where σ_{bf} was taken to be the Gaussian width fitted for *each* column using the best-fit function decided for the function of column aperture pixel and σ_G.

Values of σ_{MAX} decided and of the minimum value of σ_{bf} obtained for each spectrum (σ_{MIN}), is given in Table 2.5.

A focus correction was applied for all galaxy spectra observed using the BC94 chip. For spectra taken using the BC95 chip, variations in measured σ_G were found to be extremely small (i.e. <0.2 pixels) and for all but 2 spectra (i.e. the major and minor spectra of NGC 4339) no correction was applied.

2.2.10 Additional Preparatory Steps for Measurement of Kinematics

The FCQ method used to measure the galaxy kinematics as described in Chapter 3, requires steps in addition to the basic data reduction described above to prepare the galaxy and stellar

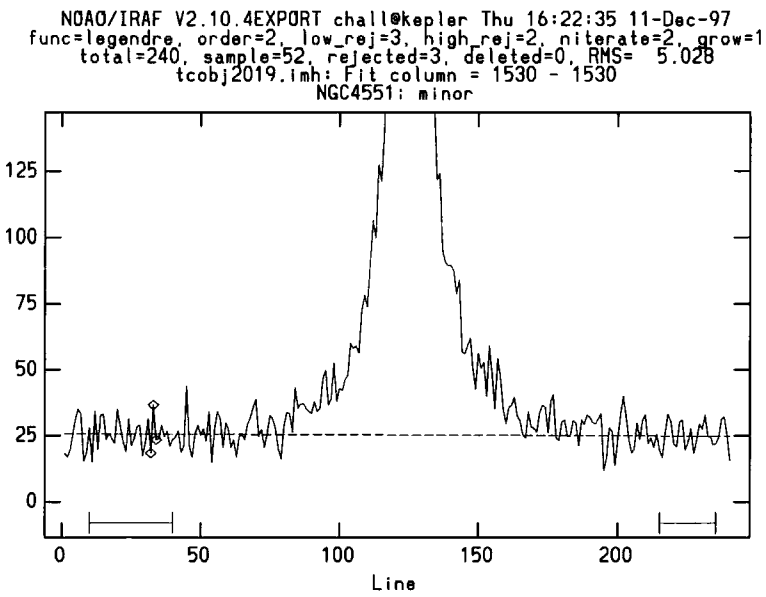

Figure 2.8: Linear fit for the background sky level for a column of the minor axis galaxy frame for NGC 4551. The axis of ordinates is given in pixel intensity units. Row apertures on both sides of the galaxy centre, used to determine the linear fit are indicated.

spectra. Stellar spectra, deredshifted to laboratory wavelengths were required as stellar templates; each galaxy spectrum was required to be perfectly aligned with the rows of their frame and their dispersion axis to be rebinned to a logarithmic scale.

One-dimensional stellar spectra were extracted from the stellar frames. "Rocked" stellar frames were chosen where possible instead of the "trailed" frames since one-dimensional spectra could be created from the two-dimensional frames with greater certainty in the geometrical alignment. A series of one-dimensional spectra were extracted from the "rocked" stellar frame using the IRAF routine **apall**. This routine enabled the position of stellar spectra within each 'strip' to be traced as a function of position across the dispersion axis; a legendre polynomial of order ~10-40 was fitted for the function of dispersion axis and spatial axis co-ordinates of each strip. A check of the relative alignment of all extracted one-dimensional spectra for a given stellar frame, was made by cross-correlating all spectra with respect to a single extracted spectrum using the IRAF task **fxcor**: any spectrum showing a significant shift in relative velocity with respect to all other spectra was removed from the list of spectra combined to produce the final one-dimensional spectrum. This provided a check of the success of extraction of spectra from the stellar frames. A single one-dimensional stellar spectrum was created by combining all selected one-dimensional spectra for each frame using the IRAF routine **scombine**. All one-dimensional stellar spectra were then deredshifted to correspond to laboratory wavelengths. This step was performed by measuring the redshift of the stellar spectrum using a program written by H. Kuntschner: this program measured the positions of various spectral features and compared the values measured for each feature with those of their corresponding laboratory wavelengths; a single value of redshift was then taken as the mean value of redshifts measured for all features. Finally the IRAF task **dopcor** was used to deredshift the spectrum to correspond to zero rest wavelength.

Since spectra were to be transformed to Fourier space, the dispersion axes for all spectra

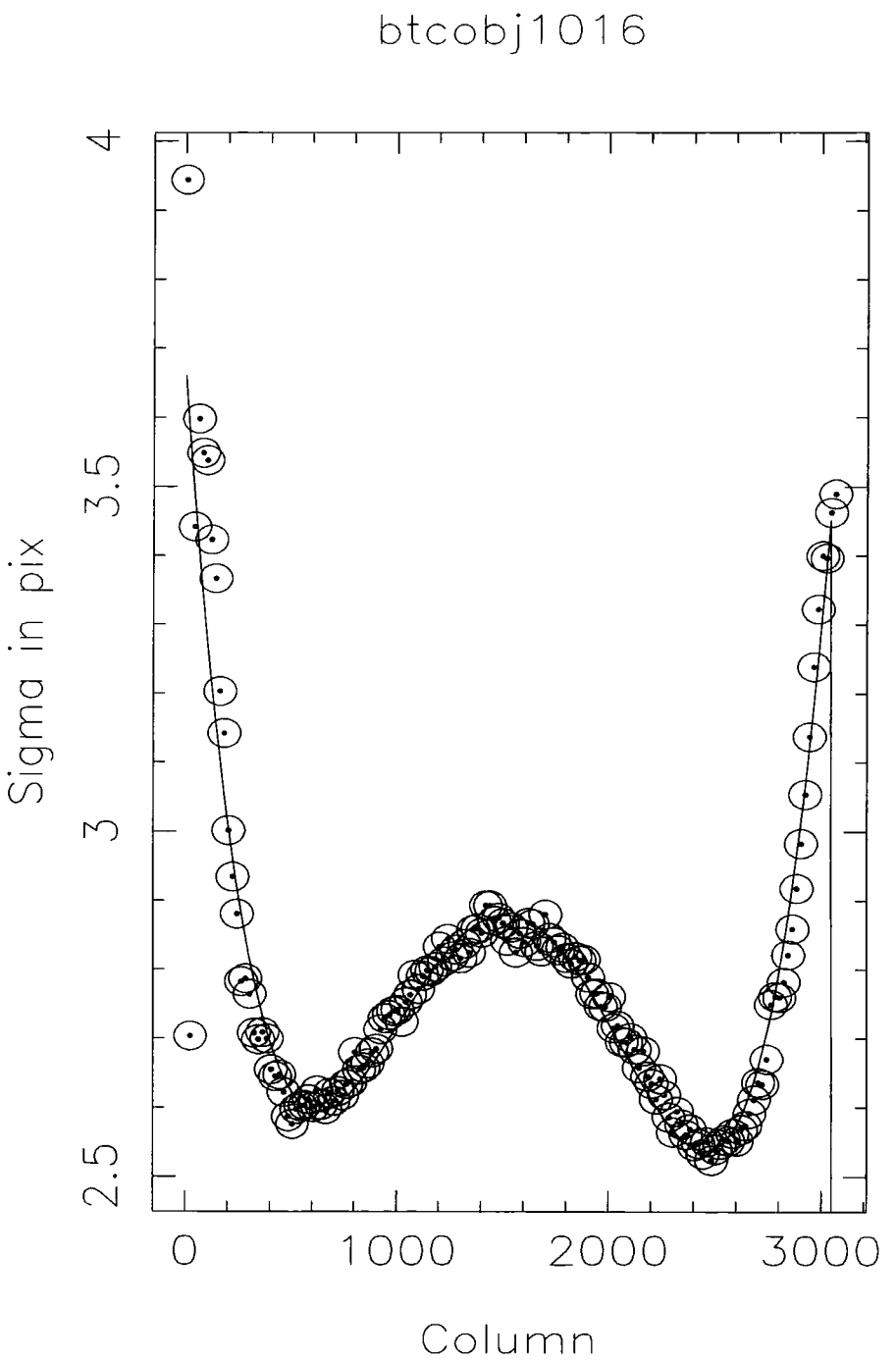

Figure 2.9: Measured values of the best-fit Gaussian width to the galaxy profile for different column apertures across the dispersion axis, and the fitted cubic spline function for these measurements. For this frame a maximum σ_G of 2.9 pixels was decided. Column pixel intensities for each aperture were smoothed by a Gaussian of width 2.9^2 - σ_{bf}^2 where σ_{bf}^2 was the best-fit function value for each pixel. This corresponded to a maximum Gaussian smoothing of ~1.38 pixels (~0.83 arcsecs).

Spectrum	σ_{MAX} (pixels)	σ_{MIN} (pixels)	σ_{eff} (arcsecs)
NGC 3605 min	3.44	2.46	1.44
NGC 3605 maj	2.78	2.53	0.69
NGC 4387 maj	2.90	2.52	0.86
NGC 4387 min	2.79	2.49	0.76
NGC 4564 min	2.66	2.32	0.78
NGC 4468 min	2.65	2.27	0.82
NGC 3608 min	3.10	2.62	0.99
NGC 2778 maj	2.80	2.45	0.81
NGC 2778 min	2.90	2.27	1.08
NGC 5582 maj	2.75	2.46	0.74
NGC 4564 maj	2.85	2.50	0.82
NGC 4468 maj	2.60	2.08	0.94
NGC 4464 min	2.55	2.22	0.75
NGC 4464 maj	2.65	2.45	0.61
NGC 5582 min	3.20	2.35	1.30
NGC 3608 maj	3.12	2.65	0.99
NGC 4339 maj	2.64	2.41	0.65
NGC 4339 min	2.53	2.39	0.50

Table 2.5: Details of focus corrections applied to galaxy spectra. The galaxy spectrum frame corrected is given in the first column. The second column gives the maximum measured Gaussian width in pixels decided interactively and the third column, an estimate of the minimum measured value of σ_{bf} in pixels. The fourth column provides an estimate of the the maximum Gaussian smoothing effectively applied, in arcsecs, for the pixel range of ~280-2800; this is the difference in the squares of the second and third columns, multiplied by the spatial scale of 0.″6.

were rebinned to a logarithmic scale. This step was performed within IRAF: the task **dispcor** was used to rebin stellar spectra, and the **transform** task was used to rebin the two-dimensional galaxy frames. For the galaxy frames this step was not performed as part of the basic reduction because additional reduction steps, i.e. focus correction, required the dispersion axis to defined linearly. The FCQ program is customised for MIDAS and all spectra were next transferred to the MIDAS environment. Steps described hereafter were performed within MIDAS. IRAF rebins to a $\log_{10}$ scale whereas a natural logarithmic scale was expected by FCQ in MIDAS. The dispersion coordinates in the header for all frames were therefore recalculated to correspond to a natural logarithmic scale. Prior to measurement of galaxy kinematics it was essential that all galaxy spectra be perfectly aligned with the rows of each CCD frame. This was performed during the basic data reduction but in general not with sufficient accuracy. An additional procedure was applied here: a second order polynomial was fitted to the position of the galaxy centre across the dispersion axis and then used to align the galaxy centre along a single pixel row. The spatial axis for each galaxy frame was changed to a scale in arcseconds and the row identified to be the centre of the galaxy brightness profile was assigned to zero arcseconds.

Chapter 3

Galaxy Kinematics: FCQ method

3.1 Introduction

By analysing the shape of absorption features throughout a given wavelength range a direct measure of the kinematics of the integrated population can be obtained (Sargent et al., 1977; Tonry and Davis, 1979). Advances in detector technology, i.e. larger format CCD arrays of smaller pixel scale, now enable more two-dimensional studies of galaxy kinematics of high spectral and spatial resolution to be made using long-slit spectroscopy. This has led to the study of the line-of-sight velocity distribution at different positions within a galaxy, allowing its kinematical structure to be more tightly constrained (Franx and Illingworth, 1988; van der Marel and Franx, 1993; Bender et al., 1994)

Modelling the dynamical structure of a galaxy can significantly constrain its evolutionary history. There however exists a degeneracy between the effects of mass and velocity dispersion anisotropy on the derived kinematical profiles; to recover the mass density distribution of a given galaxy therefore requires an accurate determination of the velocity dispersion anisotropy, that is an accurate measurement of the line-of-sight velocity distribution (LOSVD). A full determination of the galaxy dynamics would require the measurement of surface brightness profiles and is beyond the scope of this thesis but an accurate measurement of the LOSVD is an important step in achieving this (e.g. van der Marel et al. (1994)).

Until recently many analyses of the LOSVD had fitted a purely *Gaussian* function to the LOSVD to measure its first two moments, namely the streaming velocity and velocity dispersion (σ). To a first approximation, elliptical galaxies are believed to be relaxed dynamical systems. On this basis the distribution of stellar velocities and hence the measured LOSVD, can be assumed to well described by a Maxwellian distribution and approximated by a Gaussian function. Detections of multiple component structures within a number of ellipticals (e.g. kinematically-decoupled cores (Franx and Illingworth, 1988; Jedrzejewski and Schechter, 1988), central disk populations (Rix and White, 1992; van der Marel et al., 1994)) have shown the assumption of a Gaussian LOSVD, to be inaccurate, and to lead to measurements of both rotation and velocity dispersion which are incorrect by typically 10% or more (van der Marel and Franx, 1993). To improve on these earlier measurements, more general parametrisations of the LOSVD have been tested and have been

found to provide a more accurate description of the galaxy kinematical structure (Rix and White, 1992; van der Marel and Franx, 1993; Kuijken and Merrifield, 1998; Zhao and Prada, 1996). Here galaxy kinematics are measured using the Fourier Correlation Quotient (hereafter FCQ) method of Bender (1990). This method is considerably less sensitive to template-mismatching and recovers the LOSVD. The LOSVD is then analysed according to the parametrisation of van der Marel and Franx (1993) as a Gaussian plus Gauss-Hermite series terms, as described in section 3.2, enabling deviations from a Gaussian LOSVD to be detected and quantified.

The main objective of the measurement of galaxy kinematics here is to constrain the kinematical structure of the galaxy as a function of radius. In this Chapter I describe the measurement of the kinematics for our sample of elliptical galaxies. I describe the parametrisation of the LOSVD and discuss how the higher-order terms of this parametrisation can be interpreted as corresponding to particular kinematical structures (section 3.2). I then outline the FCQ method and describe simulations performed to determine appropriate values of optimal parameters required by the FCQ method. I then outline how measurements of kinematics were obtained for each galaxy (section 3.6). The measurements themselves will be presented in Chapter 4.

3.2 Parametrisation of the Line-of-Sight Velocity Distribution

Here the line-of-sight velocity profile is decomposed using a parametrisation proposed by van der Marel and Franx (1993). The LOSVD profile is described by the sum of a Gaussian and the orthogonal functions of the Gauss-Hermite series and is given by,

$$f(y) = I_0 exp\frac{(-y^2)}{2}(1 + H_3\mathcal{H}_3(y) + H_4\mathcal{H}_4(y)) \tag{3.1}$$

where $y = \frac{(\nu_{fit}-\nu)}{\sigma_{fit}}$, ν_{fit} is the measured velocity, ν is the mean of all measured velocities for a given spectrum (i.e. mean radial velocity), σ_{fit} is the measured velocity dispersion and,

$$\mathcal{H}_3(y) = \frac{(2\sqrt{2}y^3 - 3\sqrt{2}y)}{\sqrt{6}} \tag{3.2}$$

$$\mathcal{H}_4(y) = \frac{(4y^4 - 12y^2 + 3)}{\sqrt{24}} \tag{3.3}$$

are the standard Gauss-Hermite polynomials, H_3 and H_4 are their amplitudes, and I_0 is a normalization constant. The function $\mathcal{H}_3$ parametrises the antisymmetric and $\mathcal{H}_4$ the symmetric deviations from a Gaussian. To determine rotation velocity, velocity dispersion and the amplitudes H_3 and H_4, equation (3.1) was least-squares fitted to the LOSVD profile.

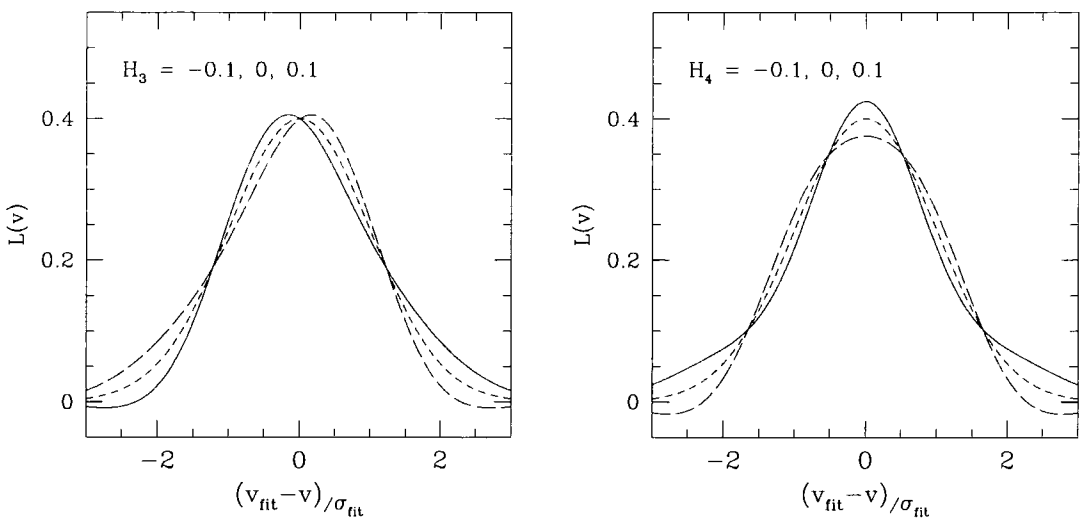

(a) $H_3 = -0.1, 0, 0.1$ (b) $H_4 = -0.1, 0, 0.1$

Figure 3.1: Plots illustrating how particular values of the parameters H_3 and H_4 relate to the shape of the LOSVD. The LOSVD function $f(v)$, defined by equation (3.1), is shown for typical measurements of v_{fit} and σ_{fit}. In both (a) & (b), the Gaussian function is plotted by a short-dashed line. In figure 3.1(a), H_4 is assumed to be zero; the solid line corresponds to $H_3 = 0.1$ and the long-dashed line to $H_3 = -0.1$. In figure 3.1(b), $H_3 = 0$; the solid line corresponds to $H_4 = 0.1$ and the long-dashed line to $H_4 = -0.1$. This figure is similar to figure 1 of van der Marel & Franx (1993).

I now briefly discuss how the parameters H_3 and H_4 can be interpreted as representing particular kinematical structures. Clearly differentiating between the possible orbital structures using kinematical measurements alone however is difficult and we can at best show the measurements to be consistent with the existence of particular structures.

As noted by Gerhard et al. (1998), the steepness of the luminosity density profile will have an important effect on the measured LOSVD: for the most steeply decreasing luminosity density profiles, stars moving close to the *tangent point* [1] for the projected position of the galaxy will have a more pronounced effect on the measured LOSVD. No detailed consideration of this effect is made here. It is noted however that ellipticals of the luminosity range of our sample have been found to have power law surface brightness profiles in towards the HST resolution limit (e.g. Lauer et al. (1995)). Measurements of the LOSVD are therefore expected to be influenced most significantly by motion close to the tangent point.

3.2.1 The H_3 Term

The antisymmetric H_3 term defined in equation (3.1), measures the asymmetry of the LOSVD. This can clearly be seen in figure 3.1(a) which illustrates the effect of a non-zero value of H_3. Measured asymmetries for elliptical galaxies can be shown to have a range of different causes, e.g. rotation, the superposition of a slowly rotating bulge and more rapidly rotating disk component, and the

[1] The tangent point, as defined by Gerhard (1993), is the position in the galaxy at which the line-of-sight with distance R from the projected galaxy centre, touches the spherical shell of true radius R.

projection of rotation along the line-of-sight. Smaller, less luminous ellipticals, the class of object studied here, are found to be well described by isotropic rotator models and to be supported by rotation without the need for anisotropy (Davies et al., 1983). Measured asymmetries are expected to be greater for these galaxies than for the more luminous ellipticals which are believed to be supported instead by velocity dispersion anisotropy. Greater asymmetries have been measured however, for ellipticals with detected kinematically-distinct components, (e.g. decoupled cores (Franx and Illingworth, 1988; Jedrzejewski and Schechter, 1988)).

3.2.2 The H_4 Term

The H_4 term quantifies the symmetric deviations of the LOSVD from a Gaussian. Figure 3.1(b) illustrates how particular measured values of H_4 relate to the shape of the LOSVD. These plots are similar to theoretical model predictions for non-rotating elliptical galaxies (e.g. van der Marel and Franx (1993)). The distribution corresponding to $H_4 = 0.1$, i.e. the solid line of figure 3.1(b), corresponds to a distribution more peaked than a Gaussian at small velocities and with more extended high velocity tails. This is similar to predictions for radial anisotropic models at intermediate radii (Gerhard, 1993). For the spherical anisotropic models presented by Gerhard (1991), extended tails similar to those shown here are reproduced for stellar density profiles that decrease sufficiently slowly with radius. In this instance the wings are interpreted as the detection of stars moving on high-velocity radial orbits, close to their perigalacticon. For the more general interpretation of LOSVD measurements however, this LOSVD shape can correspond to the detection of different orbital families depending on the projected radial position from the galaxy centre. Close to the galaxy centre, a measurement of $H_4 = 0.1$ could represent the detection of more side-on orbits and possibly the presence of a central disk. At greater radii, it would instead be consistent with detection of more radial orbits, i.e. stars moving radially towards or away from the galaxy centre, corresponding to *radial anisotropy*: this is similar to the case discussed above.

Conversely, distributions *less* peaked than a Gaussian (e.g. the long-dashed line of figure 3.1(b)) can be interpreted as corresponding to more radial orbits close to the galaxy centre, and to more tangential motion and *tangential anisotropy* at larger radii.

3.3 The Fourier-Correlation Quotient Method

3.3.1 Introduction

Bender (1990) developed the Fourier-Correlation Quotient (FCQ) method to recover the galaxy broadening function, (i.e. the LOSVD), enabling the shape of the broadening function and thus the kinematic structure of the galaxy to be accurately determined. The FCQ method is relatively insensitive to *template mismatching*, a problem caused by a choice of stellar template which does not reflect the mixture of stellar populations within a given galaxy. For previous methods such as e.g. the Fourier quotient method, template-mismatching was a particular problem. As will be shown the FCQ method reduces the adverse effect of mismatching by deconvolving only the *peak* of the template-galaxy correlation with the autocorrelation function of the template.

In this section I describe the FCQ method (section 3.3.2). I then describe the application of a Wiener filter to reduce the effects of high-frequency noise (section 3.3.3). I will outline the steps required to prepare spectra before application of the FCQ method in section 3.4.

3.3.2 Description of method

The Fourier-Correlation Quotient method is based on the deconvolution of the correlation peak of the template-galaxy correlation function $K_{S,G}$ with the peak of the autocorrelation function of the template star $K_{S,S}$.

The method is based on the following assumptions:

1. all basic reduction steps, including sky-subtraction, have been performed and spectra have been rebinned on to a logarithmic scale;
2. the intrinsic width of absorption lines in the spectra of both the template star and the typical component stars of the galaxy is neglible compared to the instrumental broadening;
3. the instrumental broadening profile does not vary significantly within the wavelength range of each spectra and is identical for both stellar and galaxy spectra;
4. the spectral continuum level is successfully removed by dividing by a low-order polynomial.

Based on these assumptions a typical stellar spectrum can be given by,

$$S(x) = \sum_m \alpha_m L(x - x_m), \tag{3.4}$$

where $L(x - x_m)$ is the instrumental broadening profile, x_m the position of the m^{th} spectral line, α_m the line strength, and the variable x corresponds to $ln\lambda$.

A galaxy spectrum can similarly be described by the convolution of the instrumental profile and the line-of-sight velocity distribution or broadening function $B(x - y)$, i.e.,

$$G(x) = \int B(x - y) \sum_m \beta_m L(y - x_m) dy, \tag{3.5}$$

where β_m is the line strength of the m^{th} spectral line.

The template-galaxy correlation function is defined by,

$$K_{S,G}(z) = \int G(x + z) S(x) dx, \tag{3.6}$$

and the autocorrelation function of the template by,

$$K_{S,S}(z) = \int S(x+z)S(x)dx. \tag{3.7}$$

Inserting equations 3.4 and 3.5 into equations 3.6 and 3.7 we obtain,

$$K_{S,G}(z) = \sum_{m,n} \alpha_m \beta_n \{ \int B(z-u)L(y-x_n)L(y-x_m-u)dydu \}, \tag{3.8}$$

and,

$$K_{S,S}(z) = \sum_{m,n} \alpha_m \alpha_n \{ \int L(y-x_n)L(y-x_m-z)dy \}. \tag{3.9}$$

Transforming to Fourier space yields,

$$\tilde{K}_{S,G}(k) = \sum_{m,n} \alpha_m \beta_n e^{ik(x_n - x_m)} \tilde{B}(k)\tilde{L}^*(k)\tilde{L}(k), \tag{3.10}$$

$$\tilde{K}_{S,S}(k) = \sum_{m,n} \alpha_m \alpha_n e^{ik(x_n - x_m)} \tilde{L}^*(k)\tilde{L}(k) \tag{3.11}$$

where $\tilde{A}$ is the Fourier transform of function A and $\tilde{L}^*(k)$ is the complex conjugate of $\tilde{L}(k)$.

Taking the ratio of $\tilde{K}_{S,G}(k)$ and $\tilde{K}_{S,S}(k)$ we obtain:

$$\frac{\tilde{K}_{S,G}(k)}{\tilde{K}_{S,S}(k)} = \frac{\sum_n \beta_n e^{ik(x_n)}}{\sum_m \alpha_m e^{ik(x_m)}} \tilde{B}(k); \tag{3.12}$$

This result is almost identical to that obtained by the Fourier quotient method by taking the ratio of the Fourier transforms of the galaxy spectrum ($\tilde{G}$) and the stellar spectrum ($\tilde{S}$). To recover $\tilde{B}(k)$ from this expression, little or no template-mismatching is required which in practice in very difficult to achieve.

The Fourier Correlation Quotient method reduces this sensitivity to template-mismatching by taking the ratio of solely the **peaks** of both $\tilde{K}_{S,G}(k)$ and $\tilde{K}_{S,S}(k)$. To illustrate this step, equations 3.8 and 3.9 can be rewritten as the sums of two parts, the first part corresponding to the cross-correlation peaks i.e. $m = n$, and the second to that for all $m \neq n$:

$$K_{S,G}(z) = \{\sum_m \alpha_m\beta_m \int B(z-u)L(y-x_m-z)L(y-x_m-u)dydu\}$$
$$+\{\sum_{m\neq n} \alpha_m\beta_n \int B(z-u)L(y-x_n)L(y-x_m-u)dydu\} \quad (3.13)$$

$$K_{S,S}(z) = \{\sum_m \alpha_m^2 \int L(y-x_m)L(y-x_m-z)dy\}$$
$$+\{\sum_{m\neq n} \alpha_m\alpha_n \int L(y-x_n)L(y-x_m-z)dy\} \quad (3.14)$$

To be able to clearly distinguish the correlation peaks it is critical that the peaks do not interfere with the neighbouring secondary peaks. The separation of the correlation peak and the next secondary peak of the correlation function depends on the minimum separation of the spectral lines $d_{min} = \mid x_m - x_n \mid_{min}$. Assuming the typical widths of the galaxy broadening function, $B(x)$, and the instrumental broadening function, $L(x)$, to be σ_B and σ_L respectively, the correlation peak will not interfere with the secondary peak where $d_{min} \gtrsim 4 \cdot \sqrt{\sigma_B^2 + 2\sigma_L^2}$. In this case we then consider the interval $[-d_{min}, +d_{min}]$ about the correlation peaks.

Taking the ratio of only the cross-correlation peaks we then obtain

$$\frac{\tilde{K}_{S,G}^{peak}(k)}{\tilde{K}_{S,S}^{peak}(k)} = \frac{\sum_m \alpha_m\beta_m}{\sum_n \alpha_n\alpha_n}\tilde{B}(k) \quad (3.15)$$

which can be rewritten

$$\frac{\tilde{K}_{S,G}^{peak}(k)}{\tilde{K}_{S,S}^{peak}(k)} = constant \cdot \tilde{B}(k). \quad (3.16)$$

This clearly recovers $\tilde{B}(k)$ independently of template-mismatching.

The isolation of the correlation peaks is more complicated where $d_{min} < 4 \cdot \sqrt{\sigma_B^2 + 2\sigma_L^2}$. This is the case where a wavelength range crowded with spectral lines is chosen, e.g. the region surrounding the Mg triplet feature which is considered here. From equations 3.10 and 3.11, it can be shown that the *stronger* spectral lines have a more pronounced effect on the problems of template-mismatching than the weaker lines. Provided the stronger lines are sufficiently well-spaced the interference of the central correlation peak with the neighbouring secondary correlation peak should not significantly affect our results. This is clearly the case here: $d_{min} \sim 4 - 5$Å, far smaller than the separation of for example the Mg_b and Fe5270 Lick/IDS defined spectral features.

3.3.3 Application of a Wiener Filter

In practice the measured galaxy spectrum is affected by noise. The effect of this on the recovery of the broadening function is now considered. The galaxy spectrum is rewritten as

$$G_N(x) = G(x) + N(x) \tag{3.17}$$

where $N(x)$ is the component of noise. The deconvolution of the correlation peaks then becomes,

$$\frac{\tilde{K}^{peak}_{S,G}(k)}{\tilde{K}^{peak}_{S,S}(k)} = \frac{\sum_n \alpha_m \beta_m}{\sum_n \alpha_n^2} \tilde{B}(k) + \frac{\sum_l \alpha_l e^{-i\kappa x_l}}{\sum_m \alpha_m^2} \cdot \frac{\tilde{N}(k)}{\tilde{L}(k)}. \tag{3.18}$$

In the transform domain the instrumental broadening $L(k)$ will contribute at frequencies $\lesssim 2\sigma_{instrum}$ where $\sigma_{instrum}$ is the corresponding frequency of the instrumental broadening in the Fourier domain. A component of noise $N(k)$ however will contribute at a far broader range of frequencies, leading to a strong amplification of signal in the deconvolution at high frequencies. The standard solution to this problem is the application of a Wiener filter, a detailed description of which has been given by Brault & White (1971). The basic principle of this method is to model the noise-affected signal, here the galaxy-template correlation function, $K_{S,G}$, by a Wiener filter. The Wiener filter is given by

$$W(k) = \frac{|\tilde{G(k)}|^2}{|\tilde{G(k)}|^2 + |\tilde{N(k)}|^2} \tag{3.19}$$

where $\tilde{G(k)}$ and $\tilde{N(k)}$ are the power spectra of the galaxy and noise signals respectively. Since $\tilde{G(k)}$ and $\tilde{N(k)}$ cannot at this stage be determined directly, an optimal value for the Wiener filter is *estimated*. Here this estimation is performed by using Monte-Carlo simulations as described in section 3.5. The broadening function may then be recovered as

$$B(k) = \Gamma \cdot \int \frac{\tilde{K}^{peak}_{S,G}(k)}{\tilde{K}^{peak}_{S,S}(k)} W(k) e^{-ikx} dk \tag{3.20}$$

where Γ is a normalisation constant.

3.4 Preprocessing of Spectra

Before any kinematical information can be derived by the FCQ method, all spectra must undergo a series of preparatory steps in addition to the data reduction described in Chapter 2: a particular

wavelength range is extracted for both stellar and galaxy spectra; galaxy spectra are rebinned to a minimum required signal-to-noise ratio in the spatial direction; the shape of the best-fit continuum level must be decided and then removed for both stellar and galaxy spectra; the end regions of spectra are then tapered by a cosine-bell function; and finally before transforming all spectra to Fourier space, filtering of high-frequency noise is required. To accurately measure the galaxy kinematics, a careful choice of the appropriate input parameters for each of these steps is essential. Optimal parameters for each step were decided by performing Monte-Carlo simulations.

In this section 3.4.1 the steps performed to prepare the spectra prior to application of the FCQ method are outlined. The Monte-Carlo simulations performed are described in section 3.5.

3.4.1 Description of Preprocessing Steps

Prior to application of the FCQ method described in section 3.3.2, a number of additional procedures were required. These were performed using FORTRAN programs written and adapted for the MIDAS environment by Ralf Bender and Roberto Saglia. All basic data reduction had been completed and the galaxy and stellar spectra were assumed to have been prepared by the steps described in section 2.2.10.

Spectra corresponding to a preselected logarithmic wavelength range, were extracted for both the galaxy and stellar spectra. Rows of each galaxy frame, centred on the row containing the galaxy centre, were then summed until a minimum value of signal-to-noise had been achieved. This produced a one-dimensional spectrum which was written as a single row of a new galaxy frame. The dispersion axis of the stellar spectrum was then rebinned in a similar way to the central row of the original galaxy frame using the MIDAS routine *rebin/ii*.

Continuum removal was performed by deciding the best-fit function for the continuum of both the star and galaxy spectra and dividing this into the original spectrum. A polynomial function of this chosen order was fitted to each pixel row of both the galaxy spectrum and to the stellar spectrum. The rms variation, σ, of pixel intensity values about this fit was found and pixels for which the value of intensity was lower by 1σ or greater than 2σ of the fitted value were eliminated and a second fit was made excluding these eliminated points. This step reduced the problem of the fitting of the strong absorption features (e.g. the MgH feature) on the fit for the spectral continuum.

The edges of the spectra were tapered using a cosine-bell function as a data window to reduce end-region effects on the Fourier deconvolution. A Wiener filter was then constructed to filter high frequency noise.

3.5 Description of Monte-Carlo Simulations

A precise assessment of the uncertainty involved in a particular measurement requires prior knowledge of the value of the quantity being measured. To decide the optimal parameters for each of the additional preprocessing steps described above, a series of Monte-Carlo simulations were performed. In these simulations, galaxy spectra of particular values of velocity dispersion σ, H_3 and H_4 were simulated by broadening the one-dimensional stellar spectra created from the stellar

frames. The effect of noise corresponding to a particular signal-to-noise ratio was recreated by adding different Gaussian noise realisations to 30 copies of the simulated galaxy spectrum. The parameters σ, H_3 and H_4 were then measured for each of the 30 newly-created galaxy spectra and the uncertainty in the measurement of each quantity due to the effect of noise was directly assessed from the root-mean-square spread in the measured values. Such simulations were repeated for different, reasonable values of each parameter. During simulations performed for a given parameter (e.g. the extracted wavelength region), only the value of this parameter was varied; all other parameters were kept constant. The optimal value of each parameter was decided as that for which σ, H_3 and H_4 were most accurately measured. Occasionally different optimal parameter values were found for σ, H_3 and H_4, most notably for the signal-to-noise simulations. Wherever possible however a single optimal parameter was decided for the measurement of all quantities.

Despite its relative insensitivity to template-mismatching compared to earlier methods, the FCQ method nevertheless requires some care to be taken in deciding an appropriate stellar template. A choice of stellar template was ultimately made by comparing measurements of kinematics obtained for each galaxy using different template stars. The series of Monte-Carlo simulations described above were repeated for each template to determine optimal parameters. Simulations were repeated for all template stars observed on different nights of observation. Results for identical templates observed on different nights were compared and found to be in broad agreement. In general, optimal parameters determined for all of the template spectra that were tested were found to be very similar.

Simulations performed to decide optimal values for each input parameter are now described. Results presented are the mean values of measurements recovered during simulations and the plotted errors indicate the root-mean-square spread in their value.

3.5.1 Extracted Logarithmic Wavelength Range

As mentioned in section 3.3.2, an ideal wavelength range is one containing a good number of strong absorption features of reasonable separation. A range centred on the Mg_b line-strength feature was the most sensible choice here. Since different spectral features can trace different stellar population components which may also be kinematically distinct, the particular range chosen can have an important effect on the measurement of galaxy kinematics. A number of different wavelength ranges were chosen to include and not to include the Hβ line-strength feature. This feature can be difficult to model for a particular galaxy since its varying strength is controlled in a luminosity-weighted way, that is a population contributing to a small amount of the total mass of the galaxy can have a large effect on its net measured spectrum (de Jong and Davies, 1997). All ranges tested are given in Table 3.1.

A typical set of results for simulations completed are given in figure 3.2. All ranges, excluding range 3, produced fairly similar results. In general however, ranges 2 & 5 consistently produced the best results. Range 2 was adopted to determine galaxy measurements; this range was preferred to range 5 since it did not include the Hβ feature.

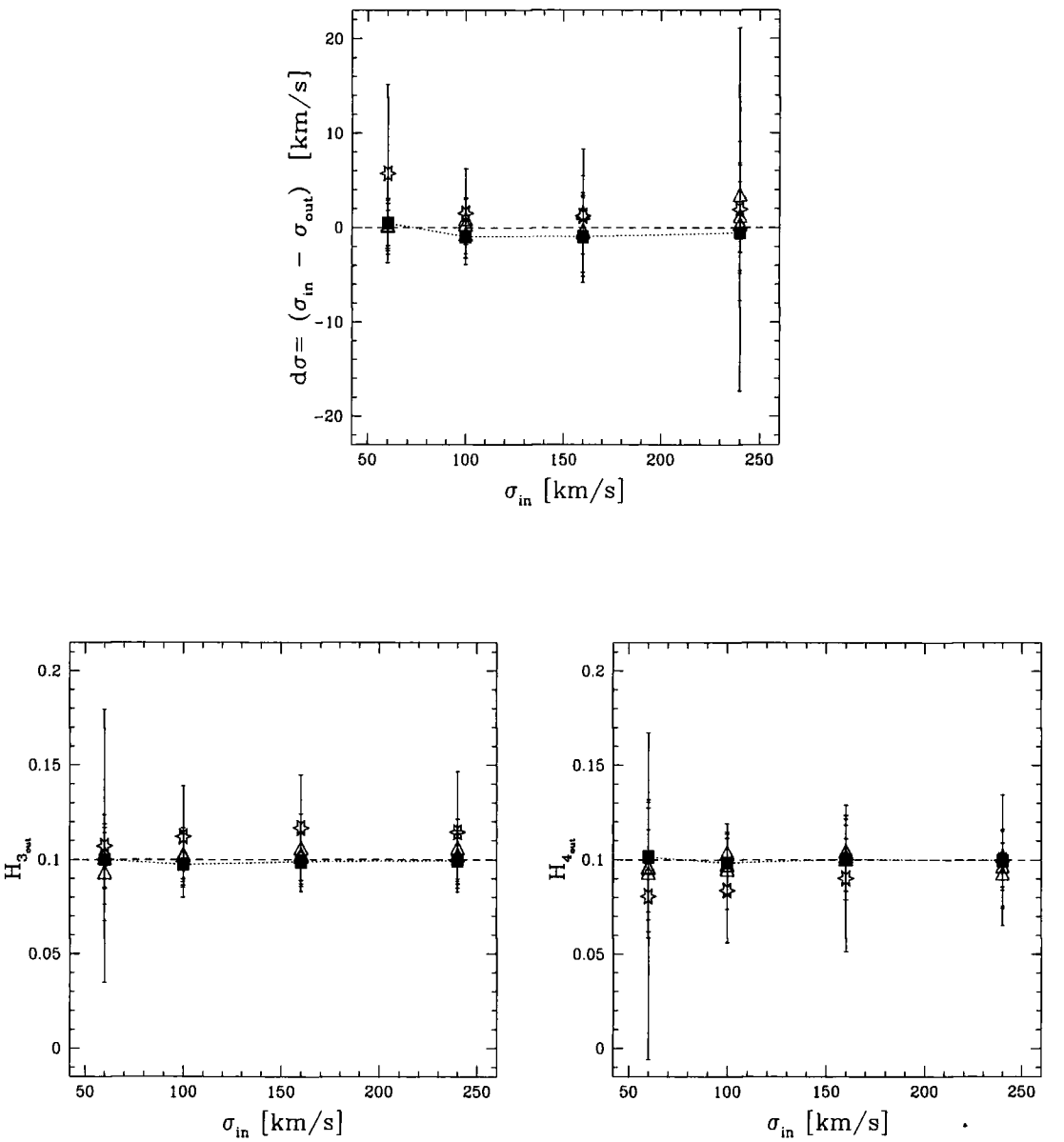

Figure 3.2: Results of FCQ simulations for all wavelength ranges 1-5. Template star is HD52071 observed during night February 23-24 1995. Simulation parameters were Wiener filter $w = 1.6$, signal-to-noise ratio S/N=50 per pixel, order-of-fit=4,and $H_3 = 0.1$ and $H_4 = 0.1$. Results for range 2 are indicated by the solid square symbols and are connected by the dotted line. Starred hexagon symbols correspond to range 3 which produced the most inaccurate results. Results for all other ranges are given by the triangle symbols.

Range no.	Wavelength range	Details
1	5090-5514Å	Medium sized range centred on Mg_b feature
2	4944-5514Å	Slightly wider range to increase accuracy
3	5350-5739Å	Not including either Mg_b nor Hβ
4	4793-5514Å	Similar to 1 but including Hβ
5	4793-5739Å	Again slightly wider range, including Hβ

Table 3.1: Wavelength ranges tested during simulations.

3.5.2 Signal-to-Noise Ratio

A minimum value of signal-to-noise ratio (S/N) is required for an accurate measurement of the LOSVD. To achieve the required S/N, FCQ sums the rows of galaxy spectra in the direction of the spectrograph slit. The particular value of S/N chosen here was a compromise between the confidence of measurement and the spatial detail of the measured kinematics.

Monte-Carlo simulations were repeated for S/N = 20, 30, 40, 50, 60 and 80 per pixel. The results for all simulations are given in figure 3.3. A value of S/N$\simeq$30 per pixel (corresponding to S/N$\simeq$60 per Å) was decided to determine all galaxy kinematics.

3.5.3 Order of Best-Fit Continuua

Due to the sensitivity of the cross-correlation technique of the FCQ method to the shape of the stellar and galaxy continuua, inaccurate removal of the continuua can significantly affect the measurement of kinematics, particularly that of H_4. Simulations were repeated for order-of-fit = 2, 4, 5, 6, 8, 12, 16 and 20. An example of typical results for all orders of fit are given in figure 3.4. Measurement of σ, H_3 and H_4 is clearly independent of the order chosen. Similar tests were performed for actual galaxy spectra, i.e. measurements were repeated for different values of continuum fit: the measurement of rotational velocity v, σ, H_3 and H_4 was again found to be independent of the value of order.

The order-of-fit was chosen by fitting different orders to true galaxy spectra and judging by eye the order which provided the most accurate fit to the continuum without fitting for the absorption features of the spectrum. The order chosen depended slightly on the wavelength range: an order of 4 was chosen for the wider wavelength ranges 4 & 5, and order of 3 for the ranges 1-3.

FCQ was programmed initially to fit polynomial functions of a single given order to both the galaxy and stellar continuua. Checks were made to ensure that the choice of most appropriate order for the galaxy spectra was the best choice for the stellar spectra. Where the chosen best orders were found to differ slightly the effect of fitting the different orders on the final measurements of velocity, σ, H_3 and H_4, was found to be negligible. A check was also made to test how the choice of order-of-fit was affected by the galaxy velocity dispersion, i.e. to test how consistently the choice of best orders were decided. Stellar spectra were broadened to the velocity dispersion of the galaxy. Orders of best-fit continuua were then decided separately for the galaxy spectra and the broadened stellar spectra, and the functions of the chosen orders fitted to the galaxy and original stellar spectra. Again this method of choosing the appropriate order had a negligible effect

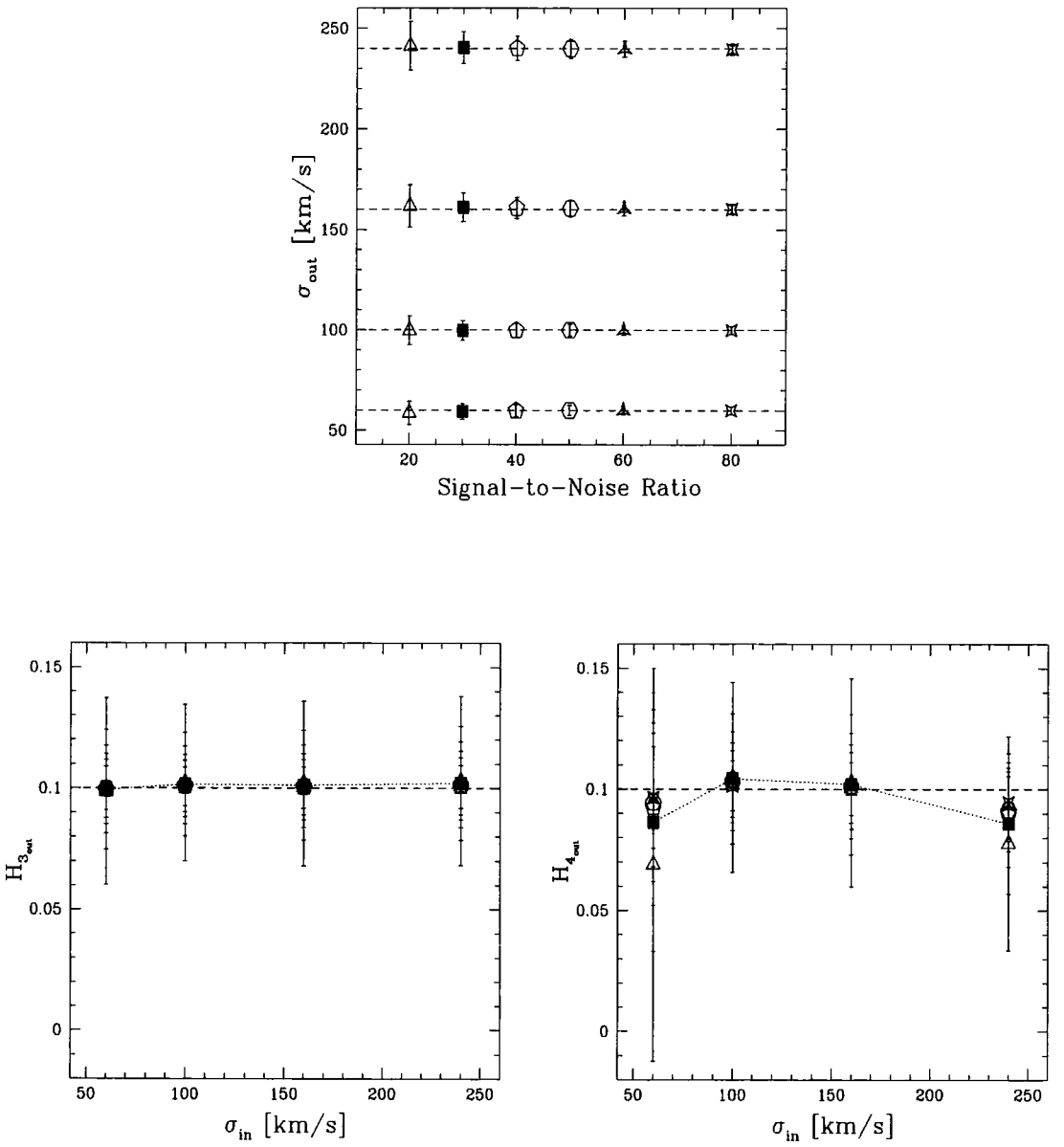

Figure 3.3: Results of simulations for all values of signal-to-noise tested. Stellar template is similar to figure (3.2). Simulation parameters were Wiener filter $w = 1.6$, order-of-fit=4, logarithmic wavelength range [8.475:8.615], $H_3 = 0.1$ and $H_4 = 0.1$. Results for S/N=30 per pixel are given by solid square symbols and connected by dotted line.

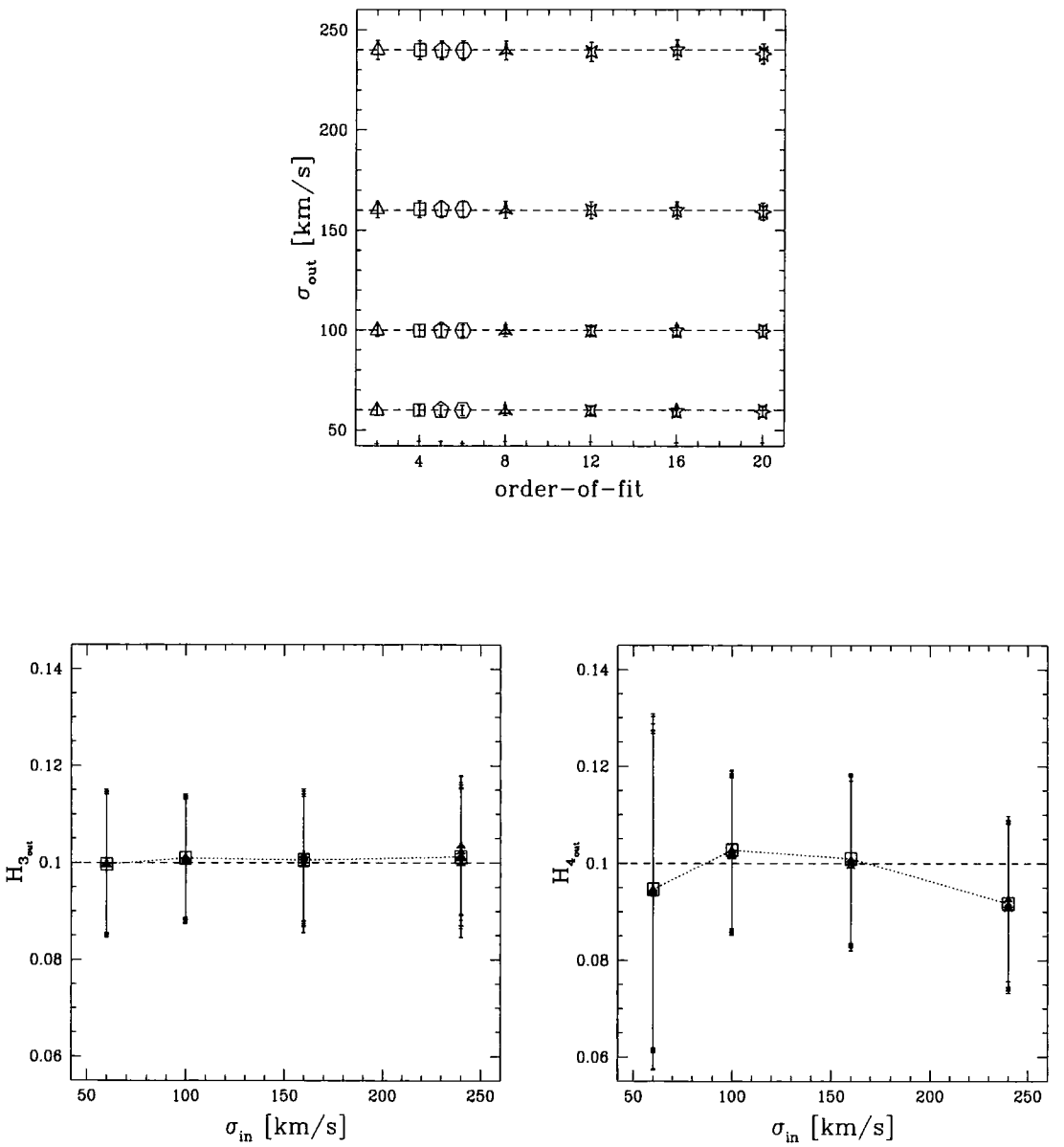

Figure 3.4: Results of simulations for all values of order-of-fit = 2,4,5,6,8,12,16 and 20. Template star is again similar to figure (3.2). For H_3 and H_4, results for order of 4 are indicated by square symbols and for all other values of order by triangles.

on the measurements of kinematics.

3.5.4 Wiener Filter

As discussed in section 3.3.3, high frequency noise must be filtered to enable deconvolution to be successful and the galaxy broadening function to be accurately measured. Filtering was performed by constructing a Wiener filter. To ensure that the higher-order information of the LOSVD, described by the higher frequencies of the galaxy-template correlation function in Fourier space, was unaffected by this filtering, care in the choice of filter was required.

The particular filter applied was decided by performing Monte Carlo simulations for different filters. Typical results for such simulations are given in figure 3.5. In this figure particular filters are indicated by the different parameter values of w. This parameter w does not directly correspond to the Wiener filter itself as defined in equation 3.19 but is an input parameter of the FCQ method that is proportional to the greatest value of frequency admitted by the Wiener filter. The greater the value of w chosen, the greater is the value of the highest frequency of the measured galaxy-template correlation function in Fourier space, retained after filtering.

Wiener filter parameters of values $w = 1.0, 1.1, 1.2, 1.3, 1.4, 1.6, 1.8$ & 2.0 were tested. Results for all filters are given figure 3.5. It is clear from these results that a Wiener filter value of at least 1.4 was required. A value of 1.4 or 1.6 was decided for all templates tested.

3.6 Measuring galaxy kinematics

After optimal values for all parameters had been decided using Monte-Carlo simulations, measurements of galaxy kinematics were obtained for a range of individual stellar templates. Only templates observed on the same night of observation were used to determine measurements for a given galaxy: this was important since a central assumption of the FCQ method is that the instrumental broadening of both galaxy and stellar spectra can be assumed to be similar. Stellar and galaxy spectra were prepared as described in section 3.4.1. The FCQ method outlined in section 3.3.2 was then applied to determine v, σ, H_3 and H_4 measurements for each galaxy spectrum.

Although the FCQ method reduces the effect of template-mismatching, measurement of the higher order terms H_3 and H_4 may still be affected. For a point-symmetric galaxy, where the spectrographic slit has been carefully centred on the galaxy centre, the H_3 profile is expected to be completely asymmetric about the galaxy centre. Templete-mismatching produces a symmetric component in H_3 i.e. a constant offset which can clearly be seen in the folded H_3 profile (see figure 3.6). This effect was noted for both major and minor axis spectra and was the most pronounced difference in profiles obtained for a galaxy spectrum using different templates. Template-mismatch is due to differences in the intrinsic *shape* of spectral features of the template star and the typical component star of the galaxy. Where the LOSVD is described by increasingly higher-order terms it can be expected that systematic differences in the spectra of galaxy and star will have a direct effect on the LOSVD recovered. In addition where there are negligible radial gradients in stellar population, this effect can be assumed to produce a constant offset in the measured profile of these higher-order terms. Moreover any offset in H_3 and H_4 will be identical for opposite sides of the

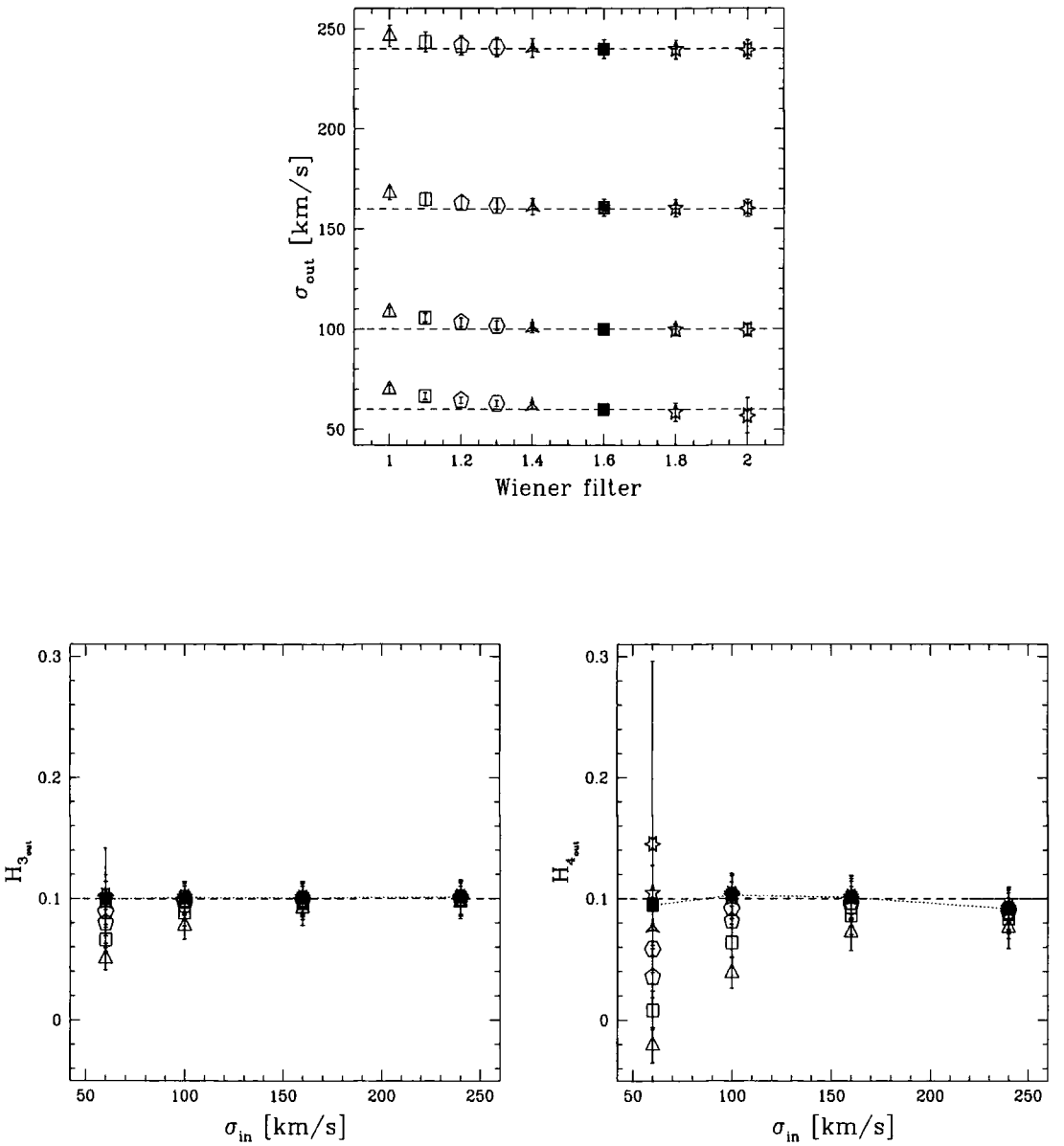

Figure 3.5: Results of FCQ simulations for all values of Wiener filter $w = 1.0, 1.1, 1.2, 1.3, 1.4, 1.6, 1.8$ & 2.0. Template star was HD52071 as before. Parameters of simulations were order-of-fit=4, logarithmic wavelength range [8.475:8.615], S/N=30 per pixel, $H_3 = 0.1$ and $H_4 = 0.1$. Results for $w = 1.6$ are given by solid squares and connected by dotted line. Triangle symbols indicate results for $w = 1.0$, squares $w = 1.1$, pentagons $w = 1.2$, hexagons $w = 1.3$, starred triangles $w = 1.4$, starred pentagons $w = 1.8$, and starred hexagons $w = 2.0$.

galaxy, producing for H_3 a constant offset in all measured values.

Measurements were derived for each galaxy spectrum for 3-8 different stellar templates. Final measurements were taken to be those for the template which produced the least symmetrical offset in H_3. Where possible, identical templates were taken to derive measurements for the major and minor axis spectrum of each a galaxy. Where major and minor observations were obtained on different nights and identical templates could not be used, templates of most closely matching stellar type possible were chosen.

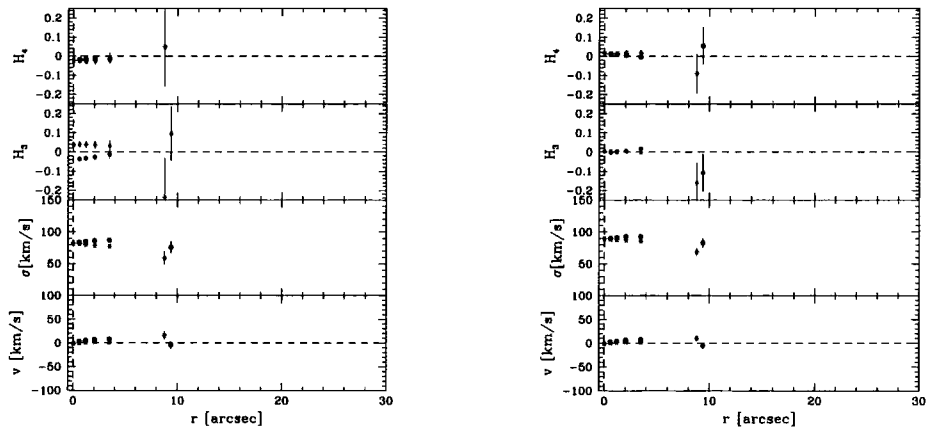

(a) Template HD52071

(b) Template HD172401

Figure 3.6: Measurements of rotation, σ, H_3 and H_4 obtained for the minor axis spectrum of NGC 3605 using 2 different stellar templates are presented folded. Measurements of rotation and H_3 for one side of the galaxy have been multiplied by -1. A symmetrical component can clearly be seen in the H_3 profile for the stellar template HD52071, due to template-mismatching.

Apart from the differences in measurements of H_3 noted above, measurements obtained for different templates were found to be in reasonable agreement. A comparison of measurements obtained using different templates for the galaxy NGC 4478 is presented in figure 3.7.

3.7 Comparison with other authors

Comparisons are performed between measurements of v, σ, H_3 & H_4 obtained here and measurements obtained previously by other authors (i.e. Davies et al. (1983) (hereafter DEFIS), Davies and Birkinshaw (1988) (hereafter DB88), Franx et al. (1989) (hereafter FIH89), Fisher et al. (1995) (hereafter FIF95), Bender et al. (1994) (hereafter BSG)). Measurements of rotation and velocity dispersion (σ) as functions of radius have been measured for a number of galaxies observed here, namely NGC 3605, 4387, 4478, 4551 (DEFIS), NGC 2778 (DEFIS & FIF95) and NGC 3379 (DB88 & FIH89); measurements of rotation, σ, H_3 & H_4 have also been obtained for major axis spectra of NGC's 3379, 3377 & 4564 by BSG, and rotation and σ for NGC 3377 by Kormendy et al. (1998) (hereafter K98). The position angle of all observations compared for a given galaxy differed slightly but in all cases by less than 5°. Results of comparisons are given in figures 3.8-3.10.

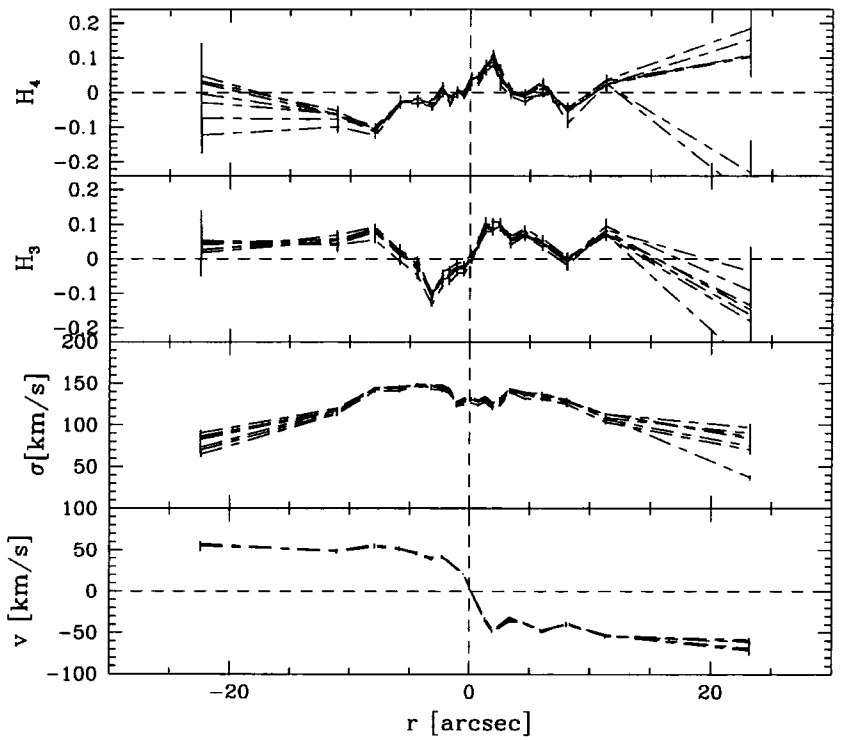

Figure 3.7: Measurements of v, σ, H_3 and H_4 obtained for the major axis spectrum of NGC 4478 using 7 different stellar templates. Measurements for each template are connected by a long-dashed-short-dashed line. Errors for all measurements were determined as described in section 3.8.

In figure 3.8, measurements obtained here are compared with those of BSG. There is in general very good agreement between measurements and differences can be attributed to the different seeing conditions, instrumental set-ups and exposure times. For NGC 3377 there is remarkably good agreement for the higher-order terms H_3 and H_4. The discrepancy in the rotation and σ measured here is probably due to the better seeing conditions of observations obtained here; the worse seeing conditions of BSG may be unable to resolve the steeply rising rotation curve, which in turn may cause an increase in the measured velocity dispersion. The measurements of rotation and σ obtained here are also in good agreement with K98 although their greater spatial resolution was able to better resolve the steeply rising central rotation curve. For NGC 3379 there is again very good agreement for measurements of H_3 and H_4; the lower value of rotation measured here at $\sim 5.5''$ and the lower values of σ found at $\gtrsim 17''$ may be due to the lower spatial resolution of the spectrum obtained here. For NGC 4564, there is slight disagreement for the measured values of H_3 for $\gtrsim 12''$ and at the centre there is evidence in my measurements for some residual template-mismatching.

In figure 3.9, measurements of rotation and σ are compared with the measurements of DEFIS. Agreement between measurements is very good although rotation is clearly better resolved close to the galaxy centre by our measurements. At greater radii the measurements of DEFIS however

have better spatial resolution.

3.8 Estimation of Errors

Errors for all quantities measured (rotation, σ, H_3 and H_4) were determined using a suite of programs written by Roberto Saglia. The underlying principle of the error estimation was to relate the quantity measured during the measurement of the galaxy kinematics, to the estimated signal-to-noise ratio of the galaxy spectrum and hence to values of errors estimated using Monte-Carlo simulations. The quantity used was the ratio R, of (i) the peak of the ratio of the cross-correlation peaks, i.e. given by equation 3.18, and (ii) the amplitude of the noise component estimated for this same cross-correlation peak function. The equation 3.18 is reproduced below:

$$\frac{\tilde{K}^{peak}_{S,G}(k)}{\tilde{K}^{peak}_{S,S}(k)} = \frac{\sum_n \alpha_m \beta_m}{\sum_n \alpha_n^2}\tilde{B}(k) + \frac{\sum_l \alpha_l e^{-i\kappa x_l}}{\sum_m \alpha_m^2}\cdot\frac{\tilde{N}(k)}{\tilde{L}(k)}.$$

A sketch of the principal components of this cross-correlation peak function, i.e. power spectra for a Gaussian broadening function, B(k), and a component of noise, N(k), is given in figure 3.12. To define the ratio R, the values (i) and (ii) were estimated for this function for some small value of k$\simeq$0. The value (i) was taken to be the amplitude of the net measured power spectrum at k$\simeq$0. To determine the value (ii), a linear fit was obtained for the noise spectrum at high values of k; the extrapolation of this function to k$\simeq$0 was then taken to define (ii).

To accurately determine errors for all quantities measured (v, σ, H_3 and H_4), the ratio R was calibrated to the value of signal-to-noise ratio. This calibration was only found to be secure when performed for each particular set of measurements of v, σ, H_3 and H_4. Measurements were firstly obtained for each galaxy as described in section 3.6. A calibration was performed for each set of kinematical measurements by completing a series of Monte-Carlo simulations for 12 different signal-to-noise ratios i.e. $S/N = 2, 10, 20, 30....100, 999$ per pixel. Simulations were identical to those described in section 3.5 and values of the Wiener filter, order-of-fit and extracted logarithmic wavelength range were set to be identical to those used to obtain the original galaxy measurements. During each simulation, the ratio R was measured for all 30 simulated galaxy spectra and the mean value obtained. To decide the final errors, the ratio R determined for the original galaxy measurements was compared to values measured for all signal-to-noise simulations. Where closest agreement between compared values of R was found, the root-mean-square uncertainties for v, σ, H_3 and H_4 determined during the respective Monte-Carlo simulation were adopted as the errors for the appropriate quantities.

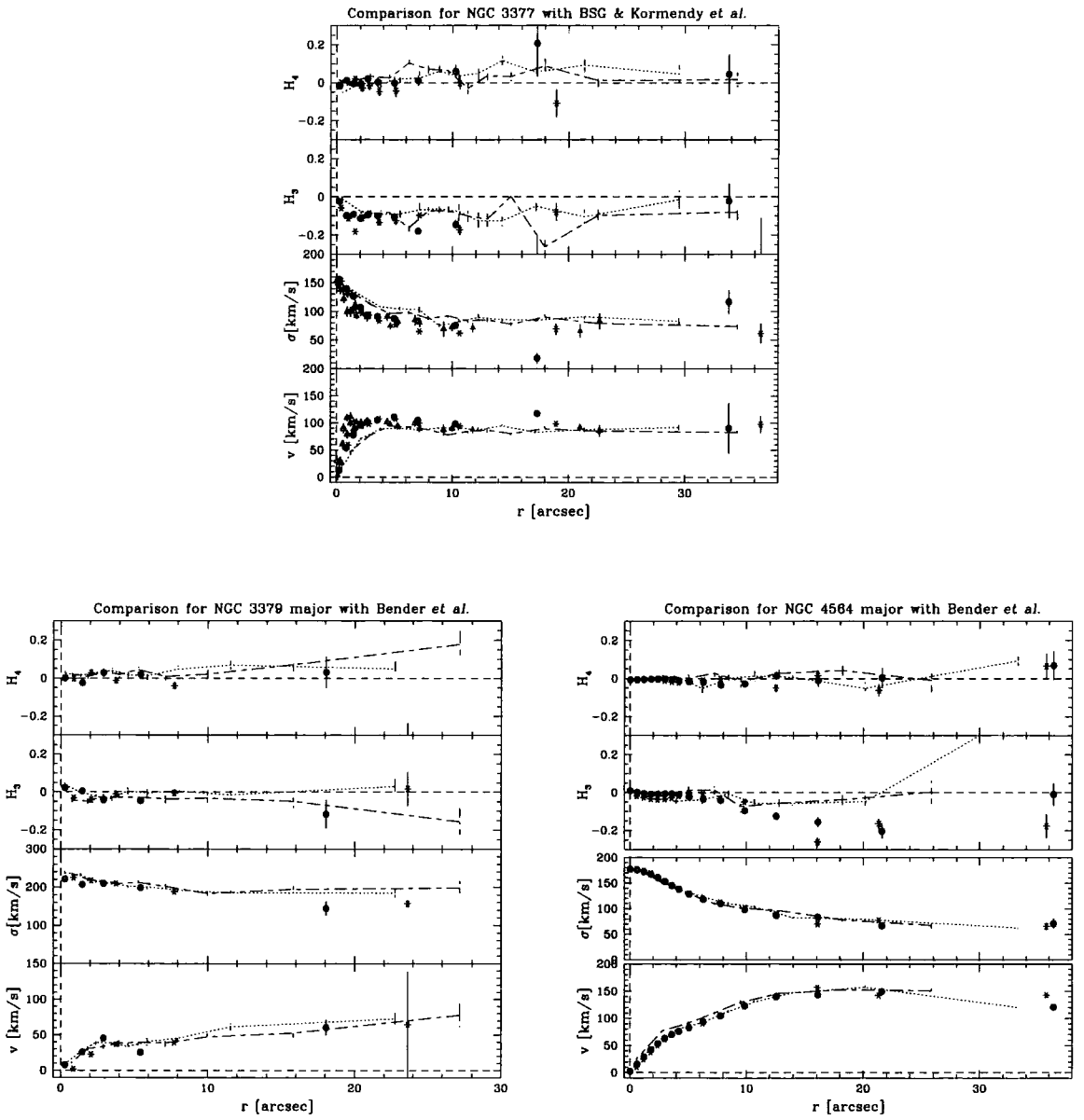

Figure 3.8: Comparison of measurements of rotation velocity, σ, H_3 and H_4 for galaxies in common with those studied by BSG and K98. Measurements obtained here are indicated by solid circles and asterisks for opposite sides of the galaxy. BSG measurements are connected by dot and dashed lines, the dotted line corresponding to points for negative values of radii, and the dashed line, points for positive values of radii. K98 measurements are given by solid and open triangle symbols for negative and positive value of radii respectively. Note the different scale for the values of σ in the plot for NGC 3379. Comparisons are discussed in the main text.

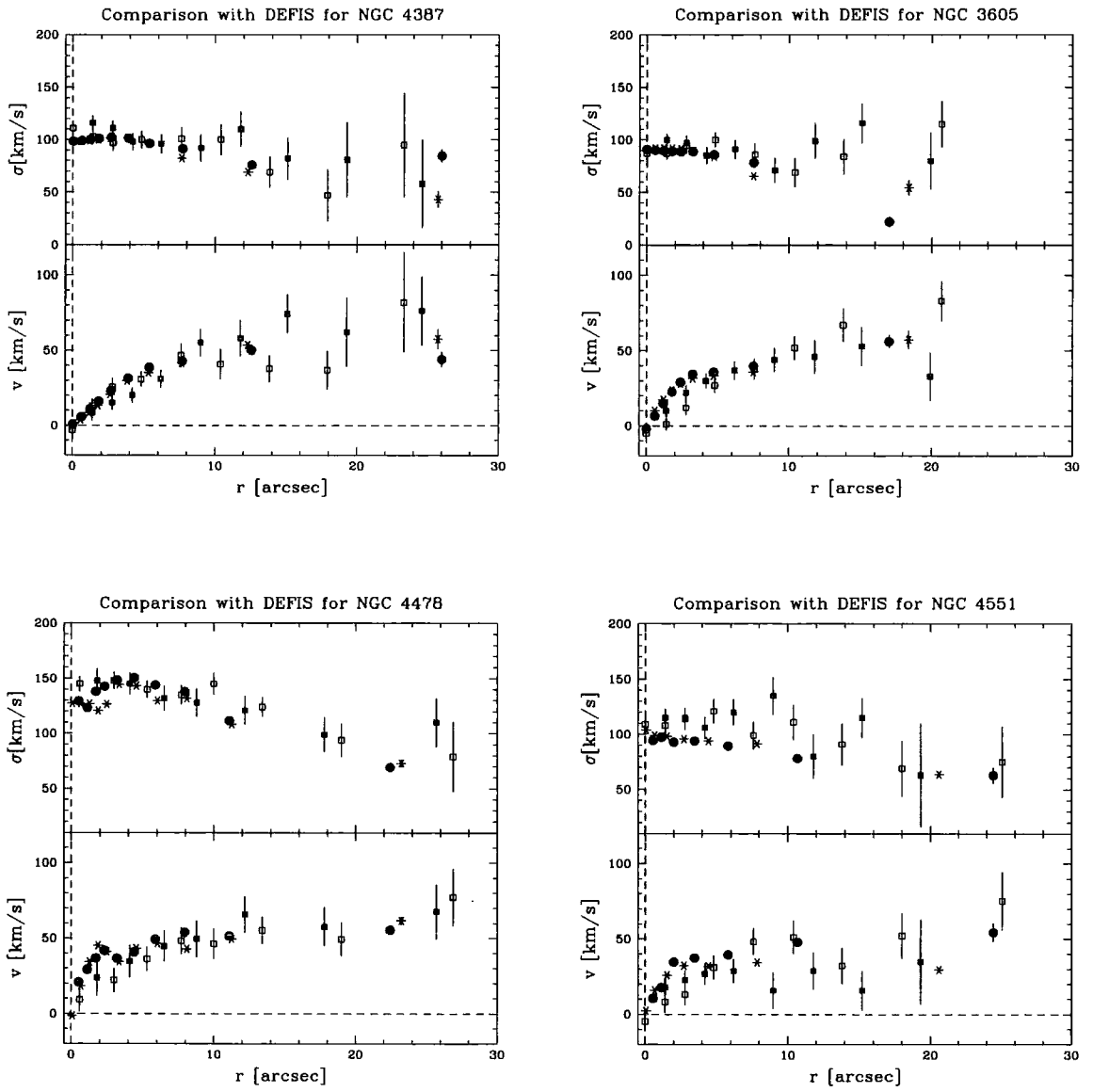

Figure 3.9: Comparison of measurements of rotation velocity and σ for galaxies in common with those studied by DEFIS. Measurements obtained here are indicated by solid circles and asterisks for opposite sides of the galaxy. DEFIS measurements are similarly indicated by open and solid square symbols.

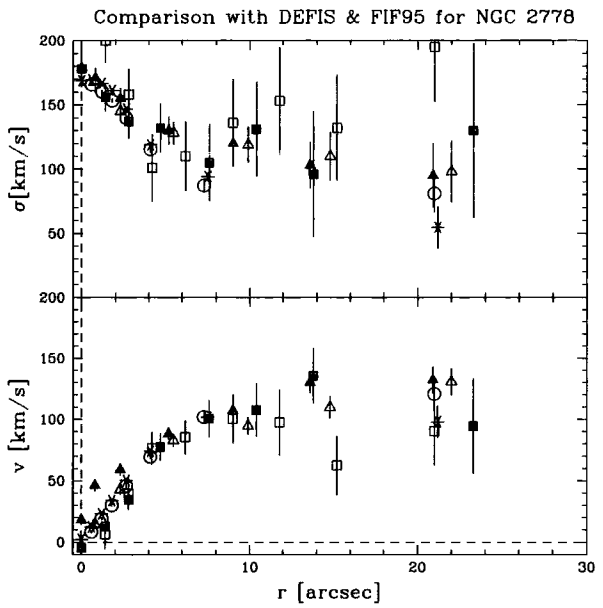

Figure 3.10: Comparisons for NGC 2778. Measurements obtained here are given by open circle and asterisk symbols for opposite sides of galaxy. Symbols for DEFIS measurements are as in figure 3.9. FIF95 measurements are given by open and solid triangle symbols.

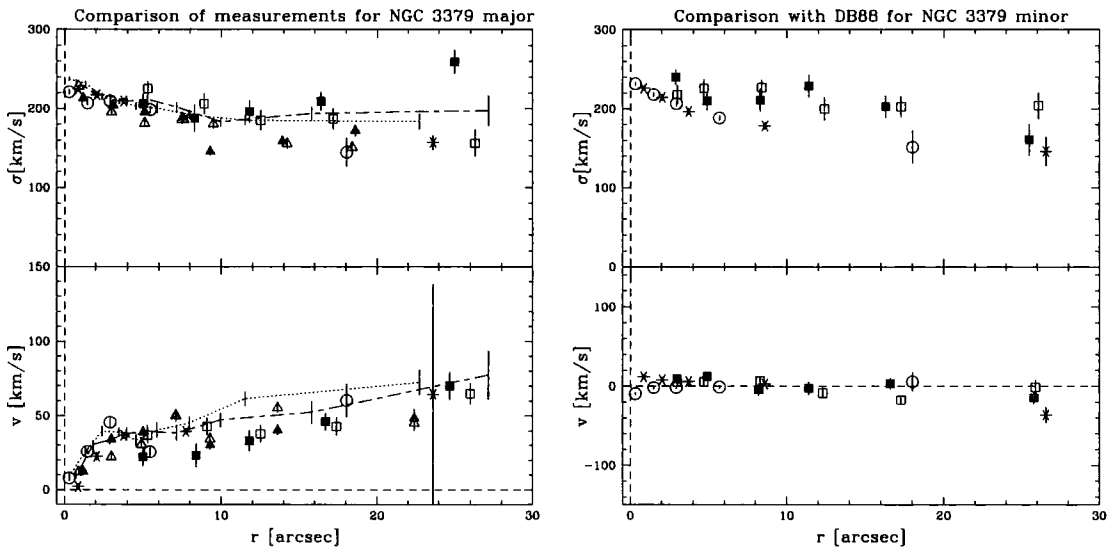

(a) NGC 3379 major

(b) NGC 3379 minor

Figure 3.11: Comparisons for NGC 3379. In figure 3.11(a), measurements of rotation and σ obtained here for the major axis of NGC 3379 are compared with those of DB88, FIH89 & BSG: results obtained here are given by open circles and asterisks, measurements for DB88 are indicated by square symbols, FIH89 measurements by triangle symbols and results for BSG are connected by long-dashed & dotted lines. In figure 3.11(b), measurements for minor axis of NGC 3379 are compared with similar measurements of DB88; symbols for different authors are as in figure 3.11(a).

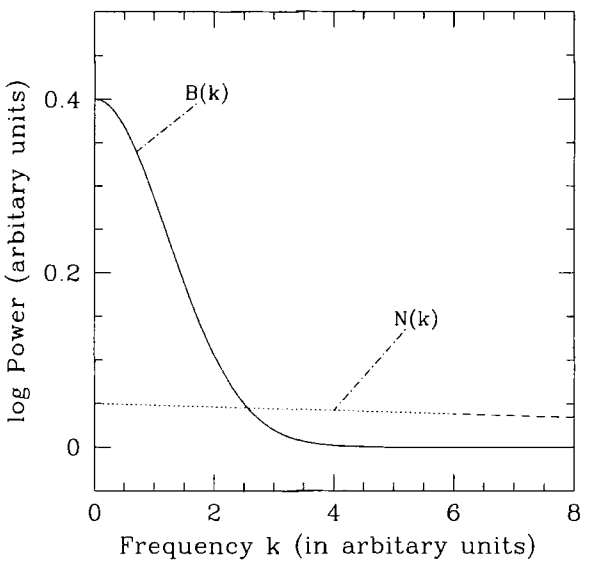

Figure 3.12: Sketch of power spectra for a Gaussian broadening function, B(k), and a component of noise, N(k). The relative amplitude of the noise is increased for clarity. The actual measured power spectrum is expected to be the sum of both components. The noise power spectrum, N(k), is expected to be a linear function. Since N(k) is the main contributer to the net power spectrum amplitude at high frequencies, a linear fit is made for the noise, by FCQ, for some range at these frequencies (given by long-dashed line). The fitted linear relation is then extrapolated to small values of frequency (indicated by dotted line).

Chapter 4

Galaxy Kinematics: Results

Measurements of galaxy kinematics are presented here. Descriptions of the adopted parametrisation of the LOSVD, the required Monte-Carlo simulations and the estimation of the errors by the FCQ method were given in Chapter 3. Here particular emphasis is given to the interpretation of measurement of the higher order terms, i.e. H_3 and H_4 of the Gauss-Hermite series, and their implications for the kinematical structure of each galaxy. Where a focus correction has been applied for a particular galaxy spectrum, this is indicated and the corresponding effective smoothing in arcseconds is given. Extensive reference is made to photometry available in the literature for all galaxies observed, i.e. U, B, and R-band photometry of Peletier et al. (1990), HST WFPC-1 V-band photometry of van den Bosch et al. (1994) and Lauer et al. (1995), and HST WFPC-2 V and I-band photometry of Carollo et al. (1997).

4.1 The Measurements

Measurements of rotation, σ, H_3 and H_4 are presented, unfolded, for each galaxy. The velocity of the galaxy has been removed by subtracting the mean measured velocity for each individual spectrum from the velocity measurements. This step was less satisfactory than subtracting a single mean value for both the major and minor axis spectra of a given galaxy, but was adopted due to uncertainty in the actual value of velocity measured by the FCQ program. Small shifts, of less than 8 km s^{-1}, were applied to the resultant values of velocity to centre the velocity profile about the apparent kinematical centre of the galaxy. The position angle (hereafter PA) of observation is indicated in each case, the sense being North through East. The measurement of both H_3 and H_4 are sensitive to systematic error due to template-mismatching. The effect of template-mismatch can be clearly seen as a symmetrical offset in the measured H_3 profile, superimposed on profiles which are measured in general to be point-symmetric in the galaxy centre. Error bars for all quantities were calculated as described in section 3.8. Comparisons between previous measurements of rotation and σ, H_3 and H_4 and measurements obtained here, were made in Chapter 3, where good agreement was found for all comparisons. Measurements of rotation, σ, H_3 and H_4 obtained for a S/N$\simeq$60 per Å are presented in all figures (excluding figures 4.6 and 4.11) by filled circular symbols. Additional measurements for rotation and σ, obtained for a lower S/N$\simeq$30-35 per Å define greater spatial detail and extend to greater radii; these are

plotted as open square symbols. In figures 4.6 and 4.11 measurements of rotation, σ, H_3 and H_4 are represented by solid circular and asterisk symbols for opposite sides of the galaxy.

An attempt to classify all galaxies is made based on the measurements of their kinematics. The first category identified, type 1, are galaxies with the strongest evidence for both a disk and bulge component. These galaxies have the greatest LOSVD asymmetries, and are strong candidates to be S0 galaxies. Type 2 galaxies show strong evidence for a *central* disk component embedded within an anisotropic or isotropic bulge. Close to the galaxy centre, galaxies of type 2 often show dips in σ and evidence of tangential anisotropy, and have photometric evidence for disk-like structures. Galaxies of type 3 show perhaps the strongest indications for completely decoupled structures at the galaxy centre. Measurements for the remaining galaxies (NGC 3379 and NGC 4468) are discussed separately. NGC 3379, probably the most "normal" galaxy of all galaxies observed, is a calibrator object for the sample as a whole. NGC 4468 is a very small, compact galaxy, possibly a dwarf galaxy.

4.1.1 Type 1

Galaxies of type 1 have a high degree of rotational support and show strong evidence for both a disk and bulge component. Most of these galaxies have been classified as E/S0 or show considerable evidence of diskiness in their photometry. Their measured values of H_3 are the greatest of all galaxies studied here.

NGC 2778

Classified as elliptical in the RC3, rotation and velocity dispersion were measured previously for this galaxy by Davies et al. (1983) and Fisher et al. (1995), and photometry has been obtained by Peletier et al. (1990). Peletier et al. (1990) detected a small amount of diskiness for $r \lesssim 7''$, and a gradual isophotal twisting between $3''.2$ and $40''.1$, from $45°.8$ to $42°.1$.

For the major axis, H_3 has a non-zero value for $r \lesssim 8''$, indicating a significant LOSVD asymmetry. H_4 is positive for $r \sim 7.5$ and slightly positive for $r \sim -7.5$. For the minor axis, H_3 is essentially zero and H_4 is positive for positive radii outside the galaxy centre and slightly negative for $r \lesssim 2''$. It is difficult to interpret the H_4 measurements in terms of an axisymmetric kinematical structure and observations of greater spatial resolution would be required to enable clearer conclusions to be made. The non-zero measurement of H_3 about the galaxy centre, is unlikely to be caused by the effect of rotation alone but instead supports the existence of a separate central component. Radii for which these measurements are obtained coincide with radii for which diskiness has been detected. This supports the idea of a central disk component. Measurements may alternatively be explained by a separate central bulge more inclined and rotationally supported than the surrounding galaxy. Where a separate component at the galaxy centre does exist, the measurements of H_4 could be explained as due to a conspiracy between the motions of a more radially anisotropic more extended bulge, and the more tangential motions of a central component. Measurements obtained at different radii would depend on the relative light contribution of the separate components. The radial orbits of an extended bulge would explain the measurements at $|r| \sim 7''$ for the major axis.

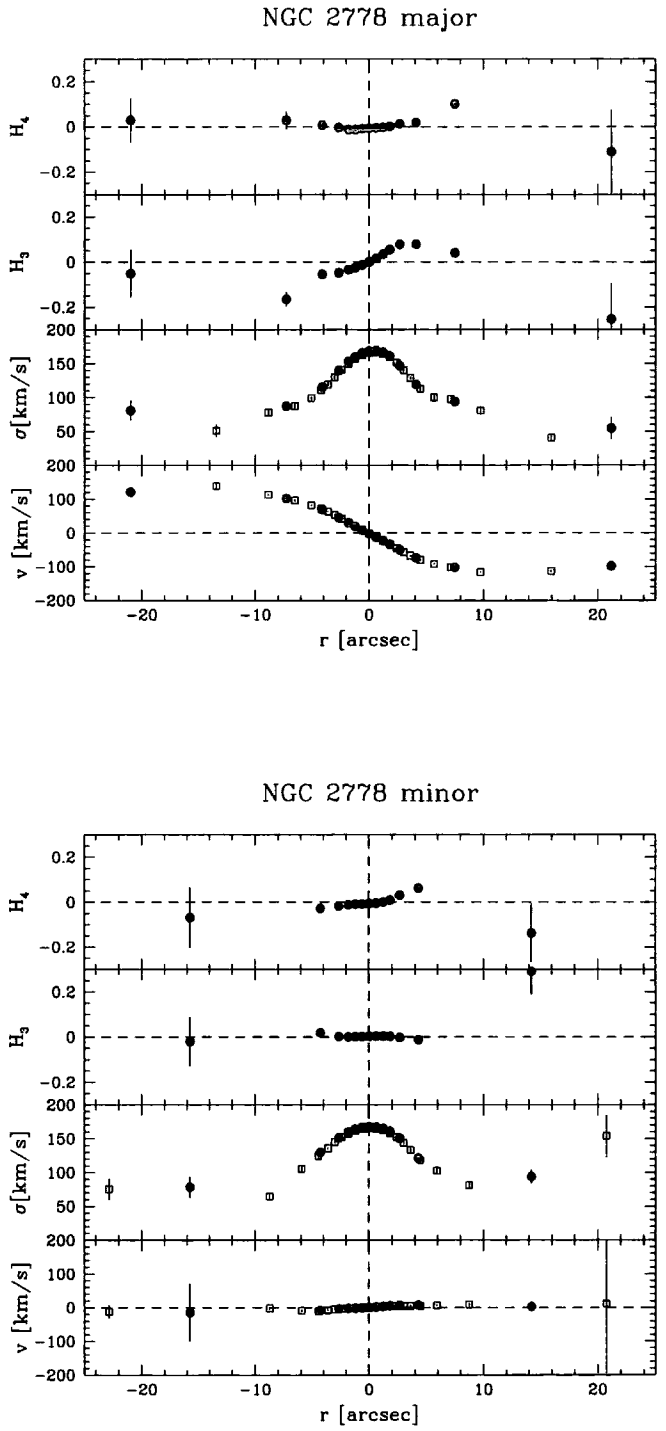

Figure 4.1: Major and minor axis observations for NGC 2778 (PA 225° and 135° respectively). Focus corrections were applied for both spectra corresponding to a maximum Gaussian smoothing of 0.″81 and 1.″08 respectively. The seeing for these observations was approximately 1″. The total smoothing in the spatial direction was 1.″29 and 1.″47 respectively. Data points cannot be assumed to be independent at this level.

NGC 3377

A member of the Leo-I group, NGC 3377 is widely considered to be a "disky" elliptical. It is classified as an intermediate E5 elliptical galaxy in the RC3 and E6 in Sandage and Tammann (1987) (hereafter RSA). Photometric measurements by both Peletier et al. (1990) and Scorza and Bender (1995) have shown this galaxy to be "disky" for the range of radii studied by measurements here. Outside these radii, the galaxy is observed to become "boxy". Measurements for the major and minor axes are presented in figure 4.2.

For the major axis, H_3 is non-zero for essentially all radii and changes sign with rotation at the galaxy centre. H_4 is slightly negative for $-6'' \lesssim r \lesssim -2''$. For the minor axis, H_4 is slightly positive for $r \sim -6''$ and otherwise almost zero.

A decomposition of major axis kinematics by Scorza and Bender (1995), into disk and bulge components has shown that the particularly steep rise in rotation close to the galaxy centre, also detected here, can be attributed to the presence of a central disk component. They measure the disk-to-bulge ratio ($\frac{D}{B}$) to peak at $r \sim 4''$ and the rotation velocity to similarly reach a maximum at this radius. At $r \sim 10''$, where they measure $\frac{D}{B}$ to become small, their measurement of rotation is approximately equal to that measured at $r \sim 4''$ and they propose that the net measured rotation curve is the result of a conspiracy between the measured kinematics of a disk and bulge component, contributing in varying proportions at different radii to the light of the galaxy.

The evidence of Scorza and Bender (1995) for a central disk component is supported here by the measured kinematics. For the major axis, the LOSVD is measured to be considerably asymmetric for radii at which the contribution of a disk component was found to reach a maximum. This is consistent with the superposition of a disk and bulge being detected along the line-of-sight. Furthermore for the major axis H_4 is measured to be negative at negative radii, corresponding to radii for which a peak in $\frac{D}{B}$ was measured by Scorza and Bender (1995). This is likely to represent detection of the tangential motion of a disk component along the line-of-sight. The measurements of H_4 however are not symmetrical about the galaxy centre. This galaxy was identified by Peletier et al. (1990) as likely to contain dust. If dust does exist at the galaxy centre this could explain the H_4 measurements as due to the partial obscuration of a separate disk component.

NGC 4339

Classified as E0 in the RC3 and S0$\frac{1}{2}$ in the RSA, this galaxy is intermediate between an elliptical and S0 galaxy. Kinematics for the major and minor axes are presented in figure 4.3.

For the major axis, the most striking result is a large positive of H_4 for small positive radii. Representing detection of motion *across* the line-of-sight, this is consistent with detection of the tangential motion of an embedded disk component. H_3 shows some degree of point-symmetry about the kinematical centre. The measured rotation curve for the central $10''$, appears to be decoupled from that of the surrounding galaxy. H_3 is non-zero for all radii representing asymmetry of the LOSVD. For the minor axis, H_4 is measured to increase to a value of ~ 0.1 at $|r| \sim 2''$, from a value of ~ 0.06 at the galaxy centre. Again this represents detection of motion across the line-of-sight, and for the minor axis, corresponds to tangential anisotropy. This measurement, taken together with the measurement of H_4 for the major axis, suggests that a highly rotationally-supported

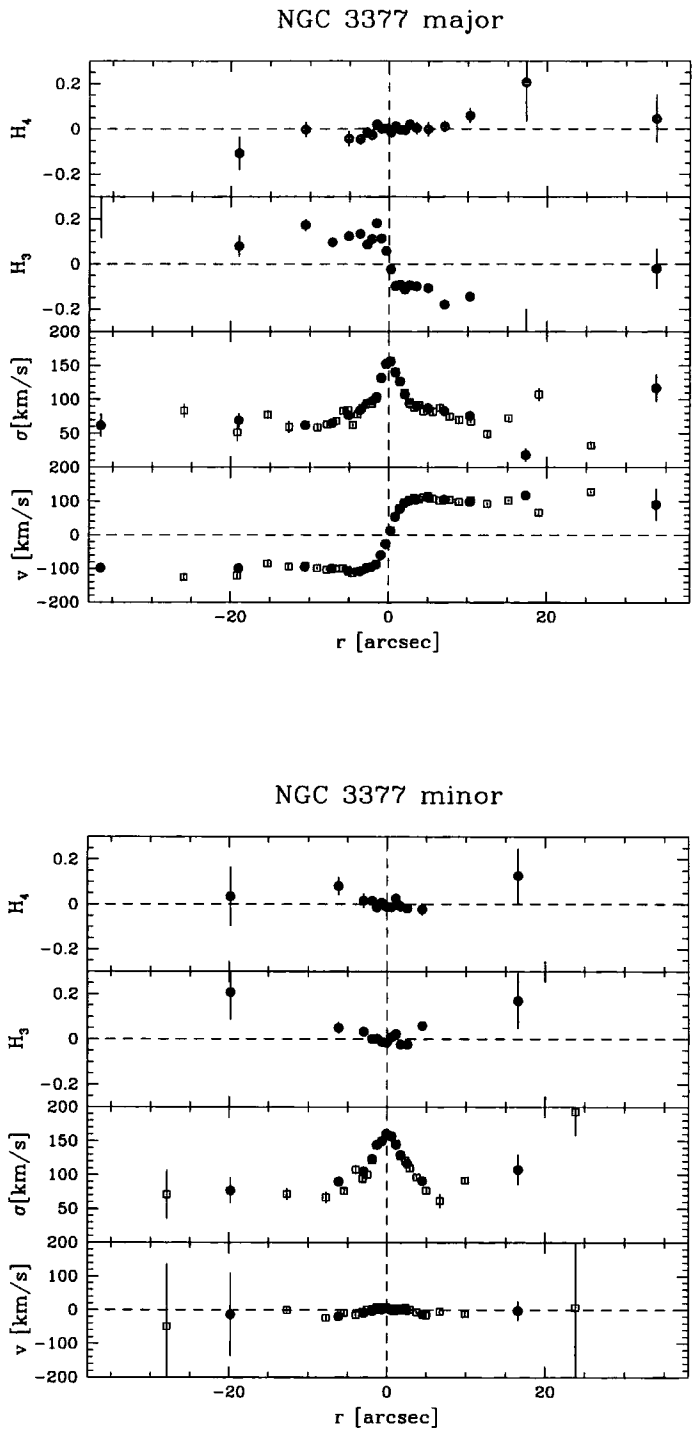

Figure 4.2: Major and minor axis observations for NGC 3377 (PA 42° and 312° respectively). Seeing for both observations was approximately 0.″8.

bulge, or a disk component, of similar extent in both the major and minor directions, is present at the galaxy centre. Since this galaxy, as an E0, is face-on, a central embedded disk component however is more likely.

A slightly higher central value of σ is measured for the minor axis compared to the major axis. This is likely to be caused by the sharp rise in rotation measured for the major axis, being detected within the 1 arcsec width of the spectroscopic slit for the minor axis observation.

NGC 4464

NGC 4464 has a doubtful classification as a spiral galaxy in the RC3. Observed by Lauer et al. (1995), $\cos 4\theta$ was measured to be almost zero for the central $4''$, and ellipticity $\epsilon \sim 0.35$ for $1'' \lesssim r \lesssim 10''$.

For $|r| \lesssim 10''$ of the major axis, significant asymmetrical and symmetrical deviations of the LOSVD from a Gaussian are measured by non-zero H_3 and H_4, respectively. The measurements of H_3 are of large amplitude and change sign with the measured rotation at the kinematical centre. $|H_3|$ reaches a maximum at radii corresponding to peaks in the measured rotation. A small amount of rotation is measured for the minor axis for $|r| \lesssim 3''$.

Measurements of H_4 for both axes, close to the galaxy centre, are consistent with the detection of radial anisotropy. The large amplitude of H_3 measured for the major axis strongly suggests the presence of two different kinematical components. For $|r| \lesssim 5''$, the measurements are consistent with the superposition of a radially-anisotropic bulge and an additional more rotationally supported component. At greater radii, rotation begins to decline suggesting a scalelength of the more rotationally supported, perhaps disk, component of $a \sim 5''$, and that a more slowly rotating bulge component begins to dominate the measured kinematics.

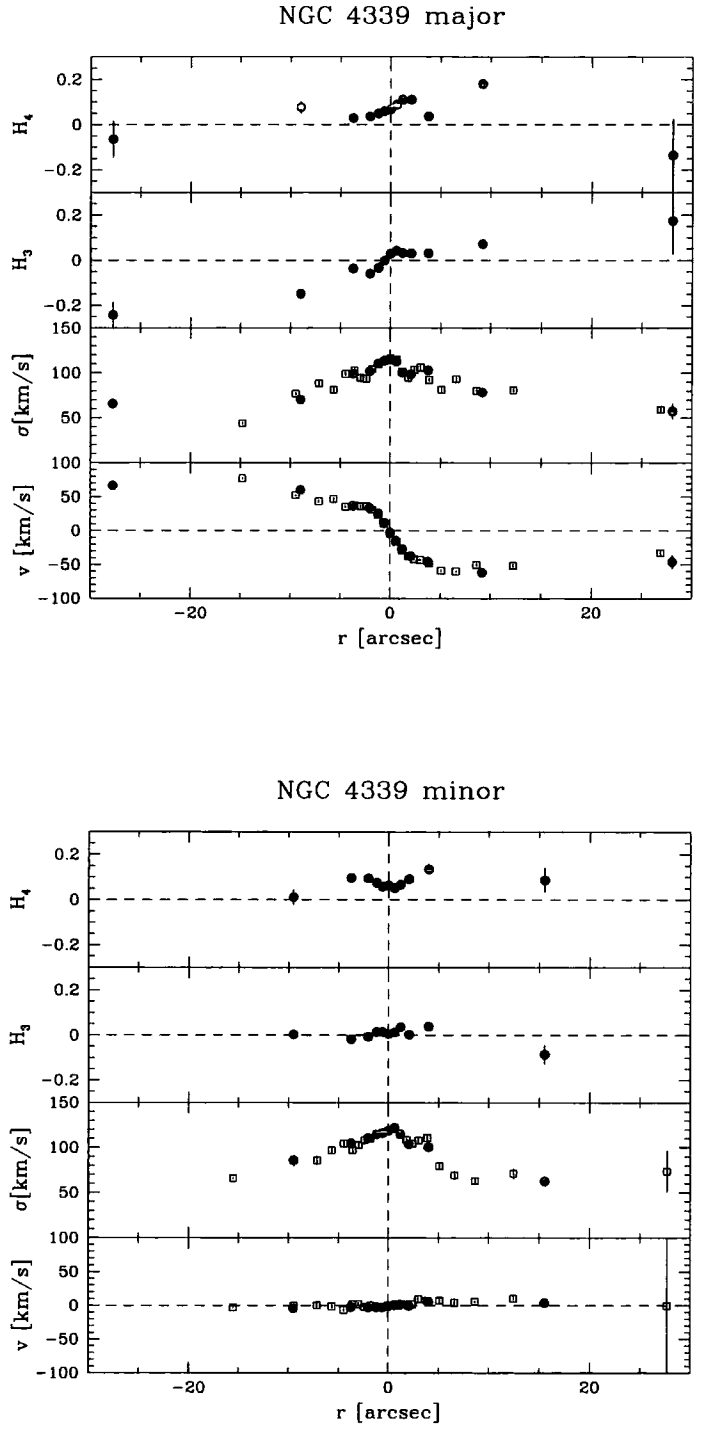

Figure 4.3: Major and minor axis observations for NGC 4339 (PA 20° and 110° respectively). Focus corrections applied to both spectra were small, i.e. 0.″65 and 0.″50 respectively. Seeing for both observations was approximately 0.″5.

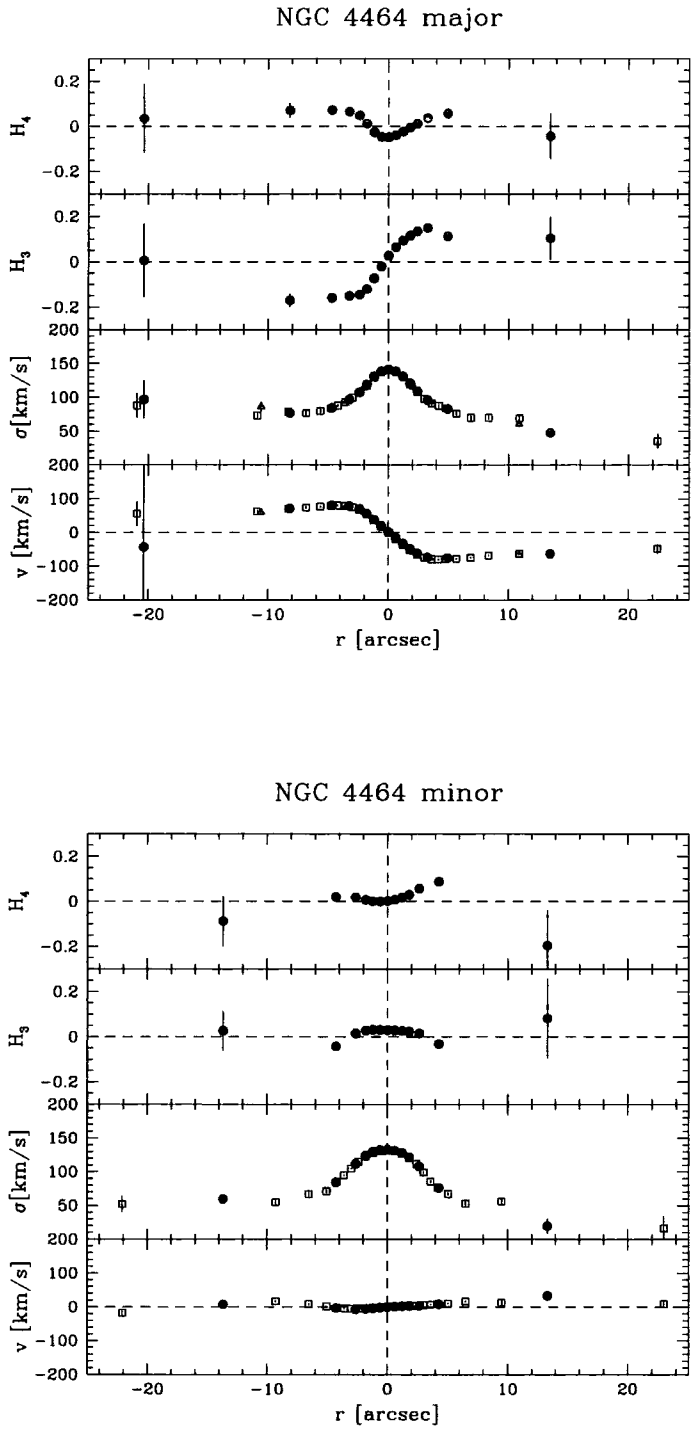

Figure 4.4: Major and minor axis observations for NGC 4464 (PA 5° and 95° respectively). Focus corrections applied to both spectra were 0.″61 and 0.″75 respectively. Seeing for both observations was $\sim$ 1.″0. Measurements are therefore independent only on spatial intervals greater than $\sim$ 1.″25. Additional measurements, obtained for a signal-to-noise ratio of 40 pixel^{-1}, are given by open triangles.

NGC 4564

NGC 4564 is classified as E6 in both the RC3 and RSA. Measurements of v, σ, H_3 and H_4 are given in figure 4.5. This galaxy has recently been studied by van den Bosch et al. (1994) using HST photometry and in figure 4.6 major axis kinematical measurements obtained here are compared with the measurements of ϵ, PA and cos4θ of van den Bosch et al. (1994), kindly supplied by him.

In figure 4.5, measurements for the major axis appear to describe two separate components, that is measurements for rotation, σ, H_3 and H_4 for $|r| \lesssim 5''$ appear to be very different from those at greater radii. A striking measurement of asymmetry is given by non-zero H_3 , for $|r| \gtrsim 5''$. For the minor axis, H_3 is non-zero for $-9'' \lesssim r \lesssim -5''$ and $r \sim 9''$. H_4 is positive for $5'' \lesssim r \lesssim 9''$. A small amount of rotation is measured for the minor axis for $|r| \lesssim 4''$.

In figure 4.6, the most interesting results from the photometry are the measurement of negative cos4θ and hence boxiness for $|r| \lesssim 3''$ and measurement of diskiness for $|r| \gtrsim 10''$, isophote twisting for $|r| \lesssim 2''.5$, and gradually increasing measurement of ϵ with radius. The measurements of cos4θ for different radii support the existence of two separate kinematical components. The measurement of boxiness for the inner $6''$ is consistent with detection of a central bulge component. The measurements of diskiness for $|r| \gtrsim 10''$ where rotation is still measured to increase with radius, and the gradual increase in ϵ with radius, are consistent with the detection of a more rotationally-supported disk component. Furthermore the measurement of H_3 suggests that two components of different kinematical properties are being detected along the line-of-sight, e.g. a rotationally-supported cold disk and more anisotropic bulge component. All measurements are consistent with detection of a disk component embedded within a more slowly rotating bulge. A two component analysis of both photometry and kinematics would provide additional constraints for the scalelengths of two such components. The isophotal twisting for $|r| \lesssim 2''.5$ should explain the measurement of rotation and the non-zero measurement of H_3 , for minor axis.

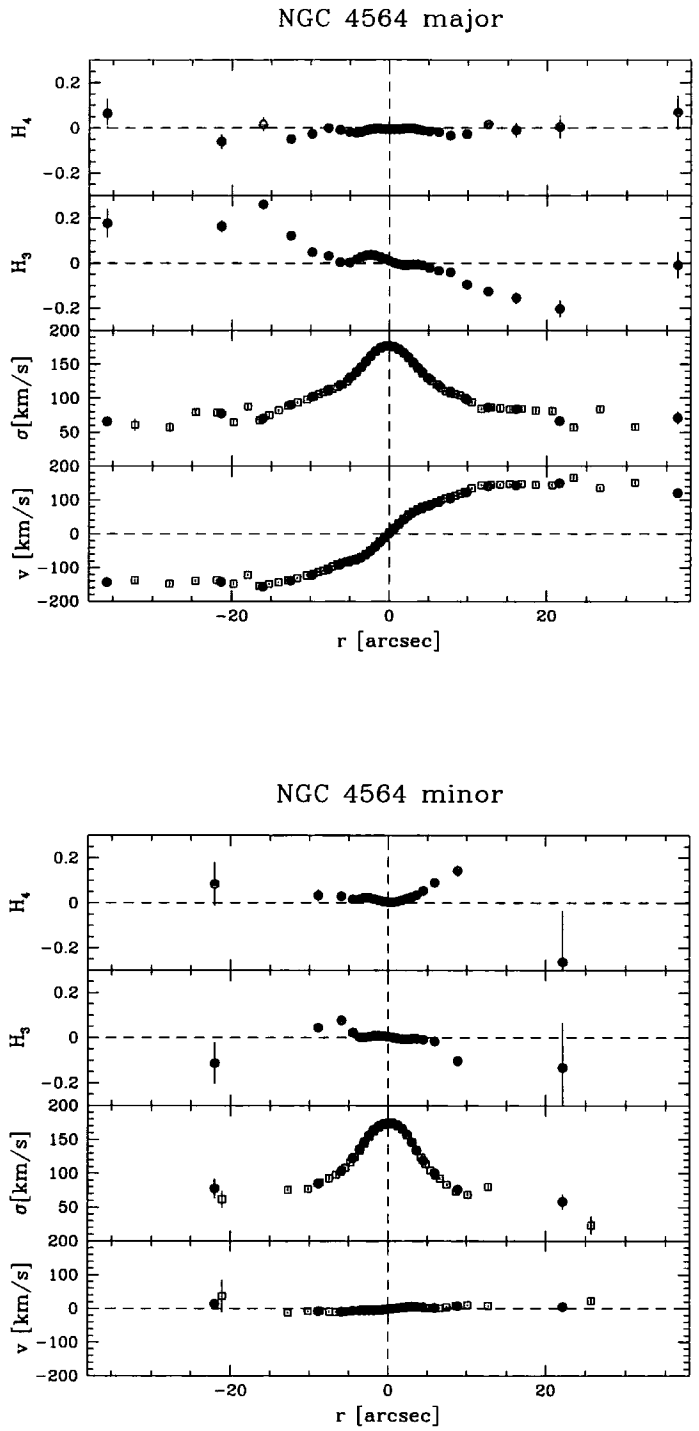

Figure 4.5: Measurements for the major and minor axes of NGC 4564 (PA 45° and 135° respectively). Both spectra were corrected for the effects of focus variations; the maximum smoothing applied, 0.″82 for the major axis spectrum, and 0.″74 for the minor axis spectrum, was in both cases smaller then the seeing of $\sim 1''$. The total effective smoothing is 1.″29 and 1.″24, respectively.

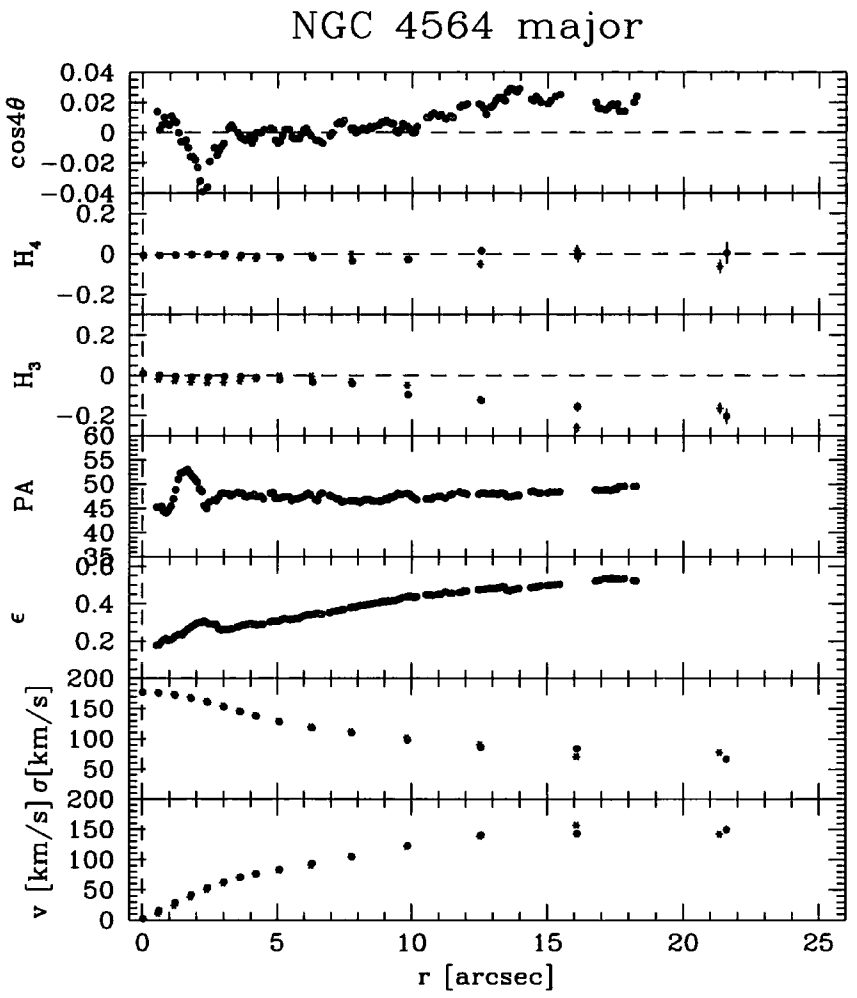

Figure 4.6: Comparison of kinematical measurements obtained here with the photometry of van den Bosch et al. (1994) (i.e. measurements of cos4θ, ellipticity (ϵ) and PA as functions of radius). Measurements of rotation and H_3 have been folded by multiplying measurements for negative values of radius by -1.

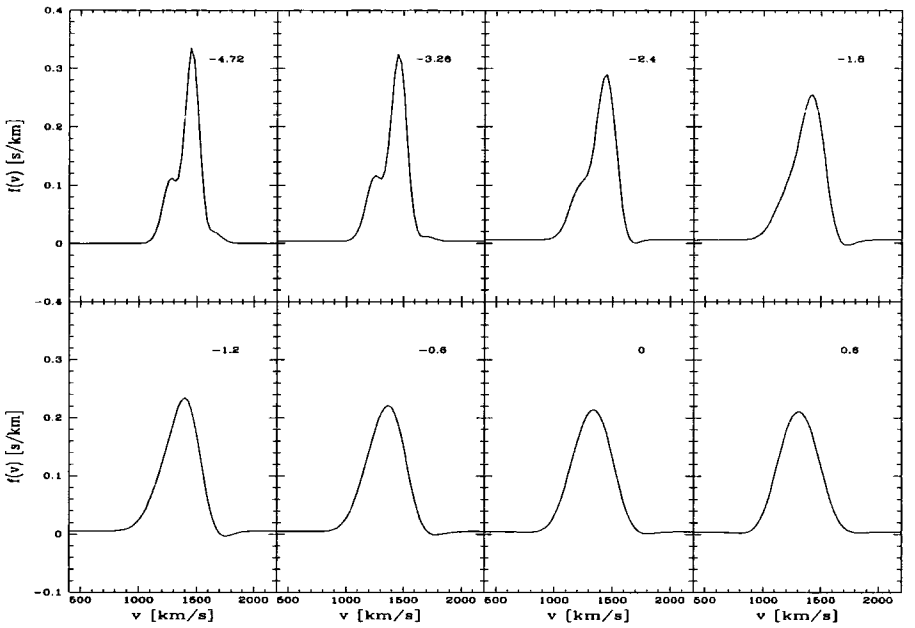

Figure 4.7: Measured LOSVDs for the major axis spectrum of NGC 5582. Radii of measurement is indicated in arcseconds for each LOSVD shape. A second component, possibly Gaussian, is clearly visible in the LOSVDs for $-4.72''$ r $< -1.2''$. It is also evident how the width of the LOSVD increases towards smaller radii, in agreement with the larger measured values of σ.

NGC 5582

Classified as elliptical in the RC3, measurements for NGC 5582 are presented in figure 4.8. For the major axis, H_3 is significantly non-zero for $|r| \lesssim 14$ $''$ and reaches a maximum amplitude for radii corresponding approximately to the point for which maximum rotation is measured. H_4 changes significantly in value with radius. For the inner $10''$, the measurements closely resemble those for the major axis of NGC 4464. For the minor axis, the non-zero measurement of both H_3 and H_4 could be due to a slight misalignment of the slit position of observation with the true minor axis of the galaxy. Measurements are consistent with detection of a central, radially-anisotropic bulge component extending out to $|r| \sim 14''$, and a rapidly rotating disk component extending to the greatest measured radii. Examples of actual fits for the galaxy broadening function i.e. the recovered LOSVD shape are given in figure 4.7. For $r \lesssim -1''$, the LOSVD is clearly asymmetric and for $r \lesssim -2''$ there is clear evidence for the existence of two separate kinematical components, one of which has greater mean velocity along the line-of-sight and appears to dominate the measured kinematics. This is indeed consistent with detection of a bright disk component, or a bulge component of high rotational support.

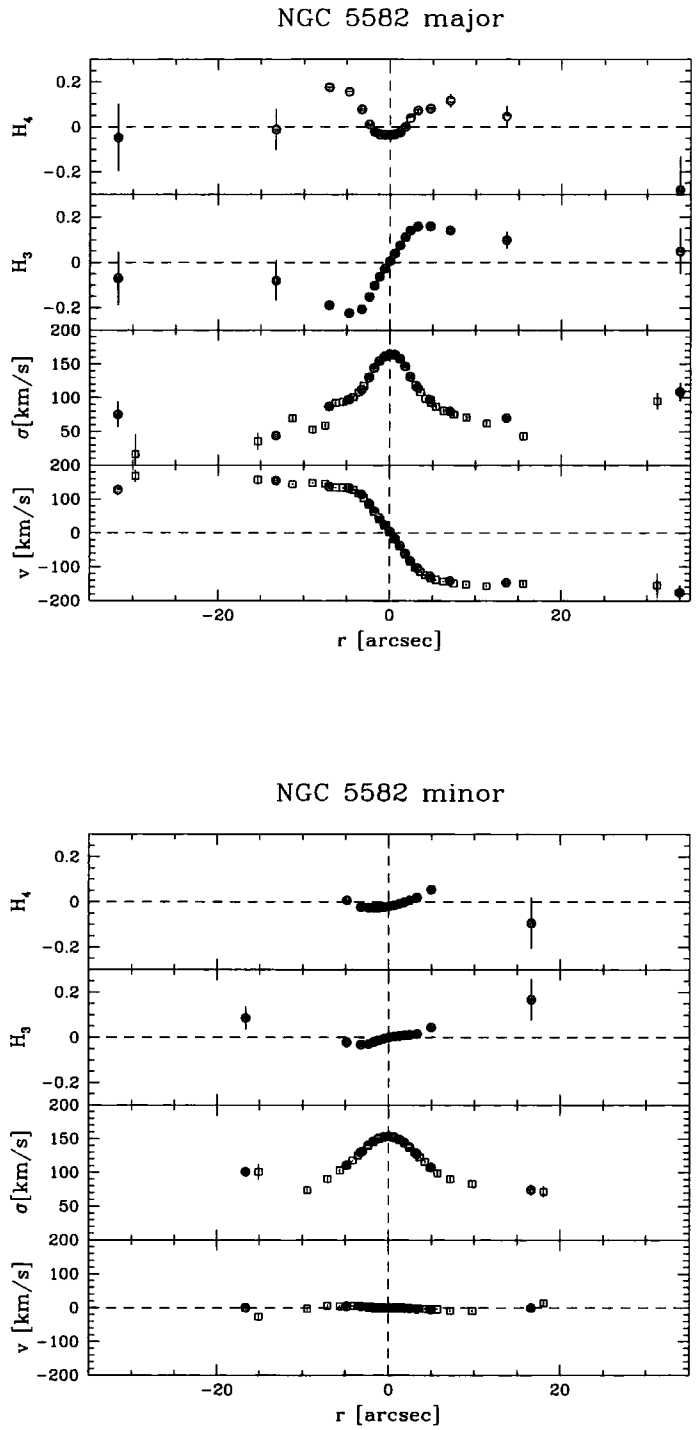

Figure 4.8: Major and minor axis observations for NGC 5582 (PA 25° and 115° respectively). Focus corrections applied for the major and minor axis spectra corresponded to a *maximum* Gaussian smoothing of 0.″74 and 1.″30 respectively. Seeing for the minor axis observation was 1″; measurements for this spectrum can not be assumed to be independent, on spatial intervals $\lesssim$1.″6.

4.1.2 Type 2

These galaxies show strong evidence for embedded disks within an elliptical bulge. Dips in σ are measured close to the galaxy centre; these measurements are often associated with measurements of positive H_4 , evidence of tangential anisotropy and possibly of a central disk component. Measurements of H_3 and H_4 , and although to a lesser extent rotation and σ, are often found to be asymmetric about the kinematical centre of the galaxy, suggesting that any nuclear component may be decoupled from the main body of the galaxy. σ is measured to be near constant as a function of radius in contrast to measurements for galaxies of types 1 & 3 which were found to steadily decrease with radius.

NGC 3605

Classified as an E4 intermediate in the RC3, and E5 in the RSA, measurements of rotation and σ for this galaxy have been obtained previously for this galaxy by Davies et al. (1983). Measurements of kinematics obtained here are given in figure 4.9. Photometry for this galaxy was studied by Peletier et al. (1990) and Lauer et al. (1995). For $r \lesssim 4''$, Lauer et al. (1995) measure $\cos 4\theta$ to be predominantly positive, a detection of diskiness. For $r \gtrsim 4''$, Peletier et al. (1990) measure $\cos 4\theta$ to become increasingly negative out to $r \sim 20''$, i.e. the galaxy is increasingly "boxy".

For the major axis spectrum in figure 4.9, the most notable feature is the non-zero measurement of H_3 for $|r| \lesssim 7''$. H_4 is essentially zero, for these radii. For the minor axis, both H_3 and H_4 are essentially zero close to the galaxy centre, becoming non-zero at greater radii although these measurements are far more uncertain. It should be noted that the minor axis spectrum was smoothed considerably in the spatial direction during a focus correction. The non-zero measurement of H_3 for the major axis and the detection of diskiness by Lauer et al. (1995) at similar radii, supports the existence of a nuclear disk component. A disk component of considerable rotational support would be expected to cause a decrease in σ at the galaxy centre. σ is measured to be constant at small radii for both axes. This measurement could represent a conspiracy between the rising σ of a bulge component and the effect of a central disk causing σ to decrease. Observations of greater resolution however could reveal a central decrease in σ.

NGC 4387

NGC 4387 was one of 8 of the 45 ellipticals imaged by Lauer et al. (1995), suspected to contain a nuclear star cluster. Such a component was proposed to explain an upturn in the measured surface brightness towards the HST resolution limit. Kinematical measurements for NGC 4387 are presented in figure 4.10.

Both major and minor axis observations shows a noticeable dip in σ at the galaxy centre. For $0'' \lesssim r \lesssim 5''$ along the minor axis, H_4 is measured to be slightly positive, representing a small amount of tangential anisotropy. For the major axis, H_3 is slightly negative for $1.5'' \lesssim r \lesssim 5''$ which could correspond to an additional kinematical component; H_4 is measured to be positive for $r \lesssim -5''$, consistent with radial anisotropy. For H_4 the measurements are not found to symmetrical about the galaxy centre: this could represent evidence of a separate component, kinematically decoupled from the main body of the galaxy. A small amount of rotation is detected at the galaxy

centre for the minor axis observation which could be due to a slight isophote twisting measured by Lauer et al. (1995), for $r \lesssim 4''$. Outside $\sim 4''$ this galaxy was observed by Peletier et al. (1990) to have predominantly boxy isophotes.

The central decrease in σ measured for both axes, is consistent with the existence of a nuclear stellar component of sufficient brightness to dominate the light of the galaxy close to the centre and more rotationally supported than a surrounding bulge component.

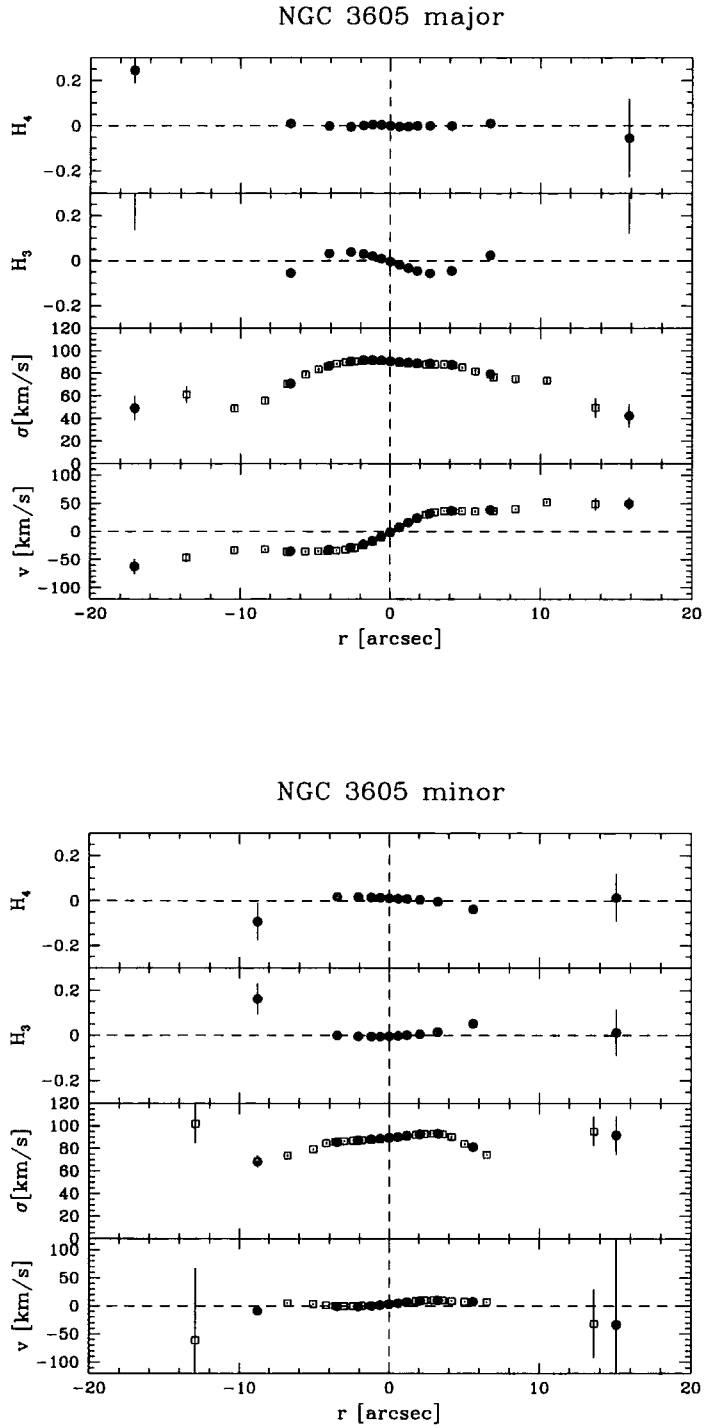

Figure 4.9: Major and minor axis observations for NGC 3605 (PA 290° and 200° respectively). The minor axis observation was subject to significant smoothing during focus corrections, i.e. a maximum Gaussian smoothing of 1.″44 was applied. For the major axis spectrum, a maximum smoothing of 0.″69 was required. Seeing for both observations was $\sim 1''$; the total effective smoothing in the spatial direction is therefore 1.″75 and 1.″21 for the minor and major axis observations respectively.

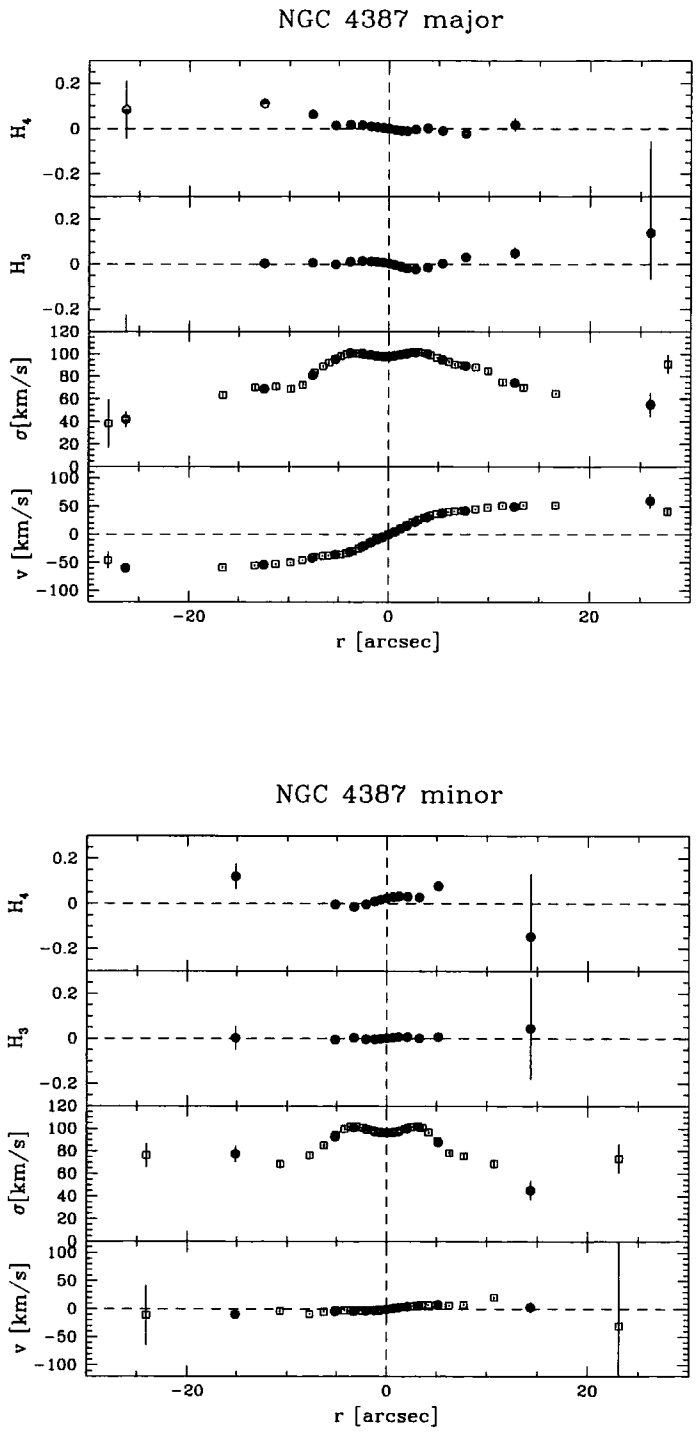

Figure 4.10: Major and minor observations for NGC 4387 (PA 142° and 52° respectively). Focus corrections corresponding to smoothing of 0.″86 and 0.″76 respectively were applied. Seeing for both observations was $\sim 1''$; the total effective smoothing in the spatial direction is therefore 1.″32 and 1.″26.

NGC 4478

Classified as E2 in both the RC3 and RSA, this elliptical has recently been studied using HST by van den Bosch et al. (1994). Kinematical measurements for the major and minor axes obtained here, are presented in figure 4.11. Measurements for the major axis are compared with measurements of ϵ, PA and $\cos 4\theta$ from van den Bosch et al. (1994), and of ϵ and PA from Peletier et al. (1990), in figure 4.12. Photometry for this galaxy was studied by Prugniel et al. (1987). From their photometric measurements, Prugniel et al. (1987) classified this galaxy as a compact elliptical and interpreted their measurement of high surface brightness, isophotal twisting through 30° between 30″ and 60″, and almost circular isophotes, as evidence that NGC 4478 had been tidally-truncated by its nearby companion M87.

In figure 4.11, measurements of rotation, σ, H_3 and H_4 for $|r| < 5''$, provide strong indications of a central component, decoupled from the surrounding galaxy. Measurements of σ and H_4 for this range of radii, are asymmetric, and rotation and H_3 are not point-symmetric, about the galaxy centre, most notably for the major axis. This could be the result of considerable isophote twisting measured by van den Bosch et al. (1994) for $|r| < 5''$, such that the measured PA deviated by up to 10° from that of the major axis observation (i.e. PA 145°) (see figure 4.12). Observations obtained for the photometric axes of the main galaxy may not therefore coincide with the similar axes of a distinct component. A central decrease in σ is measured for both axes. For the major axis, a significantly non-zero value of H_3 is measured for $|r| < 5''$, and H_4 is positive for $0 \lesssim r \lesssim 3''$. For the minor axis, the measurement of H_3 is non-zero for small positive radii, and H_4 becomes slightly negative outside the inner 3″.

In figure 4.12, measurements for the major axis are compared with photometry from the literature. Two interesting features of the photometry of van den Bosch et al. (1994), in addition to the isophote twisting mentioned above, are the significant measurement of diskiness for the inner 2″ and the sharp increase in ellipticity for $|r| \lesssim 1.5''$. These two results offer strong support to the idea that a disk component resides at the galaxy centre. From the study of residual maps of their photometry, van den Bosch et al. (1994) were unable however, to state conclusively that such a component was observed.

The measured asymmetry for the major axis, i.e. non-zero measurement of H_3, together with the positive measurement of H_4 for both axes close to the galaxy centre, are consistent with the detection of a separate kinematical component with orbital motion across the line-of-sight. The central dip in σ, for similar radii, suggests that this component is more rotationally-supported than the surrounding bulge component. Taken together these results are consistent with the detection of a nuclear disk population. The lack of conclusive evidence from the photometry could be due to the low inclination of the galaxy and of any separate component, which would increase the difficulty of detection of any disk component. Central disk components are associated with the presence of dust, which in turn could explain either the obscuration of the true nature of a central component, or a measured isophotal twisting. A recent study of the dust distribution within ellipticals imaged by HST, by van Dokkum and Franx (1995), however discovered no significant evidence for a central dust distribution in NGC 4478. This has confirmed an earlier result obtained by van den Bosch et al. (1994).

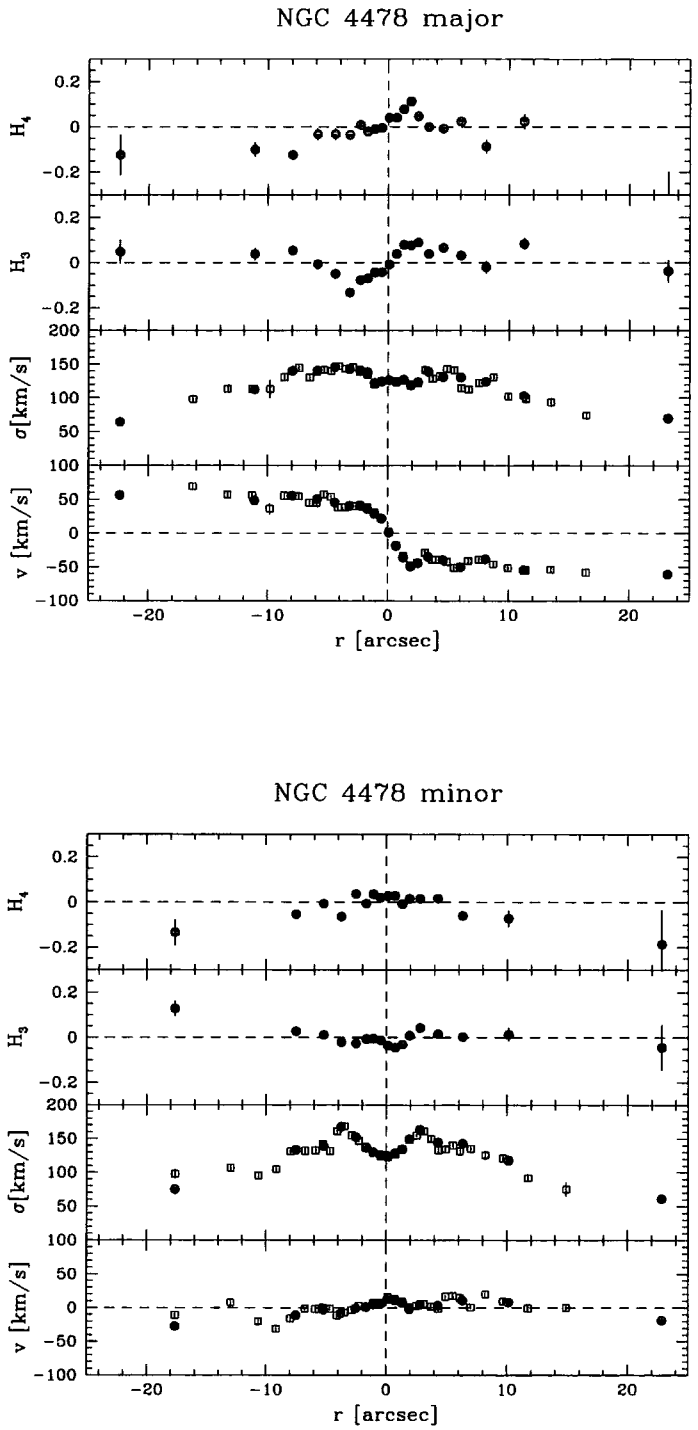

Figure 4.11: Major and minor axis observations of NGC 4478 (PA 145° and 55° respectively). Seeing for observations was approximately 0.″8 and 0.″5 respectively.

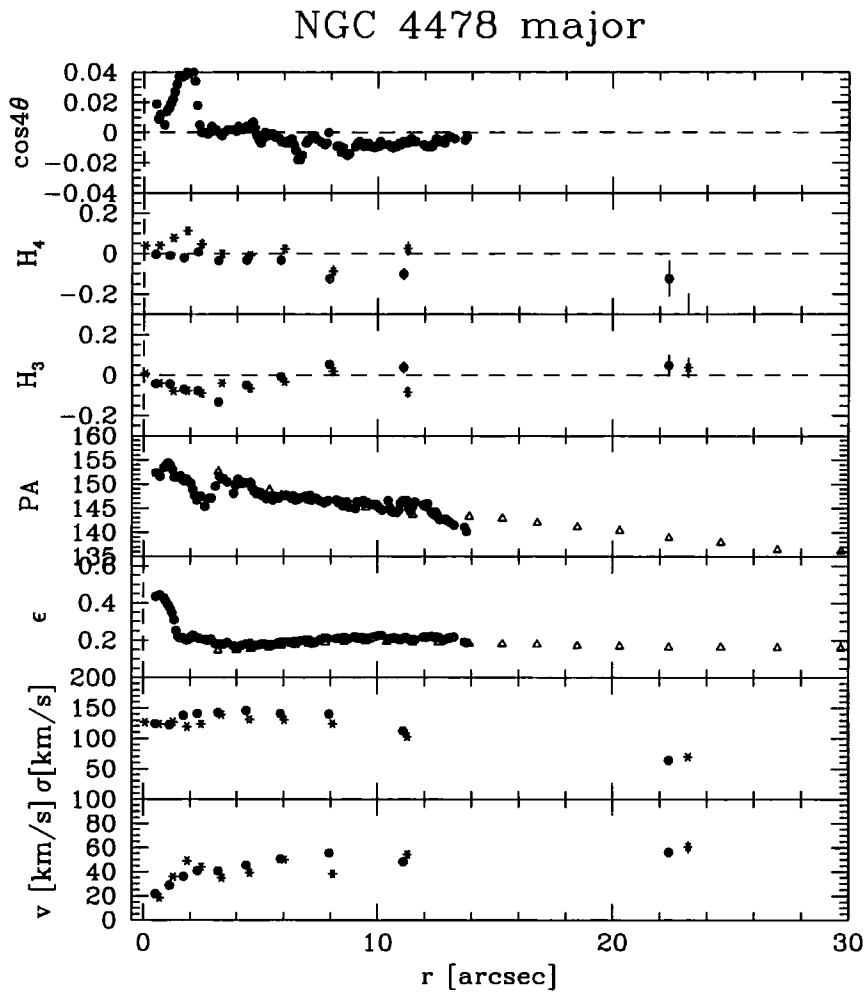

Figure 4.12: Measurements of rotation, σ , H_3 and H_4 obtained here for the major axis of NGC 4478, are shown with photometry (ϵ, PA and cos4θ). Measurements of rotation and H_3 have been folded by multiplying measurements for negative values of radius by -1. Photometry of van den Bosch et al. (1994) is given indicated by solid circles and that of Peletier et al. (1990) by open triangles.

NGC 4551

NGC 4551 has an uncertain classification as elliptical in the RC3. Measurements of kinematics for this galaxy are given in figure 4.13. This galaxy was studied by both Peletier et al. (1990) and Lauer et al. (1995). The photometric measurements of Lauer et al. (1995) found NGC 4551 to have "disky" isophotes for $1'' \lesssim |r| \lesssim 4''$. As for NGC 4387, Lauer et al. (1995) have postulated that NGC 4551 may contain a central stellar nucleus. Peletier et al. (1990) measure NGC 4551 to become increasingly "boxy" from $r \sim 4''$ to $r \sim 10''$, and at greater radii, measure $\cos 4\theta$ to tend to zero.

For the major axis observation, H_3 is significantly non-zero for $|r| \lesssim 5''$. H_4 is slightly positive close to the galaxy centre, and negative for $-7'' \lesssim |r| \lesssim 0''$ and $2'' \lesssim |r| \lesssim 8''$. For the minor axis, the measurement of H_4 changes only slightly with radius and is almost consistent with a value of zero. Rotation, of small amplitude, is measured for the major axis and essentially no rotation is detected for the minor axis. A small central decrease in σ is detected for the minor axis. This is not observed for the major axis although the rise in σ for this axis, towards the galaxy centre could be attributed to the steep central rise in measured rotation.

Measurements of kinematics for this galaxy are similar to those of NGC 4478 and their interpretation can in many respects be taken to be the same as this galaxy. The measured LOSVD asymmetry for $|r| \lesssim 5''$ of the major axis, and central rise in measured H_4, are consistent with the detection of a distinct central component of orbital motion across the line-of-sight.

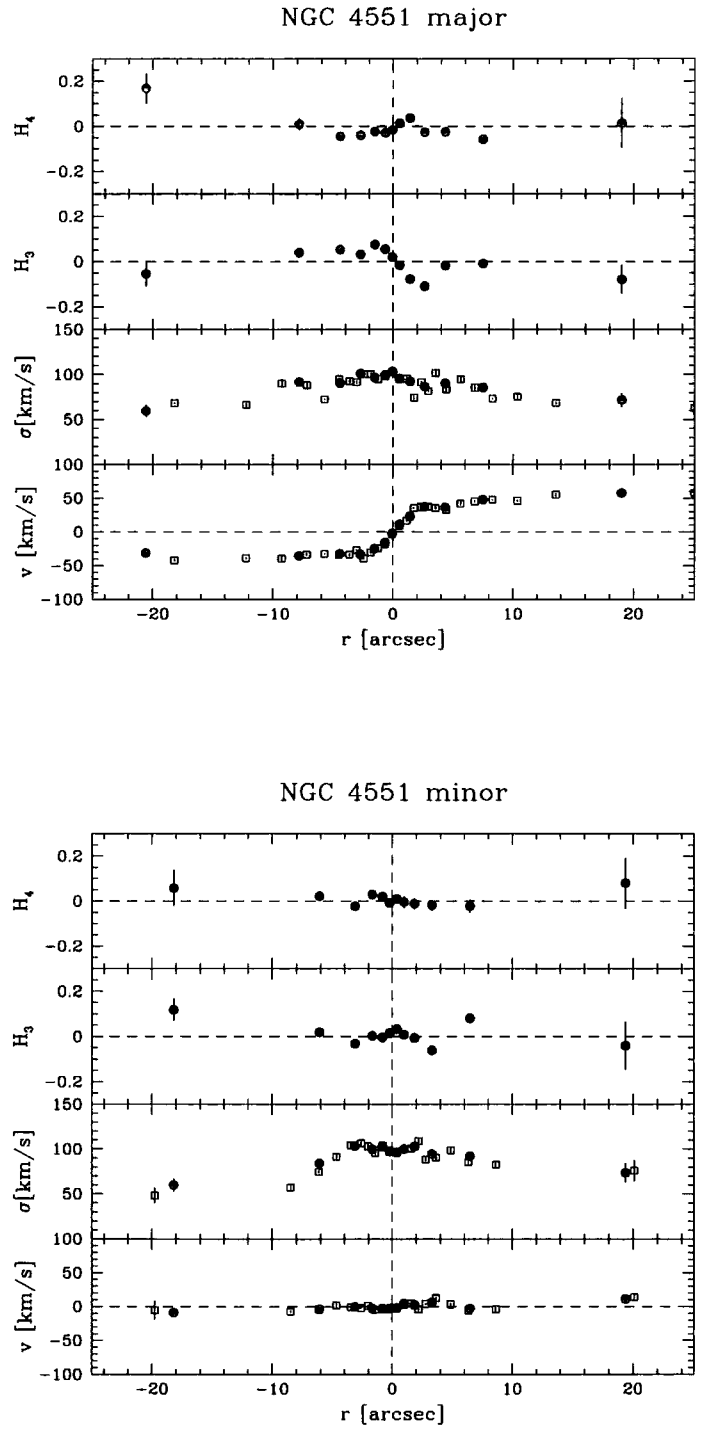

Figure 4.13: Major and minor axis observations for NGC 4551 (PA 70° and 160° respectively). Seeing for both observations was approximately 0.″8.

4.1.3 Type 3

This category contains galaxies with the clearest indications of kinematically decoupled cores of all galaxies within our sample (i.e. NGC 3608 and NGC 4458). These cores are found to be embedded within a slowly rotating, anisotropic elliptical main body. NGC 3608 has long been known to contain a kinematically-decoupled core (hereafter KDC) (Jedrzejewski and Schechter, 1988). The measurements for NGC 4458 presented here, are more ambiguous but show clear evidence for a separate, central component rotating within an almost non-rotating bulge.

NGC 3608

Classified as E2 in the RC3 and E1 in the RSA, this galaxy was one of the first to be recognised to contain a KDC. The reversal of the sense of rotation at the galaxy core was suggested by Jedrzejewski and Schechter (1988), to be the result of an interaction with another galaxy, without full merging, which caused the motion of the outer parts to be reversed. NGC 3608 is one of several KDC candidates recently imaged by Carollo et al. (1997). From measurement of the $V-I$ colour gradient, they found no significant stellar population differences between the core and surrounding galaxy of NGC 3608. They measured the ellipticity to increase from a value close to zero at $r \simeq 0\farcs1$, to $\epsilon \simeq 0.2$ at $r \simeq 4''$, and NGC 3608 to be slightly boxy for radii outside $5''$.

Measurements of kinematics are presented in figure 4.14. The profiles of H_3 and H_4 for both the major and minor axes, are asymmetric about the galaxy kinematical centre. From measurements of rotation and σ, NGC 3608 has been shown to be one of the strongest candidates to contain a counter-rotating KDC. The measured LOSVD is therefore likely to be more accurately described, for example, by a two-component Gaussian parametrisation, than the parametrisation adopted here. This would explain the ambiguous measurements of H_3 and H_4. A small amount of rotation is detected along the minor axis. The measured velocity profile is decoupled close to the galaxy centre. Measured velocity along the minor axis for $|r| \gtrsim 20''$ is consistent with zero rotation. The measured rotation and σ at radii not affected by the kinematics of the KDC, are consistent with considerable anisotropy, that is the measured rotation of ~ 40 km s^{-1} is far smaller than the measured σ of ~ 150 km s^{-1}.

NGC 4458

This galaxy is classified as an E0 intermediate elliptical galaxy in the RC3. Studied by Lauer et al. (1995), its ellipticity was measured to decrease from a value of ~ 0.5 at $r \sim 0\farcs5$ to close to zero at $r \sim 7\farcs5$.

Measurements of kinematics for this galaxy are presented in figure 4.15. For the major axis, a small amount of rotation is detected close to the galaxy centre and rotation close to zero at greater radii. No rotation is measured for the minor axis. The profiles for both H_3 and H_4 are very unusual and change sharply over between independent measurements. This could however be due to the poor spatial resolution of measurements for this galaxy. H_4 is measured to be negative close to the galaxy centre for both axes, indicating radial anisotropy. For the major axis, H_4 is measured at greater radii to alternate between positive and negative values; these measurements could represent two different types of orbits, positive H_4 values corresponding to radial orbits

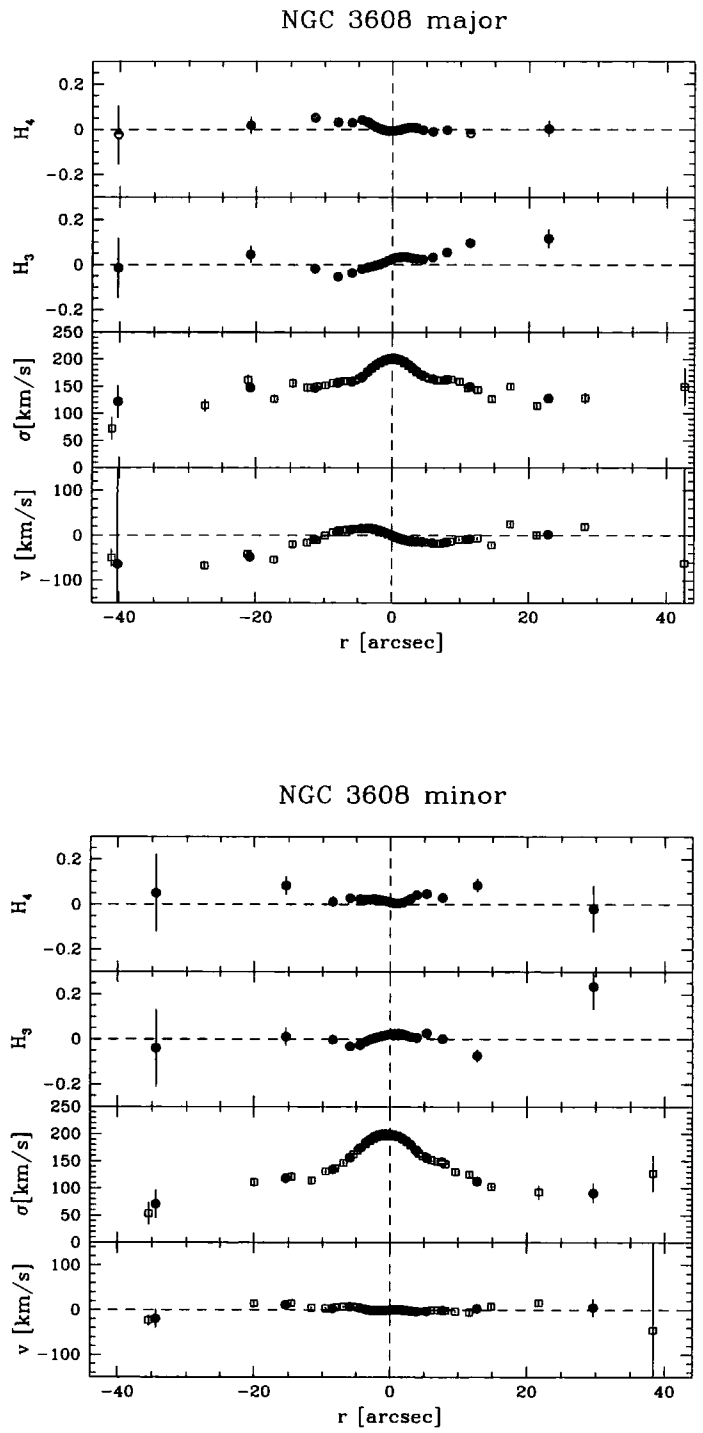

Figure 4.14: Measurements for major and minor axes of NGC 3608 (PA 81° and 351° respectively). Focus corrections were applied for both spectra corresponding to a maximum Gaussian smoothing of 0.″99 for both cases. Seeing of observations was approximately 1″ for both spectra. The total smoothing in the spatial direction was therefore ∼1.″5; data points cannot therefore be assumed to be independent at smaller spatial intervals.

detected side-on, and negative H_4 values representing detection of tangential motion along the line-of-sight. For small positive radii, H_3 is measured to be positive for both the major and minor axes, and is also measured to be slightly negative for small negative radii for the major axis. These measurements offer evidence for a central distinct kinematical component.

4.1.4 NGC 3379

NGC 3379 is a member of the Leo-I group and is a well observed elliptical, classified as E1 in the RC3. Measurements for the major and minor axes are presented in figure 4.16.

For the major axis, non-zero H_3 is measured close to the galaxy centre and changes sign at a different radii than the rotation. The rotation appears to decrease at $r \sim 5.5''$ but this is probably due to the poor spatial resolution of the measurements. H_4 is slightly positive for $r \gtrsim 2.5''$ and $r \sim -2''$, and negative for $r \sim -8''$. For the minor axis, H_4 is positive for $-9'' \lesssim r \lesssim -4''$, and, with lower amplitude, for $r \sim -1''$ and $3'' \lesssim r \lesssim 5.5''$, representing a significant measurement of radial anisotropy.

4.1.5 NGC 4468

Our exposures for the major and minor observations of this galaxy presented in figure 4.17, were too low to provide considerable spatial detail of its kinematical structure. Probably a low surface brightness dwarf elliptical or S0 galaxy, the measured rotation and velocity dispersion are very low, with $\frac{v}{\sigma} \sim 1.0$. It should be noted that these measurements mark the limits achievable for the spectral resolution of our data.

4.2 Summary

Measurements of rotation, σ, H_3 and H_4 have been presented for the major and minor axes of our sample. These measurements have been used to identify different types of object, based on the similarity of their measurements. The characteristics of each type briefly are:

1. strong evidence for both disk and bulge components; classification as E/S0; in some cases, measurement of considerable diskiness in photometry; measured values of H_3 are the greatest measured for our galaxy sample.

2. central dips in σ; strong evidence for disks embedded within bulge component; measurements of σ and H_4 asymmetric, and rotation and H_3 lacking point symmetry about galaxy centre, suggesting existence of decoupled central component.

3. galaxies clearly containing kinematically-decoupled core (KDC) with counter-rotating cores.

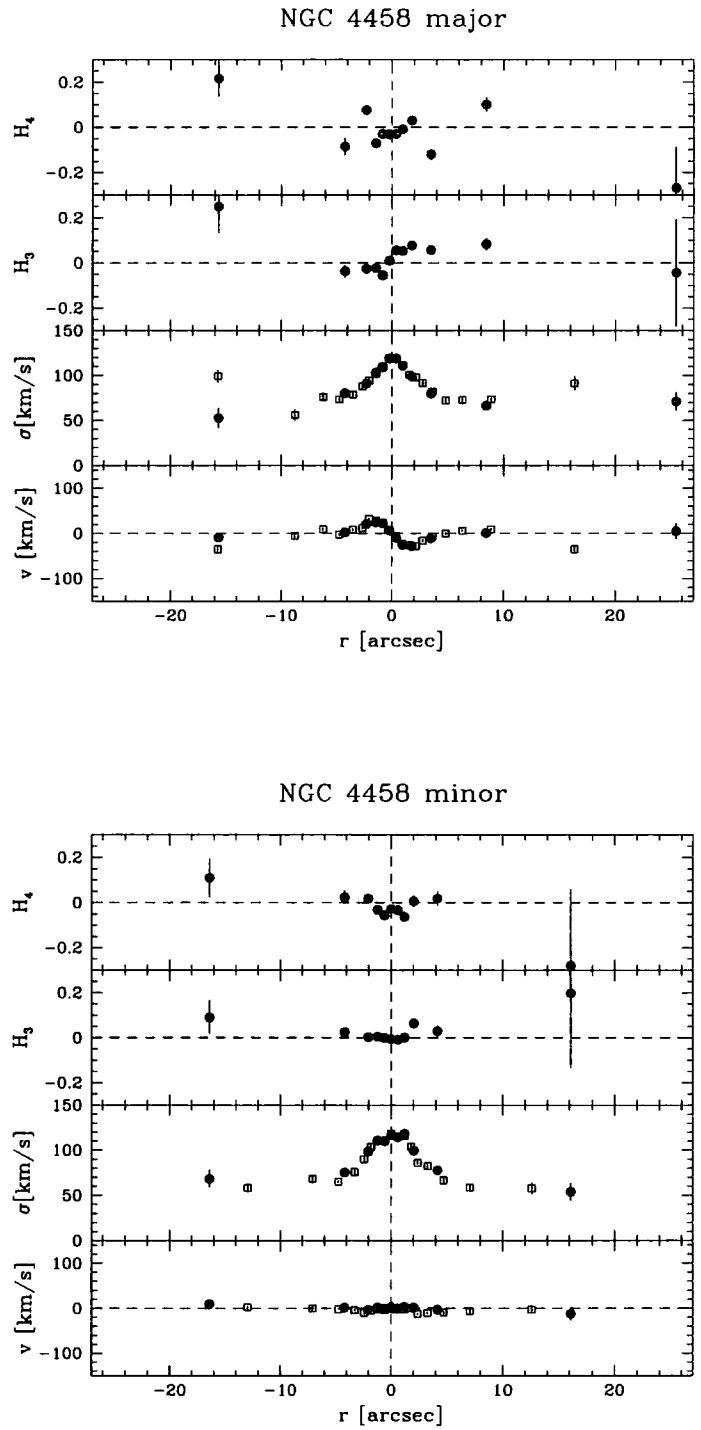

Figure 4.15: Major and minor axis observations for NGC 4458 (PA 5° and 95° respectively). Seeing for both observations was approximately 0.″8.

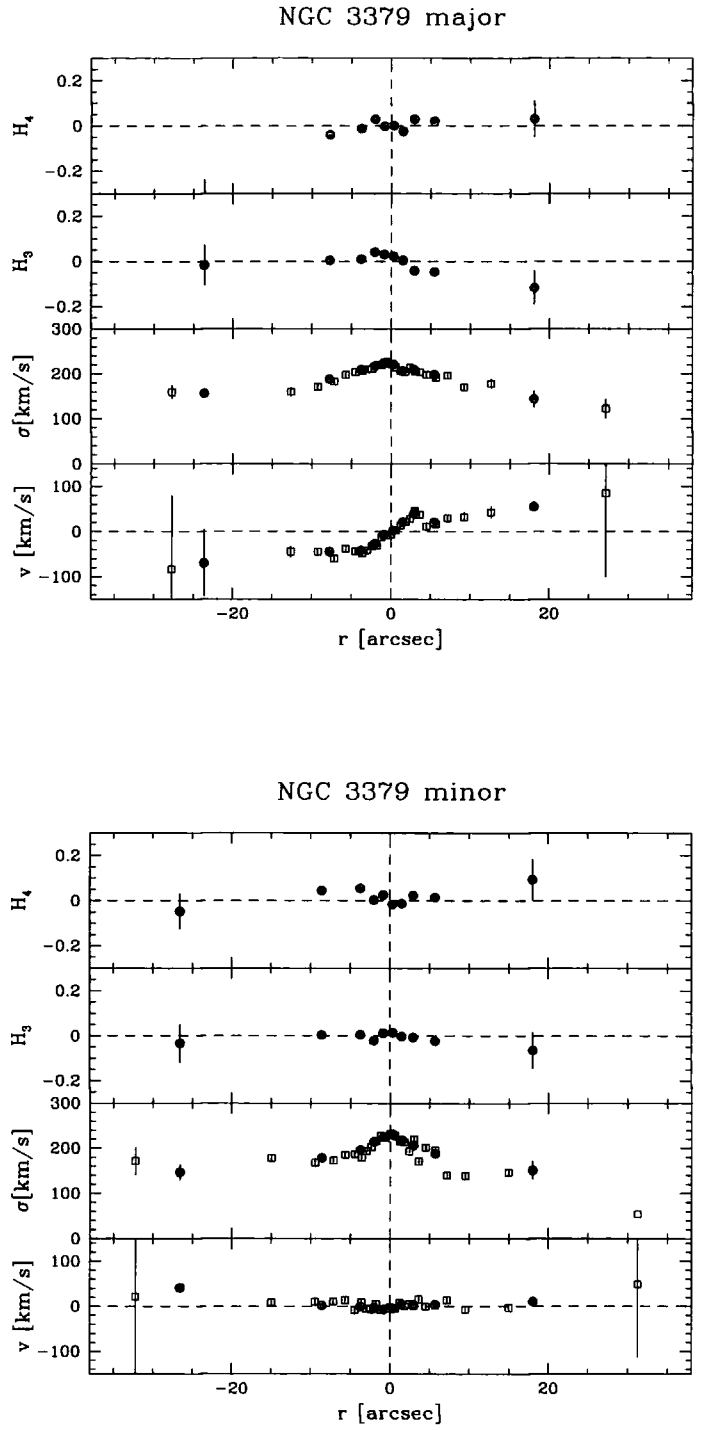

Figure 4.16: Major and minor axis observations for NGC 3379 (PA 71° and 161° respectively). Seeing for both observations was approximately 0.″8.

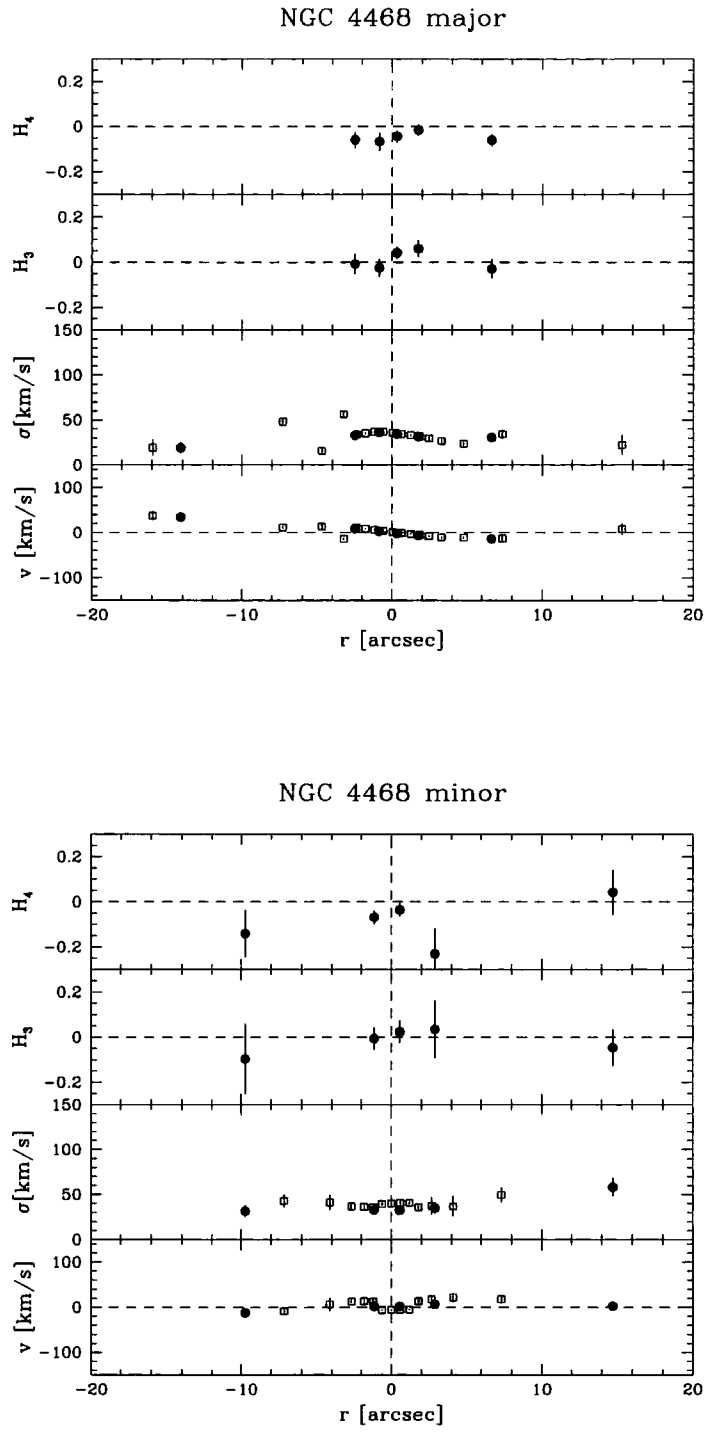

Figure 4.17: Major and minor axis observations for NGC 4468 (PA 65° and 155° respectively). Seeing for both observations was approximately 1″.

4.3 Kinematical Parameters

In this section kinematical parameters derived using the major axis measurements of each galaxy are compared. The purpose of this study is to try to uncover some physical reasoning for the different types of kinematical measurements presented in this chapter. Several parameters were found for each galaxy i.e. v_{max} the maximum measured rotation velocity, σ_0, σ_{max} and $\overline{\sigma}$ the central, maximum and mean of all measured velocity dispersions respectively, $\overline{|H_3|}$ the mean of the absolute values of H_3, and $\overline{H_4}$ the mean value of H_4. For $\overline{\sigma}$, values were taken to be the mean of all measurements within $\frac{1}{2}\mathrm{R}_e$. For H_3 and H_4, the mean of all measurements within $\frac{1}{2}\mathrm{R}_e$ not including measurements close to the galaxy centre was found. In figures 4.18 and 4.19 measurements are indicated by the galaxy kinematical type, 1, 2, 3 or O (others i.e. NGC 3379 and NGC 4468) and plotted against σ_0. Errors presented were calculated by propagating the errors determined for original measurements of rotation, σ, H_3 and H_4 (as described in section 3.8).

In figure 4.18(a) measurements of v_{max} are presented for each galaxy. Values for galaxies of "type 1" are greater than those for all other galaxies suggesting that these galaxies have greater rotational support. Conversely measurements for "type 3" galaxies are of the lowest values suggesting the detection of motion of greater anisotropy. The ratio of the central to maximum velocity dispersion is considered in figure 4.18(b). Values for this ratio differ from one for most galaxies of "type 2". This is expected since these galaxies are observed to have central decreases in σ. For all other galaxies results are consistent with σ increasing monotonically towards the galaxy centre. In figure 4.18(c) although there is no distinctive differentiation of values according to kinematical type, $\overline{|H_3|}$ is greater on average for galaxies of "type 1". These galaxies have the greatest evidence for the presence of an embedded disk component and the measured asymmetries may represent the detection of such a disk. Asymmetries of smaller amplitude are measured for the remaining galaxies which suggests that multiple component structures may be common for all galaxies studied here. The mean value of H_4 is considered in figure 4.18(d). Values are on average of the greatest amplitude and predominantly positive for galaxies of "type 1", representing a detection of tangential anisotropy. This is again consistent with the detection of an embedded disk.

In figure 4.19 the ratio of v_{max} and the mean velocity dispersion, $\overline{\sigma}$, i.e. $\frac{v_{max}}{\overline{\sigma}}$ is plotted against the mean ellipticity $\overline{\epsilon}$. Predictions of the tensor virial theorem from Binney (1978) for oblate isotropic models assuming constant ellipticity are indicated by the solid line. Measurements for galaxies of "type 1" lie very close to or above the isotropic model relation. Measurements for all other galaxies studied here lie below the model line particularly for galaxies of "type 3", suggesting that these galaxies have more anisotropic motion and are less supported by rotation.

Taken together figures 4.18 and 4.19 show that the classification scheme adopted here may have some physical basis. Further work would however be required to confirm the suggestions of these results.

4.4 Discussion

Asymmetric LOSVDs, parametrised by the Gauss-Hermite coefficient H_3, have been measured for the majority of our sample of intrinsically low-luminosity ellipticals. These asymmetries are found

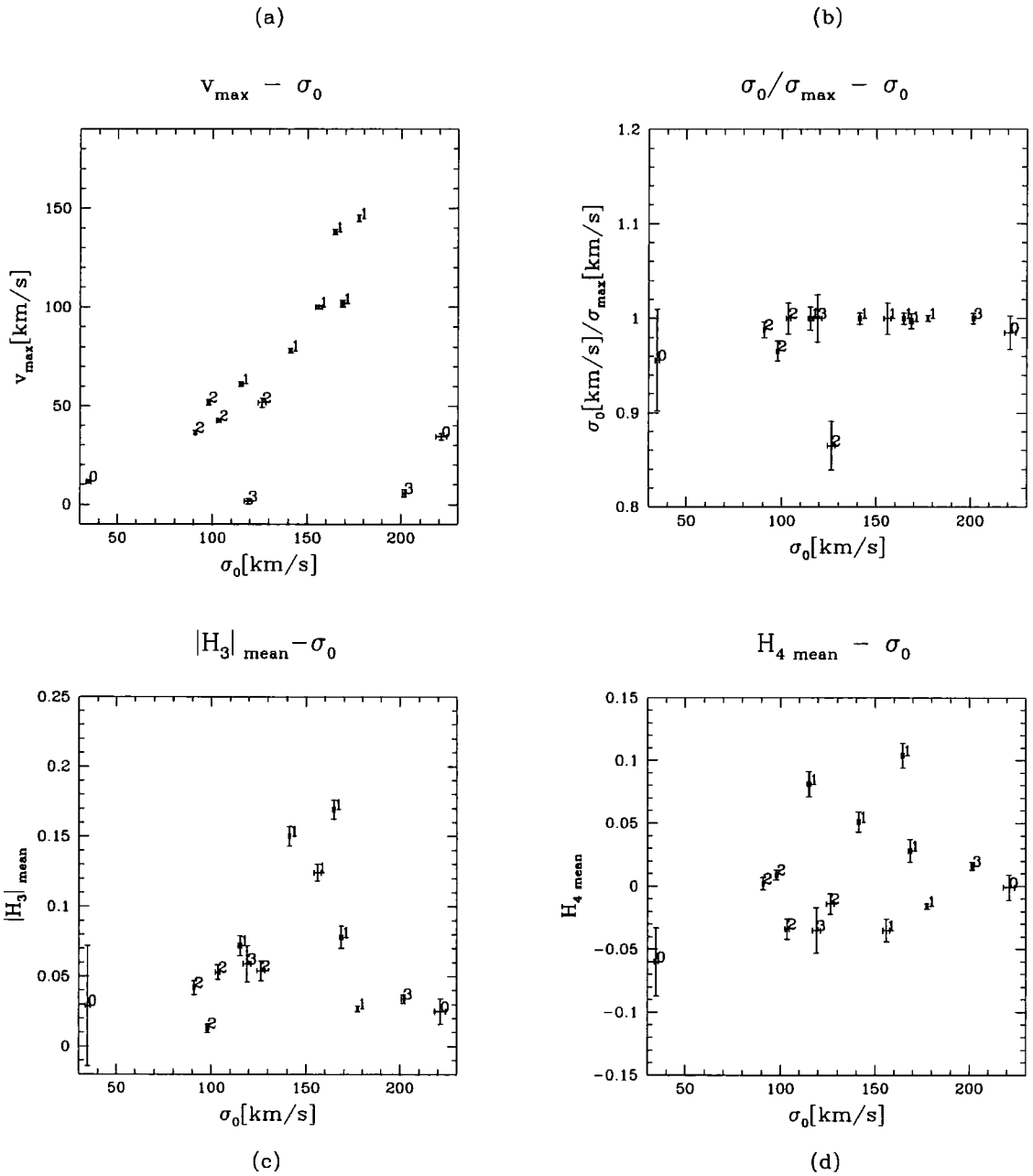

Figure 4.18: Measurements for the major axis of each galaxy, labelled according to galaxy kinematical type.

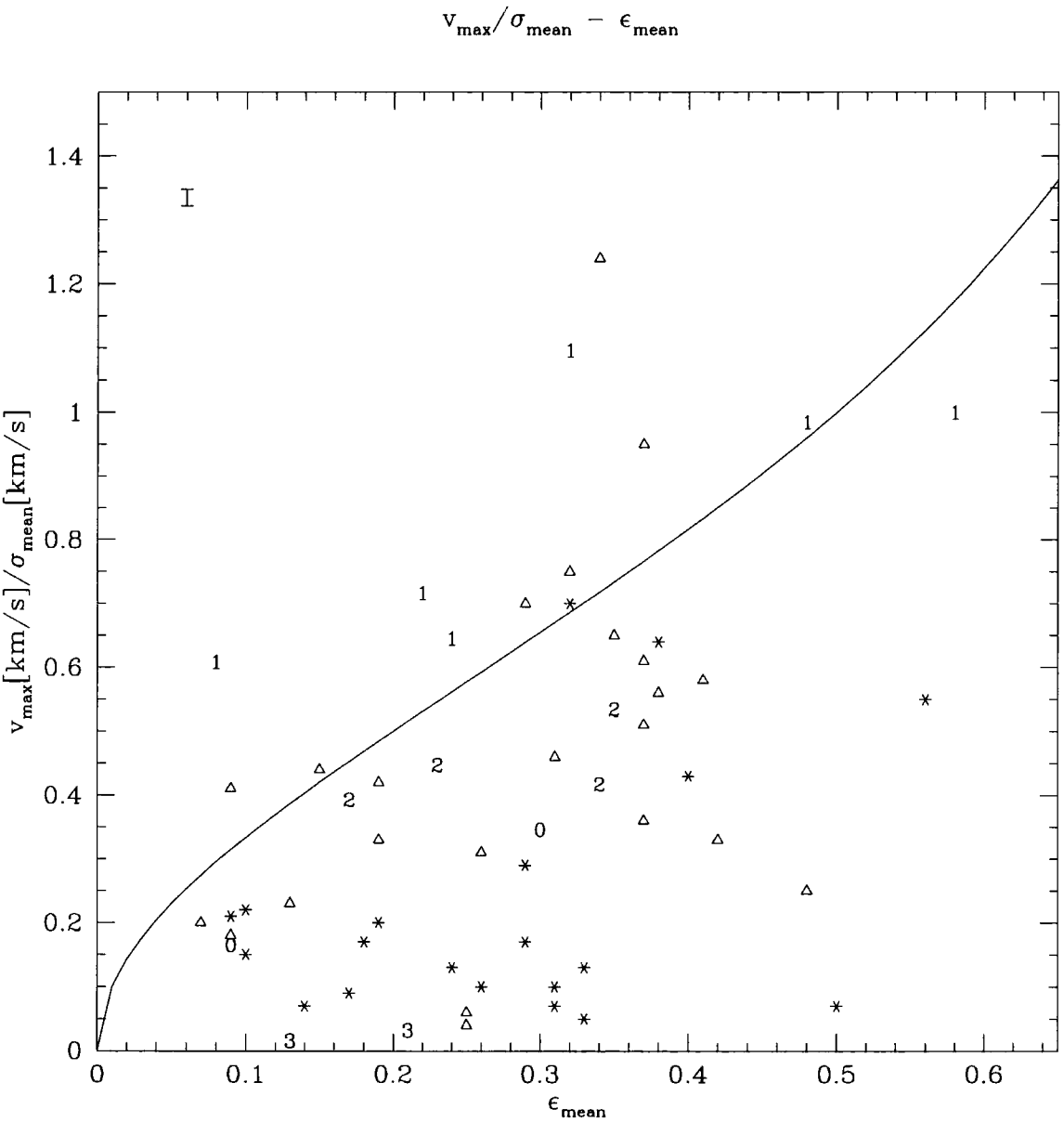

Figure 4.19: Comparison of measurements of $\frac{v_{max}}{\bar{\sigma}}$ against $\bar{\epsilon}$, with the predictions for oblate isotropic models (Binney, 1978) given by solid line. Measurements for galaxies studied here are indicated by labels of the galaxy kinematical type. A typical error bar for the quantity $\frac{v_{max}}{\bar{\sigma}}$ is given in the upper left-hand corner of figure. Additional measurements from Davies et al. (1983) are also presented: measurements for ellipticals with $M_B^{UH} < -20.5$ are given by asterisk symbols, and for $M_B^{UH} > -20.5$ by open triangles where M_B^{UH} is the absolute magnitude calculated by Davies et al. (1983) based on a uniform Hubble flow.

mainly for radii close to, and to change sign with rotation at, the galaxy centre, and suggest that the superposition of two separate components of different kinematical properties is being detected.

The different "types" of galaxy identified within our sample show evidence of having experienced very different stellar evolutionary histories. "Type 1" galaxies have considerable rotational support which is most likely to be due to embedded disks contributing to the light of the galaxy according to their various scalelengths and surface brightness profiles. The existence of disks within ellipticals is gaining in popularity to explain the E-S0 sequence of the Hubble diagram as one of continuing disk-to-bulge ratio (e.g. Scorza and van den Bosch (1998)). Measurements of rotation and velocity dispersion for galaxies of "type 1" were found to vary smoothly with radius, supporting the simultaneous formation of a disk and bulge component, or where a disk is the result of a gaseous merger, galaxy formation involving dissipation.

Galaxies of "type 2" show considerable evidence for having experienced or having formed as the result of merging. These galaxies have boxy outer isophotes which have been argued to be evidence of formation by merging (e.g. Binney and Petrou (1985)). Central decreases in velocity dispersion and in some cases, decoupled rotation curves, support the existence of a separate central kinematical component. Kinematically peculiar galaxy cores have been presented as strong evidence that ellipticals have experienced merging in their past. A scenario originally proposed by Kormendy (1984) and extended by Balcells and Quinn (1990) to explain the observations of NGC 5813, considers the near dissipationless merging of a smaller less luminous elliptical with a more luminous companion, with the denser smaller elliptical relaxing to the centre of the merger remnant. This scenario would explain central dips in velocity dispersion as due to a more rotationally supported central component but in general such a merger may be expected to produce a remnant with far less regular rotational properties, e.g. to lead to the rotational axes of one component being misaligned with respect to the other. A more likely scenario is one where an elliptical containing an embedded disk component is perturbed in its outer parts perhaps by the nearby interaction with another galaxy. Hau and Thomson (1994) considered such a scenario to explain the formation of ellipticals with counter-rotating cores; their scenario did not however predict central dips in σ. Although their study should be considered for galaxies of "type 3", a variant of such a scenario could explain the formation of our "type 2" galaxies.

"Type 3" galaxies have distinct counter-rotating cores. No central decreases in σ are measured, discounting the formation scenarios of Kormendy (1984) and Hau and Thomson (1994). Measurements are in general ambiguous and a two component analysis of the LOSVD and in both cases observations of greater spatial resolution would enable stronger conclusions to be made.

To summarise, different types of galaxies have been distinguished principally on the basis of their kinematical measurements. Evidence for the existence of a separate kinematical component is clear for all of the galaxies classified as types 1, 2 and 3, and in many cases is consistent with a separate disk component. Galaxies of "type 3" show clear evidence for a kinematically distinct central component. For galaxies of both type 1 and 2, the distinction between the kinematical behaviour is perhaps slightly less clear: galaxies of both types show evidence for disk components embedded within an elliptical bulge and for all besides the "type 1" galaxy NGC 4564, this evidence supports the idea of a central disk. For most galaxies of "type 1" this is related to a considerable non-zero amplitude in measured H_3, and for galaxies of "type 2", to a central dip in σ. Whether these different characteristics reflect very different formation scenarios will however require further

investigation.

4.5 Future Work

Measurements presented for many of the galaxies studied here have been shown to be consistent with the existence of decoupled or distinct kinematical components. For particular cases, most notably for galaxies of type 3 found to contain KDCs, a more appropriate analysis of the LOSVD should involve a decomposition of the LOSVD into two separate components. For "type 1" galaxies, strong candidates to be S0 galaxies, two component analyses would also constrain the properties of a disk component (e.g. as in the study of Scorza and Bender (1995)). Similar analyses of high resolution images of each galaxy would provide yet stronger evidence for the existence of separate disk and bulge components.

A number of the galaxies studied are of small angular extent and our data for these objects are of limited spatial detail. Corrections for chromatic focus variations which affected many of our spectra also degraded the spatial resolution for these observations. Observations of yet greater spatial resolution, attainable with spectroscopic instruments aboard HST or using ground-based facilities with adaptive optics, would enable more sound conclusions about the central structure of these galaxies to be made.

Dynamical modelling provides stronger constraints on the evolutionary history of ellipticals than analyses of the LOSVD alone. Such modelling involves the interpretion of both imaging and kinematical measurements together and would be a natural extension of the study presented here. Recently developed models consider the higher orders of the LOSVD (e.g. Rix et al. (1997)). These models also require data of in general, far greater spatial extent than data considered here (i.e. 2-4R_e). Such data require long integration times to enable high signal-to-noise measurements to be determined at large radii, and larger CCD arrays to ensure that an accurate subtraction of the background sky is made.

Chapter 5

Line-Strengths: Measurements

Measurements of line-strength indices are presented. All measurements have been calibrated to the standard defined by the group at UCO/Lick Observatory, the "Lick/IDS System" (Burstein et al., 1984; Faber et al., 1985; Worthey et al., 1994; Trager et al., 1998). Measurement of the raw line-strengths and the conversion of measurements to the Lick/IDS System is detailed in sections 5.1 and 5.2. In section 5.3, comparisons are made with similar measurements obtained by other authors. Tests performed to investigate the effects of inaccurate sky subtraction are discussed in section 5.4. Final corrected measurements of line-strength as a function of radius are then presented in section 5.5.

5.1 Measurement of Line-Strength Features

Line-strengths have been measured to an effective radius, i.e. $\sim 1 R_e$, for the major and minor axes of each galaxy in our sample, according to the latest definitions of the Lick/IDS system (Trager et al., 1998). Measurements of Hβ, Mg_2 and Mg_b, Fe5270 and Fe5335 are presented. In section 5.1.1, the line-strength indices are defined; the algorithm used to determine measurements is outlined in section 5.1.2.

5.1.1 The Line-Strength Definitions

Each line-strength index is defined as a measure of the depth of a particular absorption feature compared to the level of a locally defined continuum level. This local "pseudo-continuum" level is defined by linearly interpolating between continuum bands defined to be both redward & blueward of the central feature bandpass. Indices are of two types: *atomic* indices (i.e. Hβ, all Fe indices, Mg_b) are defined as an equivalent width in Å, by,

$$I_a = \int_{\lambda_{c_1}}^{\lambda_{c_2}} (1 - \frac{S(\lambda)}{C(\lambda)}) d\lambda \tag{5.1}$$

and *molecular* indices (i.e. Mg_1, Mg_2) as a measure, in magnitudes, of the mean ratio of flux to local continuum level within the central bandpass,

$$I_m = -2.5\ log_{10}\ \frac{\int_{\lambda_{c_1}}^{\lambda_{c_2}} \frac{S(\lambda)}{C(\lambda)} d\lambda}{\lambda_{c_1} - \lambda_{c_2}}. \tag{5.2}$$

where λ_{c_1} and λ_{c_2} are the limits of the central bandpass, $S(\lambda)$ is the object spectrum and $C(\lambda)$ is a measure of the linearly interpolated local pseudo continuum, i.e.,

$$C(\lambda) = \int_{\lambda_{l_1}}^{\lambda_{l_2}} \frac{F_\lambda(\lambda) d\lambda}{\lambda_{l_1} - \lambda_{l_2}}. \tag{5.3}$$

where λ_{l_1} and λ_{l_2} are the wavelengths defining the continuum passband, and F_λ is the flux per unit wavelength for the observed object spectrum.

The definitions of all line-strength features measured here are given in Table 5.1.

Index	λ_{b_1}	λ_{b_2}	λ_{c_1}	λ_{c_2}	λ_{r_1}	λ_{r_2}	Band type
Hβ	4827.875	4847.875	4847.875	4876.625	4876.625	4891.625	a
Mg_2	4895.125	4957.625	5154.125	5196.625	5301.125	5366.125	m
Mg_b	5142.625	5161.375	5160.125	5192.625	5191.375	5206.375	a
Fe5270	5233.150	5248.150	5245.650	5285.650	5285.650	5318.150	a
Fe5335	5304.625	5315.875	5312.125	5352.125	5353.375	5363.375	a

Table 5.1: Definitions of Lick/IDS indices measured (Trager et al., 1998). Limits of the blue and red continuum bandpasses are given as λ_{b_1} and λ_{b_2}, and λ_{r_1} and λ_{r_2} respectively; central bandpass limits are given by λ_{c_1} and λ_{c_2}. Band types are indicated as atomic (a) or molecular (m).

5.1.2 The Algorithm

The measurement of the line-strength features is now described. Line-strengths were measured as a function of radius for each galaxy spectrum, using an algorithm developed by G. Baggley and revised by H. Kuntschner. An outline of the program is now given.

The basic principles of the measurement algorithm were to extract one-dimensional spectra for different luminosity-weighted radii of each galaxy, and to determine line-strength measurements for each extracted spectrum. The main input was a galaxy frame which was assumed to have undergone a full data reduction as described in Chapter 2. Before any one-dimensional spectra were extracted, the galaxy spectrum was checked to be perfectly aligned with the rows of the CCD frame. The IRAF tasks **apfind** and **aptrace** were used to trace the position of the galaxy centre along the dispersion axis; this step was performed to an accuracy of $\simeq$0.03 pixels RMS. The pixels of each galaxy frame were then rebinned such that the galaxy spectra was centred on a single row pixel within each frame.

One-dimensional spectra were extracted by summing rows of the galaxy frame until a signal-

to-noise ratio of 40 per Å (evaluated for the wavelength range ~5100-5300Å) was achieved. Each extracted spectrum was rebinned to define logarithmic intervals of wavelength in the direction of its dispersion axis. Redshifts were measured using the IRAF task **fxcor**, by cross-correlating each extracted spectrum with a number of different one-dimensional stellar spectra. Stellar spectra were created as described in section 2.2.10 of Chapter 2. The mean of redshifts determined for all templates was adopted as the redshift for each extracted spectrum. Hβ, Mg_2, Mg_b, Fe5270 and Fe5335 line-strengths were measured for each extraction, deredshifted using the adopted value of redshift, according to the feature definitions in section 5.1.1. Final Poissonian errors, i.e. before correction of indices for the effects of velocity dispersion, were calculated based on the Poissonian noise, sky subtraction, and both the read-out noise and gain of the CCD used to obtain observations.

5.2 Conversion to the Lick/IDS system

To interpret measured line-strength indices and to compare with the measurements of other authors, measurements were transformed on to a common scale. A widely used standard is the "Lick/IDS system", defined to correspond to (i) zero velocity dispersion and (ii) the spectral resolution of the Lick/IDS. Raw measurements of line-strength, measured as described in section 5.1.2, were converted to the Lick scale via two calibration steps: (i) correction to zero velocity dispersion (σ), and (ii) correction to the Lick/IDS spectral resolution (i.e. $\sim$ 9Å).

5.2.1 Corrections for Velocity Dispersion Broadening

To correct for the effects of σ, a range of different *stellar* spectra were smoothed by Gaussians of various widths corresponding to measurements of $\sigma = 0 - 300$km s^{-1} in intervals of 20km s^{-1}. Smoothing was performed using the IRAF task **gauss**. Correction factors for different values of σ were determined by comparing line-strength measurements for each smoothed spectrum with measurements for the original unsmoothed stellar spectrum. These factors were defined differently for the atomic and molecular line-strength indices. For the molecular index Mg_2, the correction factor was defined to be the *difference* in measurements for the original unbroadened stellar spectrum and that for the spectrum broadened to a particular velocity dispersion, i.e.

$$C(\sigma) = I_{orig} - I_{\sigma}. \tag{5.4}$$

For the atomic indices (Hβ, Mg_b, Fe5270 & Fe5335), correction factors were instead defined as the ratio of the original and the smoothed line indices:

$$C(\sigma) = \frac{I_{orig}}{I_{\sigma}}. \tag{5.5}$$

The results of calibrations derived for 8 different stellar templates for the night of February 22-23 1995 are given in figure 5.1. Calibrations were repeated for different observing runs and results were found to be in very good agreement with results shown here. Corrections were therefore performed using the calibrations of figure 5.1. To enable correction factors to be determined for arbitrary

measurements of σ, linear relations were interpolated between the *mean* of all correction factors found for a given value of σ. The correction factor for a given value of σ was then determined using the relation for the appropriate range of σ.

Corrections were made using the measurements of σ, determined as a function of radius, presented for each galaxy spectrum in Chapter 4. Measurements of σ determined for S/N$\simeq$60 per Å were used; for some spectra however, the outermost measurements were very uncertain and in these cases measurements obtained for S/N$\simeq$30 per Å at smaller radii were used where possible to determine σ, and the uncertain S/N$\simeq$60 per Å measurements of σ were removed.

In general the line-strengths and σ were not measured for similar radii. A value of σ for the radius of each set of line-strength measurements was determined using a linear interpolation between the measured σ for radii bracketing the radius of the line-strength measurements. Where the radius of the line-strengths was greater than that for the measurements of σ, the linear relation determined for the two outermost measurements of σ (for the appropriate side of the galaxy) was used to determine σ. This will be a possible source of systematic error in measurements at large radii. As noted later however these measurements are also subject to the uncertainty in the accuracy of sky subtraction and should be interpreted with care.

Errors for corrected atomic and molecular line-strength measurements were calculated to be,

$$\delta I_{atomic}(\sigma) = \sqrt{(\delta I_{orig} \cdot C(\sigma))^2 \; + \; (I_{orig} \cdot \delta C(\sigma))^2} \tag{5.6}$$

and,

$$\delta I_{molecular}(\sigma) = \sqrt{\delta I_{orig}{}^2 \; + \; \delta C(\sigma)^2}, \tag{5.7}$$

respectively, where I_{orig} was the original measurement obtained for each extracted spectrum, δI_{orig}, the error of this measurement calculated assuming Poissonian noise uncertainty. $\delta C(\sigma)$ was found by adding in quadrature the standard deviations of correction factor values, for values of σ bracketing each respective σ.

5.2.2 Correction for Different Spectral Resolution

After correcting for the effects of σ, a remaining correction for the different spectral resolution of our observations and that of the Lick/IDS was required. To perform this correction, measurements were obtained for each fully-reduced major axis galaxy spectrum for a simulated Lick aperture. For our spectroscopic slit width of 1″ and spatial scale of 0.″6, this was taken to be the central 9 rows, i.e. the central ~5.″4 of each galaxy spectrum. Spectra for each galaxy frame were realigned such that the galaxy centre was defined by a single row of the frame; this step was identical to that described for the measurement of line-strength gradients in section 5.1.2. The central 9 rows of each frame, centred on the row of the galaxy centre, were summed to create a single one-dimensional spectrum. Line-strengths were measured for these spectra and corrected for velocity

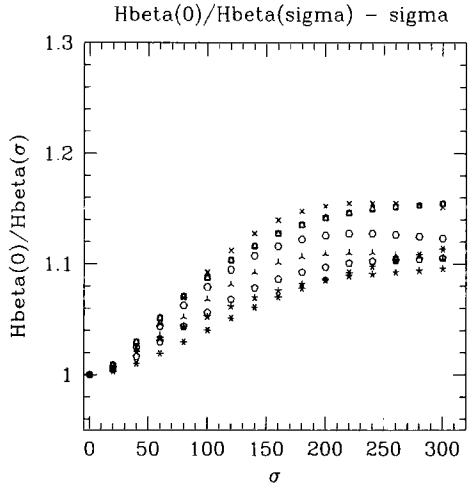

(a)

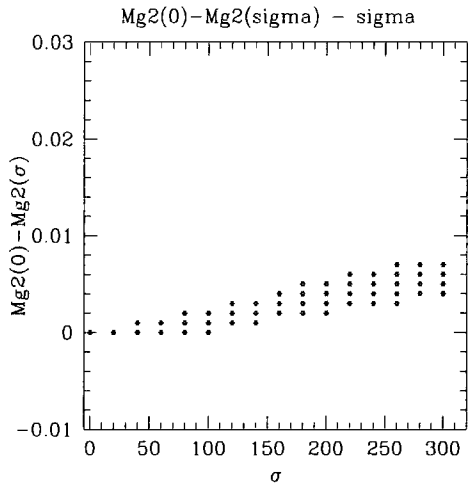

(b)

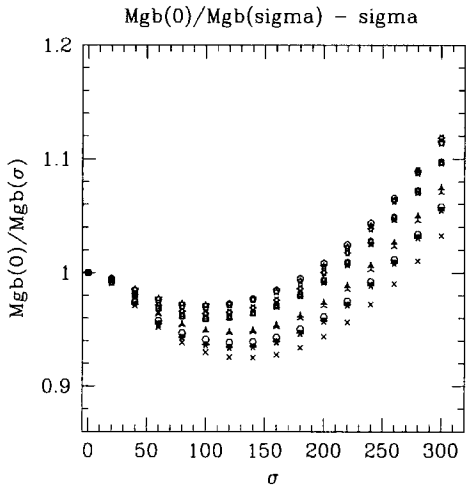

(c)

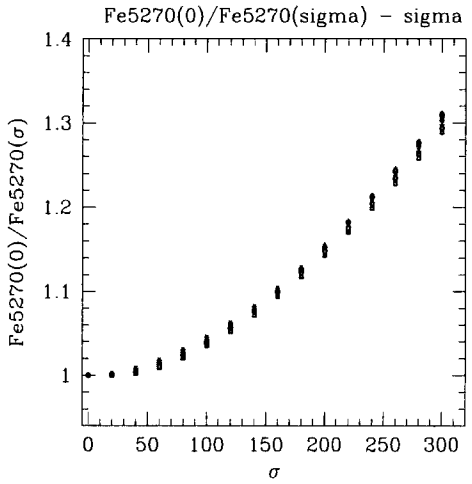

(d)

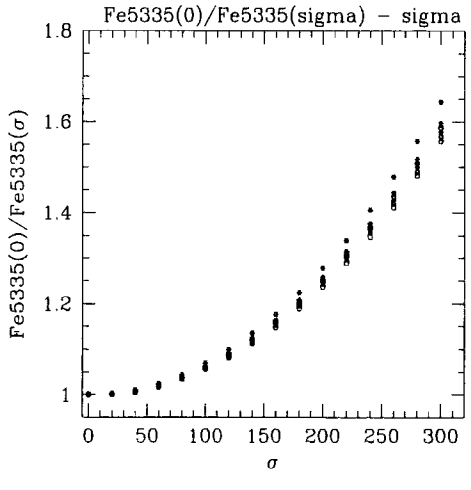

(e)

Figure 5.1: Correction factors for the conversion of line-strength measurements to zero velocity dispersion. Calibrations for (a) Hβ, (b) Mg_2, (c) Mg_b, (d) Fe5270, (e) Fe5335, are presented for $\sigma = 0 - 300$km s^{-1} in intervals of 20 km s^{-1}. Different symbols for each index correspond to results for different stellar templates.

dispersion using central measurements of σ measured for each spectrum using the IRAF task **fxcor**. These velocity dispersion corrected measurements were compared with the fully-corrected Lick/IDS 1.″4x4″ aperture measurements taken from the "pristine" IDS sample of Trager et al. (1998); the Lick/IDS measurements of Hβ corrected for velocity dispersion but *uncorrected* for Hβ emission, were taken. An attempt was made to fit relations for differences between these two measurements, i.e. the velocity dispersion corrected simulated Lick/IDS aperture measurements obtained here and the Lick/IDS measurements, as a function of our velocity dispersion corrected Lick/IDS aperture measurements. Examples of relations fitted for these measurements are given in figure 5.2. After testing a range of fitting routines, the median value of offset was found to provide a good fit for all line-strength indices. Velocity dispersion corrected measurements were then offset to the Lick scale by applying these median values. For Mg$_b$, no offset correction was made.

5.3 External and Internal Comparisons

Three different types of comparisons are made. Comparisons with measurements of line-strength gradients obtained by other authors are made in section 5.3.1. Central measurements obtained for both major and minor axes spectra are compared with the measurements of the Lick/IDS galaxy sample (Trager et al., 1998) and González (1993) in section 5.3.2. As an internal check of the consistency of line-strength measurement, central measurements obtained for the major and minor axes of the same galaxy are directly compared in section 5.3.3. Central measurements were obtained for each axis as described (for major axis spectra) in section 5.2.2. All comparisons are made between measurements fully corrected to the Lick/IDS system.

Where disagreement is found between line-strength gradients measured previously and those obtained here, the central measurements of Trager et al. (1998), and González (1993) where available, are also shown. González (1993) applied a correction to his Hβ measurements for Hβ emission, by adding the correction factor ΔH$\beta \equiv 0.7$[OIII], where [OIII] is the measured equivalent width of the [OIII] 5007Å emission line as defined by González (1993). The appropriateness of this correction has been questioned by Carrasco et al. (1996) who compared the difference in the measurements of Hβ at the same radius but for opposite sides of the galaxy, to the difference in the measured [OIII]. Assuming that the Hβ absorption, due to a stellar component, is symmetric across the face of the galaxy, they reasoned that if the relation of González (1993) holds then any difference in the measured Hβ due to Hβ emission, should be directly related to a difference in the measured [OIII]. No strong correlation between the differences was found and the slope of the relation was calculated to be consistent with a value of zero. In this thesis no correction for Hβ emission is made. To enable more consistent comparisons to be made, corrections for Hβ emission applied to the measurements of González (1993) have been reversed by *subtracting* the factor 0.7[OIII] from the fully corrected measurements of González (1993), using the corresponding measurement of [OIII]. Measurements of Hβ *uncorrected* for emission are taken for the measurements of Trager et al. (1998).

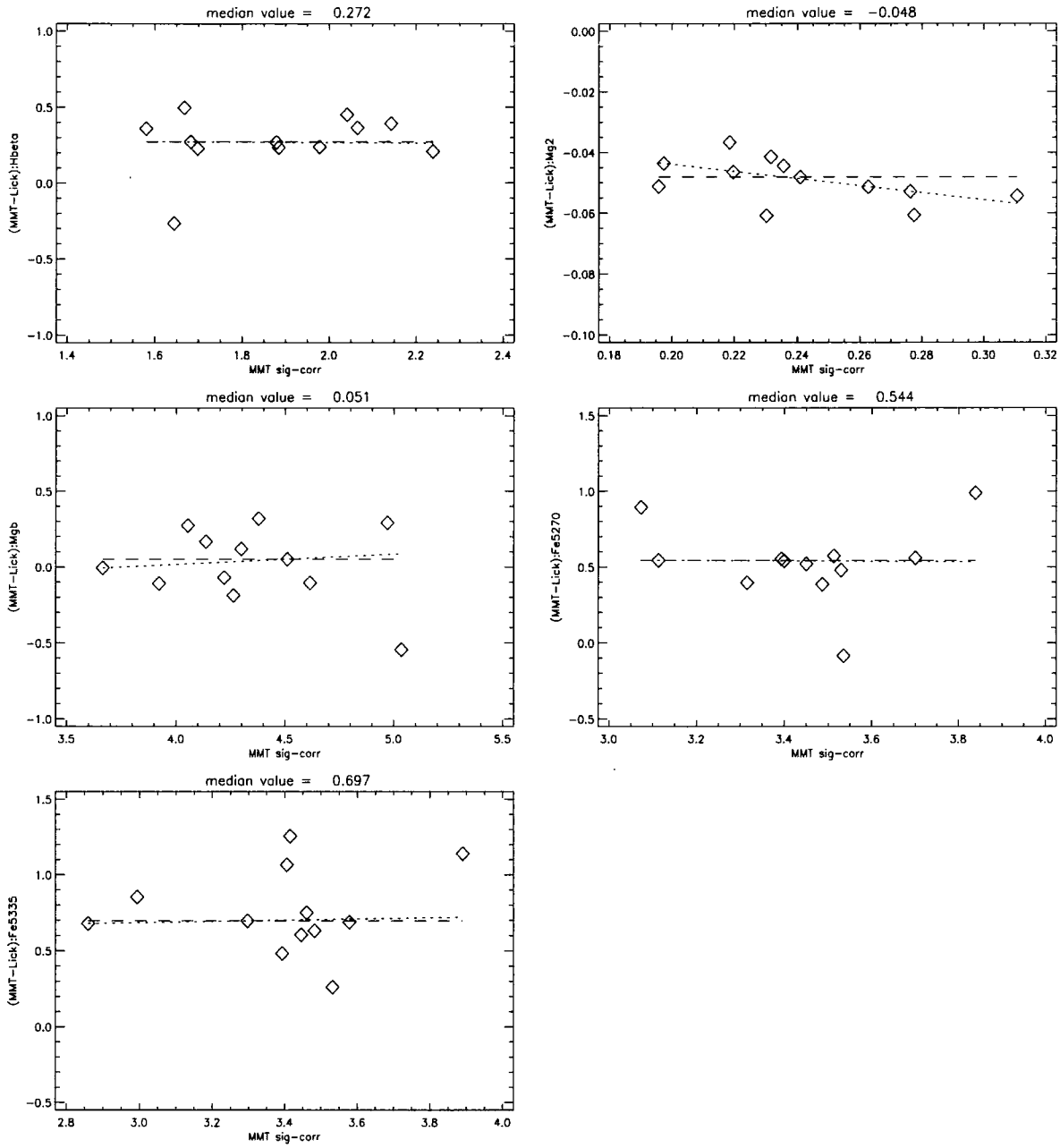

Figure 5.2: Differences between simulated Lick aperture measurements for each galaxy and measurements obtained by Lick group, for all measured indices. Actual offset values are indicated by diamond symbols. The median offset value is given above each figure and indicated in each case by a long dashed line. A robust fit for all relations is given by a dotted line. Units for measurements of the atomic indices, i.e. Hβ, Mg$_b$, Fe5270 and Fe5335, are given in units of Å; for Mg$_2$ measurements are in units of magnitudes.

5.3.1 Line-Strength Gradients

Comparisons with the line-strength gradients of other authors, are given in figures 5.3-5.6. Galaxies within our sample which were studied previously are NGC 3379 (Davies et al., 1993; González, 1993), NGC 4478 (Peletier, 1989; Gorgas et al., 1990), NGC 2778 (Fisher et al., 1995) and NGC 3608 (Gorgas et al., 1990).

In figure 5.3, the major and minor axis measurements of Hβ, Mg$_b$, Mg$_2$ and $< Fe >$ for NGC 3379, are compared with the fully-corrected Hβ, Mg$_2$ and $< Fe >$ measurements of Davies et al. (1993), and Hβ, Mg$_b$ and $< Fe >$ measurements of González (1993). Our data does not have the spatial extent of these authors, due to the shorter exposure times of our observations (i.e. 600s for each axis). There is however good agreement for all indices.

In figure 5.4, comparisons of the major axis measurements of Hβ, Mg$_b$, Mg$_2$, Fe5270, Fe5335 and $< Fe >$ for NGC 4478 are made with the measurements of Gorgas et al. (1990) and Peletier (1989). For the measurements of Gorgas et al. (1990), good agreement is found for Hβ, Mg$_b$ and Fe5335. At the galaxy centre there is a small difference in Mg$_2$ although good agreement is found for measurements at all other radii. For Fe5270 however, there is considerable disagreement. For our spectrum of NGC 4478, a single bad pixel column was interpolated for a region corresponding to the red passband of Fe5270. This alone however is unlikely to be the cause of the discrepancy here and in a check of the actual spectrum, no evidence of saturated pixels due to uncorrected bad pixel columns were found. For the measurements of Peletier (1989), good agreement is found for all indices. Measurements and errors for Fe5270 were not tabulated by Peletier (1989) and have been derived from the corresponding measurements of Fe5335 and $< Fe >$. In contrast to the comparison with the measurements of Gorgas et al. (1990), good agreement is found for the measurement of both Fe5270 and $< Fe >$. The central measurements of Fe5270 of González (1993) and Trager et al. (1998) are also given and are in clear agreement with measurements here.

In figure 5.5, measurements of Hβ and Mg$_b$ for the major axis of NGC 2778 are compared with the measurements of Fisher et al. (1995). Measurements were obtained for $S/N = 70$per Å; this was to enable comparison for more similar radii and the spatial resolution of the measurements of Fisher et al. (1995). There is clearly some disagreement with the measurements of Fisher et al. (1995), for Hβ at smaller radii and Mg$_b$ at greater radii. Checks of our spectrum showed no evidence for saturated pixels, bad pixel columns or any other obvious causes of discrepant measurements. Also shown are the central Hβ and Mg$_b$ measurements of González (1993) and Trager et al. (1998), and the central Mg$_b$ measurement of Davies et al. (1987) derived from their Mg$_2$ measurement using the Mg$'_b$–Mg$_2$ relation of Colless et al. (1998) (i.e. Mg$_2 \simeq 1.93$ Mg$'_b - 0.04$). For Hβ there is agreement between measurements obtained here and the central measurement of Trager et al. (1998), but slight disagreement for the measurement of González (1993). For Mg$_b$, the central measurements of both Davies et al. (1987) and González (1993) are in agreement with our measurements; the central measurement of Trager et al. (1998), however, is in disagreement with both measurements obtained here and the measurements of Fisher et al. (1995). Lick/IDS measurements for NGC 2778 were not included in the pristine sample of Trager et al. (1998) and for this reason they were not used to establish our calibration to the Lick system (section 5.2.2). This disagreement is however of concern although the Lick/IDS measurement of Mg$_b$ is not consistent with any of the measurements presented in figure 5.5, besides the central measurement of Davies et al. (1987).

Measurements for the major axis spectrum of NGC 3608 are compared in figure 5.6. Measurements were again obtained for $S/N = 70$per Å to enable measurements to be compared for more similar radii and the spatial resolution of Gorgas et al. (1990). The measurements of Gorgas et al. (1990) are in reasonable agreement with measurements here although there is considerably greater scatter for the Gorgas et al. (1990) measurements. Central measurements of González (1993) and Trager et al. (1998) are shown to be in good agreement.

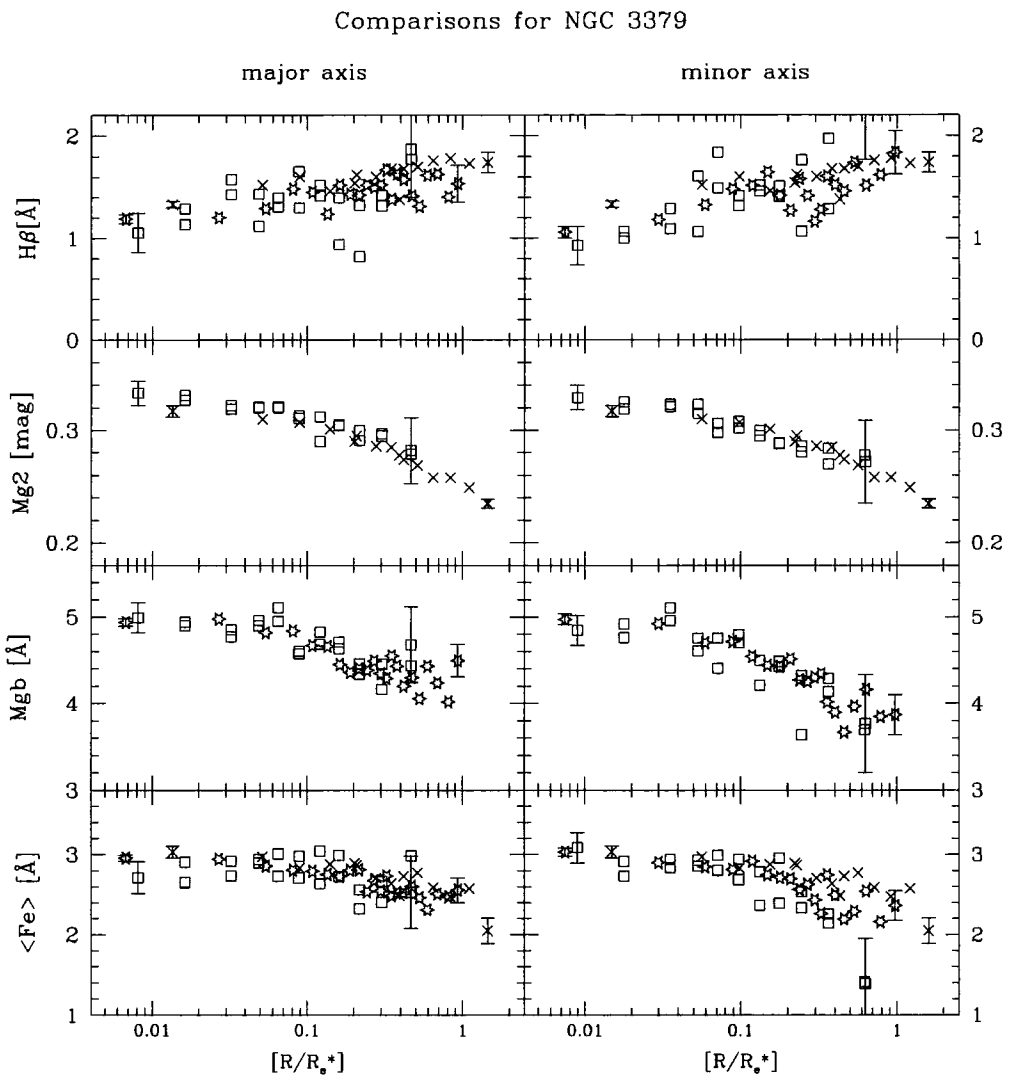

Figure 5.3: Comparison of NGC 3379 measurements of Hβ, Mg$_b$, Mg$_2$ and $< Fe >$, with those of Davies et al. (1993) (DSP) and González (1993) (G93). Measurements obtained here are indicated by open square symbols, those of DSP by crosses, and G93 by starred symbols. Radii are given as $\log(R/R_e^*)$ where $R_e^* = R_e/\sqrt{(1-\epsilon)}$ for the major axis observations and $R_e^* = R_e * \sqrt{(1-\epsilon)}$ for the minor axis, and values of R_e and ϵ are given in table 5.2. Error bars are given for the central and outermost measurements for each set of measurements. Note that our observations for NGC 3379 were of shorter exposure times, i.e. 600 seconds for each axis.

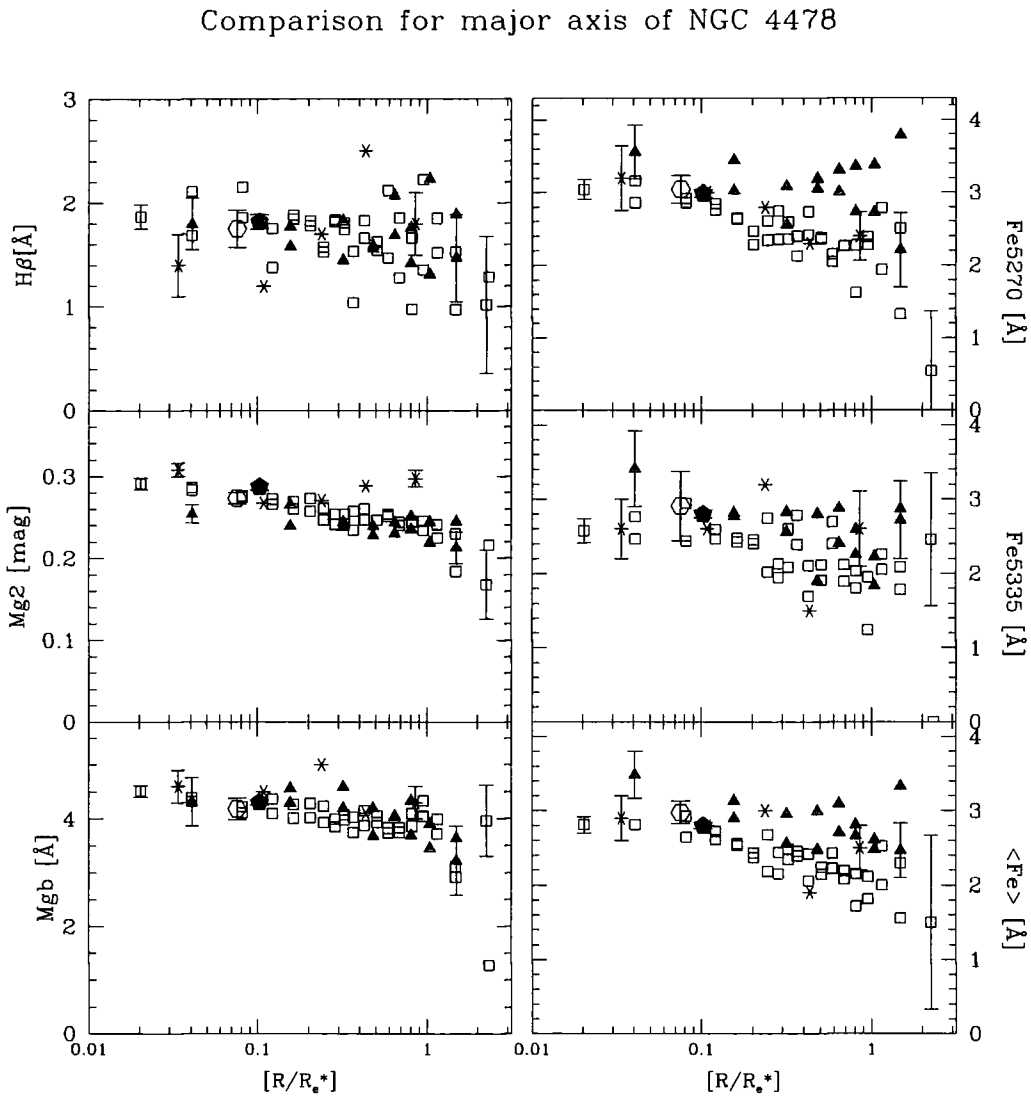

Figure 5.4: Comparison of NGC 4478 major axis measurements of Hβ, Mg_b, Mg_2, Fe5270, Fe5335 and $< Fe >$ given by open square symbols with those of Gorgas et al. (1990), given by filled triangle symbols and Peletier (1989) given by asterisk symbols. Central measurements of González (1993) and Trager et al. (1998) are given at representative radii, by closed pentagon and open hexagon respectively. Radii are given as $\log(R/R_e^*)$ where $R_e^* = R_e/\sqrt{(1-\epsilon)}$ and values of R_e and ϵ are those given in table 5.2. For line-strength gradient measurements, error bars are given for the central and outermost measurements.

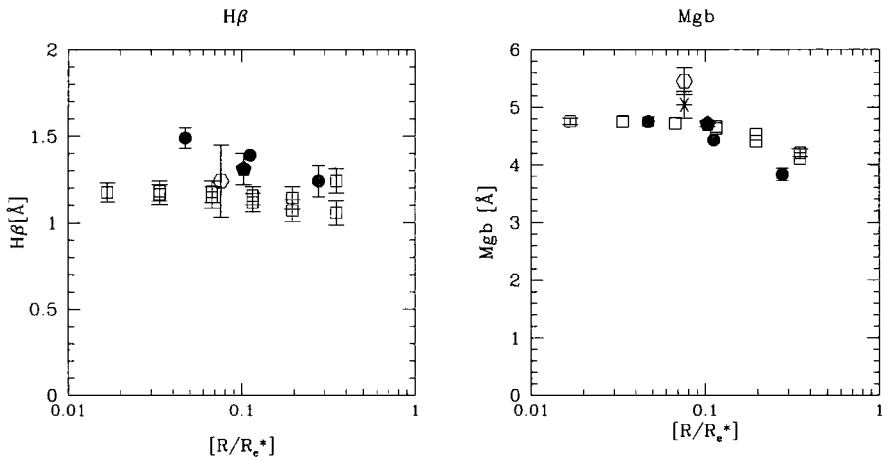

Figure 5.5: Comparison of NGC 2778 major axis measurements of Hβ and Mg$_b$ with those of Fisher et al. (1995) (FIF95) given by filled circles, and the central measurements of González (1993) given by closed pentagon, and of Trager et al. (1998) given by open hexagon; the central measurement of Mg$_b$ for Davies et al. (1987) is given by an asterisk. Measurements here were obtained for S/N = 70per Å. Radii are given as log(R/R$_e^*$) where R$_e^*$=$R_e/\sqrt{(1-\epsilon)}$, and values of R$_e$ and ϵ are given in table 5.2. For line-strength gradient measurements, errors are given for central measurements and those at greatest radii.

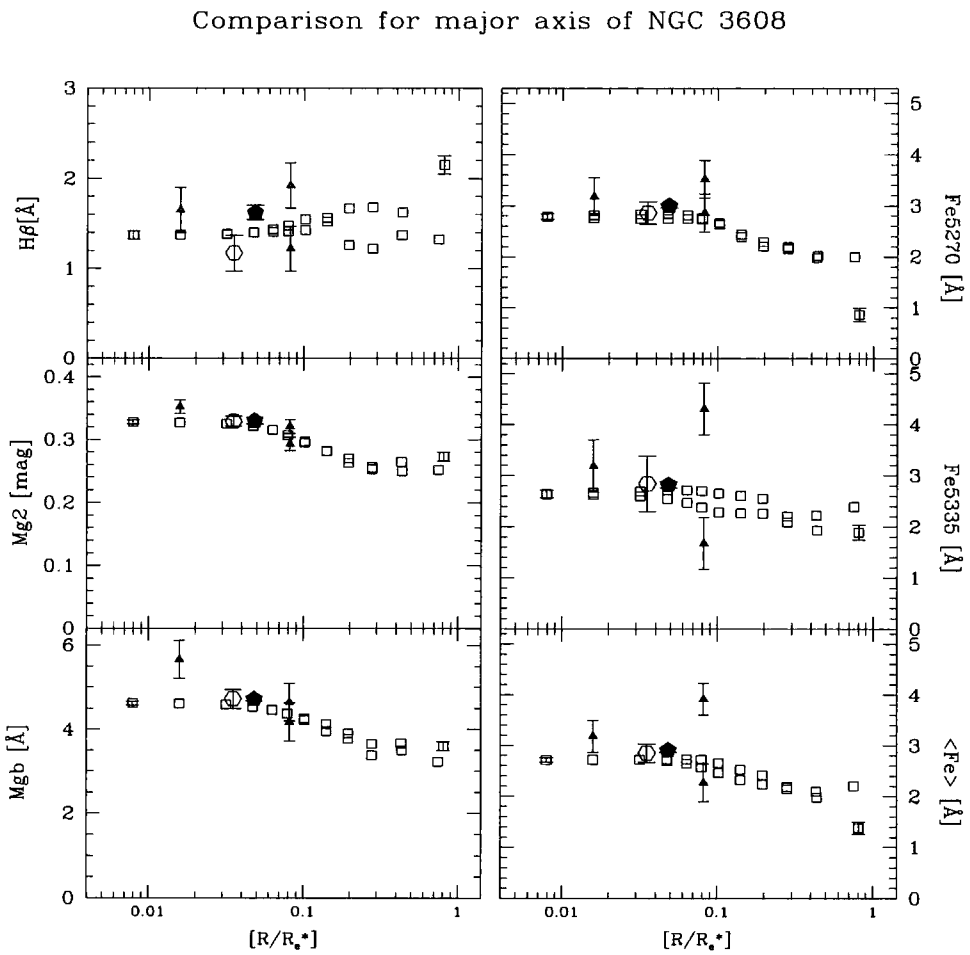

Figure 5.6: Comparison of NGC 3608 major axis measurements of Hβ, Mg_b, Mg_2, Fe5270, Fe5335 and $< Fe >$ with those of Gorgas et al. (1990), given by filled triangle symbols. Central measurements of González (1993) and Trager et al. (1998) are given at representative radii, by closed pentagon and open hexagon symbols respectively. Radii are given as $\log(R/R_e^*)$ where $R_e^* = R_e/\sqrt{(1-\epsilon)}$ and values of R_e and ϵ are those given in table 5.2. For line-strength gradient measurements obtained here, errors are given for the central and outermost measurements.

5.3.2 Central Measurements

Comparisons are made between central measurements obtained here for a simulated Lick/IDS aperture for both major and minor axis spectra, and the central measurements of González (1993) and Trager et al. (1998). In figure 5.7, Lick/IDS measurements for our galaxy sample are compared with central measurements here. Comparisons with the 2.″1 x 5″ measurements of González (1993) are given in figure 5.8. González (1993) observed 5 objects in common with our sample, i.e. NGC 2778, NGC 3377, NGC 3379, NGC 3608 and NGC 4478. A number of the central measurements of σ obtained by both González (1993) and Trager et al. (1998), differed considerably from measurements here. For the purposes of each comparison, raw central measurements obtained here were therefore corrected for the effects of σ using the central σ measurements *adopted by these authors* for each galaxy.

Comparisons with the Lick/IDS measurements are given in figure 5.7. Measurements for major axis spectra corresponding to labelled outlier points were found to be the principal outliers in relations obtained to complete corrections to the Lick scale (figure 5.2), excluding the measurements for NGC 2778 and NGC 4468: measurements for these galaxies were not included in the pristine sample of Trager et al. (1998) and were also not used in our Lick scale calibration.

For comparisons with the measurements of González (1993) (figure 5.8), there is good agreement for most measurements although small differences exist for the Hβ measurements of NGC 2778, NGC 3379 and NGC 3608, and for the Fe5270 measurements of NGC 3608. For both NGC 2778 and NGC 3379, measurements obtained here and the measurement of González (1993) are separately found to be in agreement with the Lick/IDS measurement of Trager et al. (1998), within the combined uncertainty of all measurements; all measurements have therefore individually been established to the Lick/IDS system. For NGC 3608, the Hβ measurement of González (1993) however is in *disagreement* with that of Trager et al. (1998); central measurements obtained here however are in agreement with Trager et al. (1998). There is also considerable disagreement between the Fe5270 measurement for the major axis spectrum of NGC 3608 and the measurement of González (1993); again measurements for both the major and minor axes of NGC 3608 obtained here and the measurement of González (1993) were separately found to be in agreement with the measurement of Trager et al. (1998).

5.3.3 Internal Comparison of Central Measurements

Small differences were found between central measurements for the major and minor axes of some galaxies in our sample. These differences were greatest where major and minor axis spectra were obtained during different observing runs, in particular for the runs of March and May 1994 (i.e. for galaxies NGC 3608, NGC 4468, NGC 4564 and NGC 5582). In figure 5.9, central measurements for spectra taken during these different runs are compared. Measurements presented are those compared with the Lick/IDS measurements in figure 5.7, i.e. measurements have been corrected for velocity dispersion using the central measurements of σ adopted by Trager et al. (1998); similar results were however found where values of σ obtained for the respective central spectra were used. Agreement between measurements is in general very good although exceptions do exist for each index. For Hβ, measurements for NGC 4458 were separately found to be in slight disagreement with the measurement of Trager et al. (1998) (figure 5.7) and from inspection of both spectra

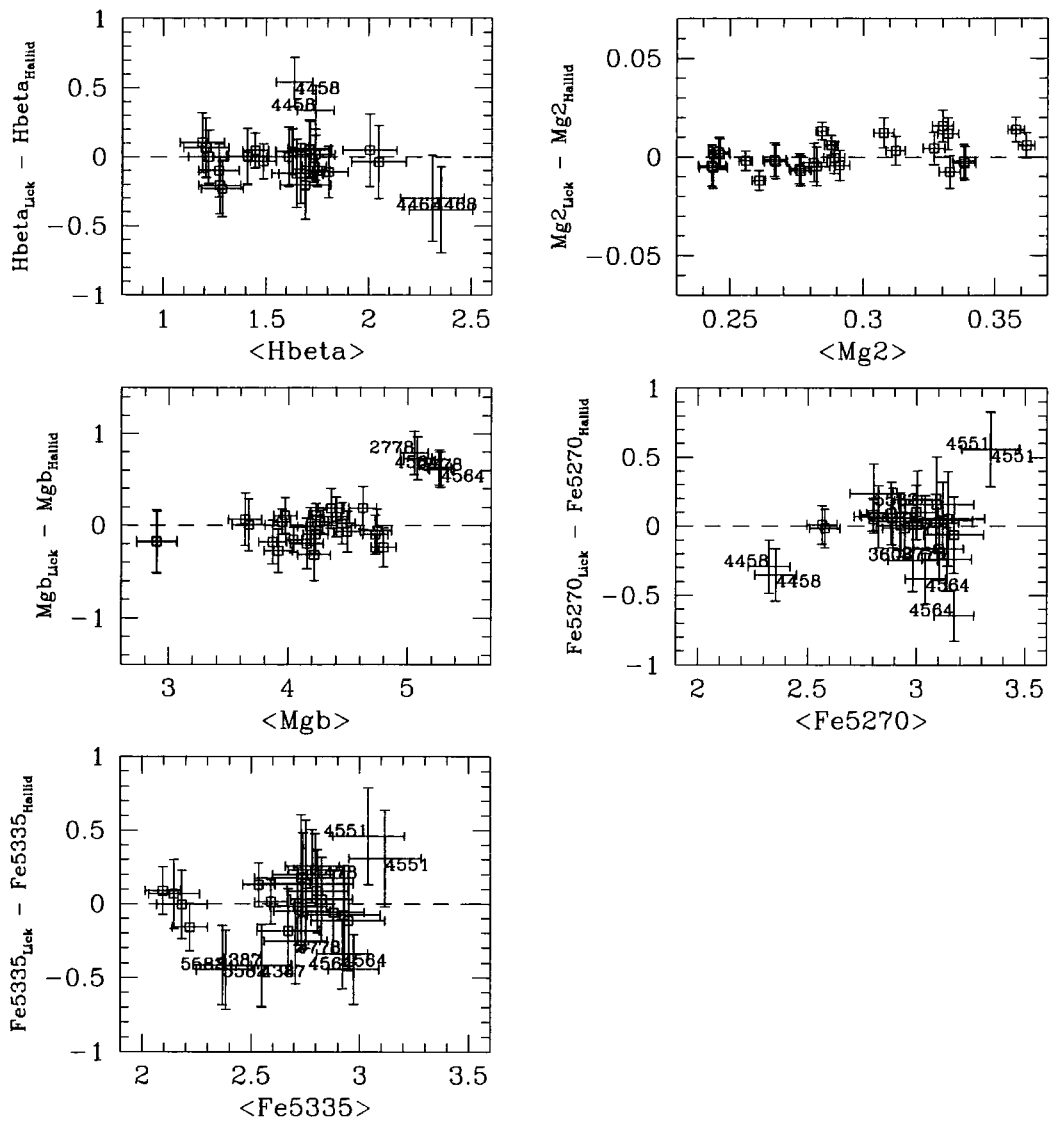

Figure 5.7: Difference between the central measurements of Hβ, Mg_2, Mg_b, Fe5270 and Fe5335 obtained here for the major and minor axes of each galaxy, and the 1.″4x4″ Lick/IDS measurements of Trager et al. (1998), are plotted against the *mean* of both central measurements. Errors for all the quantities are based on final errors for all measurements. Labels corresponding to the NGC number of galaxy are given for outlier points, for major axis measurements to the lower right of the point position marked by the centre of error bars, and for minor axis measurements to the upper left of the point position).

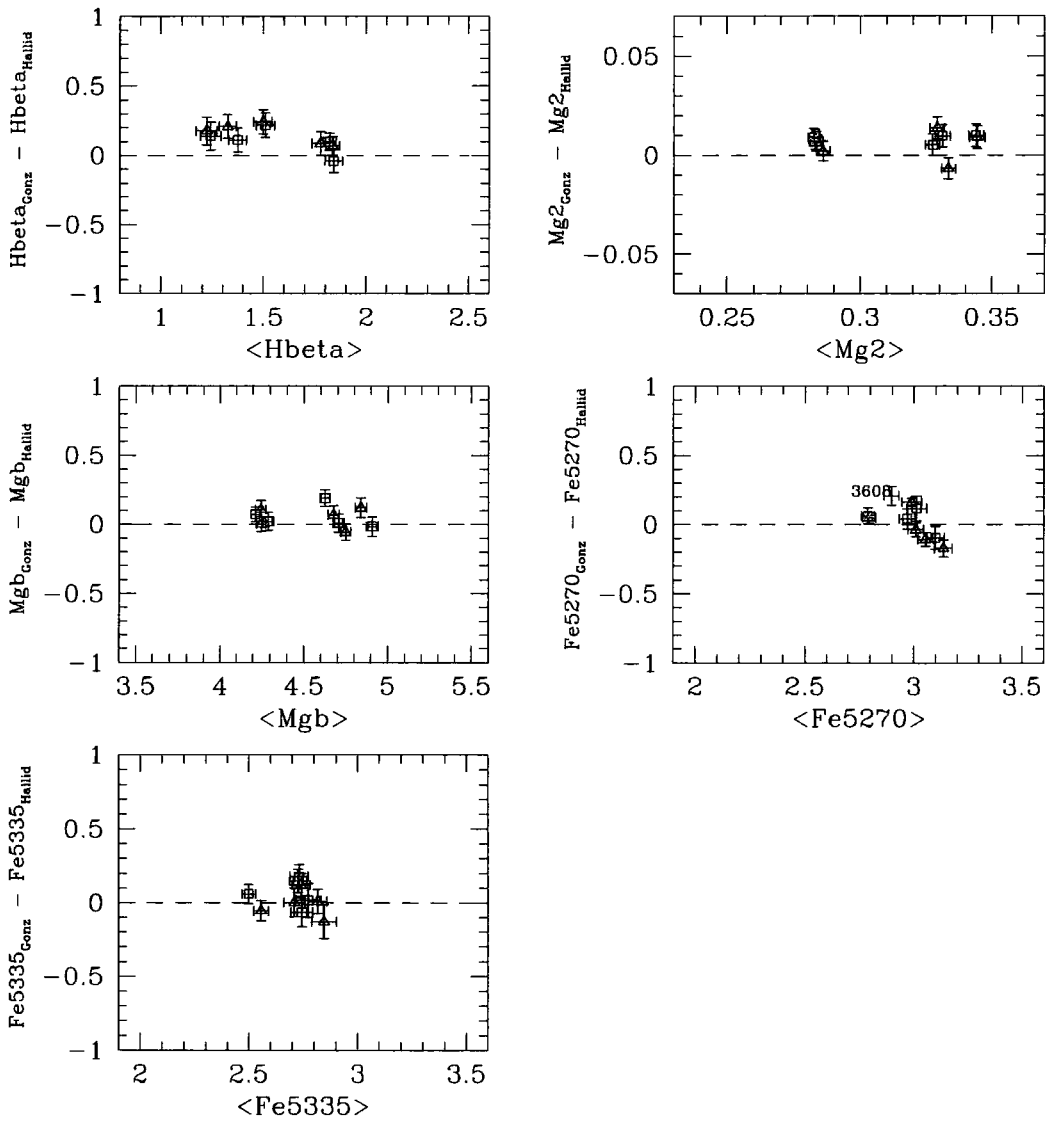

Figure 5.8: Differences between the central measurements of Hβ, Mg_2, Mg_b, Fe5270 and Fe5335 obtained here for major and minor axis axes of each galaxy, and $2''.1 \times 5''$ measurements of González (1993), are plotted against the *mean* of both central measurements. Errors are given for all quantities based on final errors for all measurements. Open square symbols correspond to major axis measurements and open triangle symbols to minor axis measurements. For outlier points, labels are given indicating the galaxy NGC number, for major axis measurements to the upper left of the point position marked by the centre of error-bars, and for minor axis measurements to the lower right of the point position.

pixels corresponding to the central passband of the Hβ feature are likely to have been affected by either a cosmic ray hit or bad pixels. For Mg_2, measurements for the major axis of NGC 4464 and the minor axis of NGC 4564 were each found to be in slight disagreement with the respective Lick/IDS central measurements. For Mg_b, measurements for NGC 3608 are in slight disagreement; measurements for both the major and minor axes have been found however to be in agreement with the central measurement of Trager et al. (1998). For Fe5270, measurements for NGC 4564 and the minor axis of NGC 3608 were all found to disagree with the Lick/IDS central measurements. For Fe5335, measurements for NGC 4464 were found to be in agreement with the central Lick/IDS measurement.

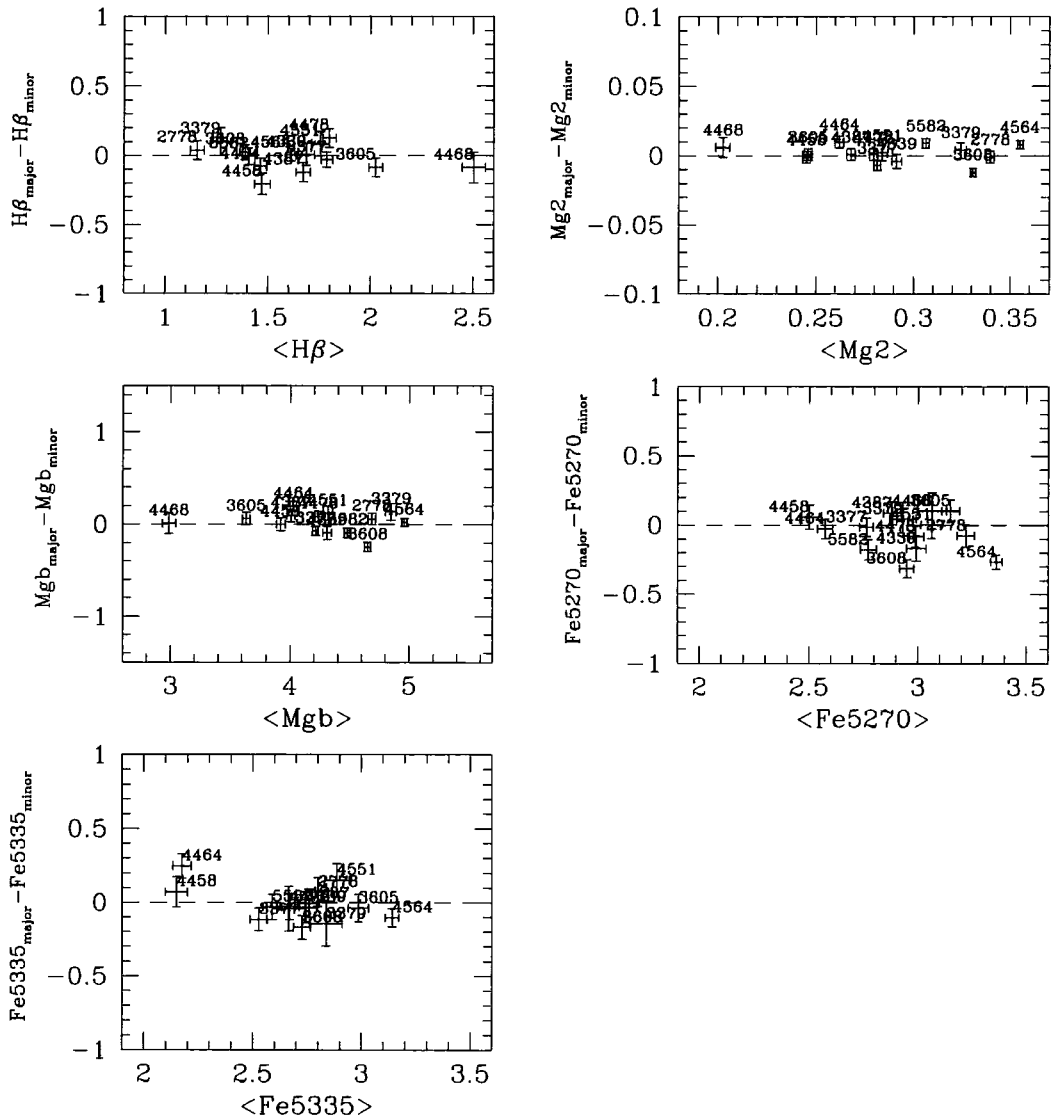

Figure 5.9: Differences in central measurements for major and minor axis spectra of each galaxy are plotted against the mean of both measurements. Galaxy NGC numbers and errors are indicated.

5.4 Sky-subtraction error

At large radii where the galaxy surface brightness becomes comparable to the brightness of the background sky, the accuracy of the sky subtraction is critical. Here the sky signal was subtracted using the level of sky signal linearly interpolated from the edges of each galaxy frame (section 2.2.8). This has the advantage of providing a measure of the actual sky signal for the galaxy exposure but the disadvantage that by estimating the sky level from regions at the edge of the galaxy frame, a measure of the galaxy signal itself may be subtracted. A sky level of typically 15-25 ADU per pixel was subtracted. Preliminary tests to assess the effect of estimating an incorrect value for the sky level were performed. For a given galaxy frame, nine additional frames were created by adding a fixed level of 1, 2, 3, 4 or 5 ADU counts or by subtracting 1, 2, 3 or 4 ADU, from pixel values across the entire galaxy frame; line-strengths were then measured for each frame. Results for the major axis spectrum of NGC 4478 are given in figure 5.10. Different symbols correspond to each of the created galaxy frames. Variations in the sky level subtracted clearly has a more important effect on measurements for $r \gtrsim 15''.0$ for which there is considerably greater scatter between measurements presented than for smaller radii; this value of radius for a particular galaxy will depend however on the actual value and variation in the galaxy surface brightness as a function of radius in relation to the surface brightness of the night sky. Such tests provide an indication of how line-strength measurements are affected by uncertainty in determining the level of the background sky brightness but may not simulate the actual cause of sky subtraction error, e.g. where the sky level is interpolated between two very different values of sky signal for opposite sides of the galaxy. Where measurements are found to vary at large radii by amounts far greater than the measurement error, it can be assumed that this is likely to be due to inaccurate sky subtraction.

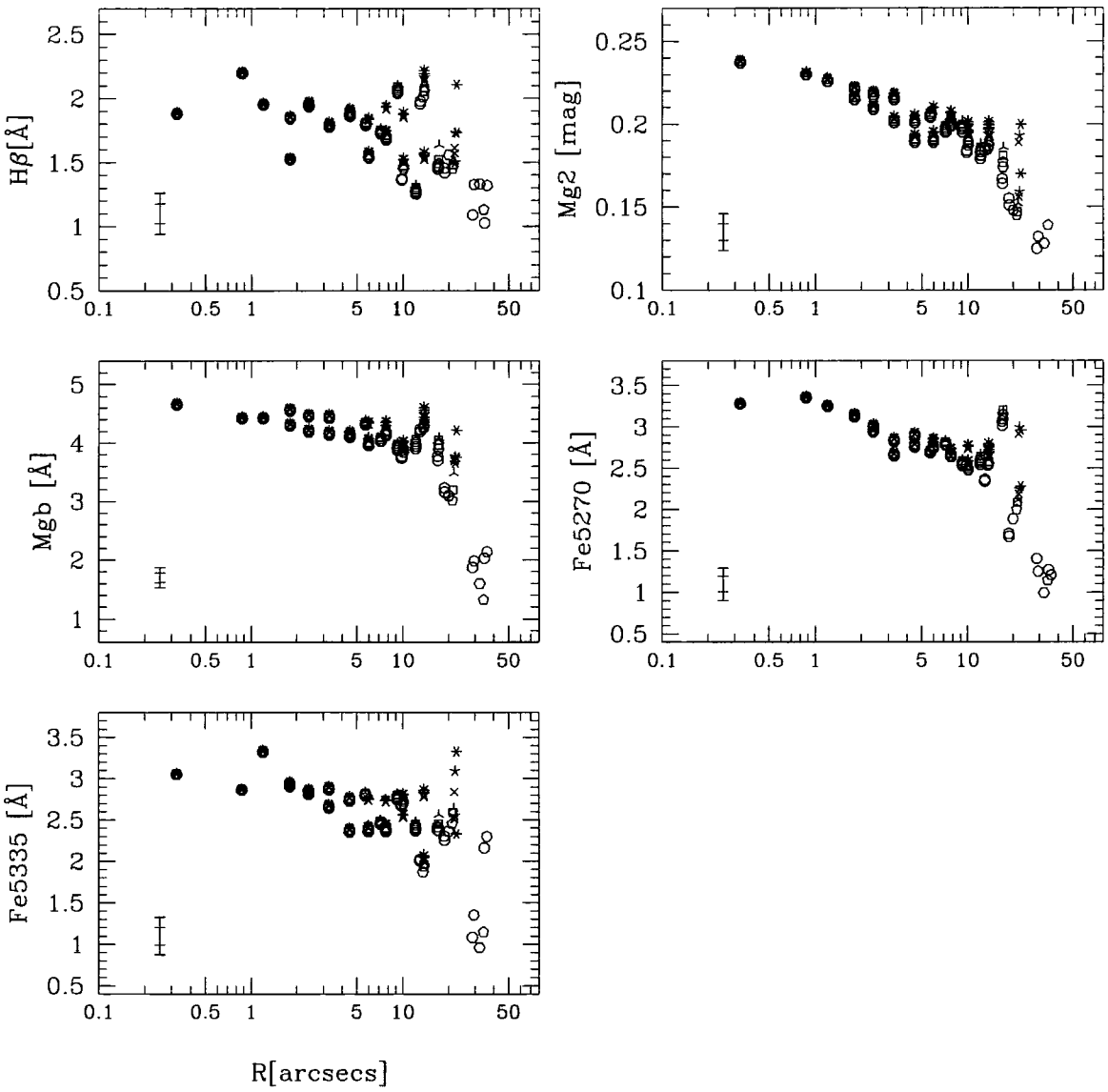

Figure 5.10: Results of tests performed for NGC 4478 for the effects of inaccurate sky subtraction. Radius is given along the x-axis of each plot in arcseconds. Different symbols correspond to different frames created as outlined in the text: measurements for the original frame are given by skeletal triangle symbols; skeletal symbols correspond to frames to which ADU counts have been added and open symbols to frames where counts have been subtracted; skeletal and open squares correspond to count of 1 ADU being added and subtracted respectively, skeletal and open pentagons to count of 2 ADU being added and subtracted respectively, and so on. Typical errors for each galaxy frame are given in lower left of each plot, the smaller error bar corresponding to the central measurement and the larger, to the outermost measurement. Raw line-strength measurements, uncorrected to the Lick/IDS system, are presented.

5.5 Line-Strength Gradients

Measurements of the line-strength indices Hβ, Mg_2, Mg_b, and <Fe>= $\frac{(Fe5270+Fe5335)}{2}$, as functions of radius for both the major and minor axes, are given in figures 5.11-5.24. In each figure, measurements for the major axis are given by the left four figures, and for the minor axis, by the right four figures. The radius is presented as $\log_{10}(R/R_e^*)$, where R_e^* =$R_e/\sqrt{(1-\epsilon)}$ for the major axis and R_e^* =$R_e * \sqrt{(1-\epsilon)}$ for the minor axis, R_e^* is the de Vaucouleurs effective radius, and ϵ is the mean ellipticity of the galaxy. The values of R_e and ϵ taken for each galaxy are given in Table 5.2. All measurements have been corrected to the Lick/IDS system as described in section 5.2. Tables of measurements for both axes are given in Appendix C.

For some spectra, measurements for the greater radii studied are clearly uncertain showing a spread in value which is far greater than the measurement uncertainty. As mentioned in section 5.4 this effect is most likely to be caused by inaccurate sky subtraction. To decide whether this is in fact the case testing as described in section 5.4, would be required for each galaxy frame. Here it is just stated that caution should be taken in interpreting measurements at large radii.

Name	R_e	ϵ	Source of ϵ	Name	R_e	ϵ	Source of ϵ
NGC 2778	15.74	0.22	Pel90	NGC 4458	26.13	0.0	L95
NGC 3377	34.45	0.48	Pel90	NGC 4464	7.54	0.24	L95
NGC 3379	35.25	0.09	Pel90	NGC 4468	27.36	0.6	estim
NGC 3605	21.24	0.34	Pel90	NGC 4478	13.40	0.17	Pel90
NGC 3608	33.66	0.21	B89	NGC 4551	13.10	0.23	Pel90
NGC 4339	32.15	0.0	estim	NGC 4564	19.82	0.58	B89
NGC 4387	15.74	0.35	Pel90	NGC 5582	32.89	0.2	estim

Table 5.2: Values of effective radius (R_e) and ellipticity ϵ for each galaxy. Values of R_e were taken from the RC3, excluding the value for NGC 4464 which was taken from Graham (1997). Sources for the value of ellipticity are given in Column 4, i.e. Peletier et al. (1990) (Pel90), Bender et al. (1989) (B89), and Lauer et al. (1995) (L95); where a value was not available, the ellipticity was estimated from the galaxy Hubble type (estim).

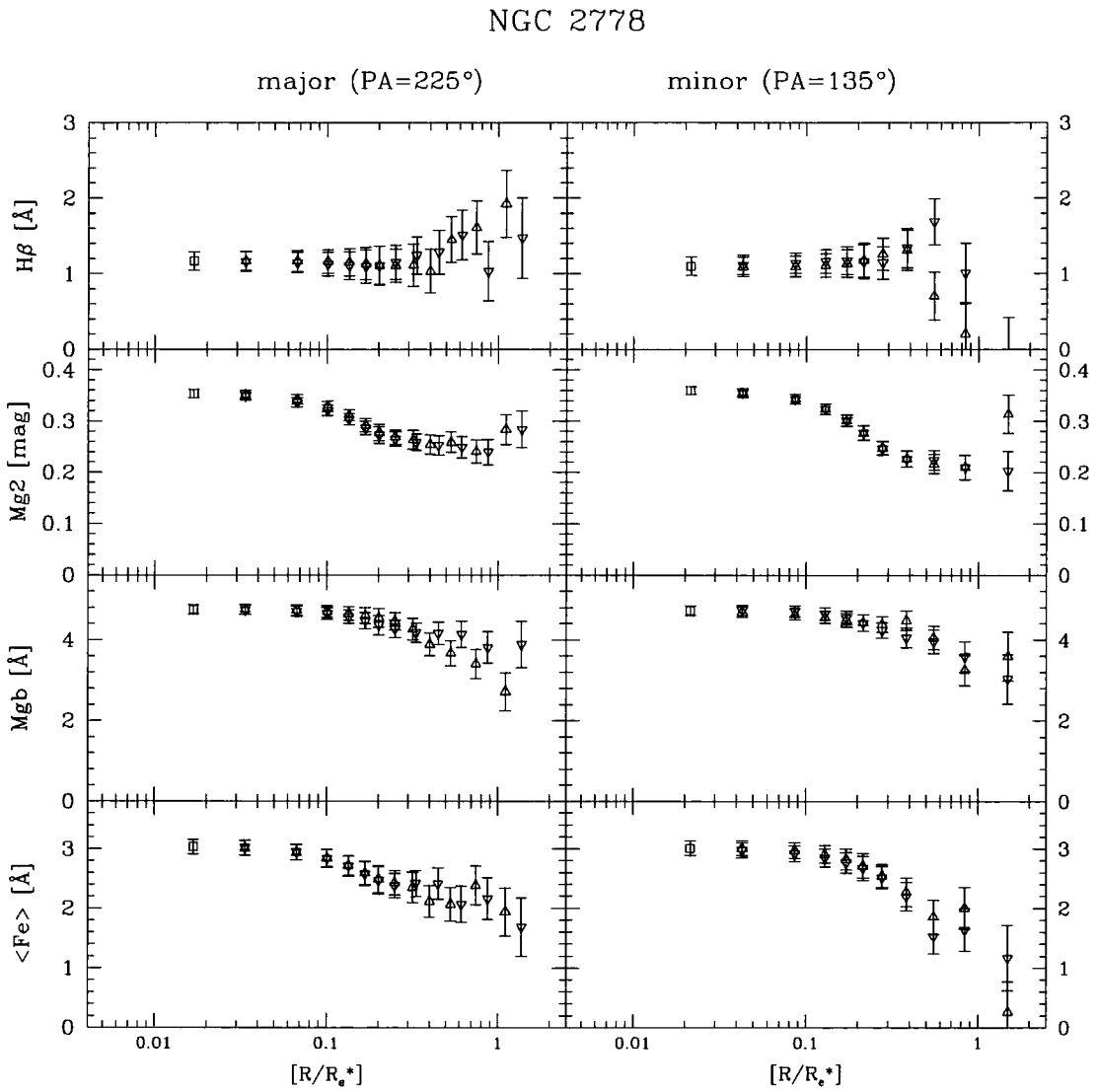

Figure 5.11: Major and minor axis line-strength gradients for NGC 2778. Measurements for the major axis are given in the left four figures, and for minor axis in the right four figures. Focus corrections were applied for both spectra corresponding to a maximum Gaussian smoothing of 0.″81 and 1.″08 for the major and minor axis respectively. The seeing for these observations was approximately 1°. The total smoothing in the spatial direction was 1.″29 and 1.″47 respectively. Data points cannot be assumed to be independent at this level.

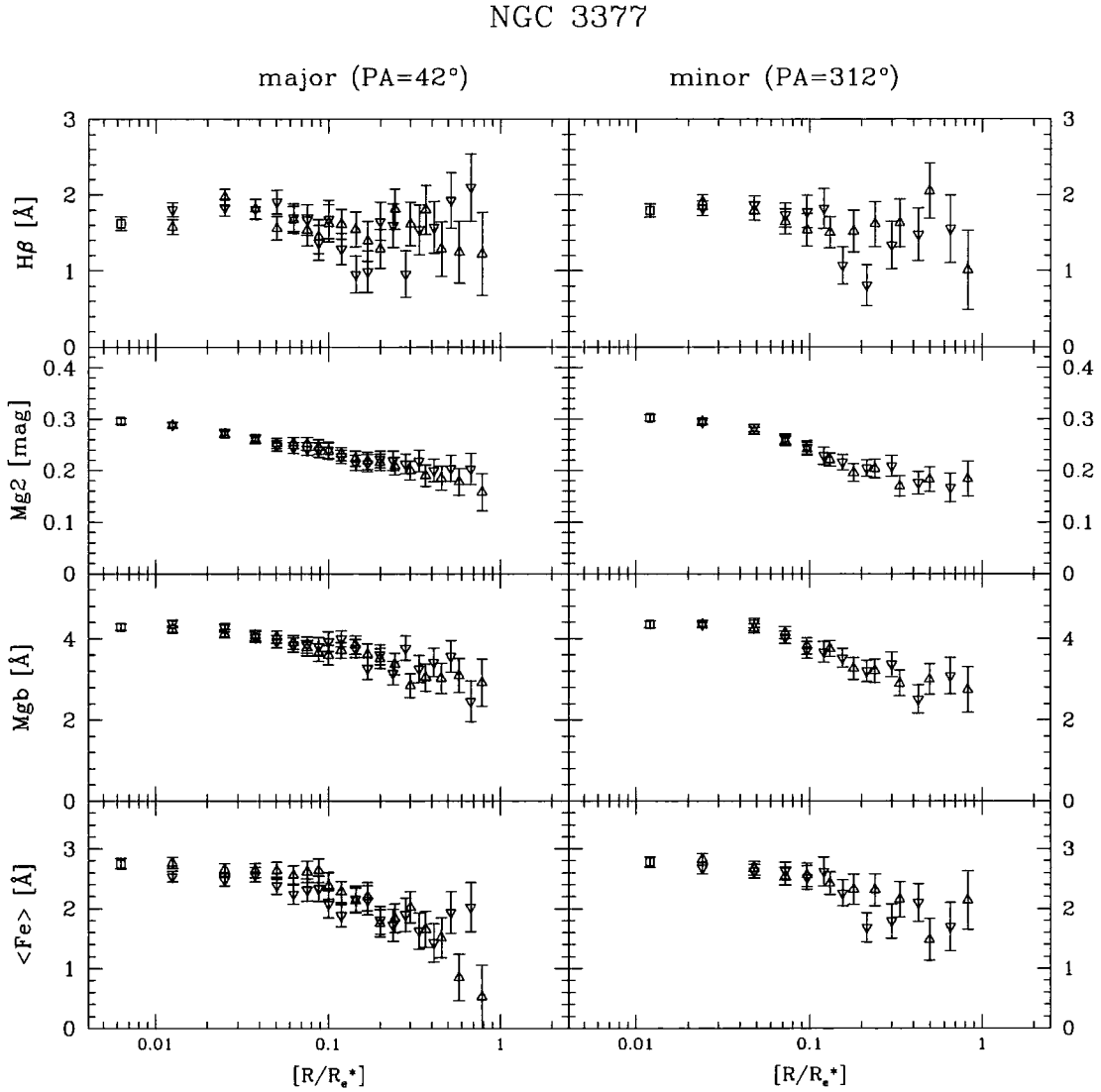

Figure 5.12: Major and minor axis line-strength gradients for NGC 3377. Plots are as in figure 5.11. The seeing for both observations was approximately 0.″8.

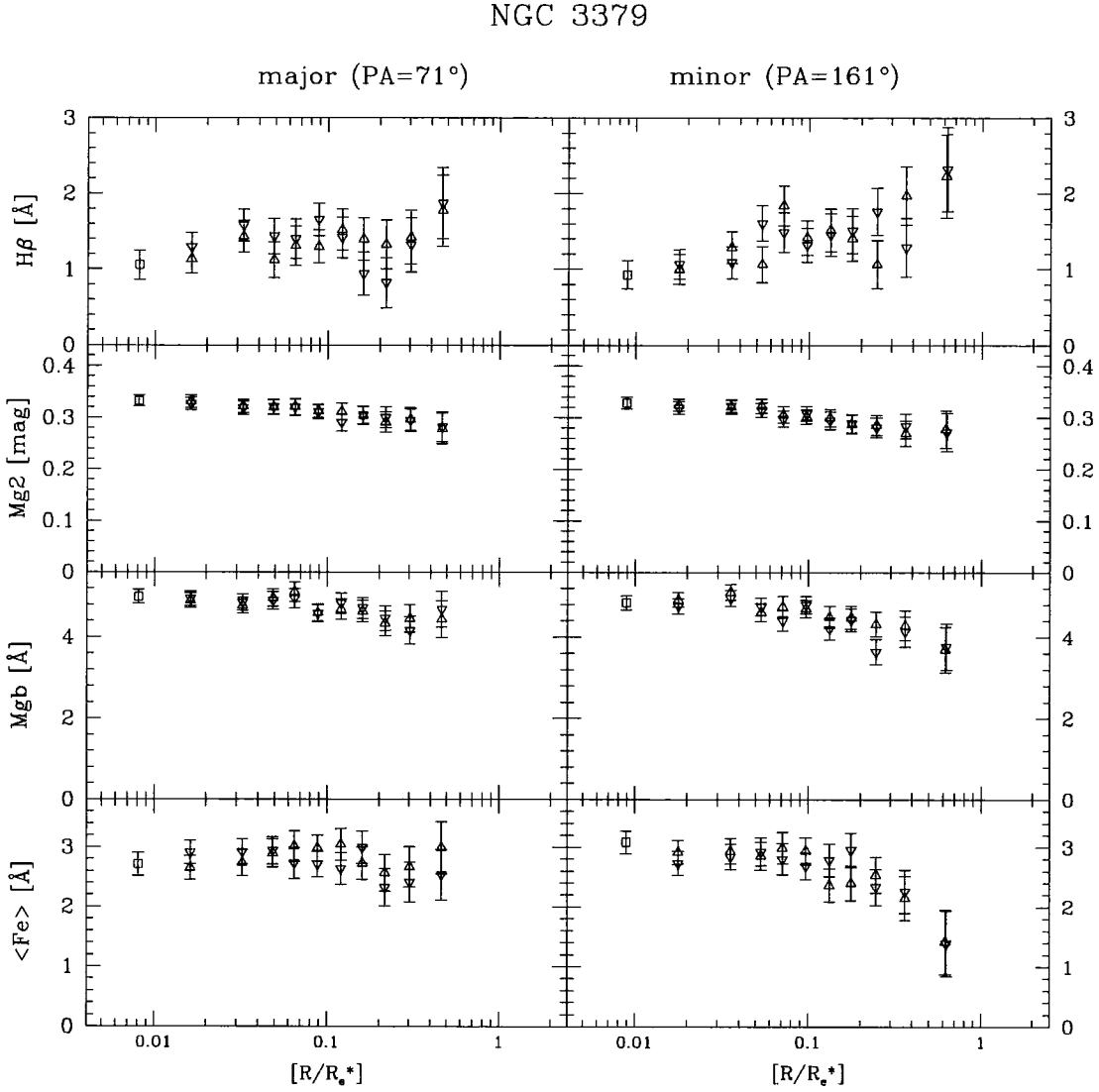

Figure 5.13: Major and minor axis line-strength gradients for NGC 3379. The seeing for both observations was approximately 0.″8.

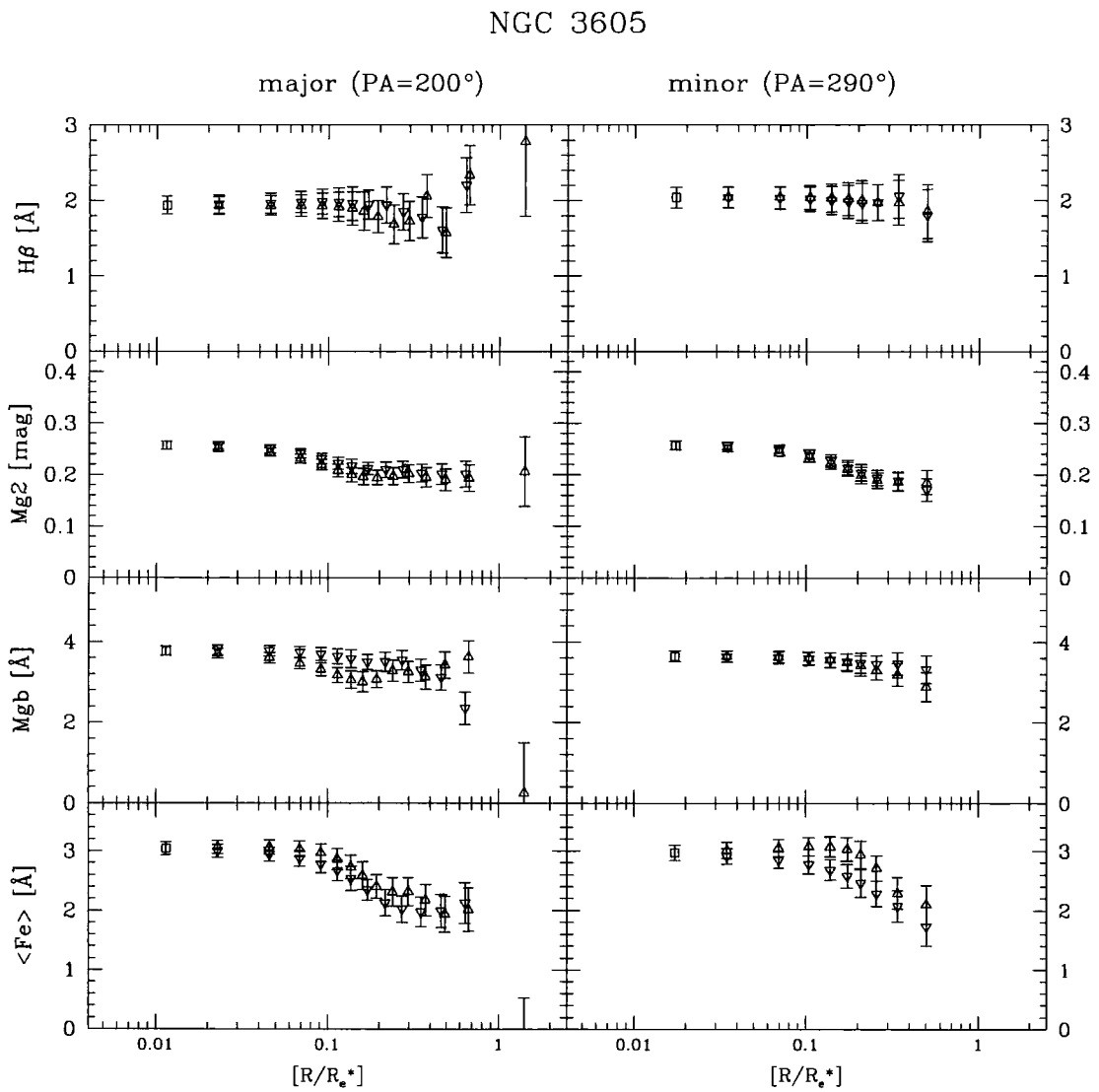

Figure 5.14: Major and minor axis line-strength gradients for NGC 3605. The minor axis observation was subject to significant smoothing during focus corrections, i.e. a maximum Gaussian smoothing of 1.″44 was applied. For the major axis spectrum, a maximum smoothing of 0.″69 was required. The seeing for both observations was $\sim 1''$; the total effective smoothing in the spatial direction is therefore 1.″75 and 1.″21 for the minor and major axis observations respectively.

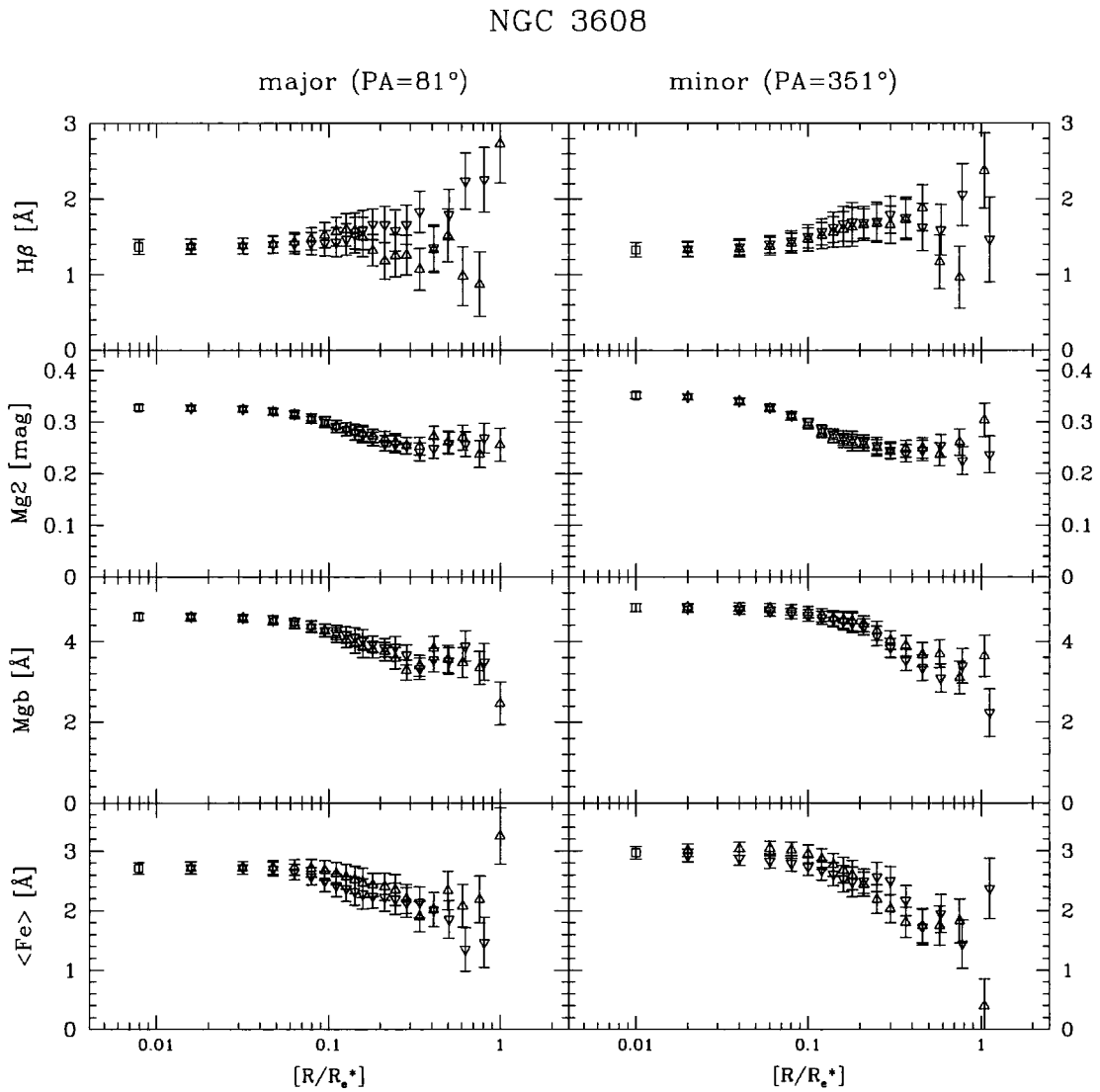

Figure 5.15: Major and minor axis line-strength gradients for NGC 3608. Focus corrections were applied for both spectra corresponding to a maximum Gaussian smoothing of 0.″99 for both cases. The seeing of observations was approximately 1″ for both spectra. The total smoothing in the spatial direction was therefore ∼1.″5; data points cannot therefore be assumed to be independent at smaller spatial intervals.

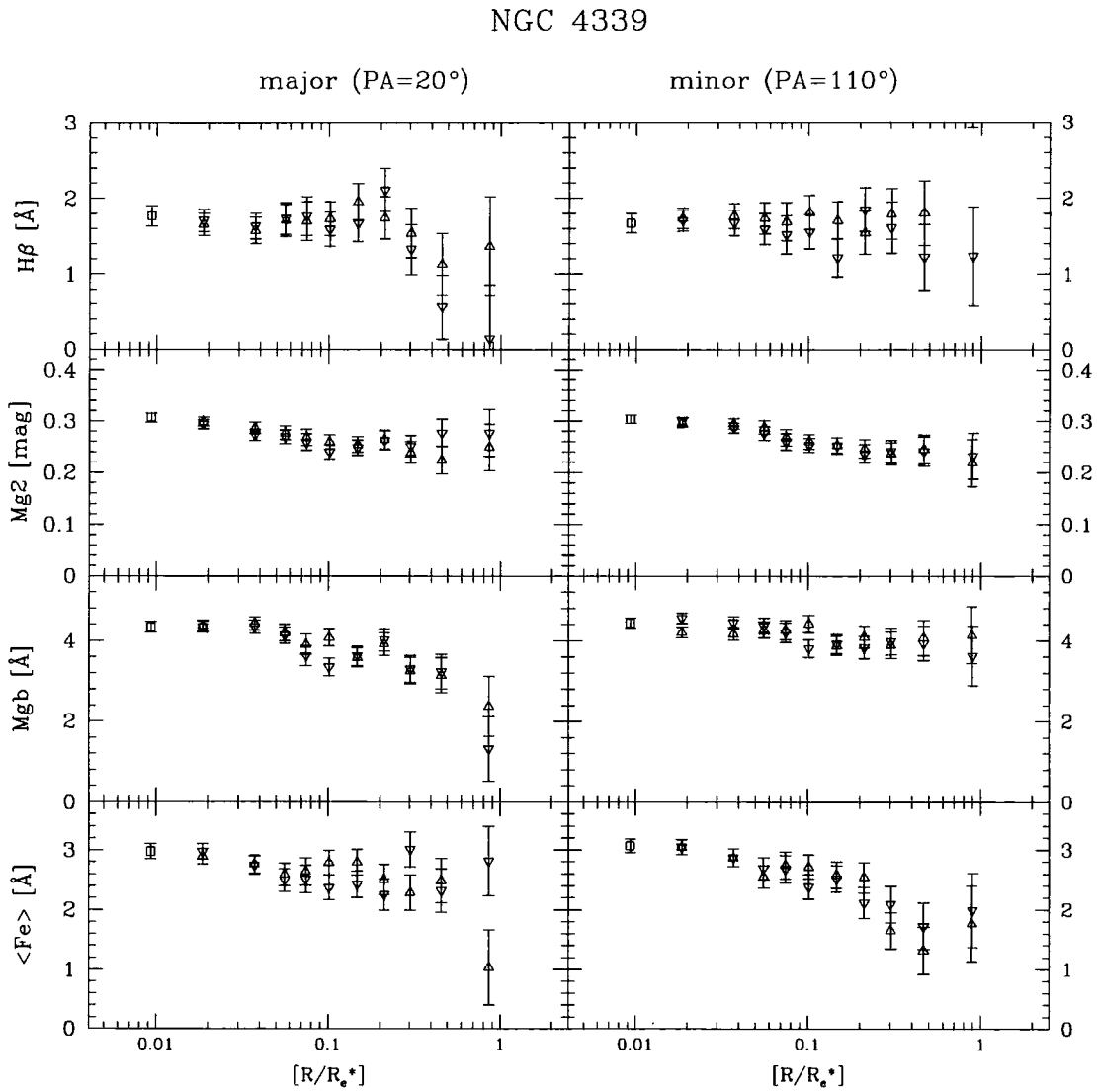

Figure 5.16: Major and minor axis line-strength gradients for NGC 4339. Focus corrections applied to both spectra were small, i.e. 0.″65 and 0.″50 respectively. The seeing for both observations was approximately 0.″5.

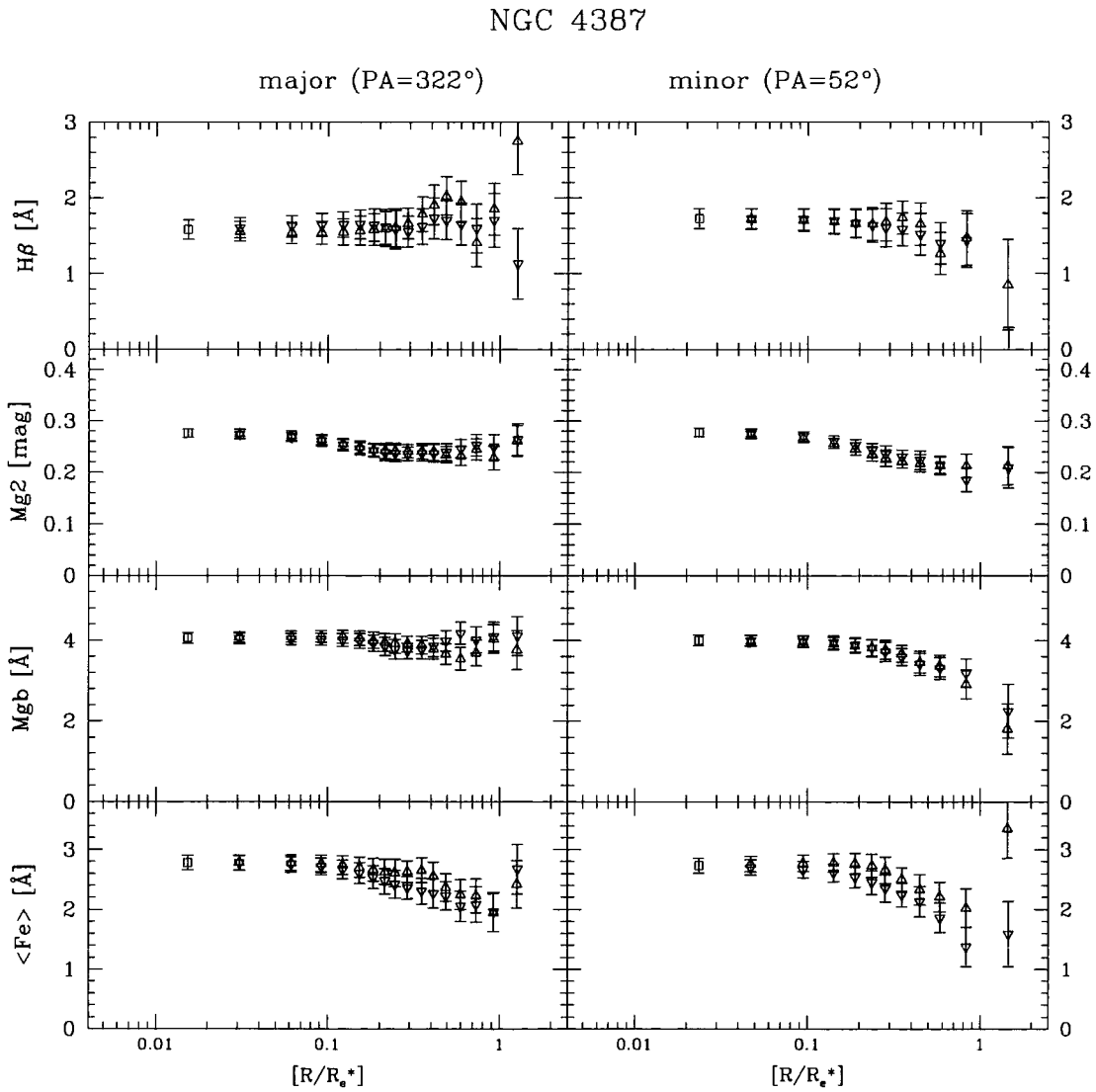

Figure 5.17: Major and minor axis line-strength gradients for NGC 4387. Focus corrections corresponding to smoothing of 0.″86 and 0.″76 respectively were applied. The seeing for both observations was $\sim 1''$; the total effective smoothing in the spatial direction is therefore 1.″32 and 1.″26.

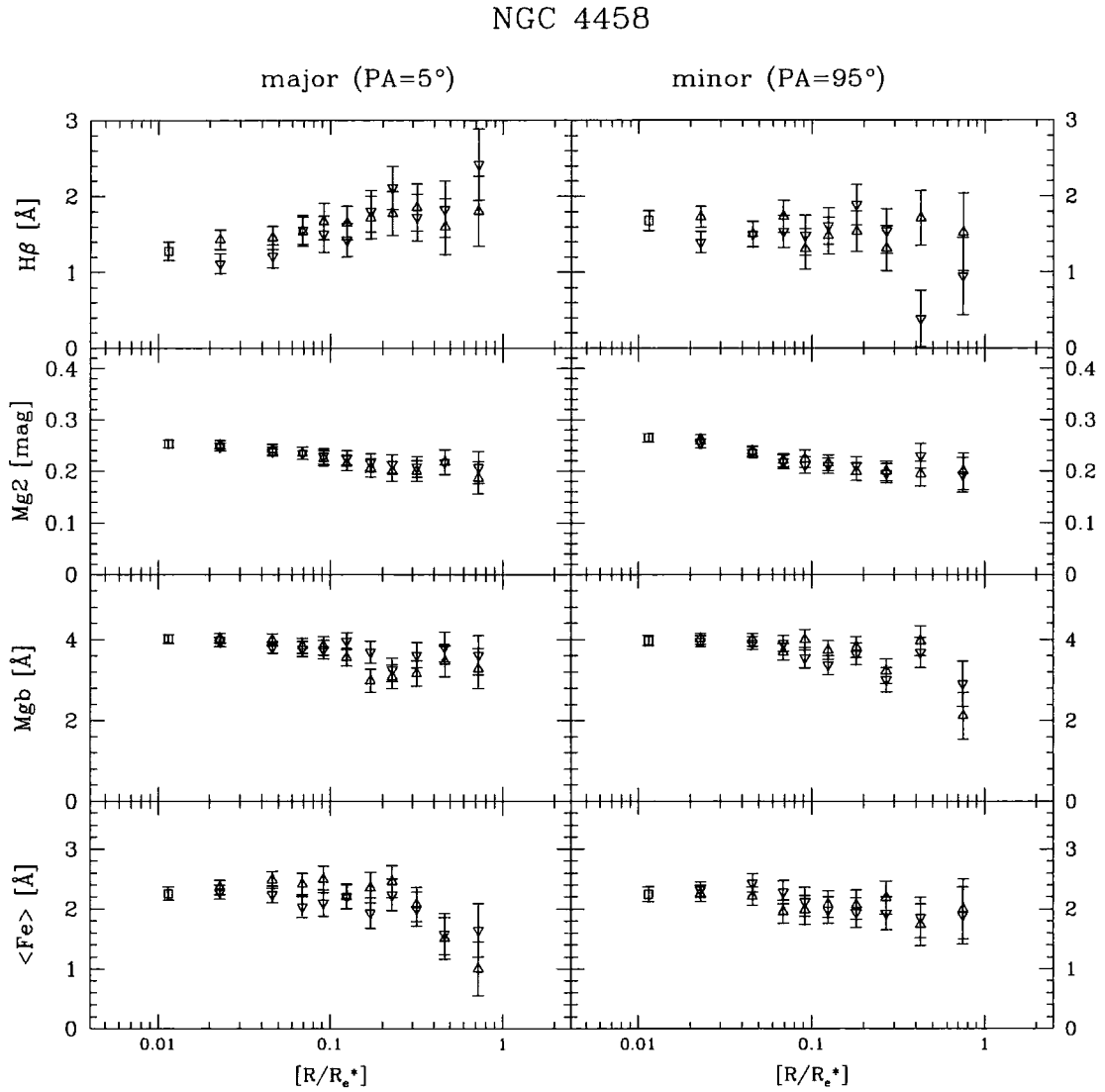

Figure 5.18: Major and minor axis line-strength gradients for NGC 4458. The seeing for both observations was approximately 0.″8.

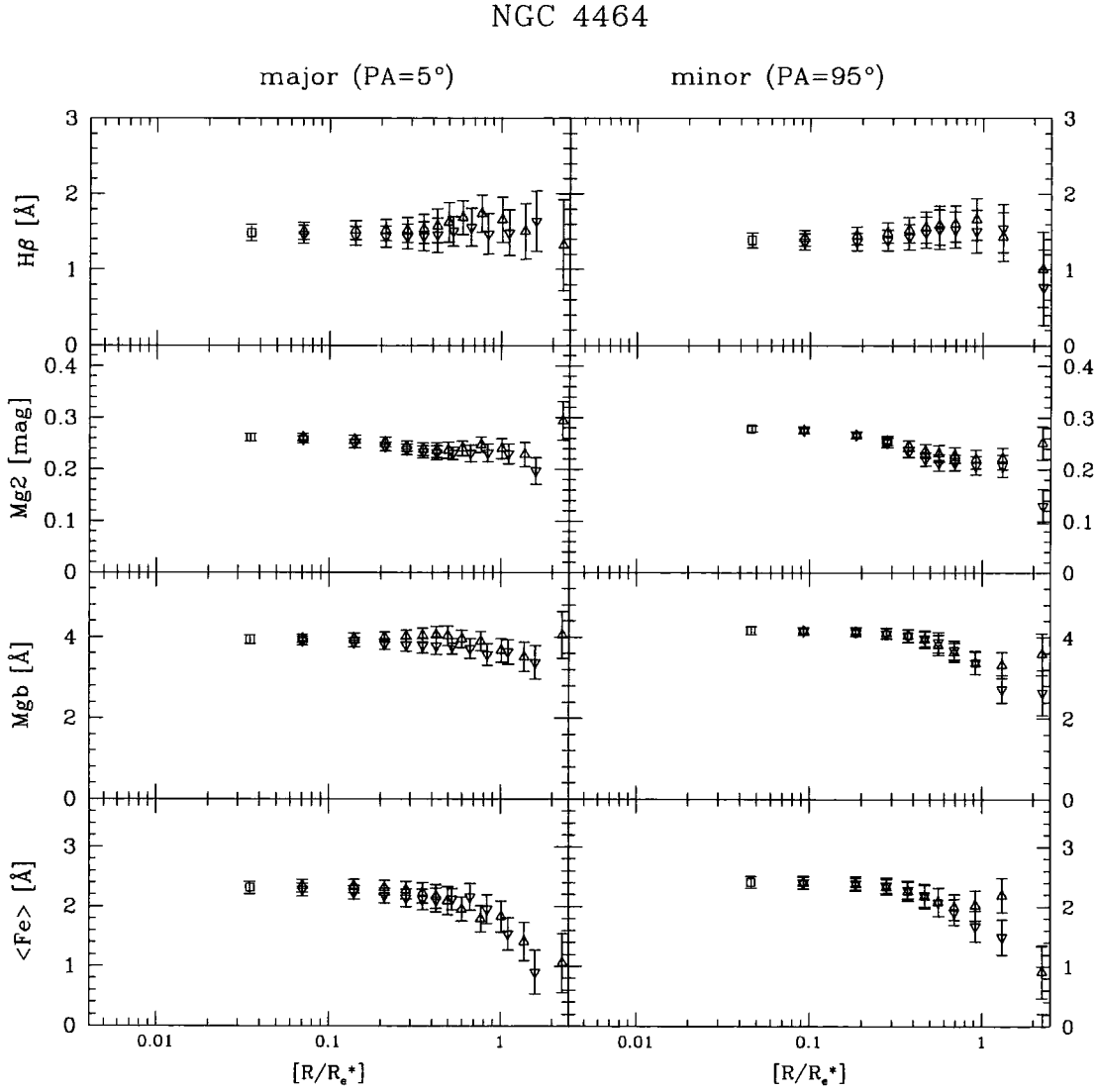

Figure 5.19: Major and minor axis line-strength gradients for NGC 4464. The seeing for both observations was $\sim 1''.0$. Measurements are therefore independent only on spatial intervals greater than $\sim 1''.25$.

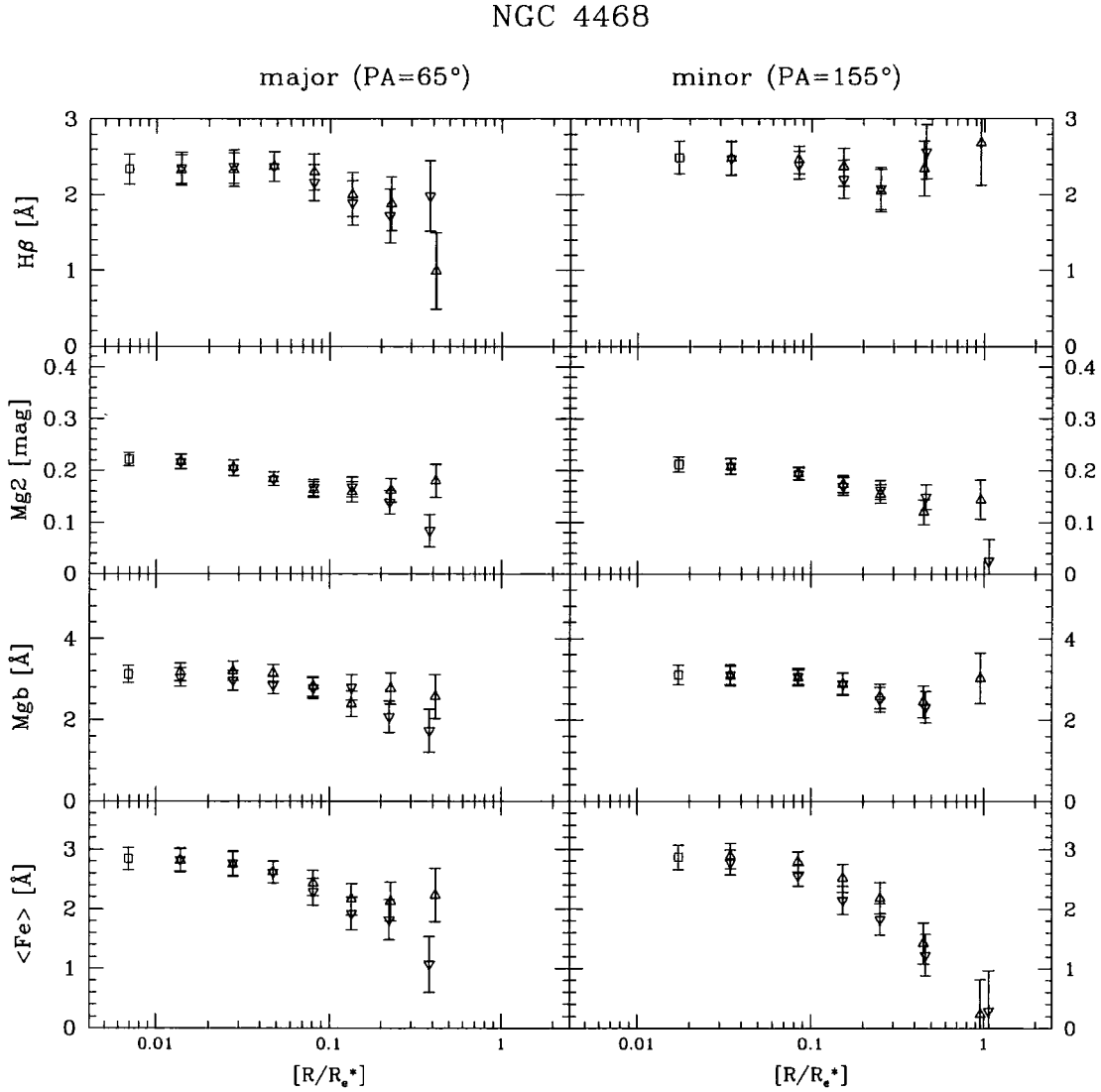

Figure 5.20: Major and minor axis line-strength gradients for NGC 4468. The seeing for both observations was approximately 1″.

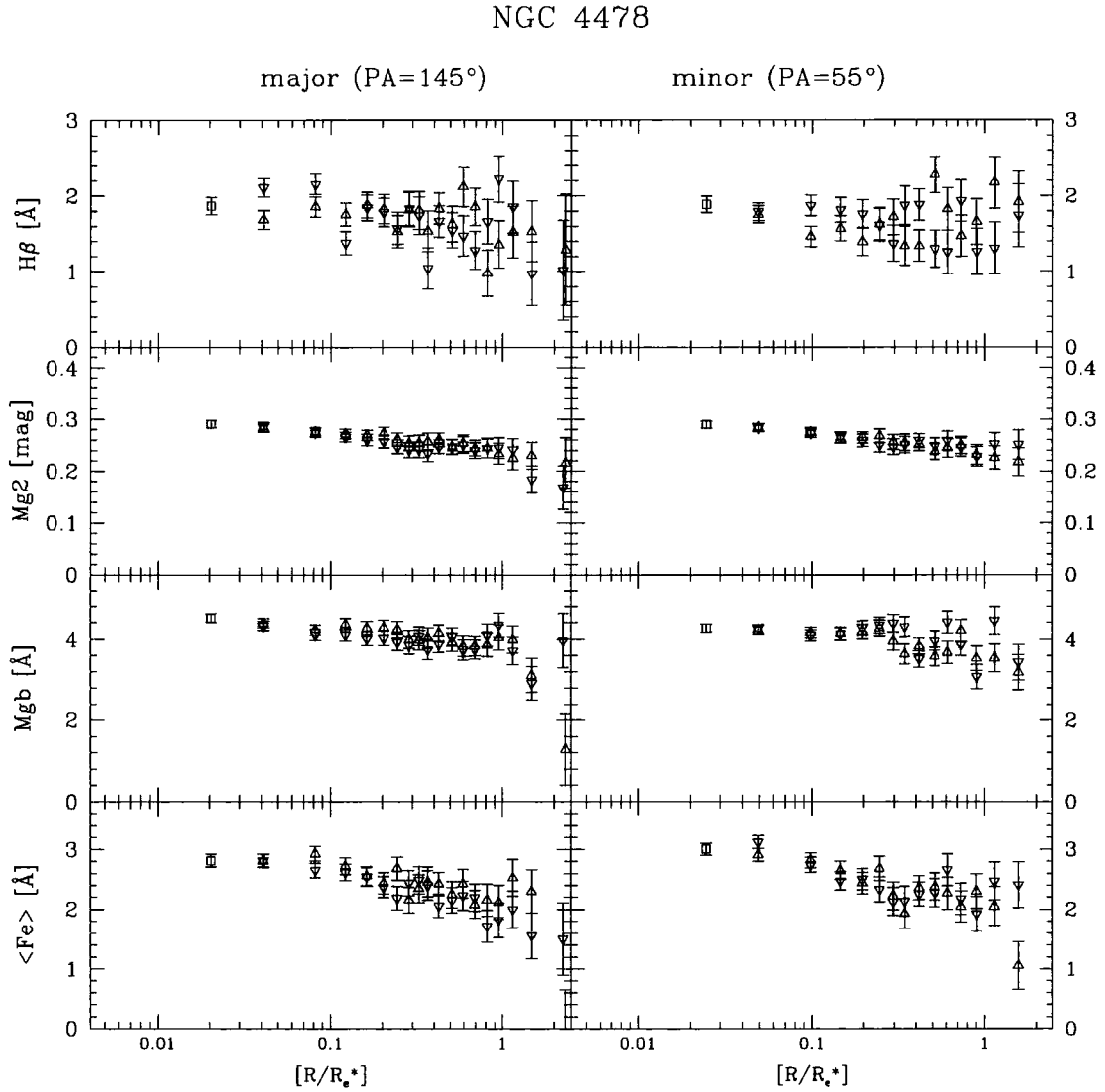

Figure 5.21: Major and minor axis line-strength gradients for NGC 4478. The seeing for observations was approximately 0.″8 and 0.″5 respectively.

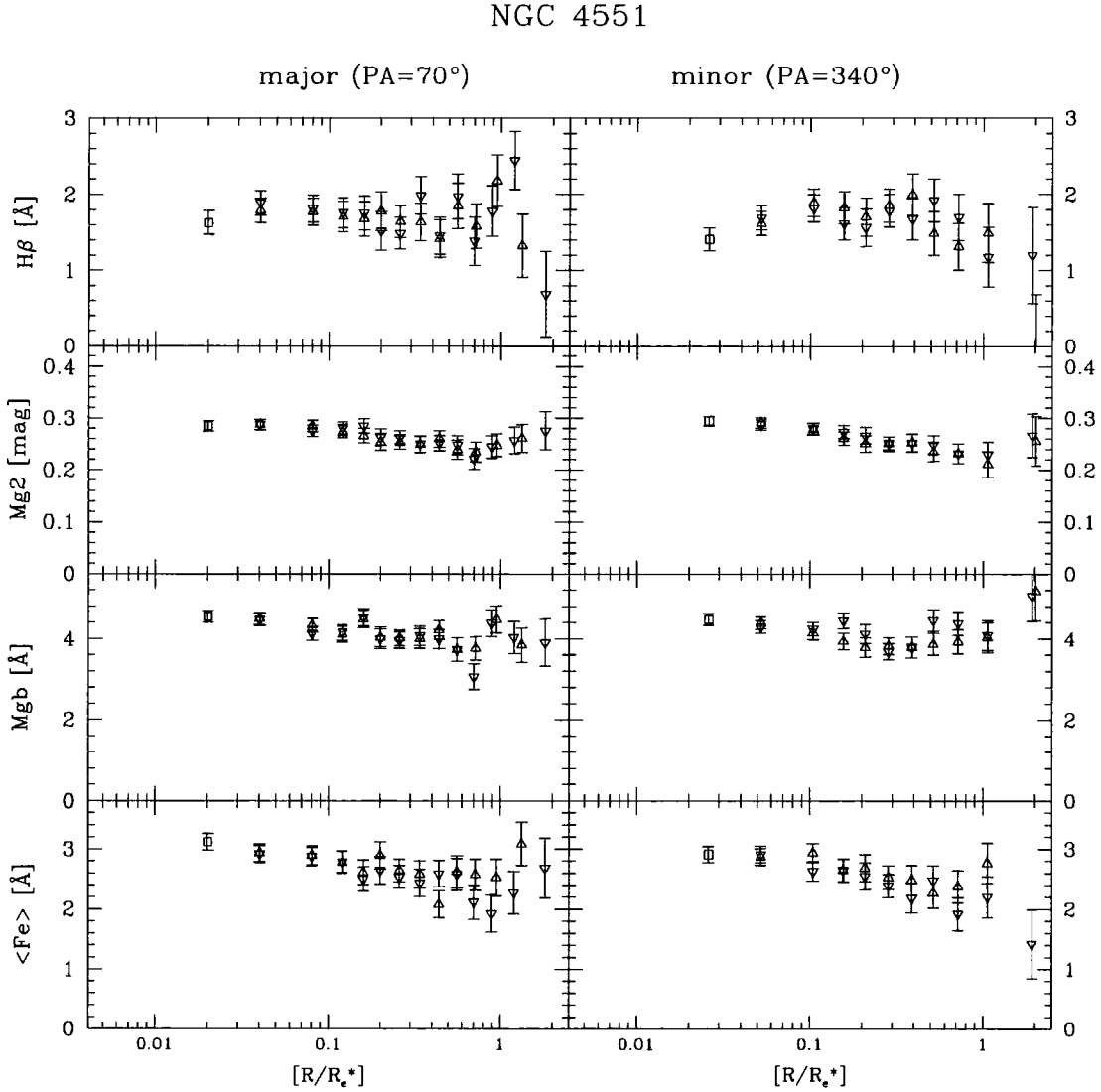

Figure 5.22: Major and minor axis line-strength gradients for NGC 4551. The seeing for both observations was approximately 0.″8.

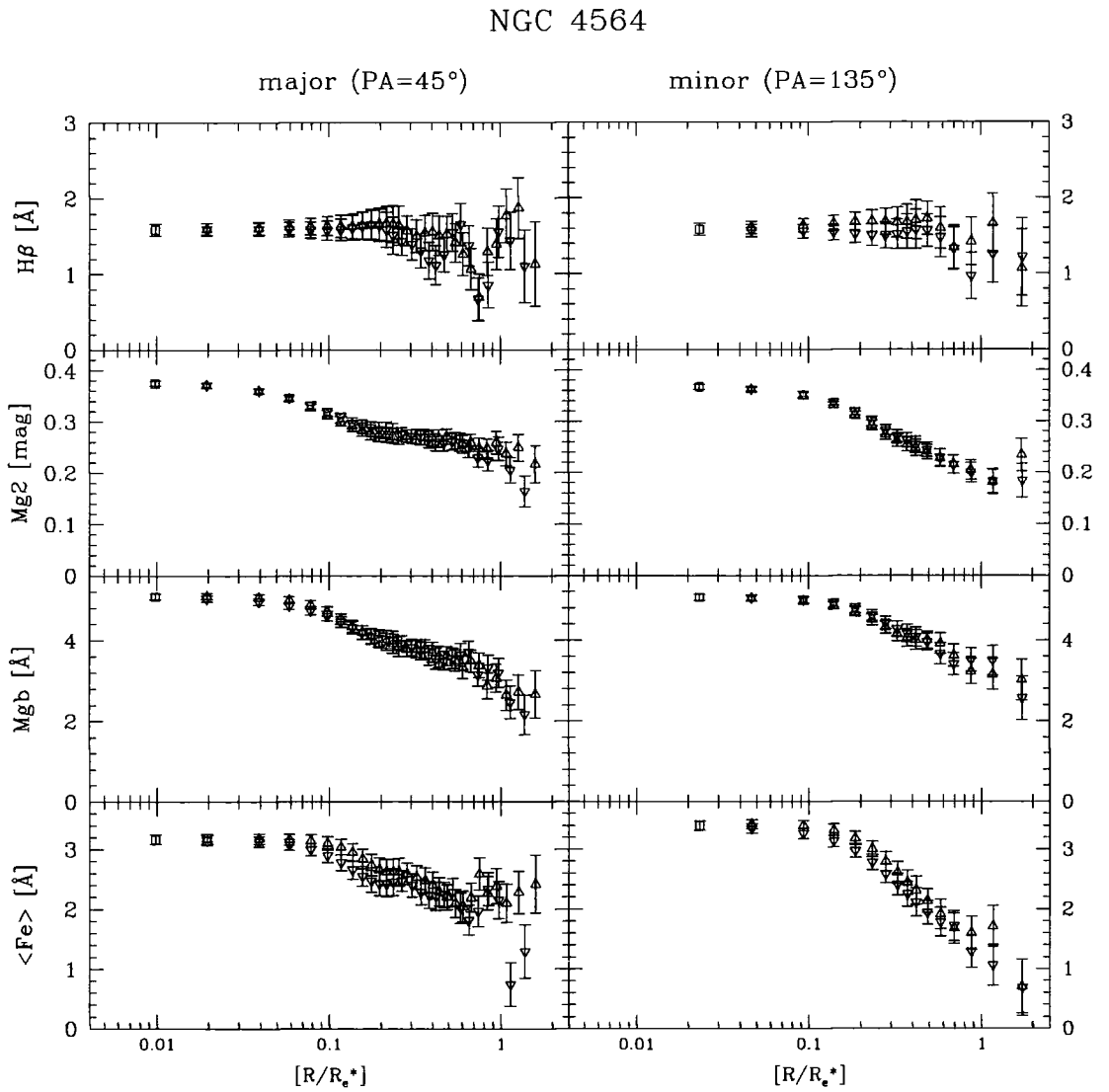

Figure 5.23: Major and minor axis line-strength gradients for NGC 4564. Both spectra were corrected for the effects of focus variations; the maximum smoothing applied, 0.″82 for the major axis spectrum, and 0.″74 for the minor axis spectrum, was in both cases lower then the seeing of $\sim 1''$. The total effective smoothing is 1.″29 and 1.″24, respectively.

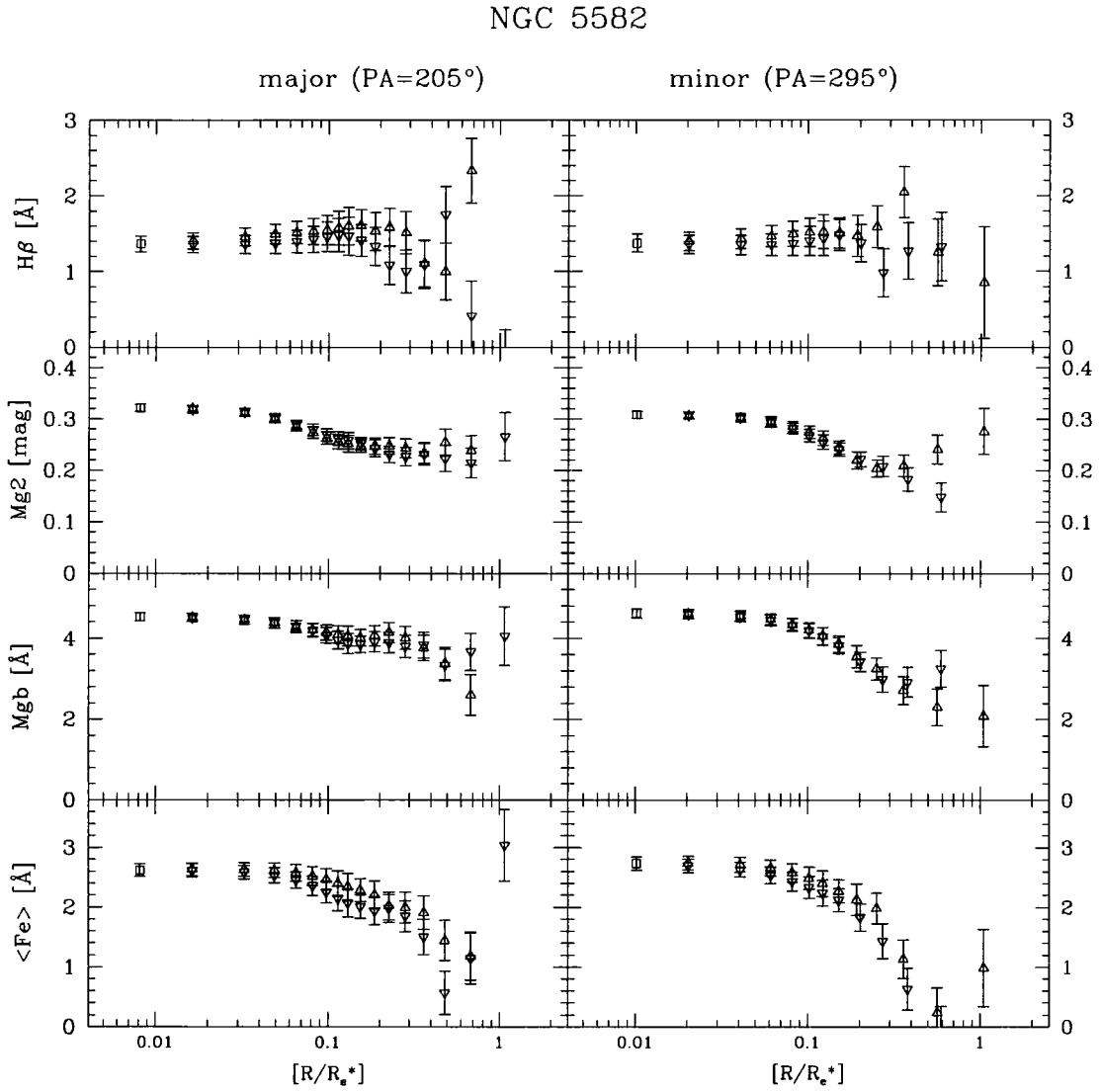

Figure 5.24: Major and minor axis line-strength gradients for NGC 5582. Focus corrections applied for the major and minor axis spectra corresponded to a maximum Gaussian smoothing of 0.″74 and 1.″30 respectively. The seeing for the minor axis observation was 1″; measurements for this spectrum cannot be assumed to be independent, on spatial intervals $\lesssim$1.″6.

Chapter 6

Line-Strengths: Relations

Line-strength gradients are interpreted both in the context of population models and by comparison with the relations of other authors. Measurements have been obtained (as described in section 5.1.2) for a signal-to-noise ratio of 70Å^{-1}, i.e. for a *higher* signal-to-noise ratio than for measurements presented in chapter 5; this enabled stronger conclusions to be made due to the smaller measurement uncertainties.

Relations between the different measurements of line-strengths, defined in section 5.1.1, are presented. Line-strengths measured as a function of radius are considered. In section 6.1, measurements of Mg'_b and Mg_2 obtained here are compared with the relations of other authors. The relations $Mg'_b - log(\sigma)$, Mg_b– <Fe> and $H\beta$–[MgFe] are then considered for each galaxy. To study the $Mg'_b - log(\sigma)$ relation, values of σ were obtained for radii of the line-strength measurements as described in section 5.2.1.

6.1 Mg'_b–Mg_2 relation

As a check of the measurement of Mg_b and Mg_2, comparisons are made with the relations and measurements of other authors. In figure 6.1, measurements of Mg'_b and Mg_2 obtained here as a function of radius, are compared with the Mg'_b–Mg_2 relation derived by the EFAR collaboration for their entire galaxy sample (Wegner et al., 1998), where Mg'_b is given by the definition due to Baggley (1996) and Colless et al. (1998), i.e.

$$Mg'_b = -2.5 \cdot log_{10}(1 - \frac{Mg_b}{\Delta\lambda}) \tag{6.1}$$

where $\Delta\lambda$ is the width of the Mg_b index central passband, i.e. 32.5Å, to be consistent with the definition of Mg_2. The principal aim of the EFAR project is to study the peculiar motions of nearby galaxy clusters using relations defining the intrinsic properties of elliptical galaxies. For this purpose, a large and homogeneous sample of galaxy data was obtained, the largest single set of such data for early-type galaxies to date. Mg_b was measured most consistently for the EFAR

galaxy data due to its smaller wavelength coverage; Mg_2 however has been more widely measured by previous authors. To enable Mg_2 to be determined where a direct measurement could not be obtained, a calibration between the more readily measured Mg_b index and Mg_2, i.e. Mg'_b–Mg_2 relation, was derived for EFAR data for which both measurements were obtained (Wegner et al., 1998). The relation derived (using a maximum likelihood fit), i.e. $Mg_2 \simeq 1.93Mg'_b - 0.04$, with perpendicular rms residual of 0.018 mag (rms of 0.039 mag in Mg_2 or 0.020 mag Mg'_b), is plotted in figure 6.1.

Also shown in figure 6.1 are the relative calibrations of Mg_b and Mg_2 obtained for the models of Worthey (1994). The EFAR relation clearly disagrees with the calibrations of Worthey, a problem which is known but has yet to be resolved. Most points corresponding to measurements obtained here lie above the best-fit relation of EFAR although there is agreement within the margins of error.

In figure 6.2, comparison is made between the pristine Lick/IDS 1.″4x4″ galaxy measurements for galaxies studied here and the calibrations of Worthey (1994) and Wegner et al. (1998). Excluding data for the galaxies NGC 4564 and NGC 4458, the Lick data are in good agreement with the models of Worthey (1994) although they are systematically offset from the EFAR relation. Considering this result it is unsurprising that our measurements are similarly in disagreement with the EFAR relation since these Lick/IDS galaxy measurements were used in our calibration to the Lick/IDS system (section 5.2.2). It is also important to note that many of the other Lick/IDS measurements are in *disagreement* with the models of Worthey (1994). The resolution of these disagreements will clearly require further investigation.

Since the index Mg_2 is defined for a far wider wavelength range than Mg_b, it is more reliably determined but is also more susceptible to chromatic focus variations which have been detected for a good proportion of the data presented here (Chapter 2). Although good agreement has been shown in section 5.3 with previous measurements of Mg_2, the Mg_b index will be used in the following relations instead of Mg_2 to ensure a more reliable study of the Mg line-strength feature for all data obtained.

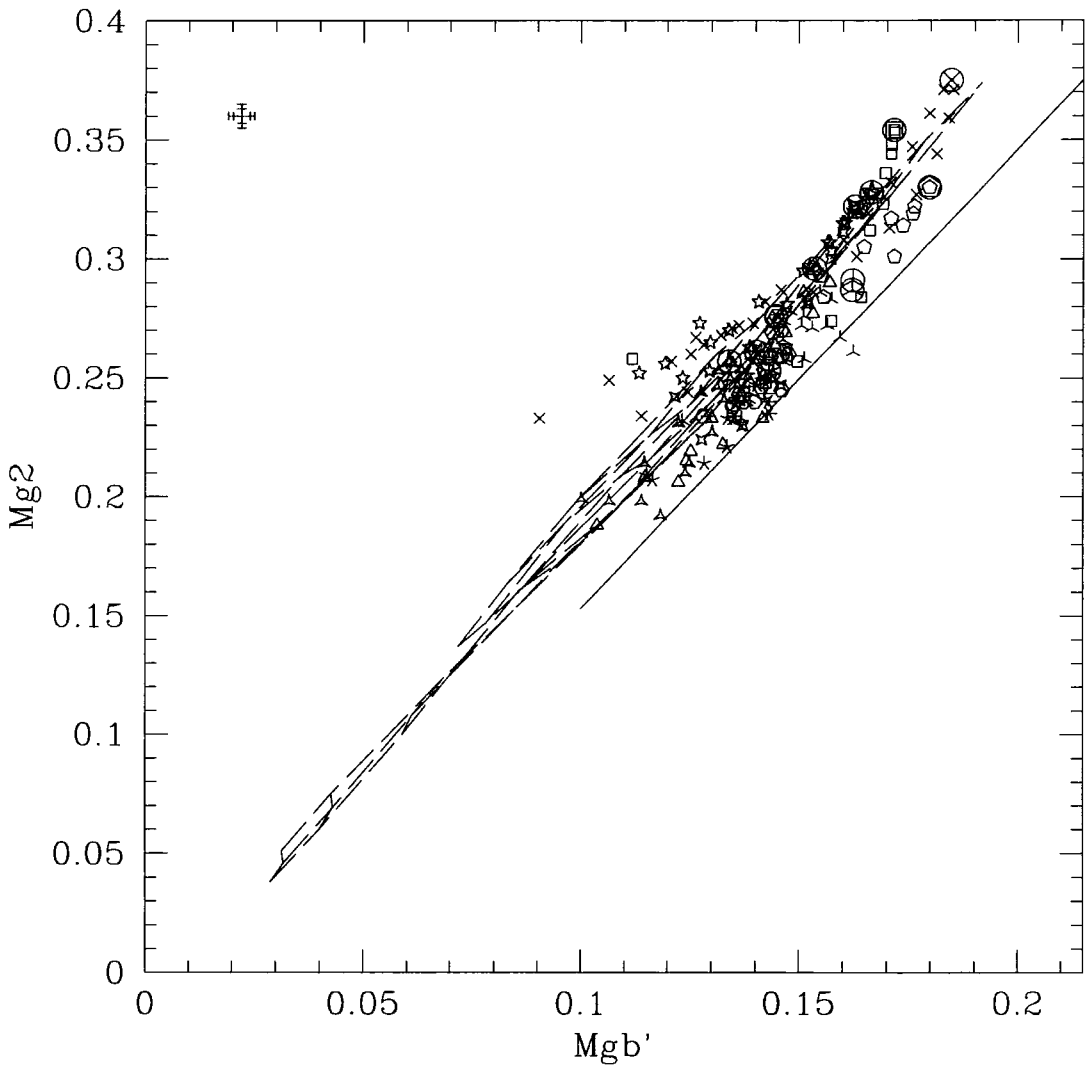

Figure 6.1: Measurements of Mg_2 and Mg'_b, obtained for the major axis of each galaxy are compared with the EFAR relation and the models of Worthey (1994). Measurements for different galaxies here are given by different symbols for each galaxy. Central measurements for each galaxy are encircled. Typical errors for all galaxies are shown in the upper left-hand corner, the smaller error bars corresponding to the central measurements and the larger errors, to measurements for the outermost radius shown. Relation obtained by the EFAR collaboration for their central cluster galaxy measurements is given by solid line for the approximate range of their measurements. Relations between Mg_2 and Mg'_b for the models of Worthey (1994) are given by the model grid, indicated by dashed lines.

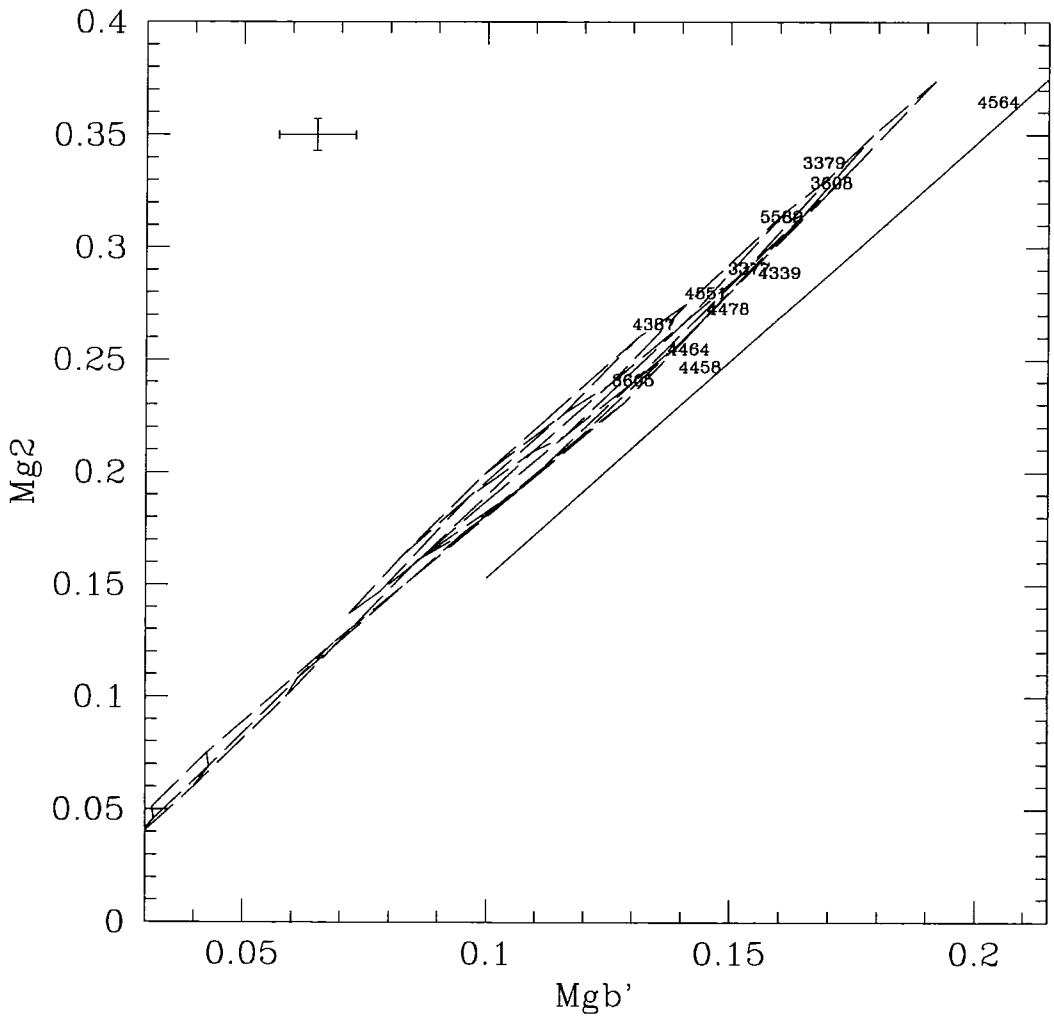

Figure 6.2: Comparison of measurement of Mg_2 and Mg_b' for the Lick/IDS pristine data for galaxies studied here, with the calibrations of Worthey (1994) and Wegner et al. (1998). Typical error bar for Lick/IDS measurements is given in upper left.

6.2 Mg–σ relation

The Mg–σ relation is one of the most important scaling relations for elliptical galaxies, its tightness having been interpreted as representing strong constraints on their evolutionary histories (Burstein et al., 1988; Bender et al., 1993; Ziegler and Bender, 1997). Davies et al. (1993) studied this relation as a function of radius for their sample of luminous ellipticals, and for a given change in Mg_2 they found the corresponding change in σ to be far smaller than predicted by the best-fit relation for *central* values. They suggested that this was due to the effects of velocity anisotropy and rotation and that this implied that σ was a far poorer indicator of metallicity than for example the escape velocity v_{esc}. In figure 6.3, measurements of Mg'_b against $\log(\sigma)$ are plotted for both the major and minor axes of each galaxy. For each plot, comparisons are made with the best-fit relation for the central measurements of Mg'_b and σ obtained by the EFAR collaboration (Colless et al., 1998). To help identify any trend in measurements for each galaxy with galaxy mass, plots are presented in order of decreasing central measurement of σ. No obvious trend with central σ however is readily apparent.

It is useful to try to distinguish between the results for galaxies of the different kinematical types identified in chapter 4. For galaxies of "type 1" (i.e. NGC 4564, NGC 5582, NGC 2778, NGC 3377, NGC 4464, NGC 4339), all measurements are found to closely follow the trend of the central EFAR relation. This is in marked contrast to the findings of Davies et al. (1993). Measurements for "type 1" galaxies in general have a slightly greater range in values of Mg'_b and σ than for the other types, particularly for NGC 4564 and NGC 3377, although measurements for some galaxies of the sample as a whole, e.g. NGC 3605, extend to a smaller fraction of the effective radius, R_e, than most. Galaxies of "type 2", excluding NGC 3605, have a slightly tighter distribution of measurements in the $Mg'_b - \sigma$ plane: this can be attributed to the central dips in σ measured for these galaxies which has the effect of shifting points for central measurements, towards the left of each diagram. Of the remaining galaxies, NGC 3379, NGC 3608 and NGC 4468, measurements appear to follow a steeper trend than defined by the central relation; this is in closer agreement with the findings of Davies et al. (1993). Excluding these galaxies it can however be said that measurements in general are in good agreement with the $Mg'_b - \sigma$ central relation.

6.3 Mg_b– <Fe> relation

The $[\frac{Mg}{Fe}]$ overabundance observed for luminous ellipticals, whereby the ratio of measured Mg line-strengths relative to those of Fe is greater than solar ratios, has been interpreted as representing an overabundance of light elements relative to Fe (Worthey et al., 1992; Davies et al., 1993). This measurement reflects an important limitation of stellar population models, that these models are dependant on the abundance ratios of the Galactic stars for which model calibrations are obtained. It is also interpreted as an important diagnostic of the star formation history of an integrated stellar population as outlined below.

Light elements contributing to the Mg line-strength feature are produced by supernovae of Type II, whereas iron is produced by supernovae of Type Ia. The progenitors of supernova e of Type II are massive stars of $\sim 20 - 40 M_\odot$; Type Ia supernovae occur where a white dwarf accretes mass from its companion in a binary star system. Scenarios proposed (e.g. Worthey (1992)) to explain

the $[\frac{Mg}{Fe}]$ overabundance include (i) control of the initial mass function (IMF): in this scenario an $[\frac{Mg}{Fe}]$ overabundance is produced where the IMF of a galaxy is skewed towards more massive stars and therefore a greater proportion of Type II supernovae; (ii) varying the duration of star formation within a galaxy: since the lifetime of progenitors of Type II supernovae is approximately 100 times shorter than that of supernovae of Type Ia, the duration of star formation within a stellar population will directly affect the ratio of the abundances of heavy to light elements. A recent study by Sansom and Proctor (1998) has shown that formation models involving a delayed starburst, expected to be triggered during a merger, can also reproduce the observed Mg and Fe line-strengths of luminous ellipticals.

Classic dissipative models for elliptical galaxy formation (e.g. Larson (1974a), Arimoto and Yoshii (1987)) invoke the onset of galactic winds to help explain e.g. the colour-magnitude relation and the increase in measured metal spectral absorption lines with increasing galaxy luminosity. In such models winds occur at a later stage in the evolution of more massive ellipticals, due to their greater potential well, causing the cessation of the bulk of star formation. Such models predict that the $[\frac{Mg}{Fe}]$ overabundance should in fact be a *decreasing* function of galactic mass in disagreement with observations. More complicated scenarios have therefore more recently be proposed (e.g. Thomas et al. (1998)).

In figure 6.4 measurements of Mg_b and <Fe> are presented for the major and minor axes of each galaxy and compared with the predictions of the models of Worthey (1994). Plots are arranged in order of decreasing value of central σ although, as found for measurements of Mg'_b and σ, no clear trend with central values of σ is evident.

For all galaxies besides NGC 3605 and NGC 4468, measurements are clearly offset from the model grid indicating *an* $[\frac{Mg}{Fe}]$ *overabundance, measured for the giant ellipticals, does exist for ellipticals of the lower luminosities studied here.* For a large fraction of our sample, this overabundance is to first order, constant as a function of radius.

6.4 Hβ – [MgFe] relation

The Hβ line-strength feature of the Lick/IDS system has been presented as an important index in breaking the age-metallicity degeneracy affecting broad-band colours and line-strength indices such as Mg_b and Mg_2. In figure 6.5 measurements of Hβ are presented for each galaxy together with measurements of the index [MgFe] = $\sqrt{Mg_b < Fe >}$ and compared with the model predictions of Worthey (1994).

In general, all galaxies are found to have gradients in *metallicity* with metallicity decreasing as a function of radius. This reflects gradients in both the Mg and Fe line-strength indices measured in chapter 5. It is also a prediction of dissipational collapse models. Some galaxies also show gradients in *age*, with the stellar population becoming *younger* in age towards the galaxy centre, i.e. for NGC 4564, NGC 3377, NGC 4478, NGC 4339 and NGC 3605. This is evidence that star formation at the galaxy centre has continued until more recently than for the surrounding galaxy. Detections supporting the existence of disk-like components within each of these galaxies was presented in chapter 4. The presence of a younger component has been shown to explain the observed Hβ absorption of a sample of disky ellipticals by de Jong and Davies (1997).

In figure 6.5 measurements for NGC 2778 lie predominantly below the model grid; this is consistent with the existence of Hβ emission causing a decrease in the measurement of absorption. Studied by both González (1993) and Fisher et al. (1995), detection of significant [OIII] emission has been noted for this galaxy which may be accompanied by Hβ emission.

6.5 Discussion

The presence of an $[\frac{Mg}{Fe}]$ overabundance for most galaxies further constrains possible evolution scenarios although quantifying these constraints would require comparison with the predictions of stellar population models for the appropriate abundance ratios. Where good agreement has been found between the measurements of Mg'_b and σ and the central EFAR $Mg'_b - \sigma$ relation (section 6.2), this suggests that σ is a accurate tracer of, and places tight constraints on, the properties (e.g. age and metallicity) of the stellar population.

Comparison of the results of figures 6.4 and 6.5 for each galaxy reveals an interesting trend: where a greater offset from the model predictions is found in figure 6.4, measurements of Hβ for a galaxy in figure 6.5 are generally lower. This may just be a qualitative reflection of the tight relation found by Fisher et al. (1995) between central measurements of $[\frac{Mg_b}{Fe5270}]$ and mean measurement of Hβ. It may represent another important relation for the stellar populations of ellipticals and may even provide a useful means of correcting for the effects of Hβ emission; further work is however required to test these ideas.

6.6 Future Work

Stellar population gradients provide invaluable insights into galaxy evolution. With the aid of stellar population models, the degenerate effects of age and metallicity can be distinguished (chapter 1). The absorption feature Hβ measured in this work has been proposed as a very sensitive age indicator and together with the metal indices of Mg and Fe can enable the measurement of gradients in age and metallicity. Hβ unfortunately suffers the effect of galactic Hβ emission which even in relatively quiescent galaxies can be severe and has the effect of diluting the measured Hβ absorption (Davies et al., 1993; González, 1993; Fisher et al., 1995). More robust age indicators proposed include the Balmer features H_δ and H_γ as defined by Worthey and Ottaviani (1997). Additional observations to determine these indices should considerably enhance the study of the stellar population gradients for objects here.

Alternatively a reliable means of detecting and correcting for Hβ emission would greatly enhance the accuracy of the Hβ line-strength as an indicator of age. An accurate measurement of Hβ emission would require a spectral synthesis modelling of the galaxy *absorption* spectrum for the observed wavelength range. Such modelling is however non-trivial since stars of different spectral types are believed to be responsible for different line-strength features (e.g. for Mg and Fe line-strength, K-type stars; for the Hβ line-strength index, A-type and F-type stars). Modelling of a given galaxy spectrum would therefore require e.g. the precise least-squared fitting of individual stellar spectra of varying contributions, to the galaxy spectrum itself. Such modelling should be attempted in the future to improve the reliability of the Hβ index as an age indicator.

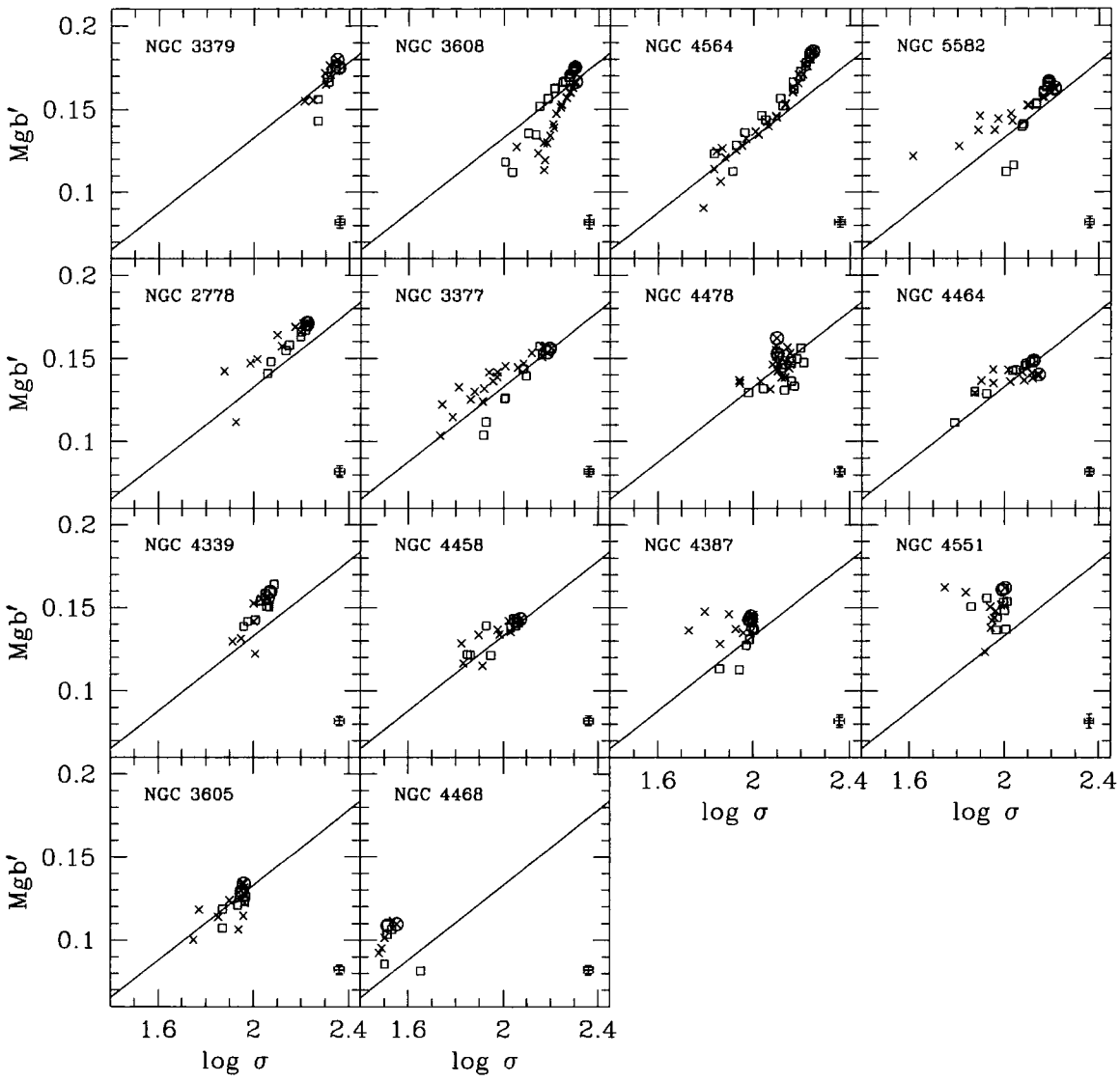

Figure 6.3: Measurements of Mg'_b and $\log(\sigma)$ for the major and minor axes of each galaxy. Major axis measurements are given by crossed symbols and minor axis by open squares. Typical errors for Mg'_b and $\log(\sigma)$ are given in lower right corner; for Mg'_b, the larger errors correspond to measurement for outermost plotted in the galaxy and the smaller error to the central measurement. Central measurements for each galaxy are given by larger symbols and are encircled. The least squares regression fit for the central measurements of EFAR i.e. $Mg'_b = (0.113 \pm 0.011)\ log(\sigma) - (0.093 \pm 0.027)$, is indicated for each plot by a solid line.

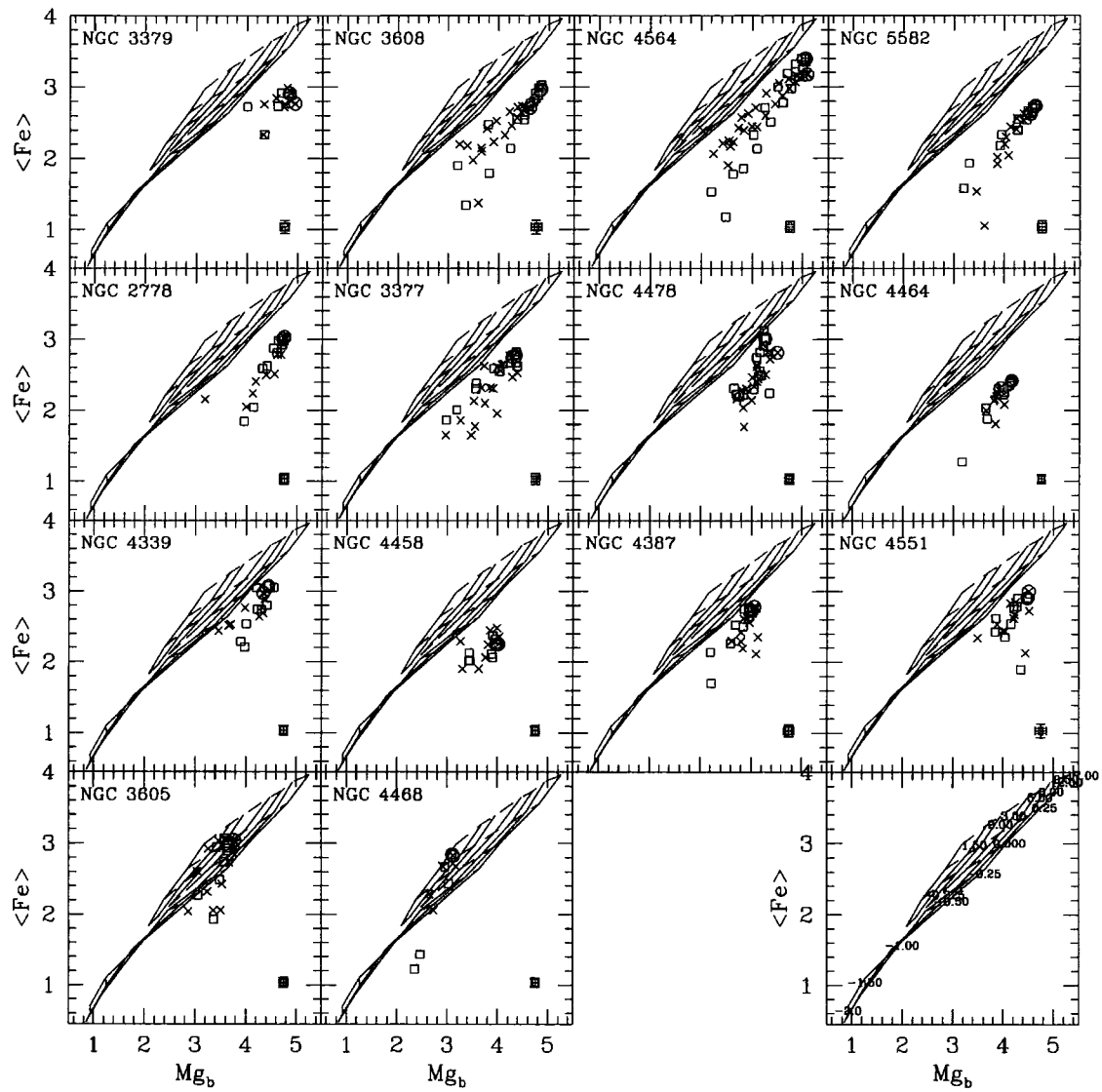

Figure 6.4: Measurements of Mg_b and <Fe> for both the major and minor axes of each galaxy are compared with the model predictions of Worthey (1994). Major axis measurements are given by crossed symbols and minor axis by open squares. Central measurements for both axes are encircled. Typical errors for Mg_b and <Fe> are given in the lower right-hand corner of each plot, the larger errors indicating errors for the outer parts of each galaxy and smaller errors, for the galaxy centre. Model grids of Worthey (1994) are over-plotted with dashed lines connecting points of equal metallicity and solid lines, points of equal age; values of age are given in Gyr and metallicity, in units of $[\frac{Fe}{H}]$. A guide plot is given in lower right where lines corresponding to particular ages and metallicities are labelled.

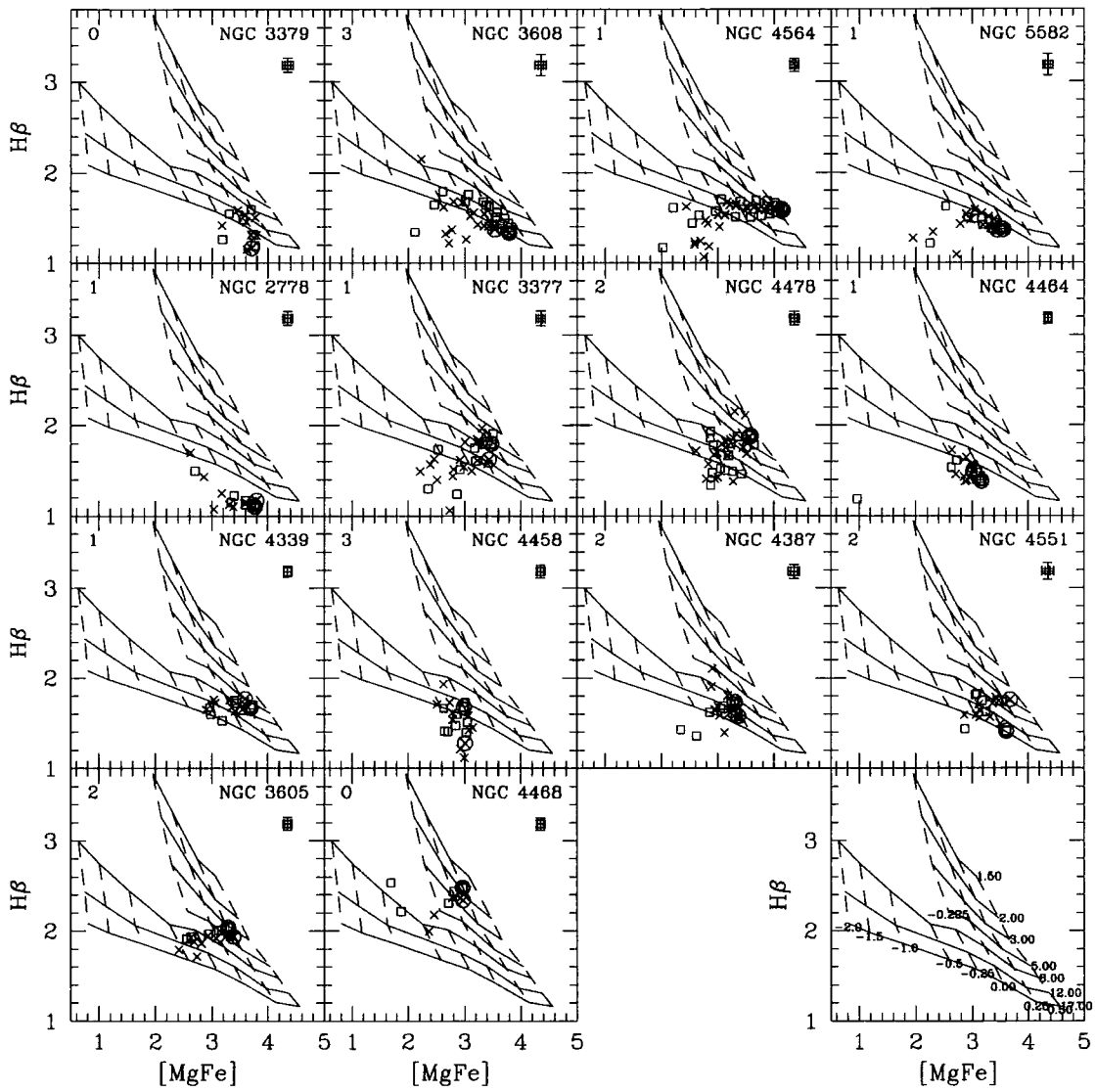

Figure 6.5: Measurements of Hβ and [MgFe] are presented for major and minor axis measurements for each galaxy in increasing value of the measured central galaxy velocity dispersion. Major axis measurements are given by crossed symbols and minor axis by open squares. Errors are given for the inner and outermost measurements in upper right corner of each plot. Model grids of Worthey (1994) are over-plotted with dashed lines connecting points of equal metallicity and solid lines, points of equal age; values of age are given in Gyr and metallicity, in units of $[\frac{Fe}{H}]$. A guide plot is given in lower right where lines corresponding to particular ages and metallicities are labelled.

Chapter 7

Conclusions

The aims of this thesis were to investigate both the kinematical structure and stellar evolutionary histories of a sample of low-luminosity elliptical galaxies. The main results and conclusions of these studies are summarised in sections 7.1 and 7.2, and interpreted together in section 7.4.

7.1 Kinematics

Measurements of rotation, velocity dispersion, H_3 and H_4 were described and presented in Chapters 3 and 4. These measurements were used to classify galaxies into different types. The characteristics of these different types can be summarised as:

- "Type 1": strong evidence for both disk and bulge components; classification as E/S0; in some cases, measurement of considerable diskiness in photometry; measured values of H_3 are the greatest measured for our galaxy sample.

- "Type 2": central decreases in σ; strong evidence for disks embedded within bulge component; measurements of σ and H_4 asymmetric, and rotation and H_3 lacking point symmetry about the galaxy centre, suggesting existence of decoupled central component.

- "Type 3": "kinematically-decoupled core" (KDC) candidates with counter-rotating cores.

Different formation scenarios were proposed for the different types. For "type 1" galaxies, a coeval formation of both disk and bulge components was suggested to explain their co-rotating and relatively homogeneous kinematical properties. For galaxies of "type 2", a likely scenario would involve the close interaction of an elliptical containing an embedded disk component, with a neighbouring galaxy. For galaxies of "type 3", no clear scenario was decided from the observations.

7.2 Line-Strength Relations

Measurements of line-strength gradients were compared with relations derived by other authors (chapter 6). The most remarkable finding was that the $[\frac{Mg}{Fe}]$ overabundance, found for the giant ellipticals (e.g. Worthey (1994)), exists in the majority (i.e. excluding the dwarf ellipticals NGC 3605 and NGC 4468) of our sample of low-luminosity elliptical galaxies. This suggests that the stellar evolutionary history of low-luminosity ellipticals may be more similar to that of the giant ellipticals than previously believed. It also shows that the stellar populations of many low-luminosity ellipticals cannot be accurately interpreted by stellar population models dependent on the abundance ratios of local Galactic stars.

The other main results were as follows:

- measurements of Mg'_b and Mg_2 are in good agreement with the models of Worthey (1994) but in slight disagreement with the central relation of Wegner et al. (1998) obtained for the measurements of the EFAR data set.

- measurements of Mg'_b and σ for the majority of our galaxy sample are in good agreement with the central relation of Colless et al. (1998).

- the "age-metallicity degeneracy" was broken for our galaxy sample by comparison of measurements of Mg_b <Fe> and $H\beta$ with the models of Worthey (1994): gradients in metallicity were distinguished for all galaxies of our sample; gradients in age were also found for the galaxies NGC 4564, NGC 3377, NGC 4478, NGC 4339 and NGC 3605, with the centre of the galaxy being younger than the outer parts.

7.3 Global Parameters

A range of characteristic parameters for our galaxy sample are presented in table 7.1. These parameters have been obtained in earlier chapters or taken from the literature and summarise properties for each galaxy.

Name	M_B	ϵ	$\overline{\sigma}$	$\delta\overline{\sigma}$	$\frac{v_{max}}{\overline{\sigma}}$	$\frac{v_{max}}{\overline{\sigma}^*}$	$\overline{H_3}$	$\delta\overline{H_3}$	$\overline{H_4}$	$\delta\overline{H_4}$	$\overline{C_4}$	$\frac{\Delta(U-R)}{\Delta logr}$	$\frac{\Delta log<Fe>}{\Delta logr}$	$\frac{\Delta logMg_b}{\Delta logr}$
NGC 2778	-19.68	0.22	142.069	0.587	0.72	1.35	0.078	0.008	0.028	0.009	-0.003	-0.21	-0.070 ± 0.025	-0.051 ± 0.019
NGC 3377	-18.87	0.48	101.633	0.548	0.99	1.03	0.124	0.006	-0.035	0.009	0.019	-0.33	-0.105 ± 0.011	-0.112 ± 0.012
NGC 3379	-19.87	0.09	209.463	1.269	0.17	0.53	0.025	0.009	-0.001	0.010	0.003	-0.24	-0.057 ± 0.011	-0.064 ± 0.011
NGC 3605	-17.44	0.34	87.585	0.227	0.42	0.58	0.042	0.005	0.002	0.005	-0.012	-0.09		
NGC 3608	-20.21	0.21	179.324	0.368	0.03	0.06	0.034	0.003	0.016	0.003			-0.026 ± 0.017	-0.118 ± 0.016
NGC 4339	-18.76	0.01	100.36	0.540	0.61	6.03	0.072	0.007	0.081	0.010				
NGC 4387	-18.01	0.35	97.067	0.289	0.53	0.73	0.013	0.003	0.009	0.004	-0.010	-0.05		
NGC 4458	-18.09	0.01	97.810	0.740	0.02	0.16	0.059	0.013	-0.035	0.018				
NGC 4464	-17.56	0.24	120.927	0.365	0.65	1.15	0.150	0.007	0.051	0.008				
NGC 4468	-17.44	0.60	33.240	0.781	0.35	0.28	0.029	0.043	-0.060	0.027				
NGC 4478	-18.66	0.17	131.707	0.811	0.39	0.87	0.054	0.007	-0.014	0.008	-0.015	-0.15	-0.090 ± 0.015	-0.029 ± 0.014
NGC 4551	-18.05	0.23	95.156	0.413	0.45	0.82	0.053	0.005	-0.034	0.008	-0.011	-0.02		
NGC 4564	-18.97	0.58	144.787	0.228	1.00	0.55	0.027	0.002	-0.016	0.002				
NGC 5582	-19.65	0.20	125.794	0.536	1.10	2.19	0.169	0.007	0.104	0.010				

Table 7.1: Table of characteristic parameters for galaxy sample. Absolute magnitude M_B was calculated in Chapter 2. Mean ellipticity ϵ is as given in table Chapter 5.2 apart from values for NGC 4339, NGC 4458, NGC 4468 and NGC 5582; values for these galaxies were obtained by E. Bell using the ELLIPSE package of IRAF. Measurements of $\overline{\sigma}$, $\frac{v_{max}}{\overline{\sigma}}$, $\frac{v_{max}}{\overline{\sigma}^*}$, $\overline{H_3}$ and $\overline{H_4}$ were found as described in Chapter 4. $\overline{C_4}$ and $\frac{\Delta(U-R)}{\Delta logr}$ are taken from Peletier et al. (1990), and $\frac{\Delta log<Fe>}{\Delta logr}$ and $\frac{\Delta logMg_b}{\Delta logr}$, from González (1993).

7.4 Final Discussion

Interpreting these results together, they suggest different evolutionary histories for the different galaxy "types". Galaxies of the adopted "type 1" appear to have formed in a homogeneous dissipational collapse. This is consistent with the traditionally accepted picture of elliptical galaxy formation and is less in favour of formation as the result of merging. For galaxies of "type 2", a less homogeneous formation is more likely, involving dissipationless interaction and subsequent violent relaxation. The detection of metallicity gradients for all galaxies however suggests that their formation has involved some degree of dissipation. Age gradients detected for some galaxies of our sample with the galaxy centre being younger that the outer parts, represent strong evidence for recent star formation which is likely to be associated with a separate disky component.

Bibliography

Arimoto, N. and Yoshii, Y. (1987). *AA*, 173:23.

Baade, W. (1944a). *ApJ*, 100:137.

Baade, W. (1944b). *ApJ*, 100:147.

Baggley, G. (1996). *Peculiar Velocities of Clusters Determined from Early-Type Galaxies.* PhD thesis, St Johns College, Oxford.

Balcells, M. and Quinn, P. J. (1990). *ApJ*, 361:381.

Barnes, J. (1992). *ApJ*, 393:484.

Bender, R. (1990). *AA*, 229:441.

Bender, R., Burstein, D., and Faber, S. M. (1992). *ApJ*, 399:462.

Bender, R., Burstein, D., and Faber, S. M. (1993). *ApJ*, 411:153.

Bender, R., Saglia, R. P., and Gerhard, O. E. (1994). *MNRAS*, 269:785.

Bender, R., Surma, P., Döbereiner, S., Möllenhoff, C., and Madejsky, R. (1989). *AA*, 217:35.

Bertola, F. and Capaccioli, M. (1975). *ApJ*, 200:439.

Bingelli, B., Taummann, G., and Sandage, A. (1985). *AJ*, 90:1681.

Binney, J. (1978). *MNRAS*, 183:501.

Binney, J. and Mamon, G. A. (1982). *MNRAS*, 200:361.

Binney, J. and Petrou, M. (1985). *MNRAS*, 214:449.

Boroson, T. A. and Thompson, I. B. (1991). *AJ*, 101:111.

Bower, R. G., Kodama, T., and Terlevich, A. (1998). *astro-ph/9805290.*

Bower, R. G., Lucey, J. R., and Ellis, R. S. (1992). *MNRAS*, 254:601.

Brault, J. W. and White, O. R. (1971). *AA*, 13:169.

Bruzual, G. and Charlot, S. (1993). *ApJ*, 405:538.

Burstein, D., Davies, R. L., Dressler, A., Faber, S. M., Lynden-Bell, D., Terlevich, R., and Wegner, G. (1988). In Kron, R. G. and Renzini, A., editors, *Towards Understanding Galaxies at Large Redshifts*, page 17, Dordrecht. Kluwer.

Burstein, D., Faber, S. M., Gaskell, C. M., and Krumm, N. (1984). *ApJ*, 287:586.

Carollo, C. M., Danziger, I. J., and Buson, L. (1993). *MNRAS*, 265:553.

Carollo, C. M., Franx, M., Illingworth, G. D., and Forbes, D. A. (1997). *ApJ*, 481:710.

Carrasco, L., Buzzoni, A., Salsa, M., and Recillas-Cruz, E. (1996). In Buzzoni, A., Renzini, A., and Serrano, A., editors, *Fresh Views of Elliptical Galaxies*, volume 86 of *ASP Conf. Ser.*, page 235, San Francisco.

Cole, S., Aragón-Salamanca, A., Frenk, C. S., Navarro, J. F., and Zepf, S. E. (1994). *MNRAS*, 271:781.

Colless, M. M., Burstein, D., Davies, R. L., McMahan, R. K., Saglia, R. P., and Wegner, G. (1998). *MNRAS*, submitted.

Davies, R. L. and Birkinshaw, M. (1988). *ApJS*, 68:409.

Davies, R. L., Burstein, D., Dressler, A., Faber, S. M., Lynden-Bell, D., Terlevich, R., and Wegner, G. (1987). *ApJS*, 64:581.

Davies, R. L., Efstathiou, G., Fall, S. M., Illingworth, G., and Schechter, P. L. (1983). *ApJ*, 266:41.

Davies, R. L., Sadler, E. M., and Peletier, R. F. (1993). *MNRAS*, 262:650.

de Jong, R. S. and Davies, R. L. (1997). *MNRAS*, 285:1L.

de Vaucouleurs, G. (1961). *ApJS*, 5:233.

de Vaucouleurs, G., de Vaucouleurs, A., Corwin, H. G. J., Buta, R. J., Paturel, G., and Fouqué, P. (1991). *Third Reference Catalogue of Bright Galaxies*. Springer Verlag.

de Zeeuw, P. T. (1997). In Arnaboldi, M., Costa, G. S. D., and Saha, P., editors, *The Nature of Elliptical Galaxies*, Second Stromlo Symposium. Am. Inst. Phys.

Dressler, A. and Richstone, D. O. (1988). *ApJ*, 324:701.

Efstathiou, G., Ellis, R. S., and Carter, D. (1982). *MNRAS*, 201:975.

Faber, S. M., Friel, E. D., Burstein, D., and Gaskell, C. M. (1985). *ApJS*, 57:711.

Fisher, D., Franx, M., and Illingworth, G. (1995). *ApJ*, 448:119.

Fisher, D., Franx, M., and Illingworth, G. (1996). *ApJ*, 459:110.

Forbes, D. A., Franx, M., and Illingworth, G. D. (1995). *AJ*, 109:1988.

Franx, M. and Illingworth, G. (1988). *ApJ*, 327:55L.

Franx, M., Illingworth, G., and Heckman, T. (1989). *ApJ*, 344:613.

Gerhard, O. (1993). *MNRAS*, 265:213.

Gerhard, O., Jeske, G., Saglia, R. P., and Bender, R. (1998). *MNRAS*, 295:197.

Gerhard, O. E. (1991). *MNRAS*, 250:812.

González, J. J. (1993). *Line Strength Gradients and Kinematic Profiles in Elliptical Galaxies.* PhD thesis, University of California.

Gorgas, J., Efstathiou, G., and Salamanca, A. A. (1990). *MNRAS*, 245:217.

Gorgas, J., Faber, S. M., Burstein, D., González, J. J., Courteau, S., and Prosser, C. (1993). *ApJS*, 86:153.

Graham, A. W. M. (1997). *Elliptical Galaxies: Structure, Dynamics and Applications.* PhD thesis, Australian National University.

Hau, G. K. T. and Thomson, R. C. (1994). *MNRAS*, 270:23L.

Hubble, E. (1936). *The Realm of the Nebulae.* Yale University Press, New Haven.

Illingworth, G. D. (1977). *ApJ*, 218:43L.

Jedrzejewski, R. I. and Schechter, P. L. (1988). *ApJL*, 330:87.

Kauffmann, G. (1996). *MNRAS*, 281:487.

Kodama, T. and Arimoto, N. (1997). *AA*, 320:41.

Kormendy, J. (1984). *ApJ*, 287:577.

Kormendy, J., Bender, R., Evans, A. S., and Richstone, D. (1998). *AJ*, 115:1823.

Kuijken, K. and Merrifield, M. (1998). *MNRAS*, 295:29L.

Kuntschner, H. and Davies, R. L. (1998). *MNRAS*, 295:29L.

Larson, R. B. (1969). *MNRAS*, 145:405.

Larson, R. B. (1974a). *MNRAS*, 166:585.

Larson, R. B. (1974b). *MNRAS*, 169:229.

Larson, R. B. (1975). *MNRAS*, 173:671.

Lauer, T. R., Ajhar, E. A., Byun, Y.-I., Dressler, A., Faber, S. M., Grillmair, C., Kormendy, J., Richstone, D., and Tremaine, S. (1995). *AJ*, 110:2622.

Mehlert, D. (1998). *Elliptische Galaxien in hoder Umgebungsdichte: Der Coma-Galaxienhaufen.* PhD thesis, Ludwig-Maximilian-Universität.

Nieto, J. L. and Bender, R. (1990). *AA*, 239:97.

Nieto, J.-L., Bender, R., and Surma, P. (1991). *AA*, 244:L37.

O'Connell, R. W. (1980). *ApJ*, 236:430.

Osterbrock, D. E. (1995). In Kruit, P. C. V. D. and Gilmore, G., editors, *Stellar Populations*, volume 164 of *IAU Symp.*, page 21, Dordrecht. Kluwer.

Peletier, R. F. (1989). *Elliptical Galaxies: Structure and Stellar Content.* PhD thesis, University of Groningen, Groningen.

Peletier, R. F., Davies, R. L., Illingworth, G. D., Davis, L. E., and Cawson, M. (1990). *AJ*, 100:1091.

Prugniel, P., Nieto, J.-L., and Simien, F. (1987). *AA*, 173:49.

Rix, H. W., de Zeeuw, P. T., Cretton, N., van der Marel, R. P., and Carollo, C. M. (1997). *ApJ*, 488:702.

Rix, H. W. and White, S. D. M. (1990). *ApJ*, 362:52.

Rix, H. W. and White, S. D. M. (1992). *MNRAS*, 254:389.

Sandage, A. and Tammann, G. A. (1987). *A Revised Shapley-Ames Catalog of Bright Galaxies*. Carnegie Institute of Washington.

Sansom, A. E. and Proctor, R. N. (1998). *MNRAS*, 297:953.

Sargent, W. L. W., Schechter, P. L., Boksenberg, A., and Shortridge, K. (1977). *ApJ*, 212:326.

Schweizer, F. (1998). In Friedli, D., Martinet, L., and Pfenniger, D., editors, *Galaxies: Interactions and Induced Star Formation*, volume 26 of *Saas-Fee Advanced Course*, page 105, Swiss Society for Astrophysics and Astronomy. Springer.

Scorza, C. and Bender, R. (1995). *AA*, 293:20.

Scorza, C. and van den Bosch, F. C. (1998). *astro-ph/9806078*.

Simkin, S. (1974). *AA*.

Statler, T. (1991). *AJ*, 102:882.

Thomas, D., Greggio, L., and Bender, R. (1998). *MNRAS*, submitted.

Thomsen, B. (1989). *ApJ*, 347:214.

Tonry, J. and Davis, M. (1979). *AJ*, 84:1511.

Trager, S. C., Worthey, G., Faber, S. M., Burstein, D., and González, J. J. (1998). *ApJS*, 116:1.

van den Bosch, F. C., Ferrarese, L., Jaffe, W., Ford, H. C., and O'Connell, R. W. (1994). *AJ*, 108:1579.

van der Marel, R. P. and Franx, M. (1993). *ApJ*, 407:525.

van der Marel, R. P., Rix, H. W., Carter, D., Franx, M., White, S. D. M., and de Zeeuw, P. T. (1994). *MNRAS*, 268:521.

van Dokkum, P. G. and Franx, M. (1995). *AJ*, 110:2027.

Wegner, G., Colless, M. M., Saglia, R. P., McMahan, R. K., Davies, R. L., Burstein, D., and Baggley, G. (1998). *MNRAS*, submitted.

Weiss, A., Peletier, R. F., and Matteucci, F. (1995). *AA*, 296:73.

Whipple, F. L. (1935). *Harv. Coll. Obs. Circ.*, 404:1.

Worthey, G. (1992). *The Controlling Parameters Of The Integrated Flux of a Stellar Population*. PhD thesis, University of California, Santa Cruz.

Worthey, G. (1994). *ApJS*, 95:107.

Worthey, G., Faber, S. M., and González, J. J. (1992). *ApJ*, 398:69.

Worthey, G., Faber, S. M., González, J. J., and Burstein, D. (1994). *ApJS*, 94:687 (Paper V).

Worthey, G. and Ottaviani, D. L. (1997). *ApJS*, 111:377.

Zhao, H. S. and Prada, F. (1996). *MNRAS*, 282:1223.

Ziegler, B. L. and Bender, R. (1997). *MNRAS*, 291:527.

Appendix A

Measurements of Kinematics: S/N=60 per Å

Measurements of kinematics obtained as described in chapter 3 and presented in chapter 4, are given. Measurements of rotation (v) and velocity dispersion (σ) are given in km s^{-1} and radius (r) in arcseconds. Negative radii correspond to measurements towards the East. Values of rotation given are actual measurements obtained using the FCQ method (i.e. version as of December 1995); these represent the relative measured velocity between the stellar template and the galaxy spectra.

Table A.1: NGC 2778 major

r	v	δv	σ	$\delta\sigma$	H_4	δH_4	H_3	δH_3
-20.98	2127.7	12.9	80.9	14.6	0.030	0.098	-0.051	0.105
-7.29	2108.8	3.7	87.2	4.4	0.029	0.038	-0.166	0.031
-4.10	2076.3	2.0	115.4	2.8	0.008	0.019	-0.054	0.019
-2.65	2052.7	1.5	139.7	2.2	-0.003	0.013	-0.048	0.012
-1.80	2036.9	1.1	153.2	1.5	-0.012	0.008	-0.034	0.008
-1.20	2026.0	1.0	160.2	1.2	-0.012	0.006	-0.025	0.006
-0.60	2015.4	0.8	165.7	0.9	-0.008	0.005	-0.013	0.004
0.00	2004.7	0.8	168.7	0.9	-0.006	0.005	0.000	0.004
0.60	1994.3	0.9	169.2	1.0	-0.004	0.005	0.016	0.005
1.20	1983.8	1.0	166.8	1.1	-0.002	0.006	0.035	0.006
1.80	1973.1	0.9	161.0	1.1	0.002	0.006	0.055	0.006
2.66	1956.6	1.0	146.7	1.3	0.014	0.008	0.078	0.007
4.10	1932.9	1.8	119.0	2.2	0.019	0.017	0.078	0.016
7.51	1905.1	2.0	94.1	3.3	0.102	0.020	0.041	0.018
21.18	1909.0	13.3	54.6	16.4	-0.110	0.186	-0.254	0.159

Table A.2: NGC 2778 minor

r	v	δv	σ	$\delta\sigma$	H_4	δH_4	H_3	δH_3
-15.74	2024.5	84.5	78.6	15.8	-0.069	0.133	-0.020	0.106
-4.27	2031.2	2.0	130.0	2.4	-0.028	0.017	0.019	0.014
-2.64	2035.6	1.4	151.3	1.5	-0.017	0.011	0.002	0.008
-1.79	2036.8	0.8	160.0	0.8	-0.011	0.005	0.000	0.004
-1.19	2037.4	0.8	164.2	0.7	-0.009	0.005	0.001	0.004
-0.59	2038.3	0.7	166.8	0.7	-0.008	0.005	0.002	0.003
0.01	2039.5	0.6	167.8	0.6	-0.006	0.004	0.003	0.003
0.61	2041.0	0.6	167.3	0.6	-0.004	0.004	0.004	0.003
1.21	2042.7	0.6	165.0	0.6	0.001	0.004	0.004	0.003
1.81	2044.4	0.6	160.8	0.7	0.010	0.004	0.003	0.003
2.66	2045.9	1.1	150.5	1.4	0.031	0.008	-0.002	0.006
4.29	2046.3	1.3	121.5	2.3	0.063	0.011	-0.012	0.010
14.21	2042.4	13.3	93.9	9.9	-0.138	0.128	0.291	0.102

Table A.3: NGC 3377 major

r	v	δv	σ	$\delta\sigma$	H_4	δH_4	H_3	δH_3
-36.53	579.1	15.0	61.7	17.0	-1.679	0.227	0.343	0.229
-18.95	578.1	3.6	69.3	10.0	-0.108	0.073	0.080	0.046
-10.60	582.1	1.8	62.1	3.0	-0.003	0.033	0.174	0.026
-7.17	577.5	1.0	65.2	0.6	-0.335	0.017	0.097	0.011
-5.10	569.3	1.7	76.9	2.0	-0.043	0.034	0.124	0.022
-3.64	569.0	1.3	83.9	1.4	-0.046	0.022	0.135	0.014
-2.77	578.7	1.7	93.7	2.2	-0.016	0.023	0.087	0.015
-2.17	581.9	1.7	97.2	2.2	-0.027	0.021	0.112	0.014
-1.57	589.3	1.1	104.1	1.5	0.021	0.011	0.182	0.008
-0.97	617.4	1.5	132.1	2.5	0.001	0.013	0.114	0.011
-0.37	650.5	1.2	152.7	2.2	0.002	0.011	0.058	0.010
0.23	689.1	1.0	156.0	1.8	-0.016	0.010	-0.024	0.010
0.83	730.6	1.2	139.8	1.8	0.012	0.011	-0.098	0.010
1.43	754.7	1.0	126.5	1.6	-0.004	0.010	-0.092	0.008
2.03	772.1	1.5	107.3	2.6	-0.005	0.017	-0.113	0.011
2.63	778.6	1.4	93.9	2.4	0.021	0.019	-0.094	0.012
3.50	781.9	1.8	91.3	2.7	0.004	0.026	-0.099	0.016
4.97	787.6	2.2	87.6	3.0	-0.002	0.032	-0.107	0.020
7.05	781.8	1.9	83.2	2.7	0.011	0.026	-0.180	0.017
10.26	775.3	2.2	75.9	3.7	0.059	0.033	-0.145	0.023
17.33	794.3	6.2	18.4	9.5	0.207	0.174	-0.358	0.159
33.76	767.2	46.2	116.8	20.3	0.045	0.104	-0.021	0.089

Table A.4: NGC 3377 minor

r	v	δv	σ	$\delta\sigma$	H_4	δH_4	H_3	δH_3
-19.82	667.5	124.1	76.9	18.5	0.035	0.133	0.208	0.123
-6.15	661.8	2.8	90.2	5.3	0.081	0.041	0.050	0.027
-2.96	672.0	2.6	105.2	4.5	0.016	0.030	0.033	0.021
-1.89	677.7	2.1	123.6	3.7	0.015	0.020	0.001	0.016
-1.29	684.2	1.9	144.5	3.5	-0.014	0.019	0.002	0.017
-0.69	683.2	1.6	149.6	3.0	0.008	0.016	-0.012	0.014
-0.09	685.4	1.1	160.6	2.0	-0.011	0.011	-0.016	0.010
0.51	681.3	1.3	157.0	2.5	-0.013	0.013	0.009	0.012
1.11	679.8	1.3	144.6	2.7	0.026	0.013	0.023	0.011
1.71	681.9	2.4	129.7	4.3	-0.009	0.024	-0.024	0.020
2.55	680.3	2.1	116.6	3.6	-0.018	0.021	-0.024	0.016
4.47	667.7	1.8	91.0	2.3	-0.022	0.026	0.059	0.017
16.57	678.4	28.8	107.5	22.6	0.127	0.122	0.170	0.123

Table A.5: NGC 3379 major

r	v	δv	σ	$\delta\sigma$	H_4	δH_4	H_3	δH_3
-23.63	843.5	73.8	157.0	9.6	-0.324	0.087	-0.017	0.089
-7.75	868.6	2.1	188.4	3.6	-0.040	0.018	0.005	0.018
-3.77	871.3	2.5	209.5	3.6	-0.012	0.017	0.010	0.015
-2.07	885.5	2.8	217.4	4.2	0.029	0.018	0.041	0.015
-0.88	906.1	2.0	224.5	2.8	-0.002	0.013	0.031	0.010
0.29	915.9	2.1	221.1	2.9	0.001	0.014	0.022	0.011
1.47	934.0	1.7	206.9	2.5	-0.024	0.012	0.005	0.011
2.92	953.7	3.1	209.5	4.5	0.029	0.021	-0.041	0.019
5.45	933.7	2.8	198.4	4.1	0.020	0.020	-0.046	0.019
18.06	968.5	11.2	144.5	18.1	0.031	0.082	-0.117	0.075

Table A.6: NGC 3379 minor

r	v	δv	σ	$\delta\sigma$	H_4	δH_4	H_3	δH_3
-26.58	953.7	9.5	146.3	18.0	-0.047	0.079	-0.034	0.085
-8.60	914.6	2.2	178.6	4.1	0.045	0.018	0.004	0.017
-3.73	911.6	2.1	196.5	3.7	0.055	0.015	0.006	0.015
-2.04	909.4	2.8	214.6	3.9	0.004	0.018	-0.021	0.016
-0.85	905.7	2.1	226.1	2.9	0.026	0.013	0.013	0.010
0.31	908.2	1.5	231.7	1.9	-0.016	0.009	0.015	0.007
1.49	915.9	1.8	218.2	2.4	-0.012	0.012	-0.002	0.010
2.94	916.1	1.8	206.6	2.8	0.024	0.013	-0.006	0.012
5.69	916.5	2.0	188.5	3.3	0.015	0.016	-0.023	0.015
18.03	923.1	11.8	151.5	21.0	0.094	0.092	-0.064	0.082

Table A.7: NGC 3605 major

r	v	δv	σ	$\delta\sigma$	H_4	δH_4	H_3	δH_3
-17.05	631.6	14.0	49.3	10.9	0.246	0.058	0.309	0.174
-6.66	658.9	1.3	71.0	1.3	0.010	0.021	-0.054	0.016
-4.10	661.8	1.1	86.6	1.1	-0.002	0.010	0.032	0.012
-2.65	665.3	0.7	90.7	0.8	-0.005	0.006	0.039	0.008
-1.80	671.1	0.6	91.8	0.7	0.001	0.005	0.030	0.007
-1.20	677.3	0.6	91.9	0.6	0.005	0.005	0.021	0.006
-0.60	684.7	0.5	91.5	0.5	0.004	0.004	0.009	0.005
0.00	692.9	0.4	90.8	0.5	0.000	0.004	-0.004	0.005
0.61	701.5	0.4	90.1	0.4	-0.004	0.003	-0.018	0.004
1.21	709.9	0.3	89.5	0.4	-0.004	0.003	-0.033	0.004
1.81	717.7	0.4	89.0	0.5	-0.001	0.003	-0.046	0.005
2.66	726.0	0.6	88.7	0.7	0.000	0.005	-0.056	0.007
4.11	730.7	0.8	87.6	0.9	-0.001	0.007	-0.045	0.009
6.68	732.2	1.4	79.4	1.4	0.010	0.016	0.024	0.016
15.86	743.3	9.9	42.4	10.1	-0.055	0.173	0.312	0.189

Table A.8: NGC 3605 minor

r	v	δv	σ	$\delta\sigma$	H_4	δH_4	H_3	δH_3
-8.79	649.6	6.5	68.5	5.7	-0.093	0.084	0.162	0.070
-3.49	657.1	0.8	85.7	0.9	0.018	0.008	0.000	0.009
-2.08	657.0	0.6	87.3	0.7	0.017	0.005	-0.004	0.007
-1.21	658.2	0.5	88.2	0.5	0.015	0.004	-0.005	0.005
-0.61	659.5	0.4	88.8	0.5	0.014	0.003	-0.005	0.004
-0.01	661.1	0.4	89.5	0.4	0.012	0.003	-0.004	0.004
0.59	662.9	0.3	90.3	0.4	0.010	0.003	-0.002	0.004
1.19	664.8	0.5	91.4	0.6	0.009	0.004	0.001	0.006
2.06	667.0	0.7	92.7	0.8	0.005	0.005	0.006	0.007
3.25	668.2	1.0	93.3	1.1	-0.003	0.008	0.016	0.011
5.61	665.5	1.2	81.3	1.2	-0.038	0.013	0.053	0.014
15.06	624.8	521.1	91.7	17.2	0.014	0.107	0.012	0.104

Table A.9: NGC 3608 major

r	v	δv	σ	$\delta\sigma$	H_4	δH_4	H_3	δH_3
-40.23	1175.5	586.9	121.8	30.1	-0.024	0.130	-0.014	0.134
-20.83	1191.8	5.2	147.5	6.3	0.019	0.036	0.046	0.036
-11.44	1231.0	3.0	147.2	4.3	0.052	0.021	-0.017	0.021
-8.02	1248.6	1.7	156.2	2.4	0.032	0.012	-0.053	0.011
-5.94	1252.8	1.4	158.1	2.0	0.030	0.010	-0.036	0.009
-4.47	1255.0	1.3	166.4	1.8	0.042	0.008	-0.019	0.008
-3.61	1255.8	1.0	176.6	1.4	0.032	0.006	-0.012	0.006

Table A.9: NGC 3608 major

r	v	δv	σ	$\delta\sigma$	H_4	δH_4	H_3	δH_3
-3.01	1255.0	0.8	183.6	1.1	0.021	0.005	-0.008	0.004
-2.41	1253.3	0.7	189.6	0.9	0.011	0.004	-0.003	0.003
-1.81	1250.7	0.7	194.3	0.9	0.003	0.004	0.003	0.003
-1.21	1247.6	0.6	198.0	0.7	-0.003	0.003	0.010	0.003
-0.61	1244.2	0.6	200.6	0.7	-0.006	0.003	0.019	0.003
-0.01	1240.6	0.6	201.6	0.8	-0.006	0.003	0.026	0.003
0.59	1236.9	0.6	201.2	0.8	-0.004	0.003	0.032	0.003
1.19	1233.5	0.6	199.1	0.8	0.000	0.003	0.035	0.003
1.79	1230.6	0.8	195.3	0.9	0.005	0.004	0.036	0.004
2.39	1228.4	0.7	190.1	0.9	0.009	0.004	0.033	0.004
2.99	1227.0	0.8	183.9	1.0	0.009	0.005	0.029	0.004
3.59	1226.2	1.0	177.8	1.2	0.006	0.006	0.026	0.005
4.46	1225.4	1.3	170.7	1.5	-0.002	0.008	0.024	0.007
5.93	1223.2	1.4	163.8	1.5	-0.010	0.008	0.033	0.008
8.01	1224.6	2.0	162.4	2.3	-0.002	0.013	0.055	0.013
11.43	1231.8	2.4	149.3	2.6	-0.017	0.016	0.097	0.017
22.81	1242.0	5.1	127.8	5.7	0.003	0.037	0.117	0.041
45.99	1158.2	28.2	68.8	20.0	-1.060	0.727	-0.150	0.653

Table A.10: NGC 3608 minor

r	v	δv	σ	$\delta\sigma$	H_4	δH_4	H_3	δH_3
-34.47	1153.5	20.3	70.9	25.4	0.051	0.171	-0.039	0.171
-15.40	1184.3	4.2	118.5	6.1	0.084	0.040	0.011	0.039
-8.46	1176.0	2.4	134.9	3.7	0.012	0.022	-0.002	0.021
-5.90	1180.0	1.5	156.7	2.3	0.028	0.010	-0.032	0.010
-4.43	1176.9	1.3	174.0	1.8	0.024	0.008	-0.026	0.007
-3.57	1173.7	1.1	184.5	1.4	0.022	0.006	-0.010	0.005
-2.97	1172.0	0.9	189.9	1.1	0.022	0.005	-0.002	0.004
-2.37	1171.2	0.8	194.8	1.0	0.024	0.005	0.005	0.004
-1.77	1171.1	0.6	197.8	0.7	0.022	0.003	0.010	0.003
-1.17	1171.4	0.6	199.5	0.7	0.018	0.003	0.015	0.002
-0.57	1172.0	0.6	200.0	0.6	0.014	0.003	0.019	0.002
0.03	1172.6	0.6	199.5	0.6	0.009	0.003	0.023	0.002
0.63	1173.0	0.7	198.1	0.8	0.006	0.004	0.025	0.003
1.23	1173.1	0.7	195.7	0.8	0.006	0.004	0.025	0.003
1.83	1172.6	0.8	191.7	0.9	0.008	0.005	0.022	0.004
2.43	1171.6	0.8	186.8	0.9	0.016	0.005	0.016	0.004
3.03	1170.3	0.8	180.3	1.1	0.027	0.005	0.010	0.004
3.89	1169.0	1.1	169.4	1.5	0.042	0.007	0.007	0.006
5.35	1169.7	1.8	156.5	2.8	0.047	0.013	0.026	0.012
7.68	1171.8	2.1	148.3	3.3	0.030	0.017	0.002	0.015

Table A.10: NGC 3608 minor

r	v	δv	σ	$\delta\sigma$	H_4	δH_4	H_3	δH_3
12.77	1175.7	3.0	112.7	4.3	0.085	0.027	-0.074	0.026
29.65	1177.8	20.0	91.3	18.0	-0.020	0.105	0.235	0.103

Table A.11: NGC 4339 major

r	v	δv	σ	$\delta\sigma$	H_4	δH_4	H_3	δH_3
-27.77	1328.3	5.2	65.7	5.5	-0.065	0.081	-0.242	0.058
-9.01	1322.0	1.8	70.5	2.9	0.077	0.025	-0.148	0.017
-3.75	1298.5	1.8	99.3	2.1	0.029	0.020	-0.036	0.013
-2.05	1295.5	1.7	101.8	1.9	0.036	0.018	-0.059	0.012
-1.20	1287.4	0.8	110.4	1.0	0.050	0.008	-0.033	0.006
-0.60	1273.9	1.0	113.8	1.2	0.060	0.009	-0.001	0.007
0.00	1259.2	0.8	115.2	1.0	0.068	0.007	0.030	0.005
0.60	1247.1	0.9	112.7	1.2	0.088	0.008	0.043	0.006
1.20	1235.0	1.0	100.4	1.2	0.111	0.011	0.033	0.007
2.05	1224.3	1.2	98.5	1.5	0.111	0.013	0.031	0.008
3.75	1216.4	1.7	103.0	2.0	0.037	0.017	0.032	0.012
9.19	1200.0	1.6	78.4	2.5	0.181	0.021	0.072	0.012
28.07	1215.8	9.5	57.5	7.9	-0.135	0.158	0.175	0.147

Table A.12: NGC 4339 minor

r	v	δv	σ	$\delta\sigma$	H_4	δH_4	H_3	δH_3
-30.39	1264.6	409.4	75.9	23.6	0.343	0.243	-0.100	0.126
-9.53	1255.8	2.8	85.9	3.3	0.012	0.033	0.004	0.020
-3.75	1257.8	1.9	104.9	2.3	0.097	0.019	-0.018	0.013
-2.04	1257.4	2.2	110.5	2.7	0.095	0.021	-0.007	0.015
-1.20	1257.4	1.2	114.7	1.6	0.076	0.011	0.015	0.009
-0.60	1257.6	1.0	116.1	1.4	0.059	0.010	0.015	0.008
0.00	1259.1	0.9	118.9	1.2	0.064	0.008	0.006	0.007
0.60	1260.6	0.8	122.1	1.1	0.051	0.007	0.013	0.006
1.20	1261.4	1.0	115.1	1.3	0.067	0.009	0.036	0.007
2.05	1259.6	1.2	103.7	1.5	0.092	0.013	0.003	0.008
3.98	1265.8	2.2	100.5	2.6	0.135	0.024	0.039	0.015
15.55	1263.9	3.2	62.6	5.2	0.087	0.054	-0.085	0.044

Table A.13: NGC 4387 major

r	v	δv	σ	$\delta\sigma$	H_4	δH_4	H_3	δH_3
-26.33	494.9	6.8	42.0	6.7	0.085	0.128	-0.365	0.140
-12.51	500.9	1.8	69.1	2.4	0.111	0.023	0.004	0.022
-7.65	512.9	1.1	81.0	1.4	0.063	0.012	0.006	0.011

Table A.13: NGC 4387 major

r	v	δv	σ	$\delta\sigma$	H_4	δH_4	H_3	δH_3
-5.33	518.7	1.5	95.3	1.9	0.014	0.014	-0.001	0.012
-3.85	523.8	1.4	101.0	1.7	0.017	0.012	0.011	0.011
-2.65	532.7	0.8	100.7	1.0	0.015	0.006	0.014	0.006
-1.78	540.2	0.5	99.3	0.6	0.010	0.004	0.012	0.004
-1.18	545.1	0.4	98.2	0.5	0.007	0.004	0.010	0.004
-0.58	549.8	0.5	97.8	0.6	0.004	0.004	0.008	0.004
0.02	554.5	0.5	97.9	0.6	0.000	0.005	0.003	0.004
0.62	559.4	0.6	98.6	0.7	-0.005	0.005	-0.003	0.005
1.22	564.7	0.7	99.6	0.8	-0.009	0.006	-0.011	0.005
1.82	569.9	0.8	100.5	0.9	-0.010	0.006	-0.019	0.006
2.69	577.1	0.8	101.4	0.9	-0.003	0.007	-0.023	0.006
3.89	585.4	1.1	100.3	1.3	0.002	0.009	-0.014	0.008
5.37	592.6	1.3	95.0	1.6	-0.010	0.012	0.003	0.011
7.69	596.5	0.9	89.4	1.0	-0.022	0.009	0.031	0.008
12.55	604.0	2.1	74.6	2.5	0.017	0.028	0.049	0.025
26.00	614.5	13.0	55.2	10.8	-0.350	0.295	0.139	0.206

Table A.14: NGC 4387 minor

r	v	δv	σ	$\delta\sigma$	H_4	δH_4	H_3	δH_3
-15.15	548.6	5.1	77.6	6.9	0.121	0.056	0.003	0.051
-5.17	554.0	1.6	92.9	1.9	-0.003	0.015	-0.005	0.013
-3.27	554.6	1.2	101.0	1.4	-0.014	0.010	0.004	0.009
-2.07	554.8	0.8	99.5	0.9	-0.003	0.007	-0.003	0.006
-1.20	555.5	0.7	97.6	0.8	0.010	0.006	-0.003	0.006
-0.60	556.3	0.6	96.7	0.7	0.018	0.005	-0.001	0.005
0.00	557.5	0.5	96.3	0.6	0.024	0.004	0.002	0.004
0.60	558.9	0.5	96.6	0.6	0.030	0.004	0.004	0.004
1.20	560.5	0.6	97.7	0.8	0.033	0.005	0.007	0.005
2.06	562.4	0.8	100.2	1.0	0.031	0.007	0.007	0.006
3.26	564.2	1.3	101.3	1.6	0.028	0.011	0.001	0.010
5.16	565.6	1.8	88.0	2.3	0.078	0.016	0.007	0.015
14.34	561.0	9.3	45.4	8.7	-0.146	0.278	0.045	0.226

Table A.15: NGC 4458 major

r	v	δv	σ	$\delta\sigma$	H_4	δH_4	H_3	δH_3
-15.65	630.5	9.8	52.7	11.2	0.216	0.078	0.250	0.116
-4.22	641.9	2.3	80.3	2.1	-0.086	0.037	-0.037	0.026
-2.28	660.3	1.2	91.1	2.5	0.076	0.016	-0.026	0.011
-1.43	663.8	1.6	103.1	1.9	-0.071	0.017	-0.023	0.012
-0.83	661.8	1.6	109.3	2.4	-0.030	0.017	-0.055	0.013

Table A.15: NGC 4458 major

r	v	δv	σ	$\delta\sigma$	H_4	δH_4	H_3	δH_3
-0.23	645.9	1.4	119.0	2.1	-0.031	0.013	0.010	0.011
0.37	629.9	1.4	118.9	1.9	-0.030	0.012	0.056	0.010
0.97	614.0	1.6	111.0	2.4	-0.009	0.015	0.053	0.012
1.80	611.3	1.6	98.9	2.6	0.030	0.018	0.077	0.014
3.51	628.6	1.3	80.0	1.1	-0.120	0.022	0.057	0.015
8.45	640.2	1.9	66.5	3.6	0.101	0.031	0.083	0.027
25.43	644.2	16.4	71.3	9.8	-0.268	0.181	-0.044	0.236

Table A.16: NGC 4458 minor

r	v	δv	σ	$\delta\sigma$	H_4	δH_4	H_3	δH_3
-16.39	650.2	5.7	68.3	9.8	0.110	0.086	0.090	0.075
-4.17	642.6	1.7	75.3	2.5	0.024	0.029	0.025	0.022
-2.03	637.2	1.7	98.7	2.7	0.018	0.020	0.003	0.014
-1.20	642.7	1.6	110.7	2.2	-0.032	0.015	0.005	0.012
-0.60	640.7	1.4	110.1	1.8	-0.056	0.014	-0.001	0.010
0.00	643.7	1.2	116.8	1.7	-0.028	0.011	-0.007	0.009
0.60	641.0	2.0	114.5	2.9	-0.033	0.019	-0.009	0.015
1.20	644.0	2.0	118.3	2.6	-0.063	0.018	0.000	0.015
2.04	642.5	2.2	99.6	3.3	0.006	0.025	0.064	0.019
4.17	638.1	1.8	77.7	2.6	0.019	0.031	0.030	0.023
16.10	628.8	14.4	53.9	9.5	-0.279	0.338	0.198	0.331

Table A.17: NGC 4464 major

r	v	δv	σ	$\delta\sigma$	H_4	δH_4	H_3	δH_3
-20.36	1241.2	529.5	97.0	28.2	0.034	0.152	0.006	0.162
-8.20	1355.1	2.4	76.7	3.4	0.071	0.033	-0.170	0.029
-4.70	1365.1	1.8	84.5	2.9	0.072	0.022	-0.159	0.018
-3.24	1363.0	1.0	96.9	1.6	0.065	0.010	-0.150	0.008
-2.39	1354.2	1.0	107.5	1.5	0.048	0.009	-0.145	0.008
-1.79	1340.6	0.9	119.2	1.1	0.012	0.008	-0.120	0.006
-1.19	1322.4	0.9	131.0	1.0	-0.027	0.007	-0.073	0.006
-0.59	1303.9	0.7	138.7	0.8	-0.047	0.006	-0.021	0.005
0.01	1286.1	0.7	141.2	0.6	-0.049	0.006	0.027	0.004
0.61	1268.4	0.8	138.6	0.8	-0.039	0.006	0.065	0.005
1.21	1251.2	0.5	131.1	0.6	-0.023	0.005	0.094	0.004
1.81	1235.4	0.7	120.8	0.9	-0.005	0.006	0.116	0.005
2.41	1222.2	0.8	109.0	1.2	0.012	0.007	0.135	0.007
3.27	1210.9	1.3	96.2	2.2	0.037	0.013	0.150	0.012
4.96	1209.1	1.6	82.9	3.1	0.057	0.023	0.113	0.020
13.50	1221.1	3.5	47.5	5.0	-0.044	0.100	0.104	0.093

Table A.18: NGC 4464 minor

r	v	δv	σ	$\delta\sigma$	H_4	δH_4	H_3	δH_3
-13.66	1295.9	4.6	59.7	5.5	-0.087	0.111	0.027	0.087
-4.29	1284.8	1.1	84.5	1.7	0.020	0.016	-0.042	0.013
-2.64	1281.2	0.9	111.7	1.3	0.019	0.008	0.015	0.007
-1.80	1282.4	0.7	124.2	0.9	0.007	0.006	0.028	0.005
-1.20	1284.1	0.7	129.7	0.8	0.001	0.006	0.031	0.005
-0.60	1285.9	0.7	132.5	0.8	0.000	0.005	0.031	0.005
0.00	1287.7	0.6	133.0	0.7	0.002	0.005	0.030	0.004
0.60	1289.3	0.5	131.5	0.6	0.008	0.004	0.029	0.004
1.20	1290.5	0.5	128.0	0.6	0.017	0.004	0.027	0.003
1.80	1291.1	0.6	121.9	0.9	0.030	0.005	0.024	0.004
2.64	1291.7	0.8	107.9	1.3	0.057	0.007	0.015	0.007
4.29	1296.5	1.1	76.1	2.4	0.088	0.020	-0.032	0.017
13.32	1321.6	13.5	19.7	10.6	-0.195	0.154	0.082	0.174

Table A.19: NGC 4468 major

r	v	δv	σ	$\delta\sigma$	H_4	δH_4	H_3	δH_3
-14.11	956.0	5.6	19.2	6.0	0.427	0.120	-0.430	0.098
-2.47	930.7	1.3	33.1	2.1	-0.059	0.035	-0.008	0.046
-0.84	924.6	1.0	36.2	1.6	-0.067	0.039	-0.025	0.038
0.33	920.2	0.7	34.6	1.2	-0.043	0.026	0.042	0.027
1.74	915.4	1.2	31.7	1.8	-0.016	0.025	0.060	0.037
6.67	907.7	1.3	30.6	1.9	-0.060	0.027	-0.029	0.043
25.14	911.0	17.3	14.7	13.3	0.273	0.314	-0.222	0.281

Table A.20: NGC 4468 minor

r	v	δv	σ	$\delta\sigma$	H_4	δH_4	H_3	δH_3
-9.74	885.7	6.5	31.5	6.8	-0.141	0.104	-0.097	0.155
-1.13	899.8	2.4	32.8	3.5	-0.069	0.031	-0.006	0.050
0.56	899.4	2.5	32.5	3.5	-0.036	0.028	0.024	0.050
2.88	904.4	7.5	35.0	6.6	-0.230	0.113	0.035	0.129
14.72	900.3	8.0	58.3	10.3	0.042	0.100	-0.046	0.081

Table A.21: NGC 4478 major

r	v	δv	σ	$\delta\sigma$	H_4	δH_4	H_3	δH_3
-22.39	1399.7	3.9	64.3	6.2	-0.123	0.089	0.048	0.053
-11.10	1391.8	3.5	112.6	3.9	-0.100	0.030	0.039	0.027
-7.95	1399.0	2.5	140.3	3.0	-0.124	0.023	0.054	0.021
-5.88	1394.2	2.6	140.8	4.0	-0.032	0.025	-0.007	0.021
-4.40	1388.9	2.5	146.0	3.7	-0.032	0.024	-0.049	0.021

Table A.21: NGC 4478 major

r	v	δv	σ	$\delta\sigma$	H_4	δH_4	H_3	δH_3
-3.20	1384.2	1.5	142.9	2.0	-0.035	0.014	-0.132	0.012
-2.32	1384.3	2.3	141.1	3.4	0.009	0.022	-0.077	0.018
-1.72	1379.6	1.7	138.1	2.6	-0.020	0.016	-0.069	0.014
-1.12	1372.3	1.6	122.2	2.5	-0.010	0.015	-0.043	0.012
-0.52	1365.1	1.7	124.3	2.7	-0.004	0.016	-0.042	0.013
0.08	1344.5	1.1	126.3	2.0	0.040	0.010	-0.008	0.008
0.68	1324.9	1.7	123.7	2.9	0.041	0.016	0.039	0.013
1.28	1307.4	1.8	127.0	3.1	0.078	0.016	0.079	0.012
1.88	1294.4	2.0	119.1	3.6	0.113	0.019	0.077	0.014
2.48	1299.2	2.4	123.7	4.1	0.047	0.022	0.090	0.017
3.35	1308.6	2.0	138.8	3.2	0.000	0.018	0.039	0.015
4.55	1304.2	2.0	131.1	3.2	-0.008	0.018	0.066	0.015
6.03	1293.4	1.9	130.5	3.2	0.024	0.017	0.032	0.014
8.10	1305.2	3.2	124.2	4.1	-0.087	0.028	-0.020	0.025
11.27	1289.0	3.2	103.0	5.1	0.025	0.033	0.083	0.026
23.21	1282.9	4.8	69.8	2.6	-0.306	0.110	-0.037	0.051

Table A.22: NGC 4478 minor

r	v	δv	σ	$\delta\sigma$	H_4	δH_4	H_3	δH_3
-17.64	1332.6	5.2	84.5	4.4	-0.096	0.054	0.118	0.039
-7.52	1346.5	1.7	137.2	2.1	-0.045	0.013	0.047	0.013
-5.21	1355.7	2.1	140.7	3.0	-0.004	0.015	0.023	0.015
-3.74	1350.7	1.9	167.0	2.3	-0.071	0.011	-0.004	0.013
-2.53	1357.3	1.4	152.6	2.2	0.029	0.009	-0.006	0.010
-1.67	1358.7	1.4	139.0	1.9	-0.003	0.010	0.007	0.010
-1.07	1362.8	1.3	133.3	1.9	0.043	0.010	0.008	0.009
-0.47	1363.1	0.8	128.0	1.0	0.023	0.006	0.001	0.006
0.13	1370.7	0.9	125.6	1.1	0.027	0.007	-0.025	0.006
0.73	1368.8	0.9	129.1	1.1	0.027	0.007	-0.033	0.006
1.33	1365.2	0.9	135.4	1.1	-0.007	0.007	-0.018	0.007
1.93	1357.0	2.0	152.0	2.9	0.004	0.013	0.027	0.014
2.80	1364.3	2.0	163.9	3.0	0.007	0.011	0.060	0.013
4.27	1362.1	1.7	147.1	2.5	0.024	0.011	0.031	0.012
6.34	1369.1	2.7	145.3	3.4	-0.051	0.020	0.013	0.021
10.14	1364.5	2.0	117.6	2.1	-0.073	0.019	0.024	0.016
22.83	1342.5	3.4	70.3	3.6	-0.068	0.055	-0.016	0.043

Table A.23: NGC 4551 major

r	v	δv	σ	$\delta\sigma$	H_4	δH_4	H_3	δH_3
-20.56	1161.7	3.6	59.6	6.3	0.168	0.066	-0.054	0.056
-7.86	1157.4	1.5	91.8	2.4	0.009	0.025	0.040	0.017
-4.45	1160.6	0.7	90.5	0.7	-0.045	0.011	0.053	0.007
-2.73	1159.7	1.4	101.2	1.4	-0.040	0.017	0.032	0.013
-1.53	1168.1	1.0	96.6	1.1	-0.024	0.014	0.075	0.010
-0.66	1176.9	1.5	99.7	1.6	-0.029	0.019	0.055	0.014
-0.06	1190.5	1.1	103.5	1.2	-0.017	0.013	0.020	0.010
0.54	1204.3	0.8	95.6	1.2	0.013	0.012	-0.016	0.009
1.41	1215.9	0.8	92.4	1.5	0.036	0.014	-0.077	0.010
2.61	1230.3	0.7	86.6	1.0	-0.027	0.015	-0.109	0.010
4.33	1229.2	1.0	90.3	1.2	-0.025	0.017	-0.018	0.012
7.50	1240.6	1.1	85.5	1.2	-0.058	0.021	-0.009	0.014
19.00	1250.6	3.7	71.7	7.5	0.014	0.109	-0.079	0.063

Table A.24: NGC 4551 minor

r	v	δv	σ	$\delta\sigma$	H_4	δH_4	H_3	δH_3
-18.19	1191.1	3.8	60.0	7.0	0.058	0.080	0.118	0.047
-6.11	1196.2	1.1	84.2	2.1	0.022	0.021	0.019	0.014
-3.13	1199.8	1.5	103.5	1.6	-0.023	0.018	-0.032	0.014
-1.67	1197.5	1.3	99.8	2.0	0.029	0.018	0.003	0.013
-0.82	1197.4	1.4	102.7	2.0	0.020	0.018	-0.004	0.014
-0.22	1197.4	1.2	97.4	1.4	-0.008	0.016	0.015	0.012
0.38	1198.4	1.0	96.6	1.3	0.010	0.013	0.033	0.010
0.98	1204.7	1.8	100.1	2.2	-0.004	0.024	0.008	0.018
1.84	1202.7	1.9	102.9	2.2	-0.011	0.023	-0.006	0.018
3.30	1206.5	1.3	94.6	1.6	-0.018	0.021	-0.061	0.015
6.47	1197.2	1.8	92.0	2.3	-0.022	0.029	0.081	0.019
19.37	1211.5	6.1	73.7	10.4	0.081	0.113	-0.040	0.107

Table A.25: NGC 4564 major

r	v	δv	σ	$\delta\sigma$	H_4	δH_4	H_3	δH_3
-35.76	1027.6	3.2	65.8	6.8	0.064	0.067	0.177	0.063
-21.33	1028.0	1.9	77.6	2.1	-0.061	0.031	0.164	0.025
-16.07	1013.6	1.7	70.3	2.2	0.015	0.030	0.261	0.023
-12.52	1031.5	1.8	90.6	1.9	-0.050	0.019	0.122	0.018
-9.83	1048.3	1.3	102.0	1.5	-0.027	0.010	0.049	0.011
-7.74	1065.3	1.6	112.4	1.9	-0.001	0.011	0.032	0.013
-6.26	1079.7	1.1	119.7	1.3	-0.009	0.008	0.004	0.009
-5.06	1088.1	0.9	129.6	1.0	-0.018	0.007	0.003	0.007
-4.18	1094.0	0.8	138.7	0.8	-0.022	0.005	0.017	0.005

Table A.25: NGC 4564 major

r	v	δv	σ	$\delta\sigma$	H_4	δH_4	H_3	δH_3
-3.58	1100.1	0.6	145.9	0.7	-0.018	0.004	0.028	0.004
-2.98	1108.7	0.8	154.2	0.7	-0.011	0.005	0.035	0.004
-2.38	1119.8	0.7	162.4	0.6	-0.005	0.004	0.037	0.004
-1.78	1132.6	0.6	169.5	0.6	-0.003	0.003	0.034	0.003
-1.18	1145.8	0.5	174.3	0.4	-0.004	0.002	0.027	0.002
-0.58	1159.3	0.4	177.0	0.4	-0.005	0.002	0.019	0.002
0.02	1172.7	0.4	177.4	0.4	-0.006	0.002	0.010	0.002
0.62	1186.0	0.4	175.8	0.4	-0.006	0.002	0.001	0.002
1.22	1199.4	0.4	172.4	0.4	-0.005	0.002	-0.005	0.002
1.82	1212.3	0.4	167.1	0.4	-0.003	0.002	-0.009	0.002
2.42	1224.0	0.5	160.4	0.5	-0.002	0.003	-0.008	0.003
3.02	1233.7	0.6	152.9	0.6	-0.002	0.004	-0.006	0.004
3.62	1240.9	0.7	145.1	0.8	-0.007	0.004	-0.006	0.004
4.22	1246.4	0.8	138.0	0.9	-0.012	0.006	-0.010	0.006
5.09	1253.5	0.8	128.6	0.9	-0.016	0.006	-0.022	0.006
6.30	1264.0	1.5	118.6	1.6	-0.019	0.011	-0.034	0.011
7.78	1274.9	2.3	110.0	2.4	-0.034	0.016	-0.041	0.018
9.86	1293.4	1.9	98.1	2.1	-0.028	0.015	-0.096	0.014
12.56	1310.9	2.0	86.5	2.9	0.016	0.020	-0.126	0.017
16.10	1313.4	3.1	83.9	3.8	-0.010	0.031	-0.156	0.025
21.59	1319.9	2.6	66.6	4.0	0.004	0.051	-0.204	0.038
36.38	1291.0	5.4	71.1	9.0	0.068	0.074	-0.009	0.059

Table A.26: NGC 4564 minor

r	v	δv	σ	$\delta\sigma$	H_4	δH_4	H_3	δH_3
-22.00	1156.5	10.7	77.8	13.8	0.084	0.094	-0.113	0.089
-8.88	1134.8	2.0	85.1	3.1	0.034	0.025	0.045	0.019
-5.93	1132.7	1.2	104.2	1.8	0.030	0.012	0.077	0.009
-4.47	1135.5	1.2	122.8	1.7	0.016	0.011	0.023	0.010
-3.61	1136.5	1.2	136.1	1.6	0.017	0.009	0.002	0.008
-3.01	1136.9	1.1	146.7	1.5	0.024	0.008	0.001	0.006
-2.41	1137.0	1.0	156.6	1.2	0.023	0.006	0.005	0.005
-1.81	1137.2	0.8	164.6	1.0	0.018	0.005	0.009	0.003
-1.21	1137.9	0.8	170.0	0.9	0.012	0.004	0.009	0.003
-0.61	1138.9	0.7	173.1	0.8	0.007	0.004	0.008	0.002
-0.01	1140.4	0.5	174.4	0.6	0.004	0.003	0.005	0.002
0.59	1142.1	0.5	174.0	0.5	0.004	0.003	0.001	0.002
1.19	1143.8	0.5	171.3	0.5	0.007	0.003	-0.003	0.002
1.79	1145.4	0.7	165.8	0.8	0.013	0.004	-0.006	0.003
2.39	1146.7	0.7	157.2	0.9	0.021	0.005	-0.006	0.003
2.99	1147.3	0.8	145.9	1.1	0.027	0.006	-0.004	0.004
3.59	1147.2	0.8	134.0	1.2	0.035	0.006	-0.004	0.006

Table A.26: NGC 4564 minor

r	v	δv	σ	$\delta\sigma$	H_4	δH_4	H_3	δH_3
4.45	1146.1	1.1	118.8	1.7	0.054	0.009	-0.008	0.009
5.91	1144.0	1.5	100.5	2.5	0.090	0.015	-0.016	0.012
8.86	1149.5	2.3	76.3	3.2	0.143	0.023	-0.103	0.018
22.12	1146.9	12.1	58.3	11.2	-0.263	0.229	-0.133	0.200

Table A.27: NGC 5582 major

r	v	δv	σ	$\delta\sigma$	H_4	δH_4	H_3	δH_3
-31.73	1432.9	15.5	75.2	19.0	-0.048	0.149	-0.070	0.118
-13.25	1460.1	2.6	44.0	4.4	-0.012	0.091	-0.080	0.088
-7.03	1442.7	2.0	87.2	3.4	0.176	0.022	-0.189	0.016
-4.72	1438.1	1.5	97.6	2.4	0.156	0.017	-0.224	0.010
-3.26	1419.1	1.0	111.6	1.5	0.078	0.013	-0.207	0.007
-2.40	1392.1	0.9	130.1	1.1	0.012	0.010	-0.152	0.006
-1.80	1369.6	0.7	144.4	0.9	-0.022	0.007	-0.103	0.005
-1.20	1349.3	0.6	154.5	0.8	-0.033	0.005	-0.063	0.004
-0.60	1329.6	0.8	161.3	1.0	-0.035	0.006	-0.028	0.005
0.00	1309.8	0.7	164.6	0.7	-0.036	0.005	0.006	0.004
0.60	1289.5	0.8	163.7	0.9	-0.033	0.006	0.040	0.004
1.20	1268.0	0.7	158.0	0.8	-0.024	0.005	0.076	0.004
1.80	1245.2	0.7	146.6	0.8	0.000	0.006	0.112	0.004
2.40	1222.8	0.7	131.2	1.1	0.040	0.007	0.142	0.005
3.26	1200.4	0.8	114.9	1.4	0.073	0.010	0.159	0.005
4.72	1178.0	1.3	97.0	2.6	0.081	0.016	0.160	0.009
7.03	1163.8	2.1	80.0	4.3	0.117	0.029	0.142	0.021
13.60	1158.8	2.1	70.0	4.4	0.046	0.048	0.099	0.037
33.79	1129.8	19.8	108.6	14.0	-0.280	0.148	0.049	0.102

Table A.28: NGC 5582 minor

r	v	δv	σ	$\delta\sigma$	H_4	δH_4	H_3	δH_3
-16.62	1432.5	4.2	101.2	2.6	-0.332	0.039	0.086	0.050
-4.86	1437.0	1.1	110.7	1.4	0.007	0.009	-0.022	0.011
-3.20	1436.3	0.8	130.0	0.8	-0.022	0.006	-0.032	0.006
-2.35	1434.3	0.7	140.3	0.7	-0.026	0.005	-0.029	0.005
-1.75	1433.0	0.7	146.3	0.7	-0.025	0.004	-0.021	0.004
-1.15	1432.2	0.6	150.8	0.6	-0.024	0.003	-0.012	0.003
-0.55	1431.9	0.5	153.4	0.5	-0.022	0.003	-0.005	0.003
0.05	1431.9	0.4	154.0	0.4	-0.019	0.003	0.001	0.002
0.65	1431.9	0.5	152.6	0.5	-0.015	0.003	0.004	0.003
1.25	1431.8	0.5	149.3	0.6	-0.008	0.003	0.007	0.003
1.85	1431.3	0.6	144.4	0.6	-0.001	0.004	0.010	0.004

Table A.28: NGC 5582 minor

r	v	δv	σ	$\delta\sigma$	H_4	δH_4	H_3	δH_3
2.45	1430.4	0.6	138.0	0.7	0.008	0.004	0.012	0.004
3.31	1428.7	0.8	127.5	1.0	0.020	0.006	0.016	0.007
4.97	1427.2	1.4	107.8	2.0	0.055	0.011	0.045	0.014
16.61	1431.9	9.7	74.1	8.1	-0.094	0.113	0.168	0.092

Appendix B

Measurements of Kinematics: S/N=30-35 per Å

Measurements of kinematics obtained for S/N = 30-35 per Å are given. Simulations were performed to ensure that optimal parameters used to obtain measurements for S/N = 60 per Å were also suitable to determine σ for this lower value of S/N; this was indeed found to be the case. Negative radii correspond to measurements towards the East. Measurements of rotation (v) and velocity dispersion (σ) are given in km s^{-1} and radius (r) in arcseconds. Values of rotation given are actual measurements obtained using the FCQ method; these represent the relative measured velocity between the stellar template and the galaxy spectra.

Table B.1: NGC 2778

major					minor				
r	v	δv	σ	$\delta\sigma$	r	v	δv	σ	$\delta\sigma$
-27.47	2134.4	15.2	62.7	21.0	-22.82	2027.8	20.3	75.5	15.6
-13.40	2145.1	8.9	50.9	8.9	-8.74	2037.8	4.5	64.7	5.6
-8.87	2119.0	2.5	77.8	3.6	-5.92	2030.7	3.3	105.4	4.2
-6.54	2102.8	3.1	87.4	4.1	-4.45	2029.4	2.1	124.5	2.0
-5.07	2088.0	2.0	99.0	2.5	-3.59	2032.2	1.6	135.9	1.5
-4.20	2077.8	1.8	110.8	2.5	-2.99	2034.5	1.4	145.1	1.5
-3.60	2069.8	1.6	118.9	2.2	-2.39	2036.2	1.3	152.0	1.4
-3.00	2059.6	1.5	129.7	2.0	-1.79	2037.2	1.1	157.7	1.3
-2.40	2048.2	1.5	140.6	2.1	-1.19	2038.0	1.0	161.9	1.0
-1.80	2037.0	1.2	149.8	1.7	-0.59	2038.7	0.9	164.5	0.9
-1.20	2025.9	0.8	157.2	1.1	0.01	2039.7	0.8	165.5	0.9
-0.60	2015.1	0.8	162.8	1.2	0.61	2040.9	0.7	164.9	0.8
0.00	2004.2	0.8	166.0	1.2	1.21	2042.3	0.7	162.7	0.8
0.60	1993.7	0.9	166.7	1.3	1.81	2043.5	0.9	158.6	1.0
1.20	1983.1	1.0	164.5	1.5	2.41	2044.2	1.1	152.3	1.3

Table B.1: NGC 2778

major					minor				
r	v	δv	σ	$\delta\sigma$	r	v	δv	σ	$\delta\sigma$
1.80	1972.3	0.9	159.5	1.2	3.01	2044.4	1.1	143.7	1.4
2.40	1960.9	1.2	151.0	1.6	3.61	2044.2	1.5	133.3	1.9
3.00	1949.3	1.5	140.1	2.0	4.46	2044.8	1.9	118.7	2.5
3.60	1938.7	1.5	128.5	2.0	5.93	2046.6	2.7	102.8	3.4
4.47	1926.0	1.9	112.8	2.7	8.76	2048.5	4.8	81.1	5.3
5.68	1914.3	2.2	100.2	3.8	20.76	2050.9	485.2	153.8	31.1
7.15	1904.1	2.0	97.4	3.8					
9.75	1890.1	2.9	80.7	5.4					
15.95	1893.5	2.4	40.7	4.9					
31.46	1902.0	19.5	13.9	30.6					

Table B.2: NGC 3377

major					minor				
r	v	δv	σ	$\delta\sigma$	r	v	δv	σ	$\delta\sigma$
-39.83	576.2	17.2	60.7	14.6	-27.93	626.4	184.7	70.9	35.8
-25.96	548.5	9.2	83.6	9.6	-12.67	674.9	5.5	71.7	8.8
-19.13	553.6	10.1	51.5	12.8	-7.76	652.0	6.1	66.8	8.3
-15.30	589.7	5.1	77.7	5.8	-5.43	666.4	4.0	76.1	4.2
-12.62	580.6	5.4	59.5	8.1	-3.96	660.0	6.1	107.6	6.1
-10.53	583.1	1.8	62.7	3.1	-3.09	668.8	3.4	94.3	3.8
-9.05	576.1	3.5	58.7	6.2	-2.49	676.4	3.5	100.2	3.5
-7.85	571.6	1.8	63.6	2.1	-1.89	678.4	2.6	122.0	2.2
-6.65	574.2	2.1	68.1	2.0	-1.29	684.0	3.4	144.2	2.5
-5.77	575.3	3.3	83.0	3.6	-0.69	683.4	3.0	149.4	2.4
-5.17	570.5	3.8	84.7	4.8	-0.09	683.9	1.9	159.3	1.4
-4.57	561.9	1.9	62.4	2.0	0.51	680.2	2.4	156.6	1.7
-3.97	566.7	3.2	78.0	3.6	1.11	679.1	2.3	146.1	2.0
-3.37	569.8	2.6	87.6	2.9	1.71	680.2	3.8	128.0	3.2
-2.77	577.5	2.4	94.0	2.6	2.31	681.6	4.0	120.9	3.4
-2.17	580.6	1.8	93.6	1.9	2.91	675.5	3.8	109.7	3.1
-1.57	589.0	2.0	102.0	1.8	3.77	668.2	2.6	96.2	2.6
-0.97	615.4	2.2	130.9	1.5	4.98	659.5	4.9	76.5	5.4
-0.37	648.9	1.7	151.8	1.2	6.71	669.9	6.5	61.7	10.2
0.23	688.4	2.0	156.5	1.5	9.89	663.6	5.0	91.7	5.2
0.83	729.8	2.7	140.5	2.3	23.82	682.3	787.7	193.0	35.0
1.43	753.4	1.5	126.8	1.3					
2.03	770.4	2.3	109.8	2.1					
2.63	777.9	2.0	96.2	2.0					
3.23	783.6	3.0	88.0	2.8					
3.83	779.6	2.8	91.5	2.6					
4.43	785.9	2.4	82.8	2.3					

Table B.2: NGC 3377

major					minor				
r	v	δv	σ	$\delta\sigma$	r	v	δv	σ	$\delta\sigma$
5.03	789.6	3.2	86.8	2.9					
5.63	781.7	5.0	81.9	6.2					
6.52	776.7	2.8	87.5	3.1					
7.72	778.2	4.2	74.8	4.0					
8.92	772.2	4.7	70.1	6.2					
10.41	777.1	2.0	67.6	1.8					
12.47	767.0	3.2	49.1	5.5					
15.17	776.6	2.7	72.5	2.4					
18.98	740.8	9.7	107.5	9.4					
25.60	801.7	4.4	32.3	5.8					
38.84	778.7	18.6	24.6	14.3					

Table B.3: NGC 3379

major					minor				
r	v	δv	σ	$\delta\sigma$	r	v	δv	σ	$\delta\sigma$
-27.72	831.7	162.7	159.2	14.9	-32.21	931.0	278.5	172.0	31.3
-12.64	870.2	12.2	160.1	9.8	-14.96	918.0	8.7	178.3	6.1
-9.22	869.9	7.7	171.0	6.1	-9.45	919.4	9.2	168.1	8.8
-7.15	854.7	7.7	182.9	5.5	-7.13	920.4	6.3	173.5	4.8
-5.68	876.6	6.6	198.2	4.4	-5.66	923.3	6.1	185.6	4.3
-4.47	871.4	6.5	203.9	4.3	-4.45	901.4	9.1	186.9	7.2
-3.60	867.2	6.0	206.8	4.2	-3.58	918.9	6.0	179.3	4.4
-3.00	873.6	7.1	210.2	5.2	-2.98	904.7	5.6	193.8	4.1
-2.40	882.1	5.7	211.2	4.0	-2.38	902.7	4.9	203.1	3.5
-1.80	884.0	6.3	219.1	4.4	-1.78	914.9	6.2	216.4	4.0
-1.20	901.9	4.6	219.2	3.2	-1.18	902.0	4.5	227.2	3.0
-0.60	907.2	4.3	226.6	2.8	-0.58	904.5	4.9	223.2	3.3
0.00	908.4	4.1	222.2	2.7	0.02	907.8	4.2	232.2	2.6
0.60	917.8	4.2	214.7	2.9	0.62	904.4	4.2	227.8	2.7
1.20	928.2	4.1	207.2	2.8	1.22	917.7	5.4	216.5	3.6
1.80	936.7	4.5	204.8	3.0	1.82	909.8	5.5	213.5	3.6
2.40	943.2	7.2	213.6	4.5	2.42	914.4	5.1	193.4	3.7
3.00	960.2	7.0	206.3	5.0	3.02	910.5	7.3	220.5	4.8
3.60	952.3	6.8	204.2	4.9	3.62	925.3	5.0	171.4	4.6
4.48	926.3	7.7	198.2	5.6	4.50	909.4	7.9	202.3	5.6
5.68	931.5	8.6	192.1	6.5	5.70	911.7	7.2	195.9	4.9
7.15	944.8	8.5	196.7	6.1	7.18	923.2	6.1	140.1	7.4
9.23	947.1	9.9	170.2	9.1	9.50	902.2	5.8	139.3	5.6
12.64	957.2	13.0	178.0	10.4	14.97	906.1	7.3	146.4	7.8
27.13	999.8	185.6	122.8	21.2	31.26	958.81	184.7	162.5	53.8

Table B.4: NGC 3605

major					minor				
r	v	δv	σ	$\delta\sigma$	r	v	δv	σ	$\delta\sigma$
-24.75	624.4	14.5	18.6	13.2	-12.93	596.5	129.3	101.8	17.4
-13.61	648.2	7.4	61.4	7.2	-6.77	662.6	1.4	73.8	1.1
-10.42	661.3	2.2	49.0	2.8	-5.07	661.1	1.2	79.3	1.0
-8.35	662.8	1.1	55.8	1.6	-4.21	659.0	0.9	84.6	0.9
-6.88	658.8	1.5	70.7	1.3	-3.61	657.8	0.8	85.9	0.8
-5.67	658.9	1.4	79.0	1.2	-3.01	657.2	0.8	86.7	0.7
-4.80	659.8	1.4	83.5	1.3	-2.41	657.1	0.7	87.1	0.6
-4.20	660.2	1.2	86.1	1.2	-1.81	657.5	0.6	87.5	0.5
-3.60	660.8	1.1	88.4	1.0	-1.21	658.4	0.5	88.0	0.5
-2.99	662.4	0.9	89.8	0.8	-0.61	659.5	0.4	88.6	0.4
-2.39	665.4	0.7	90.7	0.7	-0.01	661.1	0.4	89.3	0.4
-1.80	670.3	0.6	91.3	0.6	0.59	662.9	0.4	90.2	0.4
-1.19	676.8	0.6	91.3	0.5	1.19	664.7	0.5	91.2	0.5
-0.60	684.4	0.5	91.0	0.5	1.79	666.3	0.6	92.1	0.6
0.00	692.7	0.5	90.4	0.4	2.39	667.5	0.7	92.9	0.7
0.61	701.4	0.5	89.7	0.5	2.99	668.0	0.9	93.2	0.9
1.21	709.9	0.5	89.0	0.4	3.59	667.8	1.1	92.6	1.0
1.80	717.9	0.5	88.3	0.5	4.19	666.8	1.2	90.4	1.1
2.40	724.4	0.5	87.8	0.5	5.05	665.2	1.2	84.1	1.1
3.00	728.8	0.7	87.8	0.6	6.51	664.8	1.2	74.6	1.0
3.61	730.8	0.8	87.8	0.7	13.60	625.7	60.8	95.1	12.9
4.20	731.1	0.9	87.1	0.8					
4.81	730.7	0.9	85.2	0.8					
5.68	730.3	1.5	81.7	1.4					
6.89	731.1	1.7	76.6	1.8					
8.36	734.4	1.3	75.1	1.4					
10.44	746.5	2.6	73.7	2.7					
13.63	743.2	10.1	49.5	8.4					
22.31	729.6	7.4	54.3	7.8					

Table B.5: NGC 3608

major					minor				
r	v	δv	σ	$\delta\sigma$	r	v	δv	σ	$\delta\sigma$
-41.12	1190.0	18.7	72.2	20.5	-35.48	1147.6	12.0	53.5	20.8
-27.57	1172.9	9.9	114.7	11.0	-19.95	1185.4	4.7	111.2	8.0
-21.17	1198.4	7.3	161.8	9.8	-14.55	1185.2	4.4	121.6	7.9
-17.34	1186.0	5.9	126.9	7.3	-11.60	1174.8	3.3	114.2	6.1
-14.65	1220.3	5.1	155.6	8.7	-9.53	1173.9	2.8	131.3	4.0
-12.57	1223.9	4.3	147.5	6.9	-8.05	1176.5	2.7	136.7	3.9
-11.09	1230.1	3.5	149.4	5.6	-6.85	1177.6	2.0	146.5	3.0
-9.89	1239.3	2.5	151.9	3.7	-5.97	1178.0	1.5	156.0	2.2

Table B.5: NGC 3608

major					minor				
r	v	δv	σ	$\delta\sigma$	r	v	δv	σ	$\delta\sigma$
-8.69	1246.4	2.2	156.1	3.4	-5.37	1177.6	1.6	162.9	2.5
-7.81	1249.8	1.9	158.1	2.9	-4.77	1176.2	1.5	169.7	2.2
-7.21	1251.3	2.1	159.2	3.1	-4.17	1174.2	1.3	175.4	1.8
-6.61	1252.2	1.9	159.3	3.0	-3.57	1171.9	0.9	181.3	1.2
-6.01	1252.9	1.7	159.5	2.6	-2.97	1170.1	0.7	187.4	1.0
-5.41	1253.7	1.4	160.9	2.3	-2.37	1169.1	0.6	191.5	0.8
-4.81	1254.6	1.3	164.3	2.1	-1.77	1168.9	0.5	194.6	0.8
-4.21	1255.3	1.1	169.6	1.7	-1.17	1169.2	0.4	196.4	0.7
-3.61	1255.2	0.9	176.2	1.4	-0.57	1169.8	0.5	197.1	0.7
-3.01	1254.0	0.7	182.8	1.0	0.03	1170.3	0.5	196.7	0.8
-2.41	1251.9	0.5	188.4	0.9	0.63	1170.7	0.6	195.5	0.9
-1.81	1249.1	0.5	193.0	0.8	1.23	1170.7	0.6	193.3	1.0
-1.21	1245.8	0.5	196.4	0.8	1.83	1170.3	0.6	190.0	0.9
-0.61	1242.2	0.6	198.5	0.8	2.43	1169.4	0.7	185.3	1.0
-0.01	1238.4	0.6	199.4	0.9	3.03	1168.4	0.7	178.9	1.2
0.59	1234.7	0.6	198.9	0.9	3.63	1167.6	1.0	171.8	1.4
1.19	1231.3	0.6	196.9	0.9	4.23	1167.4	1.4	164.6	2.1
1.79	1228.6	0.7	193.2	1.0	4.83	1167.7	1.7	159.1	2.7
2.39	1226.6	0.7	188.0	1.1	5.43	1168.4	1.9	154.9	2.9
2.99	1225.4	0.6	182.0	0.9	6.03	1169.3	1.9	152.1	2.9
3.59	1224.9	0.8	176.0	1.3	6.91	1169.7	2.1	149.7	3.1
4.19	1224.8	1.1	171.2	1.7	8.11	1168.7	2.5	144.2	3.7
4.79	1224.4	1.2	167.5	1.9	9.59	1167.1	2.9	130.3	4.6
5.39	1223.7	1.3	164.8	2.1	11.66	1165.0	3.2	125.5	5.3
5.99	1222.6	1.4	162.7	2.3	14.87	1178.1	4.0	102.8	6.4
6.59	1221.8	1.5	161.3	2.4	21.75	1186.1	7.8	92.8	13.1
7.19	1222.0	1.5	161.0	2.4	38.34	1124.7	359.1	127.1	32.8
7.79	1223.3	1.8	161.6	2.9					
8.68	1226.7	2.2	162.6	3.7					
9.88	1230.3	3.0	158.5	4.8					
11.08	1230.8	2.8	147.1	4.1					
12.56	1233.1	2.7	143.3	3.5					
14.64	1218.1	3.2	126.6	3.7					
17.32	1264.8	5.1	149.5	5.2					
21.16	1240.4	6.2	114.0	7.6					
28.18	1259.0	7.0	128.3	8.8					
42.61	1177.7	569.8	149.1	33.7					

Table B.6: NGC 4339

major					minor				
r	v	δv	σ	$\delta\sigma$	r	v	δv	σ	$\delta\sigma$
-31.72	1306.6	4.5	73.7	2.8	-33.94	1219.7	11.0	67.1	15.3
-14.79	1340.3	1.3	44.2	1.5	-15.55	1255.0	1.2	65.7	1.2
-9.48	1315.3	0.9	77.0	1.1	-9.47	1257.8	3.4	85.7	6.0
-7.16	1306.4	2.2	88.4	3.0	-7.15	1258.3	3.2	85.8	5.0
-5.68	1309.8	2.2	81.1	3.3	-5.68	1256.6	2.5	97.0	3.4
-4.47	1298.6	1.2	98.8	1.6	-4.47	1251.6	1.8	104.4	3.2
-3.60	1299.7	1.5	102.8	2.5	-3.60	1260.1	2.3	97.0	4.1
-3.00	1299.4	1.5	94.5	2.5	-3.00	1259.8	1.7	102.8	3.0
-2.40	1299.5	1.5	93.7	2.2	-2.40	1256.1	2.3	108.2	4.0
-1.80	1293.8	0.9	104.5	1.3	-1.80	1258.0	1.2	110.0	2.1
-1.20	1286.6	0.5	109.6	0.9	-1.20	1256.5	0.9	114.8	1.6
-0.60	1273.4	0.7	113.5	1.2	-0.60	1256.0	0.9	116.1	1.4
0.00	1258.6	0.6	116.3	1.0	0.00	1258.1	0.6	119.0	0.9
0.60	1246.7	0.7	115.0	1.1	0.60	1259.6	0.6	121.2	0.9
1.20	1234.4	0.6	101.6	1.1	1.20	1260.2	0.8	114.5	1.4
1.80	1225.6	0.9	94.4	1.6	1.80	1259.5	1.1	108.5	1.9
2.40	1221.1	1.1	103.6	2.0	2.40	1259.8	1.4	104.4	2.6
3.00	1219.9	1.4	106.0	2.3	3.00	1267.2	2.2	107.9	3.9
3.87	1214.8	1.2	92.3	1.8	3.87	1265.2	2.1	110.8	3.4
5.08	1204.1	1.9	81.3	2.9	5.08	1265.0	2.2	79.4	4.0
6.56	1203.2	1.4	93.1	2.4	6.56	1262.1	2.6	69.1	5.0
8.62	1212.7	1.7	80.1	3.2	8.62	1263.6	1.4	63.1	3.5
12.28	1211.4	2.3	80.9	3.2	12.47	1268.3	2.8	71.2	5.7
26.89	1230.2	3.5	59.3	3.0	27.69	1257.3	190.1	73.5	22.8

Table B.7: NGC 4387

major					minor				
r	v	δv	σ	$\delta\sigma$	r	v	δv	σ	$\delta\sigma$
-28.05	507.4	14.7	38.4	21.5	-24.09	545.7	53.5	76.5	10.5
-16.62	495.0	2.2	63.5	3.5	-10.73	553.3	3.4	68.7	4.0
-13.42	498.4	2.0	70.5	3.6	-7.74	547.9	1.9	76.4	2.2
-11.35	501.1	1.7	71.2	3.3	-6.28	551.9	1.3	85.2	1.8
-9.86	503.8	1.2	69.1	2.6	-5.07	554.1	1.0	94.6	1.4
-8.66	507.8	1.0	72.7	2.0	-4.20	554.4	1.1	99.8	1.4
-7.46	513.2	0.7	83.4	1.1	-3.60	554.3	0.9	101.5	1.2
-6.58	515.4	0.9	89.0	1.2	-3.00	554.1	0.7	101.7	0.8
-5.98	516.2	1.0	92.3	1.3	-2.40	554.1	0.5	100.8	0.7
-5.38	517.0	1.0	95.5	1.3	-1.80	554.4	0.4	99.2	0.6
-4.78	518.3	1.1	98.2	1.5	-1.20	555.0	0.6	97.8	0.8
-4.18	520.6	1.0	99.9	1.3	-0.60	555.8	0.5	96.7	0.7
-3.58	524.0	0.7	100.6	0.9	0.00	556.9	0.4	96.3	0.6

Table B.7: NGC 4387

major					minor				
r	v	δv	σ	$\delta\sigma$	r	v	δv	σ	$\delta\sigma$
-2.98	528.6	0.5	100.4	0.7	0.60	558.2	0.3	96.6	0.5
-2.38	533.9	0.3	99.6	0.4	1.20	559.7	0.4	97.8	0.6
-1.78	539.1	0.3	98.8	0.3	1.80	561.0	0.5	99.5	0.6
-1.18	544.1	0.3	98.0	0.4	2.40	562.1	0.6	101.3	0.8
-0.58	548.9	0.3	97.7	0.5	3.00	562.9	0.8	102.0	1.1
0.02	553.7	0.4	97.9	0.5	3.60	563.5	0.9	100.6	1.3
0.62	558.8	0.4	98.7	0.5	4.20	564.2	0.8	96.7	1.3
1.22	564.2	0.4	99.7	0.6	5.07	564.7	1.1	89.1	2.0
1.82	569.7	0.5	100.7	0.6	6.27	563.3	1.1	78.3	2.2
2.42	575.1	0.5	101.5	0.7	7.73	564.4	1.5	75.7	3.0
3.02	579.8	0.5	101.6	0.7	10.72	577.2	2.1	68.9	4.0
3.62	583.7	0.7	100.8	0.9	23.09	526.4	408.3	73.5	12.9
4.22	587.1	0.6	98.9	0.8					
4.82	590.0	0.8	96.7	1.0					
5.42	592.4	0.9	94.2	1.1					
6.02	594.1	0.8	93.0	1.0					
6.62	595.1	0.8	90.7	1.0					
7.50	596.2	0.7	90.0	0.8					
8.70	598.3	0.8	88.2	0.9					
9.91	601.8	1.4	85.0	1.5					
11.38	604.3	2.0	75.1	3.1					
13.46	605.1	2.3	70.2	3.3					
16.65	605.4	1.4	65.0	0.9					
27.73	594.7	5.3	91.1	8.3					

Table B.8: NGC 4464

major					minor				
r	v	δv	σ	$\delta\sigma$	r	v	δv	σ	$\delta\sigma$
-20.93	1341.6	35.3	87.9	18.1	-22.10	1269.2	9.0	52.1	11.5
-10.88	1348.1	3.6	73.0	3.2	-9.29	1303.7	2.5	55.2	2.8
-8.33	1356.2	3.2	78.7	3.2	-6.53	1295.5	2.8	67.2	3.3
-6.86	1360.2	3.8	76.7	3.7	-5.07	1288.9	1.5	71.4	2.1
-5.66	1362.7	2.6	80.0	2.8	-4.20	1285.0	1.0	85.2	1.3
-4.79	1365.6	2.1	83.8	2.4	-3.60	1282.9	1.0	94.9	1.2
-4.19	1365.8	1.7	87.9	1.9	-3.00	1281.7	0.7	105.0	0.8
-3.59	1364.3	1.3	93.2	1.5	-2.40	1281.6	0.9	114.8	1.0
-2.99	1360.8	0.9	99.3	1.0	-1.80	1282.4	0.8	122.7	0.8
-2.39	1353.6	1.1	107.0	1.3	-1.20	1283.9	0.8	128.0	0.8
-1.79	1340.6	1.1	117.6	1.2	-0.60	1285.7	0.7	130.9	0.8
-1.19	1322.0	0.8	129.4	1.0	0.00	1287.4	0.7	131.6	0.7
-0.59	1302.9	0.7	137.4	0.7	0.60	1289.1	0.6	130.3	0.6

Table B.8: NGC 4464

major					minor				
r	v	δv	σ	$\delta\sigma$	r	v	δv	σ	$\delta\sigma$
0.01	1284.7	0.8	140.1	0.8	1.20	1290.3	0.6	126.9	0.7
0.61	1266.9	0.8	137.6	0.7	1.80	1291.1	0.7	121.0	0.8
1.21	1249.6	0.7	130.1	0.7	2.40	1291.3	0.7	111.6	0.9
1.81	1233.6	0.8	119.4	0.7	3.00	1292.2	0.9	99.0	1.3
2.41	1220.2	0.9	107.6	1.0	3.60	1294.1	1.1	85.6	1.9
3.01	1211.0	1.3	97.6	1.6	4.20	1295.7	1.4	76.6	2.1
3.61	1206.7	1.6	91.1	2.2	5.06	1297.8	1.6	67.3	2.5
4.21	1206.1	1.8	87.5	2.5	6.53	1302.7	2.2	53.1	2.9
4.81	1207.1	1.5	84.0	2.2	9.50	1299.8	7.3	56.0	4.9
5.69	1208.2	1.6	75.8	2.5	22.99	1296.0	11.4	16.2	18.0
6.89	1210.9	2.3	69.6	3.3					
8.36	1217.4	2.6	69.6	3.2					
10.91	1223.1	4.1	68.9	4.2					
22.39	1237.7	12.3	35.0	10.4					

Table B.9: NGC 4468

major					minor				
r	v	δv	σ	$\delta\sigma$	r	v	δv	σ	$\delta\sigma$
-36.61	42.2	21.1	43.6	24.3	-20.95	820.7	6.5	67.5	6.9
-15.94	956.0	10.6	19.3	8.9	-7.16	877.2	5.5	43.1	7.3
-7.28	930.3	2.8	48.1	4.0	-4.12	892.5	14.6	41.2	8.6
-4.70	932.0	6.4	15.7	3.4	-2.66	898.6	3.1	36.8	3.7
-3.23	904.9	1.8	56.6	2.8	-1.80	899.3	7.4	36.3	2.8
-2.36	929.6	1.7	34.0	1.7	-1.20	898.4	4.2	36.0	1.4
-1.76	927.4	1.1	35.4	1.1	-0.60	879.7	0.8	39.3	1.4
-1.16	924.8	0.6	37.1	0.7	0.00	879.8	1.1	39.9	1.6
-0.56	922.4	0.6	36.9	0.7	0.60	880.0	1.1	40.5	1.6
0.04	920.0	0.6	35.8	0.6	1.20	880.4	0.9	40.7	1.4
0.64	917.9	0.6	34.4	0.6	1.80	899.2	4.4	36.0	1.6
1.24	916.0	0.8	33.1	0.8	2.66	903.3	6.9	37.1	9.7
1.84	913.7	1.1	31.6	1.2	4.11	907.6	9.9	36.7	11.7
2.44	911.1	1.4	29.7	1.4	7.35	903.3	8.5	49.5	8.0
3.30	908.1	2.8	26.6	3.6	21.68	867.3	26.9	62.5	29.8
4.78	907.5	2.2	23.5	2.1					
7.38	905.8	5.8	34.3	4.9					
15.30	926.9	12.8	22.3	10.9					
35.99	893.51	494.5	147.0	70.1					

Table B.10: NGC 4458

major					minor				
r	v	δv	σ	$\delta\sigma$	r	v	δv	σ	$\delta\sigma$
-33.43	634.7	32.7	23.1	258.0	-30.73	737.4	404.5	111.6	27.1
-15.70	601.3	4.3	99.3	6.6	-12.94	647.0	4.2	58.1	4.5
-8.74	631.3	4.1	56.2	5.6	-7.06	644.5	3.5	68.0	4.4
-6.18	646.0	3.3	76.1	4.9	-4.73	642.7	1.0	65.0	1.2
-4.71	634.0	2.3	73.6	2.8	-3.26	640.5	2.3	75.8	4.3
-3.50	644.7	2.1	78.8	2.9	-2.40	635.0	2.3	90.2	3.9
-2.63	648.5	2.6	88.0	4.1	-1.80	640.1	1.7	103.7	2.5
-2.03	668.9	1.5	94.5	2.7	-1.20	642.6	1.3	110.6	1.7
-1.43	664.7	1.2	102.2	1.6	-0.60	641.3	1.2	110.6	1.5
-0.83	660.0	1.3	109.7	1.7	0.00	643.2	1.1	118.4	1.4
-0.23	644.9	1.1	119.6	1.3	0.60	641.6	1.7	114.4	2.2
0.37	630.1	1.3	118.9	1.6	1.20	642.5	1.8	116.2	2.2
0.97	613.4	1.4	111.7	1.8	1.80	644.5	2.0	103.9	3.0
1.57	610.6	1.7	100.6	2.4	2.40	632.5	1.5	85.9	2.0
2.17	608.2	2.3	98.0	3.1	3.27	634.4	2.1	82.4	3.0
2.77	620.3	2.3	91.6	3.2	4.74	635.7	3.0	66.6	4.1
3.64	629.6	1.9	82.1	2.5	7.07	638.1	4.7	58.5	2.9
4.85	636.1	2.2	72.4	2.6	12.60	641.7	6.3	57.7	6.2
6.32	642.0	2.9	72.9	4.1	28.81	625.1	25.2	76.8	30.4
8.90	645.7	3.0	73.6	3.2					
16.38	601.4	4.7	91.5	7.5					
35.05	681.41	300.3	185.1	63.2					

Table B.11: NGC 4478

major					minor				
r	v	δv	σ	$\delta\sigma$	r	v	δv	σ	$\delta\sigma$
-27.55	1387.9	117.1	119.8	17.3	-31.56	1316.8	20.7	50.0	25.2
-16.28	1411.4	3.8	98.2	6.3	-17.62	1341.5	4.0	97.7	6.6
-13.36	1399.2	4.6	113.4	6.1	-12.96	1360.3	3.0	107.0	4.0
-11.29	1398.1	3.6	113.0	4.6	-10.62	1332.3	2.6	95.7	2.6
-9.81	1378.4	7.8	113.2	12.8	-9.15	1320.8	2.4	105.2	3.5
-8.61	1397.4	4.0	130.8	3.5	-7.95	1336.3	3.2	131.4	2.9
-7.41	1396.7	3.9	144.5	3.2	-6.75	1350.7	3.1	132.2	3.6
-6.52	1387.1	5.3	130.0	4.9	-5.87	1350.4	5.0	132.6	5.3
-5.92	1386.7	3.6	139.0	3.9	-5.27	1352.3	3.1	142.2	4.0
-5.32	1399.5	2.6	141.5	3.2	-4.67	1350.7	2.5	132.1	3.4
-4.72	1395.6	2.8	140.3	2.6	-4.07	1341.0	3.1	161.3	2.8
-4.12	1380.2	3.7	147.2	4.7	-3.47	1345.2	3.8	168.4	3.9
-3.52	1380.8	3.4	143.3	4.3	-2.87	1348.7	1.9	154.8	2.8
-2.92	1382.2	2.0	145.3	1.9	-2.27	1355.2	1.3	146.8	1.6
-2.32	1383.2	2.3	138.8	2.9	-1.67	1353.6	1.2	136.1	1.4

Table B.11: NGC 4478

major					minor				
r	v	δv	σ	$\delta\sigma$	r	v	δv	σ	$\delta\sigma$
-1.72	1380.5	1.7	134.3	2.0	-1.07	1359.2	1.2	128.7	1.6
-1.12	1373.4	1.4	119.9	1.7	-0.47	1359.9	1.3	124.1	1.8
-0.52	1364.0	1.6	124.9	1.9	0.13	1368.6	0.9	123.0	1.3
0.08	1344.3	1.2	126.5	1.7	0.73	1365.3	0.9	126.5	1.3
0.68	1324.0	1.7	123.9	2.3	1.33	1361.4	1.8	134.5	2.2
1.28	1308.4	2.0	126.8	2.9	1.93	1353.4	2.5	148.4	3.1
1.88	1294.7	2.1	118.3	3.4	2.53	1355.3	1.7	154.8	1.9
2.48	1298.8	2.4	122.5	3.1	3.13	1358.0	2.7	161.1	3.2
3.08	1313.5	2.7	141.5	2.8	3.73	1354.0	2.6	149.9	3.5
3.68	1303.0	2.5	128.7	3.1	4.33	1350.9	3.0	133.1	3.6
4.28	1303.1	4.7	132.2	5.9	4.93	1368.7	1.9	134.3	2.3
4.88	1300.0	3.8	142.8	4.4	5.53	1369.7	3.5	140.3	3.1
5.48	1290.9	3.6	141.2	4.0	6.13	1366.9	5.7	131.7	6.7
6.08	1292.8	3.9	114.5	5.8	7.01	1353.0	2.7	135.0	2.4
6.68	1301.0	4.5	112.8	5.8	8.22	1372.1	4.5	125.6	6.9
7.56	1302.8	5.0	122.3	5.5	9.69	1361.5	3.9	121.2	3.7
8.76	1296.2	3.4	130.5	3.6	11.76	1351.3	3.8	91.7	5.4
9.96	1290.6	2.5	102.3	3.7	14.92	1352.0	2.9	75.3	10.1
11.44	1287.7	4.7	98.9	6.7	26.73	1338.8	36.8	17.4	21.4
13.51	1288.3	4.5	93.6	6.5					
16.43	1284.0	2.7	74.5	4.0					
28.50	1248.5	227.0	111.9	24.0					

Table B.12: NGC 4551

major					minor				
r	v	δv	σ	$\delta\sigma$	r	v	δv	σ	$\delta\sigma$
-33.68	1172.0	13.3	47.2	7.9	-19.75	1195.4	13.9	48.1	8.4
-18.18	1151.7	1.6	68.2	0.7	-8.48	1193.3	1.8	57.2	3.9
-12.23	1154.9	0.8	66.4	1.9	-6.16	1196.9	0.9	74.5	1.5
-9.29	1154.3	2.5	90.1	4.0	-4.69	1202.7	2.6	91.3	4.3
-7.22	1160.3	1.2	88.2	1.7	-3.48	1199.9	1.9	104.2	3.5
-5.74	1160.9	0.6	72.5	0.7	-2.62	1198.6	1.2	106.3	2.2
-4.54	1159.5	1.0	95.1	1.7	-2.02	1201.8	1.6	102.9	3.1
-3.66	1160.0	1.4	92.6	1.8	-1.42	1196.4	1.1	95.5	1.9
-3.06	1167.0	1.0	91.4	1.6	-0.82	1197.0	0.9	103.7	1.5
-2.46	1154.2	1.1	100.8	1.7	-0.22	1197.3	0.9	96.8	1.5
-1.86	1163.4	1.2	100.3	1.9	0.38	1198.3	0.9	95.5	1.5
-1.26	1169.4	0.7	95.0	1.0	0.98	1203.9	1.1	100.0	2.1
-0.66	1175.9	0.9	97.9	1.4	1.58	1205.5	1.0	100.8	1.8
-0.06	1190.7	0.6	102.7	1.1	2.18	1196.6	1.7	108.8	2.9
0.54	1203.1	0.6	95.3	1.0	2.78	1204.8	1.2	88.4	2.0

Table B.12: NGC 4551

major					minor				
r	v	δv	σ	$\delta\sigma$	r	v	δv	σ	$\delta\sigma$
1.14	1210.5	0.9	95.4	1.7	3.65	1213.3	2.1	90.4	3.4
1.74	1229.2	1.0	74.3	1.7	4.86	1204.3	1.9	98.7	2.9
2.34	1230.7	0.9	91.5	1.5	6.33	1195.2	3.0	85.4	3.9
2.94	1231.1	0.8	81.6	1.1	8.65	1196.6	2.2	82.5	3.2
3.54	1229.3	1.2	101.7	2.1	20.11	1214.5	5.7	76.1	12.0
4.42	1226.4	1.5	83.7	2.4					
5.62	1235.4	1.5	94.7	2.6					
6.82	1239.0	1.1	85.4	1.7					
8.30	1241.4	0.9	73.3	0.6					
10.38	1239.9	1.3	75.4	2.0					
13.57	1249.0	2.7	68.6	1.5					
24.97	1251.6	5.6	62.7	8.4					

Table B.13: NGC 4564

major					minor				
r	v	δv	σ	$\delta\sigma$	r	v	δv	σ	$\delta\sigma$
-53.11	1025.6	17.0	53.7	16.0	-21.05	1179.5	47.9	61.8	12.5
-40.65	1028.5	4.9	64.6	7.1	-12.75	1129.8	2.2	75.7	2.4
-32.22	1028.2	4.2	60.6	8.6	-10.16	1134.4	2.1	77.1	2.5
-27.81	1018.1	4.2	57.2	6.4	-8.69	1135.6	1.6	87.3	2.1
-24.53	1027.2	3.8	79.4	3.8	-7.49	1133.0	1.5	92.9	2.2
-21.85	1029.1	3.7	78.7	4.4	-6.61	1132.0	1.6	98.1	2.5
-19.76	1017.9	3.6	64.7	5.1	-6.01	1132.2	1.4	102.3	2.2
-17.96	1044.4	2.5	87.6	3.6	-5.41	1133.0	1.0	108.4	1.6
-16.47	1012.1	2.6	67.3	3.5	-4.81	1134.1	0.9	115.8	1.4
-15.27	1017.5	2.6	75.1	3.2	-4.21	1135.2	1.0	124.7	1.4
-14.07	1022.6	2.1	82.2	2.1	-3.61	1136.0	0.8	133.9	1.0
-12.87	1028.4	2.5	89.1	2.3	-3.01	1136.4	0.9	144.2	1.3
-11.67	1035.0	2.1	93.8	1.9	-2.41	1136.7	0.8	154.2	1.2
-10.47	1042.8	1.3	98.1	1.1	-1.81	1137.0	0.7	162.2	1.0
-9.58	1049.0	1.4	102.6	1.2	-1.21	1137.6	0.7	167.8	1.0
-8.98	1053.2	1.5	105.8	1.3	-0.61	1138.5	0.7	171.2	1.0
-8.38	1058.0	1.5	108.7	1.4	-0.01	1139.6	0.6	172.7	0.8
-7.78	1063.6	1.6	110.7	1.5	0.59	1141.0	0.5	172.5	0.7
-7.18	1069.8	1.7	113.5	1.7	1.19	1142.5	0.4	170.1	0.6
-6.58	1075.9	1.4	116.3	1.3	1.79	1144.0	0.4	165.0	0.6
-5.98	1081.0	1.1	119.9	1.1	2.39	1145.2	0.6	156.7	0.8
-5.38	1084.9	0.8	124.5	0.8	2.99	1145.9	0.5	146.0	0.7
-4.78	1088.3	1.1	131.8	1.1	3.59	1145.8	0.6	134.7	0.9
-4.18	1092.3	1.0	138.2	0.9	4.19	1145.3	0.7	123.8	1.1
-3.58	1098.1	0.7	145.4	0.7	4.79	1144.4	0.9	113.6	1.3

Table B.13: NGC 4564

major					minor				
r	v	δv	σ	$\delta\sigma$	r	v	δv	σ	$\delta\sigma$
-2.98	1106.3	0.8	153.3	0.8	5.39	1143.5	1.1	104.6	1.7
-2.38	1117.3	0.7	161.6	0.7	5.99	1143.0	1.2	97.4	1.8
-1.78	1130.1	0.6	168.5	0.6	6.59	1143.4	1.4	92.4	2.0
-1.18	1143.5	0.5	173.4	0.5	7.46	1146.0	1.2	83.6	1.4
-0.58	1157.1	0.4	176.1	0.4	8.67	1151.1	1.4	73.1	1.8
0.02	1170.7	0.5	176.6	0.5	10.14	1152.5	1.7	68.6	2.2
0.62	1184.2	0.4	175.0	0.5	12.72	1149.6	2.8	80.2	2.8
1.22	1197.9	0.4	171.5	0.4	25.70	1164.6	12.2	23.4	12.8
1.82	1210.9	0.5	166.2	0.5					
2.42	1222.8	0.6	159.4	0.6					
3.02	1232.6	0.7	151.6	0.7					
3.62	1239.9	0.8	143.8	0.8					
4.22	1245.5	1.0	136.7	1.0					
4.82	1250.4	1.0	130.4	1.0					
5.42	1255.4	1.3	125.3	1.3					
6.02	1260.7	1.3	120.3	1.4					
6.62	1266.0	1.7	114.8	1.6					
7.22	1270.6	1.5	110.4	1.4					
7.82	1274.8	1.4	107.3	1.3					
8.42	1279.0	1.6	106.1	1.4					
9.02	1284.3	1.8	104.0	1.6					
9.62	1290.6	1.8	100.6	1.5					
10.51	1300.5	2.0	94.0	1.7					
11.71	1309.7	1.5	84.7	1.5					
12.91	1311.0	2.4	86.7	2.5					
14.11	1311.8	2.7	85.6	2.6					
15.31	1313.4	3.1	84.0	3.0					
16.80	1313.9	3.1	84.5	3.1					
18.60	1311.2	3.4	81.9	4.0					
20.68	1310.1	4.0	81.3	4.4					
23.37	1332.0	5.1	57.2	3.3					
26.65	1301.5	4.8	83.9	3.8					
31.05	1317.5	5.6	57.9	4.3					
40.18	1287.2	8.2	75.8	8.0					
53.48	1259.9	247.0	64.1	33.8					

Table B.14: NGC 5582

major					minor				
r	v	δv	σ	$\delta\sigma$	r	v	δv	σ	$\delta\sigma$
-29.68	1474.5	17.7	16.2	29.7	-15.07	1403.6	11.5	101.0	11.7
-15.33	1463.5	13.9	35.5	12.6	-9.41	1426.7	3.4	73.9	4.1

Table B.14: NGC 5582

major					minor				
r	v	δv	σ	$\delta\sigma$	r	v	δv	σ	$\delta\sigma$
-11.29	1449.9	2.2	69.6	3.1	-7.08	1435.4	2.4	90.3	2.7
-8.96	1454.1	1.3	53.0	2.4	-5.61	1434.6	1.7	103.4	1.8
-7.48	1451.9	1.4	58.7	2.4	-4.75	1434.2	1.1	111.2	1.2
-6.28	1440.0	1.7	92.1	2.3	-4.15	1434.8	0.9	117.8	1.1
-5.40	1439.9	1.8	94.0	2.4	-3.55	1435.0	0.9	125.0	1.1
-4.80	1438.1	1.4	96.6	2.0	-2.95	1434.3	0.7	132.6	0.9
-4.20	1433.2	1.2	100.9	1.6	-2.35	1433.0	0.5	139.5	0.7
-3.60	1423.9	1.2	107.9	1.7	-1.75	1431.9	0.4	145.4	0.6
-3.00	1409.6	1.1	117.6	1.5	-1.15	1431.0	0.4	149.8	0.6
-2.40	1390.4	0.9	130.5	1.1	-0.55	1430.8	0.3	152.2	0.5
-1.80	1368.5	0.7	144.1	0.8	0.05	1430.7	0.4	152.8	0.5
-1.20	1347.8	0.7	154.2	0.7	0.65	1430.7	0.4	151.5	0.7
-0.60	1328.0	0.7	160.8	0.7	1.25	1430.5	0.5	148.3	0.7
0.00	1308.2	0.7	164.0	0.7	1.85	1430.1	0.6	143.5	0.8
0.60	1287.8	0.7	163.2	0.8	2.45	1429.2	0.5	137.1	0.7
1.20	1266.3	0.6	157.5	0.7	3.05	1428.1	0.7	130.0	0.9
1.80	1243.5	0.7	146.2	0.9	3.65	1426.9	1.0	122.9	1.3
2.40	1221.6	0.7	131.3	1.0	4.25	1426.1	1.0	115.8	1.2
3.00	1204.8	0.7	118.7	1.2	4.85	1425.4	1.3	107.6	1.5
3.60	1191.9	0.9	108.2	1.5	5.72	1424.9	2.2	99.1	2.5
4.20	1181.3	0.9	98.8	1.5	7.19	1421.0	3.1	90.5	3.4
4.80	1173.7	1.4	92.2	2.4	9.77	1420.7	3.3	83.5	3.3
5.40	1168.3	1.5	86.7	2.5	18.08	1443.7	10.6	71.5	7.9
6.27	1162.9	1.4	80.5	2.5					
7.48	1158.0	1.9	75.3	3.3					
8.95	1154.0	2.1	70.9	3.6					
11.29	1149.6	2.8	61.9	4.1					
15.57	1156.0	3.9	43.1	4.5					
31.21	1151.0	35.3	95.1	12.1					

Appendix C

Measurements of Line-Strengths

Measurements of Hβ, Mg_2 and Mg_b, Fe5270 and Fe5335 line-strengths, fully corrected to the Lick/IDS system, are given. A description of how measurements were obtained is given in Chapter 5. Negative radii correspond to measurements towards the East. Values of σ obtained for the radii of line-strength measurements, are also given. These values of σ were determined as described in section 5.2.1 of chapter 5, and were obtained to (i) enable line-strength measurements to be corrected for the effects of velocity dispersion and to (ii) compare line-strengths and velocity dispersion with the relations established by other authors (Chapter 6). These values of σ, particularly for the outermost radii, should not be used for any other purpose.

Table C.1: NGC 2778 major

r	Hβ	δHβ	Mg_2	δMg_2	Mg_b	δMg_b	Fe5270	δFe5270	Fe5335	δFe5335	σ
-0.300	1.168	0.122	0.354	0.008	4.752	0.118	3.216	0.155	2.848	0.187	167.2
-0.600	1.171	0.125	0.352	0.008	4.753	0.121	3.211	0.159	2.811	0.191	165.7
-1.200	1.169	0.136	0.343	0.009	4.731	0.130	3.167	0.169	2.709	0.204	160.2
-1.800	1.164	0.154	0.329	0.010	4.699	0.145	3.099	0.188	2.585	0.226	153.2
-2.400	1.153	0.180	0.312	0.011	4.651	0.167	2.997	0.215	2.435	0.258	143.7
-3.000	1.135	0.213	0.292	0.013	4.598	0.196	2.889	0.252	2.292	0.301	133.8
-3.600	1.113	0.252	0.278	0.016	4.544	0.232	2.806	0.296	2.168	0.352	123.8
-4.466	1.107	0.221	0.269	0.014	4.462	0.207	2.812	0.258	2.035	0.309	112.2
-5.674	1.114	0.280	0.264	0.018	4.267	0.268	2.876	0.329	1.823	0.393	101.5
-7.146	1.036	0.290	0.255	0.019	3.889	0.285	2.655	0.341	1.571	0.406	88.5
-9.481	1.452	0.302	0.259	0.020	3.672	0.308	2.701	0.361	1.430	0.431	86.2
-13.291	1.614	0.352	0.241	0.023	3.405	0.360	3.186	0.417	1.577	0.497	84.4
-19.780	1.925	0.442	0.284	0.029	2.719	0.472	3.020	0.523	0.852	0.607	81.5
0.600	1.162	0.125	0.349	0.008	4.740	0.121	3.193	0.160	2.844	0.192	169.2
1.200	1.149	0.136	0.337	0.009	4.707	0.130	3.123	0.171	2.769	0.205	166.8
1.800	1.129	0.154	0.321	0.010	4.651	0.145	3.019	0.190	2.653	0.229	161.0
2.400	1.106	0.181	0.304	0.011	4.570	0.168	2.885	0.219	2.525	0.261	151.0
3.000	1.097	0.215	0.287	0.013	4.470	0.198	2.736	0.256	2.416	0.305	140.2
3.600	1.108	0.255	0.273	0.016	4.367	0.236	2.585	0.303	2.349	0.357	128.6
4.465	1.151	0.224	0.265	0.014	4.270	0.210	2.421	0.267	2.336	0.312	116.3
5.935	1.243	0.244	0.259	0.016	4.179	0.234	2.373	0.292	2.458	0.338	105.6
8.014	1.287	0.290	0.253	0.019	4.159	0.281	2.528	0.344	2.291	0.400	92.6
10.961	1.513	0.328	0.249	0.021	4.139	0.325	2.500	0.394	1.631	0.460	84.1
15.597	1.032	0.391	0.240	0.025	3.818	0.391	2.330	0.463	1.987	0.528	70.7
24.530	1.473	0.530	0.284	0.036	3.890	0.570	1.987	0.665	1.389	0.712	44.9

Table C.2: NGC 2778 minor

r	Hβ	δHβ	Mg_2	δMg_2	Mg_b	δMg_b	Fe5270	δFe5270	Fe5335	δFe5335	σ
-0.300	1.100	0.121	0.360	0.008	4.725	0.119	3.267	0.157	2.749	0.189	167.3
-0.600	1.094	0.125	0.355	0.008	4.688	0.122	3.293	0.161	2.728	0.193	166.8
-1.200	1.096	0.135	0.343	0.009	4.628	0.131	3.281	0.171	2.673	0.208	164.1
-1.800	1.111	0.155	0.324	0.010	4.559	0.147	3.229	0.191	2.596	0.230	159.9
-2.400	1.137	0.184	0.301	0.011	4.488	0.170	3.138	0.221	2.510	0.266	153.8
-3.000	1.176	0.224	0.277	0.014	4.424	0.204	3.010	0.262	2.427	0.316	146.6
-3.851	1.258	0.213	0.248	0.013	4.386	0.192	2.780	0.246	2.313	0.295	135.5
-5.311	1.311	0.264	0.227	0.016	4.479	0.239	2.354	0.309	2.193	0.368	125.3
-7.656	0.705	0.316	0.217	0.019	4.053	0.291	1.644	0.375	2.069	0.436	114.8
-11.653	0.206	0.397	0.210	0.024	3.254	0.377	2.242	0.455	1.763	0.531	96.9
-20.795	-0.164	0.583	0.314	0.037	3.592	0.599	1.523	0.670	-0.992	0.759	55.9
0.600	1.118	0.125	0.356	0.008	4.738	0.122	3.217	0.161	2.740	0.194	167.3
1.200	1.142	0.135	0.343	0.009	4.713	0.131	3.149	0.172	2.694	0.207	165.0
1.800	1.163	0.155	0.324	0.010	4.647	0.147	3.073	0.192	2.623	0.231	160.9
2.400	1.172	0.183	0.302	0.011	4.546	0.170	2.994	0.222	2.538	0.267	153.7
3.000	1.161	0.224	0.278	0.014	4.420	0.204	2.910	0.264	2.444	0.316	144.5
3.851	1.144	0.213	0.247	0.013	4.238	0.193	2.747	0.246	2.289	0.293	129.3
5.311	1.337	0.261	0.226	0.016	4.061	0.244	2.442	0.309	1.955	0.368	118.7
7.656	1.686	0.306	0.224	0.019	3.958	0.295	2.092	0.374	0.963	0.451	112.1
11.662	1.009	0.389	0.210	0.024	3.590	0.374	2.514	0.460	0.768	0.555	101.0
20.756	-0.986	0.639	0.203	0.038	3.034	0.609	0.937	0.738	1.400	0.807	75.7

Table C.3: NGC 3377 major

r	Hβ	δHβ	Mg_2	δMg_2	Mg_b	δMg_b	Fe5270	δFe5270	Fe5335	δFe5335	σ
-0.300	1.621	0.089	0.296	0.006	4.286	0.083	2.844	0.109	2.663	0.129	153.1
-0.600	1.577	0.094	0.288	0.006	4.227	0.088	2.869	0.115	2.663	0.136	144.8
-1.200	1.970	0.109	0.271	0.007	4.121	0.103	2.879	0.130	2.426	0.154	121.4
-1.800	1.818	0.131	0.260	0.008	4.078	0.124	2.839	0.154	2.441	0.179	101.5
-2.400	1.563	0.156	0.253	0.010	4.042	0.148	2.845	0.182	2.426	0.212	95.9
-3.000	1.672	0.179	0.254	0.011	3.912	0.172	2.801	0.210	2.314	0.245	91.1
-3.600	1.535	0.201	0.252	0.013	3.774	0.195	2.854	0.235	2.379	0.273	84.4
-4.200	1.452	0.224	0.246	0.014	3.657	0.217	2.813	0.261	2.459	0.302	81.2
-4.800	1.628	0.246	0.238	0.016	3.598	0.240	2.629	0.290	2.136	0.336	78.3
-5.679	1.615	0.196	0.232	0.013	3.715	0.193	2.296	0.235	2.265	0.268	73.6
-6.881	1.546	0.229	0.223	0.015	3.847	0.224	2.312	0.272	1.957	0.315	66.8
-8.084	1.393	0.265	0.219	0.017	3.612	0.263	2.110	0.317	2.297	0.359	64.4
-9.563	1.289	0.252	0.216	0.016	3.512	0.249	2.205	0.298	1.307	0.349	63.0
-11.646	1.813	0.263	0.209	0.017	3.372	0.265	2.323	0.316	1.356	0.367	61.2
-14.332	1.619	0.287	0.200	0.018	2.849	0.295	1.805	0.350	2.241	0.390	58.7
-17.615	1.805	0.323	0.190	0.021	3.047	0.333	1.691	0.398	1.621	0.449	55.8
-21.757	1.287	0.359	0.185	0.023	3.021	0.370	1.491	0.442	1.539	0.499	52.0
-27.611	1.248	0.408	0.178	0.026	3.097	0.420	0.721	0.513	0.982	0.571	46.7
-37.475	1.224	0.546	0.158	0.036	2.918	0.582	-0.707	0.728	1.762	0.770	37.8
0.600	1.804	0.094	0.289	0.006	4.370	0.088	2.702	0.115	2.368	0.137	146.0
1.200	1.835	0.110	0.274	0.007	4.273	0.103	2.582	0.132	2.377	0.156	131.6
1.800	1.811	0.132	0.262	0.008	4.042	0.125	2.690	0.157	2.445	0.185	114.7
2.400	1.906	0.156	0.248	0.010	3.933	0.150	2.553	0.186	2.217	0.217	99.0
3.000	1.701	0.181	0.244	0.011	3.845	0.174	2.486	0.215	2.003	0.252	92.8
3.600	1.671	0.204	0.242	0.013	3.848	0.197	2.543	0.244	2.088	0.283	91.0

Table C.3: NGC 3377 major

r	Hβ	δHβ	Mg$_2$	δMg$_2$	Mg$_b$	δMg$_b$	Fe5270	δFe5270	Fe5335	δFe5335	σ
4.200	1.371	0.231	0.240	0.014	3.817	0.220	2.399	0.272	2.270	0.314	89.5
4.800	1.679	0.251	0.240	0.016	3.932	0.242	2.271	0.301	1.885	0.351	88.0
5.680	1.291	0.205	0.227	0.013	3.999	0.194	1.966	0.245	1.806	0.282	86.1
6.883	0.954	0.239	0.215	0.015	3.758	0.226	2.292	0.280	2.029	0.324	83.6
8.084	0.990	0.274	0.214	0.017	3.271	0.264	2.589	0.318	1.693	0.373	80.8
9.567	1.650	0.252	0.222	0.016	3.604	0.248	2.033	0.305	1.584	0.353	77.5
11.372	1.597	0.290	0.219	0.019	3.154	0.292	1.971	0.352	1.479	0.406	73.4
13.449	0.959	0.304	0.213	0.019	3.771	0.297	2.555	0.361	1.247	0.423	68.6
16.135	1.542	0.325	0.218	0.021	3.259	0.332	1.490	0.397	1.762	0.451	62.5
19.679	1.572	0.341	0.200	0.022	3.420	0.350	1.551	0.426	1.310	0.479	54.5
24.699	1.927	0.366	0.204	0.025	3.563	0.391	2.633	0.454	1.237	0.526	43.1
32.186	2.101	0.443	0.203	0.030	2.461	0.506	2.165	0.561	1.885	0.610	26.0

Table C.4: NGC 3377 minor

r	Hβ	δHβ	Mg$_2$	δMg$_2$	Mg$_b$	δMg$_b$	Fe5270	δFe5270	Fe5335	δFe5335	σ
-0.300	1.796	0.088	0.303	0.006	4.350	0.083	2.944	0.110	2.615	0.130	156.8
-0.600	1.907	0.096	0.296	0.006	4.355	0.091	2.912	0.118	2.738	0.140	151.3
-1.200	1.791	0.121	0.277	0.007	4.256	0.113	2.721	0.146	2.624	0.174	145.3
-1.800	1.652	0.162	0.258	0.010	4.153	0.150	2.543	0.194	2.541	0.226	126.7
-2.400	1.541	0.214	0.242	0.013	3.824	0.202	2.362	0.256	2.765	0.295	114.8
-3.255	1.506	0.207	0.221	0.013	3.754	0.195	2.538	0.245	2.305	0.285	103.8
-4.471	1.522	0.277	0.196	0.017	3.273	0.266	2.531	0.330	2.116	0.385	98.1
-5.940	1.616	0.295	0.204	0.018	3.210	0.288	2.282	0.351	2.340	0.403	91.2
-8.273	1.630	0.318	0.170	0.020	2.905	0.314	2.453	0.382	1.855	0.446	84.2
-12.301	2.056	0.363	0.183	0.024	3.005	0.377	1.476	0.462	1.493	0.529	72.7

Table C.4: NGC 3377 minor

r	Hβ	δHβ	Mg$_2$	δMg$_2$	Mg$_b$	δMg$_b$	Fe5270	δFe5270	Fe5335	δFe5335	σ
-20.555	1.013	0.516	0.184	0.034	2.749	0.556	2.250	0.649	2.040	0.735	49.3
0.600	1.824	0.096	0.294	0.006	4.350	0.090	2.676	0.118	2.667	0.141	155.1
1.200	1.869	0.120	0.283	0.007	4.383	0.112	2.864	0.146	2.388	0.173	142.4
1.800	1.733	0.161	0.261	0.010	4.036	0.152	2.771	0.195	2.482	0.230	128.3
2.400	1.780	0.214	0.245	0.013	3.723	0.205	2.630	0.258	2.411	0.302	118.9
3.000	1.822	0.263	0.229	0.017	3.673	0.253	2.498	0.318	2.747	0.367	110.6
3.864	1.071	0.240	0.216	0.015	3.525	0.228	2.502	0.284	2.022	0.331	99.1
5.333	0.810	0.266	0.205	0.016	3.205	0.257	1.765	0.319	1.599	0.368	89.0
7.421	1.340	0.315	0.209	0.020	3.369	0.307	2.036	0.375	1.547	0.435	84.1
10.588	1.480	0.346	0.176	0.022	2.517	0.347	2.376	0.412	1.832	0.475	76.6
16.243	1.554	0.444	0.167	0.028	3.087	0.446	1.462	0.538	1.933	0.601	63.3

Table C.5: NGC 3379 major

r	Hβ	δHβ	Mg$_2$	δMg$_2$	Mg$_b$	δMg$_b$	Fe5270	δFe5270	Fe5335	δFe5335	σ
-0.300	1.054	0.191	0.333	0.011	4.994	0.177	2.917	0.239	2.509	0.304	222.8
-0.600	1.137	0.195	0.331	0.012	4.901	0.183	2.765	0.246	2.543	0.312	223.7
-1.200	1.431	0.210	0.322	0.013	4.774	0.199	2.876	0.266	2.597	0.338	222.6
-1.800	1.119	0.236	0.320	0.014	4.964	0.217	3.045	0.292	2.753	0.370	219.0
-2.400	1.308	0.262	0.321	0.016	5.110	0.241	2.910	0.327	3.113	0.408	215.9
-3.273	1.299	0.218	0.313	0.013	4.602	0.204	2.999	0.271	2.960	0.338	211.8
-4.474	1.522	0.269	0.312	0.016	4.685	0.252	3.230	0.330	2.859	0.413	205.8
-5.946	1.397	0.282	0.304	0.017	4.636	0.262	2.659	0.346	2.796	0.422	198.0
-8.019	1.324	0.323	0.291	0.020	4.339	0.301	2.792	0.388	2.333	0.475	187.9
-11.181	1.422	0.359	0.297	0.022	4.452	0.335	2.427	0.435	2.912	0.513	181.6
-17.247	1.773	0.470	0.279	0.030	4.440	0.448	2.809	0.569	3.168	0.666	169.6

Table C.5: NGC 3379 major

r	Hβ	δHβ	Mg$_2$	δMg$_2$	Mg$_b$	δMg$_b$	Fe5270	δFe5270	Fe5335	δFe5335	σ
0.600	1.289	0.195	0.327	0.012	4.944	0.182	3.119	0.244	2.697	0.308	217.4
1.200	1.578	0.208	0.319	0.013	4.857	0.194	2.888	0.262	2.954	0.325	210.1
1.800	1.436	0.232	0.321	0.014	4.899	0.215	2.854	0.289	3.028	0.356	207.5
2.400	1.399	0.260	0.320	0.016	4.952	0.241	2.855	0.324	2.607	0.404	208.6
3.272	1.654	0.217	0.311	0.013	4.576	0.205	2.798	0.273	2.625	0.339	208.0
4.475	1.416	0.271	0.290	0.016	4.828	0.250	2.826	0.336	2.450	0.419	202.7
5.946	0.939	0.286	0.305	0.017	4.714	0.262	3.149	0.343	2.839	0.421	196.3
8.020	0.822	0.331	0.300	0.020	4.460	0.305	2.596	0.397	2.048	0.486	187.4
11.195	1.319	0.360	0.295	0.022	4.163	0.339	2.314	0.433	2.506	0.507	173.8
17.243	1.872	0.473	0.282	0.029	4.680	0.439	2.908	0.554	2.158	0.650	148.0

Table C.6: NGC 3379 minor

r	Hβ	δHβ	Mg$_2$	δMg$_2$	Mg$_b$	δMg$_b$	Fe5270	δFe5270	Fe5335	δFe5335	σ
-0.300	0.928	0.188	0.329	0.011	4.847	0.177	2.987	0.237	3.183	0.300	228.8
-0.600	1.000	0.194	0.325	0.012	4.919	0.180	2.976	0.244	2.857	0.311	227.3
-1.200	1.290	0.210	0.321	0.013	5.108	0.194	2.833	0.265	3.040	0.334	222.7
-1.800	1.064	0.237	0.323	0.014	4.609	0.221	3.134	0.294	2.581	0.374	216.9
-2.400	1.839	0.263	0.306	0.016	4.755	0.248	2.852	0.333	3.133	0.414	210.7
-3.270	1.417	0.226	0.302	0.014	4.702	0.211	3.109	0.279	2.773	0.348	201.4
-4.473	1.517	0.283	0.300	0.017	4.496	0.268	2.813	0.350	1.916	0.439	193.8
-5.950	1.408	0.296	0.288	0.018	4.485	0.278	2.174	0.368	2.623	0.447	188.3
-8.272	1.066	0.318	0.286	0.019	4.322	0.297	2.850	0.383	2.225	0.464	179.8
-12.261	1.971	0.383	0.270	0.024	4.291	0.366	2.585	0.467	1.711	0.570	172.0
-20.869	2.232	0.550	0.278	0.036	3.696	0.562	1.150	0.705	1.679	0.820	156.6
0.600	1.068	0.193	0.319	0.012	4.763	0.182	2.677	0.246	2.789	0.313	228.4

Table C.6: NGC 3379 minor

r	Hβ	δHβ	Mg$_2$	δMg$_2$	Mg$_b$	δMg$_b$	Fe5270	δFe5270	Fe5335	δFe5335	σ
1.200	1.092	0.211	0.323	0.013	4.959	0.195	2.743	0.265	2.937	0.333	221.5
1.800	1.607	0.232	0.315	0.014	4.755	0.218	3.037	0.293	2.823	0.368	215.7
2.400	1.488	0.263	0.298	0.016	4.408	0.249	2.900	0.331	2.709	0.414	210.9
3.269	1.319	0.225	0.308	0.014	4.796	0.209	2.796	0.281	2.580	0.349	204.4
4.474	1.456	0.281	0.295	0.017	4.208	0.267	2.742	0.350	2.826	0.429	196.5
5.945	1.510	0.295	0.289	0.018	4.426	0.278	2.945	0.362	2.965	0.438	187.7
8.266	1.762	0.312	0.281	0.019	3.640	0.307	2.099	0.389	2.574	0.463	180.8
12.259	1.287	0.386	0.284	0.024	4.135	0.369	2.626	0.465	1.889	0.560	168.8
21.145	2.322	0.555	0.272	0.037	3.767	0.566	1.537	0.705	1.245	0.837	142.2

Table C.7: NGC 3605 major

r	Hβ	δHβ	Mg$_2$	δMg$_2$	Mg$_b$	δMg$_b$	Fe5270	δFe5270	Fe5335	δFe5335	σ
-0.300	1.940	0.116	0.257	0.008	3.776	0.115	3.176	0.141	2.902	0.163	91.2
-0.600	1.935	0.119	0.253	0.008	3.712	0.118	3.226	0.145	2.897	0.167	91.5
-1.200	1.936	0.128	0.244	0.008	3.605	0.127	3.254	0.155	2.870	0.179	91.9
-1.800	1.935	0.143	0.231	0.009	3.468	0.141	3.248	0.171	2.817	0.199	91.8
-2.400	1.928	0.165	0.219	0.010	3.317	0.162	3.193	0.196	2.737	0.227	91.0
-3.000	1.915	0.191	0.208	0.012	3.173	0.188	3.073	0.228	2.647	0.263	89.7
-3.600	1.895	0.222	0.200	0.014	3.061	0.220	2.888	0.265	2.565	0.305	88.0
-4.200	1.862	0.254	0.196	0.016	3.008	0.253	2.659	0.306	2.501	0.352	86.0
-5.073	1.787	0.213	0.194	0.014	3.073	0.213	2.370	0.258	2.433	0.296	80.7
-6.279	1.684	0.259	0.197	0.017	3.286	0.259	2.234	0.313	2.386	0.359	73.3
-7.753	1.729	0.259	0.202	0.017	3.252	0.261	2.356	0.311	2.266	0.359	68.7
-9.827	2.058	0.287	0.195	0.019	3.127	0.295	2.178	0.348	2.161	0.401	64.4
-12.762	1.576	0.329	0.190	0.021	3.428	0.330	2.072	0.390	1.799	0.453	58.3

Table C.7: NGC 3605 major

r	Hβ	δHβ	Mg_2	δMg_2	Mg_b	δMg_b	Fe5270	δFe5270	Fe5335	δFe5335	σ
-17.526	2.338	0.394	0.193	0.026	3.627	0.405	1.928	0.479	2.095	0.544	48.3
-36.956	2.783	0.993	0.206	0.068	0.258	1.234	1.180	1.372	-2.185	1.539	7.7
0.600	1.951	0.119	0.256	0.008	3.797	0.118	3.109	0.145	2.887	0.167	90.1
1.200	1.966	0.128	0.250	0.008	3.781	0.126	3.029	0.156	2.855	0.178	89.5
1.800	1.981	0.142	0.241	0.009	3.745	0.140	2.937	0.172	2.803	0.198	89.0
2.400	1.987	0.165	0.231	0.010	3.696	0.160	2.831	0.198	2.729	0.227	88.8
3.000	1.977	0.191	0.222	0.012	3.641	0.187	2.709	0.230	2.625	0.264	88.4
3.600	1.958	0.223	0.216	0.014	3.579	0.218	2.576	0.268	2.499	0.309	88.0
4.468	1.945	0.192	0.212	0.012	3.500	0.188	2.386	0.232	2.303	0.267	86.5
5.676	1.942	0.238	0.210	0.015	3.506	0.236	2.169	0.290	2.081	0.336	82.6
7.151	1.851	0.241	0.210	0.016	3.545	0.240	2.068	0.295	1.974	0.339	77.5
9.225	1.778	0.271	0.203	0.017	3.298	0.273	2.061	0.328	1.881	0.378	69.1
12.157	1.611	0.305	0.201	0.020	3.121	0.315	1.790	0.370	2.184	0.419	57.3
16.727	2.205	0.364	0.201	0.025	2.352	0.408	2.132	0.448	2.112	0.512	38.9

Table C.8: NGC 3605 minor

r	Hβ	δHβ	Mg_2	δMg_2	Mg_b	δMg_b	Fe5270	δFe5270	Fe5335	δFe5335	σ
-0.300	2.041	0.135	0.257	0.009	3.650	0.139	3.025	0.171	2.912	0.197	89.2
-0.600	2.044	0.137	0.254	0.009	3.650	0.142	3.059	0.174	2.974	0.200	88.8
-1.200	2.044	0.147	0.247	0.010	3.635	0.149	3.090	0.183	3.017	0.209	88.2
-1.800	2.043	0.161	0.236	0.011	3.606	0.162	3.114	0.199	3.036	0.228	87.6
-2.400	2.036	0.185	0.223	0.012	3.559	0.183	3.121	0.222	3.019	0.255	86.9
-3.000	2.023	0.217	0.211	0.014	3.496	0.212	3.095	0.256	2.961	0.294	86.3
-3.600	2.002	0.260	0.199	0.016	3.417	0.250	3.018	0.302	2.860	0.347	85.3
-4.457	1.974	0.240	0.189	0.015	3.299	0.230	2.771	0.278	2.663	0.319	82.6

Table C.8: NGC 3605 minor

r	Hβ	δHβ	Mg_2	δMg_2	Mg_b	δMg_b	Fe5270	δFe5270	Fe5335	δFe5335	σ
-5.910	1.973	0.294	0.186	0.018	3.191	0.287	2.163	0.348	2.421	0.397	77.8
-8.640	1.859	0.358	0.185	0.023	2.890	0.360	1.956	0.425	2.243	0.485	69.0
0.600	2.039	0.137	0.255	0.009	3.638	0.142	2.990	0.174	2.839	0.201	90.3
1.200	2.032	0.147	0.248	0.010	3.616	0.150	2.949	0.184	2.755	0.212	91.4
1.800	2.021	0.162	0.238	0.011	3.587	0.162	2.895	0.200	2.658	0.231	92.3
2.400	2.003	0.185	0.227	0.012	3.552	0.182	2.825	0.224	2.547	0.261	92.9
3.000	1.983	0.217	0.214	0.014	3.514	0.211	2.737	0.260	2.425	0.301	93.2
3.600	1.965	0.260	0.204	0.016	3.479	0.248	2.629	0.306	2.291	0.355	91.5
4.457	1.978	0.239	0.194	0.015	3.450	0.228	2.463	0.280	2.107	0.325	87.2
5.910	2.055	0.289	0.188	0.018	3.465	0.282	2.278	0.345	1.873	0.401	79.8
8.649	1.804	0.345	0.171	0.022	3.323	0.347	1.899	0.421	1.563	0.492	65.8

Table C.9: NGC 3608 major

r	Hβ	δHβ	Mg_2	δMg_2	Mg_b	δMg_b	Fe5270	δFe5270	Fe5335	δFe5335	σ
-0.300	1.370	0.098	0.328	0.006	4.618	0.092	2.788	0.124	2.636	0.153	201.1
-0.600	1.373	0.101	0.327	0.006	4.609	0.094	2.758	0.127	2.670	0.157	200.6
-1.200	1.382	0.106	0.325	0.006	4.587	0.100	2.734	0.134	2.702	0.166	198.0
-1.800	1.403	0.116	0.320	0.007	4.535	0.110	2.720	0.147	2.725	0.181	194.4
-2.400	1.434	0.129	0.315	0.008	4.466	0.124	2.714	0.165	2.735	0.202	189.7
-3.000	1.476	0.147	0.307	0.009	4.378	0.141	2.702	0.187	2.719	0.228	183.7
-3.600	1.525	0.168	0.299	0.010	4.272	0.160	2.667	0.212	2.682	0.257	176.7
-4.200	1.571	0.190	0.291	0.012	4.162	0.182	2.600	0.238	2.647	0.288	169.6
-4.800	1.597	0.213	0.286	0.013	4.048	0.204	2.506	0.265	2.631	0.318	164.5
-5.400	1.579	0.235	0.281	0.015	3.939	0.226	2.406	0.292	2.626	0.349	161.1
-6.000	1.500	0.258	0.278	0.016	3.849	0.247	2.318	0.318	2.619	0.380	158.0

Table C.9: NGC 3608 major

r	Hβ	δHβ	Mg$_2$	δMg$_2$	Mg$_b$	δMg$_b$	Fe5270	δFe5270	Fe5335	δFe5335	σ
-6.880	1.322	0.208	0.273	0.013	3.789	0.198	2.264	0.254	2.601	0.302	157.2
-8.083	1.184	0.243	0.267	0.015	3.758	0.229	2.286	0.294	2.512	0.350	156.0
-9.285	1.252	0.277	0.261	0.017	3.584	0.263	2.290	0.334	2.401	0.397	152.9
-10.764	1.261	0.262	0.254	0.016	3.285	0.252	2.139	0.316	2.256	0.375	149.0
-12.844	1.071	0.277	0.253	0.017	3.401	0.264	1.940	0.332	1.862	0.397	147.2
-15.521	1.334	0.308	0.273	0.019	3.839	0.293	2.057	0.370	1.982	0.440	147.3
-18.820	1.521	0.352	0.261	0.022	3.564	0.337	1.854	0.424	2.822	0.488	147.4
-22.971	0.981	0.391	0.270	0.024	3.473	0.372	1.786	0.468	2.377	0.538	147.6
-28.875	0.874	0.428	0.238	0.026	3.348	0.410	1.859	0.520	2.517	0.589	147.8
-37.942	2.732	0.519	0.256	0.032	2.470	0.529	2.995	0.641	3.500	0.695	148.0
0.600	1.376	0.101	0.327	0.006	4.610	0.094	2.828	0.127	2.615	0.157	201.2
1.200	1.384	0.106	0.325	0.006	4.584	0.100	2.856	0.134	2.584	0.166	199.0
1.800	1.397	0.116	0.321	0.007	4.526	0.111	2.862	0.146	2.534	0.182	195.2
2.400	1.407	0.129	0.315	0.008	4.448	0.124	2.839	0.164	2.461	0.202	190.0
3.000	1.413	0.147	0.307	0.009	4.362	0.141	2.782	0.186	2.369	0.229	183.8
3.600	1.417	0.168	0.300	0.010	4.282	0.161	2.697	0.212	2.287	0.258	177.7
4.200	1.432	0.190	0.292	0.012	4.224	0.181	2.595	0.239	2.250	0.292	172.8
4.800	1.468	0.213	0.286	0.013	4.172	0.203	2.487	0.267	2.251	0.324	169.1
5.400	1.525	0.236	0.280	0.015	4.116	0.225	2.386	0.295	2.263	0.356	166.3
6.000	1.592	0.259	0.275	0.016	4.048	0.247	2.303	0.322	2.259	0.388	163.8
6.881	1.668	0.206	0.267	0.013	3.938	0.198	2.239	0.257	2.249	0.310	163.2
8.083	1.662	0.239	0.259	0.015	3.846	0.229	2.185	0.296	2.266	0.357	162.1
9.285	1.587	0.274	0.257	0.017	3.864	0.262	2.175	0.337	2.222	0.405	157.5
10.765	1.660	0.260	0.254	0.016	3.669	0.250	2.260	0.317	2.013	0.383	151.8
12.843	1.834	0.271	0.242	0.017	3.324	0.265	2.143	0.331	2.140	0.397	146.6
15.517	1.356	0.307	0.248	0.019	3.546	0.296	2.219	0.370	1.816	0.444	141.6

Table C.9: NGC 3608 major

r	Hβ	δHβ	Mg$_2$	δMg$_2$	Mg$_b$	δMg$_b$	Fe5270	δFe5270	Fe5335	δFe5335	σ
19.081	1.795	0.331	0.259	0.021	3.522	0.329	1.791	0.409	1.916	0.479	134.8
23.839	2.237	0.373	0.257	0.024	3.889	0.375	1.700	0.466	1.003	0.562	125.9
30.712	2.257	0.428	0.269	0.029	3.492	0.455	0.427	0.570	2.506	0.619	112.9

Table C.10: NGC 3608 minor

r	Hβ	δHβ	Mg$_2$	δMg$_2$	Mg$_b$	δMg$_b$	Fe5270	δFe5270	Fe5335	δFe5335	σ
-0.300	1.331	0.097	0.352	0.006	4.840	0.096	3.116	0.131	2.825	0.163	199.8
-0.600	1.332	0.099	0.349	0.006	4.854	0.098	3.160	0.133	2.861	0.165	200.0
-1.200	1.347	0.105	0.341	0.007	4.853	0.103	3.195	0.139	2.881	0.174	199.4
-1.800	1.376	0.116	0.327	0.007	4.832	0.112	3.202	0.150	2.881	0.187	197.6
-2.400	1.419	0.132	0.312	0.008	4.788	0.124	3.168	0.167	2.857	0.207	194.6
-3.000	1.468	0.152	0.296	0.009	4.724	0.140	3.088	0.189	2.810	0.233	189.6
-3.600	1.519	0.176	0.281	0.011	4.652	0.161	2.971	0.215	2.758	0.264	184.1
-4.200	1.564	0.203	0.271	0.012	4.582	0.185	2.829	0.245	2.706	0.300	176.8
-4.800	1.601	0.232	0.264	0.014	4.538	0.210	2.680	0.279	2.680	0.338	169.6
-5.400	1.632	0.259	0.260	0.016	4.506	0.237	2.526	0.314	2.663	0.378	162.6
-6.276	1.660	0.212	0.257	0.013	4.439	0.195	2.282	0.258	2.601	0.308	153.5
-7.480	1.678	0.251	0.250	0.016	4.264	0.235	1.965	0.308	2.416	0.365	143.2
-8.956	1.663	0.247	0.243	0.015	4.035	0.234	1.895	0.302	2.162	0.357	133.7
-11.033	1.730	0.268	0.248	0.017	3.895	0.257	2.004	0.326	1.602	0.390	128.8
-13.709	1.886	0.306	0.249	0.020	3.674	0.303	1.968	0.376	1.531	0.449	122.5
-17.261	1.171	0.353	0.237	0.022	3.697	0.342	2.007	0.423	1.486	0.502	113.9
-22.510	0.966	0.407	0.261	0.026	3.107	0.406	3.036	0.469	0.613	0.571	100.8
-31.302	2.379	0.498	0.304	0.033	3.643	0.512	1.731	0.601	-0.947	0.700	78.8
0.600	1.343	0.099	0.349	0.006	4.814	0.098	3.069	0.133	2.776	0.165	198.2

Table C.10: NGC 3608 minor

r	Hβ	δHβ	Mg_2	δMg_2	Mg_b	δMg_b	Fe5270	δFe5270	Fe5335	δFe5335	σ
1.200	1.368	0.105	0.340	0.007	4.782	0.103	3.028	0.140	2.725	0.172	195.8
1.800	1.405	0.116	0.328	0.007	4.742	0.112	2.988	0.152	2.675	0.187	191.9
2.400	1.452	0.131	0.312	0.008	4.696	0.125	2.949	0.168	2.630	0.206	187.0
3.000	1.508	0.151	0.298	0.009	4.642	0.141	2.901	0.190	2.581	0.232	180.6
3.600	1.569	0.174	0.284	0.011	4.588	0.162	2.840	0.216	2.518	0.265	173.1
4.200	1.627	0.200	0.275	0.012	4.543	0.186	2.773	0.248	2.444	0.301	166.7
4.800	1.674	0.229	0.269	0.014	4.503	0.212	2.713	0.282	2.358	0.341	161.4
5.400	1.696	0.257	0.266	0.016	4.462	0.240	2.678	0.316	2.290	0.382	156.3
6.276	1.692	0.212	0.262	0.013	4.364	0.198	2.694	0.261	2.292	0.314	153.2
7.480	1.705	0.253	0.254	0.016	4.140	0.240	2.768	0.311	2.368	0.373	149.0
8.957	1.795	0.248	0.245	0.016	3.844	0.238	2.838	0.302	2.171	0.364	139.4
11.031	1.756	0.269	0.239	0.017	3.539	0.264	2.756	0.325	1.587	0.394	124.9
13.707	1.629	0.311	0.245	0.020	3.344	0.313	2.242	0.381	1.204	0.458	111.5
17.509	1.592	0.337	0.254	0.022	3.097	0.349	2.440	0.413	1.468	0.489	106.7
23.376	2.061	0.410	0.225	0.027	3.395	0.427	2.196	0.512	0.683	0.627	99.3
33.557	1.467	0.562	0.237	0.036	2.235	0.592	2.314	0.677	2.427	0.756	86.3

Table C.11: NGC 4339 major

r	Hβ	δHβ	Mg_2	δMg_2	Mg_b	δMg_b	Fe5270	δFe5270	Fe5335	δFe5335	σ
-0.300	1.770	0.136	0.307	0.009	4.342	0.130	3.070	0.161	2.879	0.187	114.5
-0.600	1.659	0.146	0.299	0.009	4.372	0.137	2.937	0.171	2.852	0.197	113.8
-1.200	1.577	0.171	0.287	0.011	4.429	0.160	2.701	0.201	2.822	0.231	110.4
-1.800	1.709	0.208	0.277	0.013	4.201	0.198	2.617	0.247	2.562	0.284	104.3
-2.400	1.699	0.253	0.268	0.016	3.911	0.245	2.865	0.298	2.407	0.347	101.3
-3.266	1.730	0.225	0.259	0.014	4.083	0.215	2.837	0.264	2.734	0.305	100.0

Table C.11: NGC 4339 major

r	Hβ	δHβ	Mg$_2$	δMg$_2$	Mg$_b$	δMg$_b$	Fe5270	δFe5270	Fe5335	δFe5335	σ
-4.738	1.955	0.240	0.254	0.015	3.588	0.239	2.957	0.285	2.626	0.330	93.9
-6.815	1.741	0.279	0.264	0.018	3.918	0.278	2.695	0.329	2.313	0.380	82.5
-9.726	1.541	0.326	0.239	0.021	3.263	0.334	2.195	0.390	2.373	0.440	70.3
-14.769	1.125	0.411	0.224	0.027	3.146	0.430	2.048	0.496	2.929	0.547	69.0
-27.704	1.366	0.654	0.249	0.045	2.375	0.745	-0.238	0.848	2.304	0.933	65.7
0.600	1.709	0.146	0.294	0.009	4.343	0.137	3.124	0.170	2.814	0.198	112.7
1.200	1.635	0.171	0.273	0.011	4.348	0.160	2.973	0.199	2.508	0.230	100.4
1.800	1.733	0.210	0.269	0.013	4.138	0.199	2.602	0.246	2.384	0.285	99.1
2.400	1.767	0.255	0.259	0.016	3.626	0.247	2.500	0.302	2.520	0.346	99.4
3.266	1.591	0.226	0.240	0.014	3.351	0.220	2.680	0.267	2.065	0.312	101.7
4.737	1.669	0.245	0.248	0.015	3.626	0.238	2.959	0.288	1.893	0.338	98.5
6.823	2.111	0.282	0.262	0.018	4.019	0.279	2.568	0.338	1.936	0.392	89.1
9.727	1.323	0.334	0.251	0.021	3.303	0.338	2.191	0.394	3.819	0.424	77.8
14.783	0.561	0.426	0.277	0.027	3.233	0.432	2.565	0.486	2.071	0.555	72.2
27.655	0.140	0.712	0.277	0.046	1.321	0.799	1.480	0.786	4.149	0.854	58.0

Table C.12: NGC 4339 minor

r	Hβ	δHβ	Mg$_2$	δMg$_2$	Mg$_b$	δMg$_b$	Fe5270	δFe5270	Fe5335	δFe5335	σ
-0.300	1.669	0.128	0.304	0.008	4.445	0.119	3.265	0.149	2.876	0.174	117.5
-0.600	1.738	0.137	0.297	0.009	4.210	0.130	3.224	0.160	2.873	0.187	116.1
-1.200	1.765	0.165	0.295	0.010	4.175	0.157	2.910	0.195	2.832	0.225	114.7
-1.800	1.734	0.206	0.288	0.013	4.274	0.195	2.537	0.243	2.573	0.282	111.7
-2.400	1.690	0.253	0.268	0.016	4.265	0.236	2.761	0.295	2.727	0.341	109.3
-3.265	1.812	0.225	0.260	0.014	4.421	0.210	2.928	0.262	2.507	0.306	106.5
-4.736	1.706	0.247	0.253	0.015	3.884	0.236	2.466	0.288	2.692	0.330	101.7

Table C.12: NGC 4339 minor

r	Hβ	δHβ	Mg_2	δMg_2	Mg_b	δMg_b	Fe5270	δFe5270	Fe5335	δFe5335	σ
-6.817	1.545	0.289	0.246	0.018	4.098	0.275	2.414	0.336	2.668	0.384	94.8
-9.723	1.791	0.333	0.237	0.021	3.892	0.326	1.804	0.402	1.499	0.457	85.8
-14.958	1.803	0.426	0.245	0.028	4.067	0.428	1.379	0.521	1.248	0.593	83.3
-28.658	3.569	0.641	0.219	0.046	4.142	0.699	0.808	0.861	2.728	0.923	76.7
0.600	1.703	0.138	0.299	0.009	4.558	0.127	3.271	0.161	2.837	0.189	122.1
1.200	1.674	0.165	0.287	0.010	4.451	0.154	3.062	0.194	2.684	0.226	115.1
1.800	1.595	0.205	0.276	0.013	4.370	0.193	2.956	0.241	2.424	0.282	107.1
2.400	1.518	0.252	0.260	0.016	4.204	0.239	3.019	0.296	2.344	0.348	103.1
3.265	1.559	0.226	0.253	0.014	3.814	0.218	2.608	0.269	2.160	0.312	101.7
4.738	1.211	0.250	0.252	0.016	3.928	0.237	2.710	0.291	2.328	0.335	98.0
6.818	1.849	0.288	0.237	0.018	3.837	0.278	2.312	0.342	1.926	0.394	91.2
9.724	1.609	0.341	0.241	0.022	3.988	0.332	1.769	0.403	2.416	0.450	81.7
14.961	1.221	0.433	0.241	0.028	3.944	0.431	1.902	0.513	1.551	0.583	64.5
28.925	1.230	0.655	0.232	0.045	3.624	0.741	0.499	0.892	3.487	0.863	18.8

Table C.13: NGC 4387 major

r	Hβ	δHβ	Mg_2	δMg_2	Mg_b	δMg_b	Fe5270	δFe5270	Fe5335	δFe5335	σ
-0.300	1.584	0.129	0.276	0.008	4.060	0.128	2.890	0.159	2.679	0.184	97.8
-0.600	1.560	0.131	0.275	0.009	4.078	0.130	2.910	0.162	2.663	0.187	97.8
-1.200	1.543	0.140	0.271	0.009	4.094	0.136	2.915	0.170	2.643	0.197	98.2
-1.800	1.542	0.152	0.264	0.010	4.100	0.147	2.902	0.184	2.626	0.213	99.3
-2.400	1.553	0.169	0.256	0.011	4.089	0.162	2.872	0.202	2.606	0.234	100.3
-3.000	1.570	0.189	0.249	0.012	4.053	0.180	2.823	0.224	2.583	0.260	100.8
-3.600	1.584	0.210	0.244	0.013	4.002	0.200	2.770	0.249	2.554	0.289	100.9
-4.200	1.594	0.231	0.242	0.015	3.952	0.221	2.719	0.274	2.529	0.319	99.7

Table C.13: NGC 4387 major

r	Hβ	δHβ	Mg$_2$	δMg$_2$	Mg$_b$	δMg$_b$	Fe5270	δFe5270	Fe5335	δFe5335	σ
-4.800	1.610	0.252	0.241	0.016	3.923	0.242	2.680	0.300	2.533	0.348	97.3
-5.681	1.664	0.200	0.241	0.013	3.914	0.194	2.637	0.238	2.623	0.275	93.1
-6.883	1.785	0.229	0.241	0.015	3.882	0.225	2.566	0.274	2.742	0.314	85.7
-8.084	1.907	0.261	0.240	0.017	3.794	0.260	2.446	0.313	2.650	0.359	79.9
-9.560	2.023	0.251	0.234	0.016	3.662	0.254	2.271	0.304	2.458	0.347	76.3
-11.635	1.949	0.270	0.232	0.018	3.545	0.276	2.091	0.327	2.400	0.372	71.2
-14.308	1.414	0.316	0.245	0.021	3.691	0.323	2.061	0.377	2.391	0.427	65.6
-18.094	1.853	0.342	0.228	0.023	4.040	0.353	1.583	0.420	2.311	0.471	58.2
-24.728	2.749	0.441	0.261	0.030	3.764	0.480	2.641	0.530	2.199	0.591	45.1
0.600	1.608	0.132	0.274	0.009	4.043	0.130	2.864	0.162	2.685	0.187	98.6
1.200	1.629	0.139	0.268	0.009	4.032	0.136	2.830	0.170	2.676	0.197	99.6
1.800	1.644	0.152	0.261	0.010	4.026	0.148	2.786	0.185	2.648	0.213	100.5
2.400	1.651	0.168	0.253	0.011	4.015	0.163	2.732	0.204	2.600	0.236	101.1
3.000	1.653	0.189	0.246	0.012	3.988	0.181	2.667	0.227	2.541	0.262	101.1
3.600	1.644	0.210	0.242	0.013	3.931	0.201	2.594	0.252	2.481	0.292	100.6
4.200	1.620	0.231	0.238	0.015	3.853	0.223	2.519	0.277	2.430	0.322	99.2
4.800	1.586	0.252	0.237	0.016	3.781	0.245	2.450	0.304	2.392	0.352	97.0
5.680	1.556	0.202	0.236	0.013	3.738	0.196	2.375	0.242	2.348	0.280	94.3
6.882	1.624	0.233	0.237	0.015	3.775	0.228	2.318	0.281	2.291	0.324	91.4
8.084	1.733	0.268	0.237	0.017	3.861	0.263	2.252	0.322	2.279	0.372	88.2
9.561	1.707	0.256	0.239	0.017	3.985	0.252	2.203	0.309	2.255	0.357	83.7
11.633	1.657	0.275	0.246	0.018	4.174	0.273	2.122	0.332	1.984	0.385	77.4
14.313	1.596	0.319	0.253	0.021	4.014	0.322	2.244	0.382	1.919	0.443	72.1
18.088	1.706	0.354	0.249	0.024	4.096	0.359	2.024	0.426	1.890	0.492	66.6
24.892	1.131	0.465	0.264	0.031	4.109	0.482	3.446	0.534	1.899	0.626	56.8

Table C.14: NGC 4387 minor

r	Hβ	δHβ	Mg_2	δMg_2	Mg_b	δMg_b	Fe5270	δFe5270	Fe5335	δFe5335	σ
-0.300	1.727	0.131	0.278	0.009	4.002	0.133	2.783	0.165	2.681	0.190	96.5
-0.600	1.720	0.136	0.275	0.009	3.989	0.135	2.814	0.169	2.698	0.194	96.7
-1.200	1.706	0.145	0.267	0.009	3.963	0.144	2.845	0.179	2.702	0.206	97.6
-1.800	1.686	0.163	0.257	0.010	3.924	0.158	2.868	0.197	2.695	0.228	98.9
-2.400	1.664	0.186	0.246	0.012	3.874	0.179	2.865	0.222	2.677	0.257	99.9
-3.000	1.657	0.216	0.236	0.014	3.824	0.206	2.820	0.255	2.646	0.296	100.7
-3.600	1.680	0.250	0.228	0.016	3.770	0.238	2.724	0.293	2.592	0.341	99.6
-4.467	1.738	0.216	0.222	0.014	3.671	0.207	2.555	0.254	2.449	0.295	95.9
-5.672	1.657	0.278	0.218	0.017	3.468	0.270	2.426	0.327	2.233	0.381	92.1
-7.380	1.267	0.278	0.213	0.017	3.370	0.269	2.285	0.322	2.132	0.376	89.5
-10.510	1.472	0.360	0.213	0.023	2.921	0.363	1.358	0.425	2.690	0.478	84.7
-18.445	0.856	0.595	0.213	0.037	1.813	0.617	2.885	0.657	3.814	0.725	72.5
0.600	1.726	0.135	0.276	0.009	4.002	0.135	2.753	0.169	2.652	0.194	96.6
1.200	1.717	0.145	0.270	0.009	3.987	0.144	2.717	0.179	2.611	0.207	97.7
1.800	1.698	0.162	0.261	0.010	3.953	0.159	2.668	0.198	2.554	0.230	99.4
2.400	1.669	0.185	0.252	0.012	3.896	0.180	2.599	0.226	2.477	0.261	100.5
3.000	1.636	0.215	0.243	0.014	3.816	0.208	2.516	0.259	2.386	0.300	101.1
3.600	1.609	0.249	0.236	0.016	3.724	0.241	2.425	0.299	2.287	0.347	98.9
4.467	1.586	0.215	0.230	0.014	3.593	0.210	2.297	0.258	2.185	0.299	92.9
5.672	1.520	0.276	0.224	0.018	3.418	0.272	2.100	0.331	2.164	0.382	85.6
7.382	1.400	0.272	0.215	0.017	3.314	0.271	1.739	0.326	1.981	0.375	77.7
10.514	1.437	0.354	0.186	0.023	3.192	0.357	0.891	0.431	1.861	0.487	63.2
18.623	-0.315	0.604	0.209	0.039	2.253	0.665	0.705	0.733	2.470	0.798	25.5

Table C.15: NGC 4458 major

r	Hβ	δHβ	Mg$_2$	δMg$_2$	Mg$_b$	δMg$_b$	Fe5270	δFe5270	Fe5335	δFe5335	σ
-0.300	1.280	0.119	0.253	0.007	4.017	0.111	2.409	0.142	2.102	0.168	117.9
-0.600	1.430	0.127	0.251	0.008	4.034	0.119	2.459	0.151	2.260	0.178	113.0
-1.200	1.455	0.153	0.242	0.010	3.989	0.144	2.746	0.181	2.224	0.212	105.5
-1.800	1.538	0.194	0.235	0.012	3.849	0.184	2.641	0.229	2.197	0.269	97.9
-2.400	1.670	0.241	0.225	0.015	3.849	0.232	2.477	0.289	2.510	0.331	90.4
-3.264	1.651	0.219	0.215	0.014	3.560	0.214	2.498	0.262	1.911	0.306	85.6
-4.475	1.721	0.280	0.206	0.018	2.984	0.279	2.731	0.332	1.977	0.389	79.7
-5.945	1.775	0.289	0.199	0.019	3.087	0.291	2.552	0.346	2.361	0.401	76.1
-8.265	1.855	0.310	0.200	0.020	3.165	0.312	2.162	0.377	1.993	0.428	70.5
-12.132	1.603	0.370	0.218	0.024	3.462	0.380	1.277	0.458	1.748	0.512	61.2
-18.940	1.805	0.461	0.187	0.031	3.283	0.495	1.570	0.591	0.440	0.686	44.8
0.600	1.115	0.129	0.247	0.008	3.942	0.119	2.564	0.152	1.996	0.180	115.9
1.200	1.213	0.153	0.238	0.009	3.809	0.144	2.495	0.181	1.996	0.213	107.6
1.800	1.559	0.190	0.235	0.012	3.768	0.183	2.225	0.229	1.843	0.269	98.9
2.400	1.505	0.240	0.229	0.015	3.759	0.231	2.332	0.287	1.866	0.336	92.3
3.264	1.423	0.218	0.226	0.014	3.960	0.210	2.505	0.260	1.921	0.304	82.7
4.474	1.804	0.274	0.216	0.018	3.693	0.271	2.129	0.335	1.740	0.388	77.4
5.946	2.112	0.282	0.214	0.018	3.254	0.290	2.510	0.346	1.963	0.399	73.3
8.274	1.723	0.307	0.208	0.020	3.617	0.308	2.515	0.368	1.490	0.431	67.0
12.072	1.832	0.367	0.217	0.024	3.818	0.369	2.462	0.444	0.706	0.529	67.5
18.969	2.421	0.471	0.207	0.031	3.613	0.485	1.385	0.598	1.907	0.658	69.5

Table C.16: NGC 4458 minor

r	Hβ	δHβ	Mg_2	δMg_2	Mg_b	δMg_b	Fe5270	δFe5270	Fe5335	δFe5335	σ
-0.300	1.680	0.130	0.265	0.008	3.976	0.126	2.441	0.161	2.057	0.188	113.4
-0.600	1.729	0.137	0.262	0.009	4.020	0.132	2.545	0.169	1.973	0.199	110.1
-1.200	1.506	0.166	0.239	0.010	3.996	0.156	2.430	0.199	2.000	0.235	110.7
-1.800	1.737	0.210	0.221	0.013	3.701	0.200	2.275	0.252	1.636	0.299	102.0
-2.400	1.309	0.266	0.224	0.017	3.996	0.252	2.210	0.318	1.756	0.373	94.7
-3.261	1.479	0.242	0.216	0.015	3.745	0.234	2.162	0.291	2.002	0.337	85.2
-4.736	1.536	0.268	0.199	0.017	3.817	0.264	2.125	0.327	2.021	0.377	75.0
-7.062	1.316	0.298	0.200	0.019	3.224	0.301	2.050	0.362	2.328	0.414	73.6
-11.071	1.714	0.360	0.195	0.024	3.968	0.365	1.423	0.461	2.053	0.521	71.3
-19.585	1.527	0.511	0.200	0.035	2.117	0.577	1.461	0.668	2.543	0.740	66.5
0.600	1.396	0.139	0.254	0.009	3.956	0.133	2.439	0.170	2.208	0.200	114.5
1.200	1.500	0.167	0.237	0.010	3.907	0.156	2.647	0.201	2.220	0.235	118.3
1.800	1.538	0.212	0.218	0.013	3.909	0.197	2.487	0.250	2.078	0.294	104.9
2.400	1.484	0.265	0.212	0.016	3.554	0.253	2.021	0.315	2.224	0.365	95.9
3.262	1.610	0.238	0.211	0.015	3.370	0.234	1.788	0.288	2.181	0.331	87.0
4.731	1.889	0.262	0.211	0.017	3.652	0.263	1.966	0.323	1.918	0.372	76.6
7.064	1.542	0.295	0.196	0.019	3.018	0.301	2.712	0.355	1.147	0.424	71.9
11.085	0.389	0.371	0.230	0.024	3.689	0.371	2.354	0.438	1.359	0.514	63.9
19.426	0.947	0.509	0.193	0.034	2.914	0.556	2.311	0.621	1.477	0.724	47.3

Table C.17: NGC 4464 major

r	Hβ	δHβ	Mg_2	δMg_2	Mg_b	δMg_b	Fe5270	δFe5270	Fe5335	δFe5335	σ
-0.300	1.487	0.114	0.262	0.007	3.941	0.103	2.593	0.133	2.036	0.159	139.9
-0.600	1.508	0.116	0.262	0.007	3.964	0.106	2.612	0.138	2.076	0.162	138.6

Table C.17: NGC 4464 major

r	Hβ	δHβ	Mg_2	δMg_2	Mg_b	δMg_b	Fe5270	δFe5270	Fe5335	δFe5335	σ
-1.200	1.520	0.125	0.258	0.008	3.977	0.114	2.605	0.147	2.081	0.173	130.8
-1.800	1.522	0.141	0.253	0.009	3.995	0.129	2.572	0.164	2.057	0.192	119.0
-2.400	1.521	0.164	0.245	0.010	4.019	0.150	2.523	0.188	2.022	0.220	107.4
-3.000	1.538	0.192	0.239	0.012	4.043	0.177	2.473	0.221	1.979	0.259	99.9
-3.600	1.575	0.226	0.237	0.014	4.055	0.210	2.424	0.261	1.916	0.304	93.8
-4.200	1.625	0.262	0.237	0.016	4.036	0.246	2.361	0.304	1.827	0.355	88.7
-5.069	1.685	0.224	0.241	0.014	3.959	0.215	2.224	0.262	1.683	0.306	83.7
-6.535	1.739	0.243	0.248	0.015	3.900	0.234	2.092	0.283	1.498	0.330	80.4
-8.601	1.658	0.298	0.240	0.019	3.672	0.289	2.299	0.341	1.366	0.400	75.8
-11.732	1.506	0.369	0.229	0.023	3.512	0.358	1.951	0.416	0.877	0.487	68.8
-19.544	1.320	0.602	0.294	0.037	4.053	0.578	1.441	0.664	0.669	0.728	51.4
0.600	1.463	0.117	0.258	0.007	3.910	0.106	2.567	0.138	1.995	0.163	138.6
1.200	1.444	0.126	0.250	0.008	3.867	0.114	2.525	0.147	1.939	0.175	131.2
1.800	1.435	0.141	0.244	0.008	3.825	0.129	2.480	0.165	1.883	0.194	121.0
2.400	1.433	0.164	0.238	0.010	3.800	0.151	2.440	0.191	1.842	0.223	109.2
3.000	1.440	0.192	0.234	0.012	3.785	0.179	2.411	0.223	1.820	0.261	100.2
3.600	1.455	0.226	0.232	0.014	3.781	0.213	2.395	0.264	1.814	0.307	93.6
4.465	1.504	0.197	0.231	0.012	3.772	0.189	2.410	0.232	1.832	0.270	86.8
5.673	1.557	0.251	0.231	0.016	3.721	0.245	2.464	0.296	1.857	0.344	79.9
7.140	1.472	0.267	0.232	0.017	3.568	0.263	2.163	0.314	1.748	0.362	73.9
9.447	1.482	0.301	0.230	0.019	3.641	0.299	1.724	0.355	1.360	0.408	64.3
13.597	1.638	0.399	0.197	0.026	3.374	0.411	1.021	0.480	0.783	0.559	47.1

Table C.18: NGC 4464 minor

r	Hβ	δHβ	Mg$_2$	δMg$_2$	Mg$_b$	δMg$_b$	Fe5270	δFe5270	Fe5335	δFe5335	σ
-0.300	1.389	0.100	0.279	0.006	4.163	0.097	2.578	0.128	2.244	0.152	132.8
-0.600	1.416	0.104	0.276	0.007	4.157	0.101	2.565	0.133	2.237	0.156	132.5
-1.200	1.449	0.116	0.267	0.007	4.139	0.110	2.537	0.145	2.219	0.171	129.7
-1.800	1.485	0.136	0.256	0.009	4.103	0.129	2.488	0.168	2.179	0.197	124.2
-2.400	1.523	0.167	0.246	0.010	4.041	0.157	2.415	0.201	2.105	0.237	115.3
-3.000	1.559	0.209	0.236	0.013	3.938	0.197	2.328	0.248	2.011	0.290	105.8
-3.600	1.586	0.258	0.231	0.016	3.808	0.247	2.242	0.305	1.914	0.358	95.9
-4.459	1.608	0.238	0.228	0.015	3.628	0.233	2.149	0.282	1.839	0.330	84.1
-5.924	1.665	0.278	0.220	0.018	3.367	0.277	2.018	0.331	2.025	0.386	80.2
-8.465	1.432	0.320	0.221	0.021	3.313	0.325	1.922	0.375	2.457	0.434	73.5
-14.525	1.002	0.497	0.251	0.032	3.580	0.511	0.335	0.586	1.478	0.660	57.4
0.600	1.371	0.104	0.276	0.007	4.157	0.101	2.572	0.132	2.250	0.156	131.5
1.200	1.368	0.115	0.267	0.007	4.134	0.110	2.538	0.145	2.252	0.171	128.0
1.800	1.387	0.137	0.252	0.009	4.092	0.129	2.464	0.167	2.246	0.196	121.9
2.400	1.431	0.168	0.234	0.010	4.042	0.157	2.352	0.203	2.220	0.236	111.9
3.000	1.490	0.210	0.220	0.013	3.970	0.197	2.222	0.250	2.161	0.291	101.0
3.600	1.532	0.260	0.213	0.016	3.877	0.247	2.107	0.308	2.056	0.358	89.4
4.458	1.528	0.241	0.213	0.015	3.684	0.235	1.997	0.286	1.822	0.333	75.1
5.924	1.504	0.280	0.208	0.018	3.380	0.283	1.791	0.337	1.558	0.392	65.9
8.463	1.544	0.319	0.207	0.021	2.727	0.341	1.027	0.392	1.957	0.445	50.0
14.640	0.765	0.502	0.129	0.033	2.640	0.550	-1.433	0.647	0.859	0.754	11.5

Table C.19: NGC 4468 major

r	Hβ	δHβ	Mg$_2$	δMg$_2$	Mg$_b$	δMg$_b$	Fe5270	δFe5270	Fe5335	δFe5335	σ
-0.300	2.339	0.197	0.222	0.013	3.126	0.216	3.140	0.247	2.546	0.281	35.5
-0.600	2.328	0.203	0.218	0.014	3.177	0.222	3.139	0.254	2.490	0.289	35.9
-1.200	2.332	0.223	0.206	0.015	3.202	0.240	3.074	0.276	2.425	0.314	35.5
-2.062	2.373	0.196	0.184	0.013	3.153	0.206	2.903	0.237	2.341	0.269	33.9
-3.511	2.302	0.240	0.163	0.015	2.826	0.249	2.665	0.283	2.199	0.322	31.9
-5.846	2.004	0.293	0.159	0.019	2.400	0.311	2.297	0.348	2.026	0.396	29.1
-9.897	1.882	0.357	0.162	0.023	2.770	0.382	1.917	0.435	2.331	0.485	24.2
-17.937	0.994	0.504	0.180	0.032	2.574	0.537	3.460	0.571	1.001	0.681	14.6
0.600	2.356	0.203	0.217	0.014	3.054	0.223	3.079	0.255	2.574	0.289	34.0
1.200	2.373	0.223	0.205	0.015	2.967	0.243	2.975	0.277	2.558	0.314	32.8
2.061	2.375	0.196	0.184	0.013	2.855	0.212	2.803	0.241	2.423	0.273	31.6
3.511	2.162	0.241	0.167	0.016	2.783	0.255	2.508	0.292	2.066	0.334	31.3
5.851	1.892	0.294	0.168	0.019	2.800	0.313	2.197	0.359	1.646	0.412	30.8
9.708	1.723	0.357	0.139	0.023	2.081	0.391	2.186	0.438	1.450	0.511	28.0
16.578	1.982	0.466	0.084	0.031	1.733	0.522	0.246	0.620	1.894	0.700	22.1

Table C.20: NGC 4468 minor

r	Hβ	δHβ	Mg$_2$	δMg$_2$	Mg$_b$	δMg$_b$	Fe5270	δFe5270	Fe5335	δFe5335	σ
-0.300	2.492	0.216	0.212	0.015	3.109	0.237	3.043	0.272	2.689	0.306	32.7
-0.600	2.485	0.223	0.208	0.015	3.088	0.244	3.054	0.279	2.722	0.314	32.7
-1.468	2.461	0.183	0.195	0.012	3.035	0.199	2.985	0.227	2.599	0.256	32.7
-2.660	2.367	0.252	0.174	0.017	2.885	0.271	2.832	0.308	2.200	0.352	32.6
-4.358	2.054	0.283	0.155	0.018	2.587	0.303	2.546	0.343	1.820	0.398	32.3
-7.776	2.347	0.363	0.120	0.024	2.452	0.391	0.739	0.462	2.108	0.516	31.8

Table C.20: NGC 4468 minor

r	Hβ	δHβ	Mg_2	δMg_2	Mg_b	δMg_b	Fe5270	δFe5270	Fe5335	δFe5335	σ
-16.626	2.687	0.561	0.144	0.038	3.030	0.617	-0.114	0.770	0.586	0.868	30.5
0.600	2.478	0.223	0.209	0.015	3.116	0.244	2.974	0.280	2.588	0.316	32.5
1.468	2.394	0.183	0.194	0.012	3.070	0.198	2.761	0.229	2.358	0.258	33.5
2.660	2.205	0.254	0.170	0.017	2.896	0.269	2.319	0.312	1.983	0.355	34.8
4.356	2.084	0.282	0.163	0.018	2.504	0.303	2.067	0.347	1.591	0.401	37.9
7.989	2.570	0.359	0.149	0.024	2.319	0.388	1.498	0.453	0.964	0.529	45.1
18.535	-0.982	0.720	0.025	0.042	-3.358	0.820	0.283	0.863	0.302	1.040	65.8

Table C.21: NGC 4478 major

r	Hβ	δHβ	Mg_2	δMg_2	Mg_b	δMg_b	Fe5270	δFe5270	Fe5335	δFe5335	σ
-0.300	1.870	0.117	0.291	0.007	4.509	0.109	3.047	0.139	2.577	0.163	125.0
-0.600	1.686	0.123	0.283	0.008	4.385	0.113	2.859	0.144	2.765	0.168	124.0
-1.200	1.858	0.134	0.276	0.008	4.223	0.124	2.920	0.157	2.943	0.183	124.3
-1.800	1.755	0.152	0.272	0.009	4.362	0.138	2.849	0.178	2.596	0.211	138.5
-2.400	1.882	0.171	0.269	0.010	4.268	0.157	2.640	0.204	2.477	0.241	141.3
-3.000	1.830	0.191	0.273	0.012	4.282	0.176	2.472	0.229	2.406	0.270	142.5
-3.600	1.529	0.211	0.261	0.013	4.231	0.193	2.613	0.252	2.750	0.296	143.9
-4.200	1.819	0.228	0.254	0.014	3.990	0.212	2.360	0.277	1.950	0.331	145.5
-4.800	1.809	0.247	0.254	0.015	3.974	0.230	2.603	0.299	2.085	0.357	144.6
-5.400	1.537	0.270	0.257	0.016	4.029	0.247	2.129	0.324	2.784	0.377	142.5
-6.285	1.833	0.205	0.260	0.013	4.150	0.192	2.735	0.247	2.110	0.296	140.7
-7.485	1.628	0.235	0.246	0.014	3.926	0.218	2.363	0.282	2.120	0.335	140.4
-8.685	2.120	0.258	0.254	0.016	3.828	0.248	2.157	0.316	2.697	0.366	133.8
-10.161	1.857	0.246	0.244	0.015	3.834	0.235	2.271	0.297	1.893	0.349	120.9
-11.964	0.978	0.304	0.245	0.019	3.863	0.284	2.276	0.353	2.034	0.409	108.9

Table C.21: NGC 4478 major

r	Hβ	δHβ	Mg$_2$	δMg$_2$	Mg$_b$	δMg$_b$	Fe5270	δFe5270	Fe5335	δFe5335	σ
-14.036	1.358	0.314	0.234	0.020	4.043	0.299	2.280	0.370	1.954	0.430	100.0
-16.959	1.523	0.340	0.225	0.022	3.988	0.330	2.793	0.398	2.259	0.463	87.5
-21.770	1.532	0.401	0.230	0.026	3.113	0.419	2.510	0.474	2.086	0.548	67.0
-34.374	1.288	0.731	0.216	0.049	1.282	0.878	-0.130	0.957	0.002	1.068	13.0
0.600	2.112	0.122	0.286	0.008	4.319	0.114	3.166	0.143	2.465	0.170	124.0
1.200	2.153	0.134	0.274	0.008	4.102	0.126	2.860	0.158	2.441	0.187	126.6
1.800	1.379	0.154	0.266	0.009	4.100	0.141	2.767	0.179	2.465	0.209	120.2
2.400	1.845	0.171	0.260	0.011	4.007	0.159	2.655	0.202	2.426	0.237	123.1
3.000	1.783	0.191	0.257	0.012	4.021	0.177	2.287	0.230	2.458	0.268	132.7
3.600	1.575	0.212	0.247	0.013	3.931	0.195	2.348	0.254	2.022	0.301	137.2
4.200	1.838	0.229	0.241	0.014	3.853	0.213	2.752	0.273	2.133	0.326	133.3
4.800	1.744	0.248	0.242	0.015	4.073	0.229	2.366	0.298	2.609	0.347	131.0
5.400	1.041	0.273	0.234	0.016	3.748	0.250	2.404	0.320	2.392	0.376	130.8
6.285	1.665	0.209	0.247	0.013	3.875	0.195	2.418	0.248	1.696	0.297	129.7
7.485	1.544	0.233	0.247	0.014	4.054	0.217	2.383	0.278	1.914	0.329	126.1
8.685	1.470	0.265	0.251	0.016	3.738	0.250	2.050	0.316	2.403	0.363	120.3
10.163	1.280	0.252	0.240	0.015	3.749	0.236	2.268	0.297	2.122	0.344	110.4
11.968	1.661	0.293	0.244	0.018	4.098	0.276	1.624	0.352	1.809	0.404	101.1
14.030	2.223	0.305	0.245	0.020	4.337	0.296	2.392	0.369	1.243	0.439	95.3
16.952	1.853	0.340	0.241	0.022	3.717	0.338	1.942	0.408	2.054	0.465	87.2
21.814	0.974	0.421	0.184	0.026	2.916	0.414	1.329	0.505	1.787	0.571	73.7
33.220	1.018	0.660	0.168	0.042	3.967	0.658	0.542	0.822	2.460	0.891	42.0

Table C.22: NGC 4478 minor

r	Hβ	δHβ	Mg_2	δMg_2	Mg_b	δMg_b	Fe5270	δFe5270	Fe5335	δFe5335	σ
-0.300	1.887	0.109	0.290	0.007	4.266	0.104	3.105	0.132	2.911	0.154	125.9
-0.600	1.758	0.117	0.285	0.007	4.226	0.109	3.050	0.139	2.770	0.164	127.2
-1.200	1.463	0.138	0.276	0.008	4.158	0.128	3.033	0.162	2.606	0.191	131.7
-1.800	1.571	0.162	0.264	0.010	4.136	0.150	2.924	0.193	2.373	0.229	139.6
-2.400	1.395	0.187	0.265	0.011	4.180	0.173	2.807	0.225	2.069	0.272	150.2
-3.000	1.628	0.211	0.268	0.013	4.268	0.196	2.853	0.257	2.514	0.310	158.5
-3.600	1.722	0.234	0.256	0.014	3.955	0.220	2.252	0.293	2.193	0.353	166.1
-4.200	1.339	0.261	0.255	0.016	3.641	0.246	2.310	0.319	1.544	0.390	158.9
-5.078	1.340	0.209	0.252	0.013	3.833	0.197	2.772	0.251	1.944	0.305	141.7
-6.282	2.277	0.239	0.237	0.015	3.580	0.233	2.460	0.297	2.293	0.351	136.6
-7.481	1.821	0.280	0.245	0.018	3.679	0.271	1.692	0.352	2.841	0.402	133.8
-8.957	1.472	0.273	0.250	0.017	4.210	0.260	2.214	0.338	1.878	0.396	125.4
-11.022	1.660	0.301	0.232	0.019	3.535	0.298	2.280	0.373	2.325	0.433	113.5
-13.950	2.175	0.339	0.226	0.022	3.541	0.344	2.220	0.424	1.879	0.493	96.5
-19.195	1.919	0.402	0.218	0.027	3.194	0.433	1.665	0.520	0.444	0.614	66.2
0.600	1.789	0.117	0.283	0.007	4.242	0.110	3.242	0.139	3.009	0.163	127.6
1.200	1.871	0.137	0.273	0.008	4.096	0.128	3.009	0.164	2.477	0.193	133.0
1.800	1.818	0.162	0.266	0.010	4.130	0.151	2.700	0.197	2.246	0.236	146.3
2.400	1.761	0.188	0.259	0.012	4.270	0.175	2.669	0.231	2.338	0.278	157.1
3.000	1.614	0.214	0.250	0.013	4.336	0.198	2.601	0.264	2.061	0.320	161.0
3.600	1.371	0.238	0.247	0.015	4.380	0.218	2.304	0.293	1.953	0.353	153.3
4.200	1.874	0.256	0.251	0.016	4.303	0.241	2.287	0.320	1.984	0.383	145.7
5.078	1.883	0.207	0.259	0.013	3.522	0.202	2.525	0.257	1.983	0.308	144.1
6.282	1.298	0.247	0.249	0.015	3.961	0.233	2.412	0.302	2.142	0.359	143.0
7.481	1.259	0.287	0.259	0.018	4.410	0.268	3.067	0.343	2.252	0.412	135.4

Table C.22: NGC 4478 minor

r	Hβ	δHβ	Mg_2	δMg_2	Mg_b	δMg_b	Fe5270	δFe5270	Fe5335	δFe5335	σ
8.955	1.935	0.275	0.246	0.018	3.871	0.267	2.070	0.343	2.275	0.399	125.7
11.032	1.264	0.307	0.228	0.019	3.084	0.301	2.253	0.373	1.588	0.437	113.9
13.943	1.310	0.346	0.252	0.022	4.449	0.332	2.575	0.416	2.364	0.479	100.9
19.216	1.741	0.413	0.251	0.028	3.441	0.434	2.564	0.511	2.253	0.570	77.3

Table C.23: NGC 4551 major

r	Hβ	δHβ	Mg_2	δMg_2	Mg_b	δMg_b	Fe5270	δFe5270	Fe5335	δFe5335	σ
-0.300	1.629	0.154	0.285	0.010	4.548	0.145	3.354	0.179	2.882	0.207	102.0
-0.600	1.790	0.160	0.288	0.010	4.496	0.151	3.040	0.187	2.838	0.214	100.1
-1.200	1.771	0.176	0.285	0.011	4.332	0.168	3.121	0.206	2.673	0.238	97.8
-1.800	1.712	0.199	0.275	0.013	4.114	0.192	2.876	0.234	2.680	0.271	97.6
-2.400	1.679	0.226	0.266	0.014	4.488	0.212	2.655	0.268	2.576	0.309	99.9
-3.000	1.778	0.253	0.254	0.016	4.041	0.243	3.255	0.298	2.532	0.347	99.5
-3.876	1.642	0.209	0.253	0.013	4.021	0.199	2.734	0.246	2.557	0.283	94.1
-5.079	1.636	0.248	0.249	0.016	4.011	0.239	3.203	0.290	1.955	0.342	90.7
-6.560	1.419	0.246	0.260	0.016	4.220	0.235	2.430	0.290	1.731	0.337	91.3
-8.364	1.849	0.296	0.239	0.019	3.729	0.290	2.685	0.352	2.555	0.404	90.5
-10.693	1.584	0.292	0.235	0.019	3.763	0.288	2.980	0.343	2.167	0.398	84.6
-14.241	2.178	0.338	0.248	0.022	4.481	0.335	2.874	0.404	2.177	0.464	75.6
-19.926	1.324	0.416	0.261	0.027	3.844	0.427	2.738	0.492	3.436	0.533	61.2
0.600	1.889	0.159	0.288	0.010	4.475	0.151	2.974	0.187	2.862	0.214	95.4
1.200	1.814	0.175	0.276	0.011	4.133	0.168	2.949	0.206	2.802	0.236	93.2
1.800	1.758	0.198	0.280	0.013	4.159	0.191	2.830	0.234	2.746	0.266	90.5
2.400	1.754	0.224	0.285	0.014	4.529	0.215	2.349	0.270	2.650	0.304	87.6
3.000	1.517	0.255	0.263	0.016	4.000	0.245	2.654	0.301	2.638	0.344	87.4

Table C.23: NGC 4551 major

r	Hβ	δHβ	Mg_2	δMg_2	Mg_b	δMg_b	Fe5270	δFe5270	Fe5335	δFe5335	σ
3.875	1.490	0.209	0.263	0.013	3.965	0.203	2.700	0.249	2.366	0.286	89.3
5.081	1.986	0.246	0.250	0.016	4.075	0.241	2.513	0.298	2.360	0.340	89.2
6.560	1.457	0.242	0.252	0.015	3.996	0.236	2.624	0.287	2.557	0.328	86.9
8.359	1.974	0.292	0.248	0.019	3.728	0.291	2.600	0.351	2.557	0.399	84.5
10.443	1.386	0.318	0.221	0.020	3.063	0.316	2.169	0.378	2.067	0.427	82.0
13.370	1.782	0.334	0.245	0.022	4.387	0.329	2.305	0.403	1.558	0.465	78.5
17.972	2.446	0.383	0.257	0.026	4.036	0.396	2.506	0.471	2.048	0.531	72.9
27.245	0.686	0.566	0.276	0.037	3.911	0.580	3.996	0.648	1.374	0.752	61.8

Table C.24: NGC 4551 minor

r	Hβ	δHβ	Mg_2	δMg_2	Mg_b	δMg_b	Fe5270	δFe5270	Fe5335	δFe5335	σ
-0.300	1.411	0.153	0.295	0.009	4.481	0.142	2.920	0.174	2.902	0.200	98.1
-0.600	1.621	0.159	0.291	0.010	4.397	0.149	2.992	0.183	2.748	0.211	100.8
-1.200	1.890	0.179	0.279	0.011	4.157	0.170	3.103	0.208	2.770	0.241	101.4
-1.800	1.827	0.213	0.261	0.013	3.942	0.203	2.970	0.248	2.337	0.289	100.1
-2.400	1.703	0.253	0.251	0.016	3.793	0.241	2.923	0.295	2.451	0.343	101.6
-3.268	1.853	0.219	0.251	0.014	3.823	0.210	2.700	0.257	2.358	0.299	102.6
-4.476	1.998	0.274	0.253	0.017	3.796	0.265	2.320	0.325	2.648	0.369	94.8
-5.945	1.487	0.285	0.235	0.018	3.873	0.271	2.263	0.332	2.292	0.379	85.3
-8.264	1.315	0.306	0.232	0.019	3.935	0.294	2.258	0.357	2.497	0.403	79.9
-12.234	1.493	0.384	0.211	0.025	4.034	0.375	2.524	0.451	3.007	0.502	71.9
-23.349	-0.026	0.710	0.256	0.048	5.172	0.722	5.319	0.786	3.517	0.910	49.7
0.600	1.695	0.158	0.288	0.010	4.299	0.149	3.030	0.183	2.790	0.210	97.9
1.200	1.820	0.178	0.280	0.011	4.249	0.168	2.818	0.208	2.447	0.241	100.8
1.800	1.617	0.211	0.274	0.013	4.455	0.196	2.914	0.246	2.381	0.286	102.8

Table C.24: NGC 4551 minor

r	Hβ	δHβ	Mg$_2$	δMg$_2$	Mg$_b$	δMg$_b$	Fe5270	δFe5270	Fe5335	δFe5335	σ
2.400	1.565	0.248	0.267	0.016	4.128	0.234	2.744	0.291	2.352	0.337	99.7
3.268	1.787	0.213	0.252	0.013	3.693	0.206	2.760	0.250	2.025	0.293	94.8
4.475	1.677	0.269	0.252	0.017	3.797	0.258	2.815	0.316	1.554	0.372	93.6
5.943	1.921	0.280	0.249	0.018	4.463	0.263	2.981	0.325	1.969	0.383	92.4
8.262	1.699	0.306	0.232	0.019	4.382	0.286	1.770	0.361	2.070	0.410	89.5
12.247	1.176	0.393	0.230	0.024	4.088	0.370	2.461	0.447	1.947	0.515	83.8
22.130	1.196	0.636	0.267	0.042	5.053	0.616	1.260	0.766	1.578	0.861	69.8

Table C.25: NGC 4564 major

r	Hβ	δHβ	Mg$_2$	δMg$_2$	Mg$_b$	δMg$_b$	Fe5270	δFe5270	Fe5335	δFe5335	σ
-0.300	1.592	0.077	0.375	0.005	5.083	0.075	3.213	0.100	3.129	0.121	177.2
-0.600	1.596	0.079	0.371	0.005	5.096	0.076	3.244	0.102	3.112	0.123	176.9
-1.200	1.607	0.085	0.360	0.005	5.069	0.081	3.282	0.108	3.076	0.130	174.1
-1.800	1.622	0.095	0.345	0.006	4.998	0.090	3.307	0.118	3.031	0.141	169.3
-2.400	1.634	0.108	0.328	0.007	4.879	0.101	3.299	0.131	2.988	0.157	162.1
-3.000	1.636	0.126	0.314	0.008	4.720	0.115	3.244	0.149	2.962	0.178	153.9
-3.600	1.634	0.144	0.301	0.009	4.531	0.132	3.141	0.169	2.938	0.200	145.7
-4.200	1.633	0.162	0.291	0.010	4.343	0.151	2.992	0.190	2.906	0.225	138.5
-4.800	1.639	0.180	0.283	0.011	4.198	0.169	2.824	0.212	2.860	0.249	132.3
-5.400	1.649	0.196	0.277	0.012	4.095	0.186	2.674	0.233	2.803	0.272	126.8
-6.000	1.658	0.212	0.274	0.013	4.024	0.202	2.574	0.252	2.752	0.294	121.8
-6.600	1.664	0.226	0.273	0.014	3.970	0.217	2.541	0.271	2.713	0.314	118.0
-7.200	1.662	0.241	0.273	0.015	3.914	0.232	2.561	0.288	2.681	0.335	115.1
-7.800	1.640	0.256	0.272	0.016	3.855	0.248	2.605	0.304	2.634	0.354	112.1
-8.687	1.570	0.195	0.272	0.012	3.794	0.190	2.649	0.231	2.535	0.270	107.7

Table C.25: NGC 4564 major

r	Hβ	δHβ	Mg_2	δMg_2	Mg_b	δMg_b	Fe5270	δFe5270	Fe5335	δFe5335	σ
-9.889	1.501	0.214	0.271	0.014	3.786	0.209	2.654	0.253	2.414	0.295	101.8
-11.091	1.543	0.231	0.270	0.015	3.789	0.227	2.620	0.274	2.339	0.318	96.7
-12.292	1.555	0.247	0.268	0.016	3.706	0.244	2.596	0.293	2.203	0.339	91.6
-13.492	1.507	0.262	0.267	0.017	3.601	0.262	2.534	0.311	2.047	0.361	85.0
-14.979	1.528	0.230	0.271	0.015	3.618	0.234	2.387	0.275	2.016	0.316	76.5
-16.782	1.415	0.254	0.263	0.016	3.506	0.258	2.301	0.303	1.890	0.348	71.3
-18.582	1.265	0.280	0.256	0.018	3.338	0.283	2.112	0.334	1.986	0.380	73.8
-20.667	1.068	0.273	0.259	0.017	3.496	0.272	2.261	0.321	2.124	0.366	76.7
-23.070	0.692	0.309	0.248	0.020	3.389	0.307	2.799	0.355	2.381	0.408	76.2
-25.749	1.295	0.312	0.247	0.020	2.882	0.319	2.441	0.365	2.100	0.418	74.0
-29.035	1.396	0.336	0.259	0.022	3.074	0.344	2.844	0.390	1.934	0.447	71.3
-33.171	1.767	0.354	0.237	0.023	2.649	0.373	2.186	0.429	2.021	0.477	67.9
-38.995	1.871	0.400	0.249	0.026	2.722	0.425	2.072	0.477	2.487	0.523	63.2
-48.954	1.131	0.559	0.217	0.036	2.669	0.585	1.953	0.657	2.887	0.717	55.0
0.600	1.594	0.079	0.371	0.005	5.037	0.076	3.194	0.102	3.125	0.123	175.9
1.200	1.595	0.085	0.360	0.005	4.960	0.082	3.170	0.108	3.093	0.129	172.5
1.800	1.592	0.095	0.347	0.006	4.858	0.090	3.128	0.119	3.033	0.142	167.3
2.400	1.585	0.108	0.332	0.007	4.732	0.102	3.054	0.133	2.944	0.159	160.6
3.000	1.579	0.126	0.319	0.008	4.599	0.117	2.949	0.152	2.842	0.180	153.1
3.600	1.587	0.144	0.308	0.009	4.457	0.135	2.821	0.173	2.731	0.205	145.4
4.200	1.612	0.162	0.298	0.010	4.316	0.152	2.690	0.196	2.621	0.230	138.2
4.800	1.640	0.180	0.292	0.011	4.200	0.171	2.587	0.218	2.513	0.257	131.7
5.400	1.657	0.197	0.288	0.012	4.113	0.188	2.531	0.238	2.409	0.281	126.0
6.000	1.644	0.213	0.285	0.014	4.059	0.205	2.522	0.258	2.334	0.303	121.1
6.600	1.588	0.228	0.284	0.015	4.028	0.221	2.552	0.276	2.303	0.325	116.9
7.200	1.510	0.243	0.281	0.016	3.995	0.236	2.593	0.293	2.313	0.344	113.4

Table C.25: NGC 4564 major

r	Hβ	δHβ	Mg_2	δMg_2	Mg_b	δMg_b	Fe5270	δFe5270	Fe5335	δFe5335	σ
8.086	1.431	0.187	0.276	0.012	3.928	0.182	2.609	0.224	2.336	0.262	108.2
9.288	1.396	0.206	0.271	0.013	3.829	0.202	2.513	0.247	2.280	0.288	101.4
10.490	1.310	0.224	0.269	0.014	3.741	0.221	2.345	0.269	2.215	0.312	95.4
11.691	1.177	0.242	0.265	0.016	3.631	0.241	2.179	0.291	2.297	0.335	90.2
12.892	1.118	0.258	0.260	0.017	3.550	0.258	2.107	0.311	2.330	0.356	86.3
14.380	1.255	0.227	0.258	0.015	3.503	0.228	2.259	0.274	2.223	0.315	85.2
16.180	1.550	0.248	0.261	0.016	3.561	0.252	2.236	0.302	2.333	0.346	83.6
17.981	1.656	0.272	0.260	0.018	3.654	0.279	2.003	0.334	2.035	0.382	78.0
20.063	1.374	0.265	0.247	0.017	3.715	0.270	1.935	0.324	1.704	0.373	71.4
22.747	0.671	0.279	0.229	0.018	3.156	0.285	1.966	0.336	1.961	0.383	67.0
26.028	0.857	0.300	0.224	0.020	3.330	0.307	2.672	0.358	2.005	0.416	68.0
29.894	1.559	0.340	0.247	0.023	3.196	0.357	2.120	0.416	2.186	0.470	69.1
34.911	1.438	0.380	0.205	0.025	2.469	0.400	0.464	0.485	1.021	0.548	70.7
42.396	1.103	0.477	0.164	0.030	2.165	0.490	1.476	0.580	1.110	0.676	72.9

Table C.26: NGC 4564 minor

r	Hβ	δHβ	Mg_2	δMg_2	Mg_b	δMg_b	Fe5270	δFe5270	Fe5335	δFe5335	σ
-0.300	1.585	0.080	0.367	0.005	5.058	0.075	3.574	0.099	3.224	0.120	173.8
-0.600	1.607	0.082	0.362	0.005	5.037	0.078	3.611	0.102	3.231	0.123	173.1
-1.200	1.634	0.089	0.350	0.006	4.972	0.084	3.592	0.110	3.206	0.132	170.1
-1.800	1.664	0.102	0.332	0.006	4.858	0.095	3.500	0.124	3.146	0.148	164.7
-2.400	1.687	0.120	0.312	0.007	4.697	0.111	3.318	0.144	3.057	0.172	156.7
-3.000	1.693	0.143	0.292	0.009	4.506	0.132	3.062	0.169	2.944	0.201	146.9
-3.600	1.685	0.170	0.274	0.010	4.312	0.156	2.772	0.200	2.817	0.235	136.3
-4.200	1.675	0.198	0.262	0.012	4.157	0.184	2.508	0.233	2.700	0.274	127.0

Table C.26: NGC 4564 minor

r	Hβ	δHβ	Mg_2	δMg_2	Mg_b	δMg_b	Fe5270	δFe5270	Fe5335	δFe5335	σ
-4.800	1.682	0.228	0.255	0.014	4.055	0.213	2.286	0.268	2.595	0.313	118.6
-5.400	1.707	0.258	0.248	0.016	4.005	0.244	2.098	0.305	2.513	0.355	111.0
-6.271	1.726	0.218	0.240	0.014	3.998	0.206	1.842	0.256	2.422	0.297	102.0
-7.475	1.598	0.272	0.228	0.017	3.919	0.258	1.541	0.320	2.279	0.371	94.2
-8.945	1.345	0.285	0.216	0.018	3.620	0.273	1.321	0.332	2.027	0.385	85.1
-11.265	1.422	0.311	0.205	0.019	3.228	0.304	1.001	0.362	2.194	0.418	83.8
-15.049	1.662	0.388	0.181	0.024	3.154	0.378	1.193	0.449	2.230	0.523	81.7
-22.318	1.072	0.508	0.234	0.032	3.022	0.504	1.002	0.585	0.406	0.690	77.6
0.600	1.568	0.082	0.363	0.005	5.047	0.078	3.506	0.103	3.195	0.124	174.0
1.200	1.556	0.090	0.353	0.006	5.000	0.084	3.403	0.110	3.124	0.132	171.2
1.800	1.542	0.102	0.337	0.006	4.910	0.095	3.261	0.125	3.014	0.150	165.7
2.400	1.524	0.120	0.319	0.007	4.778	0.110	3.076	0.145	2.871	0.173	157.0
3.000	1.506	0.143	0.300	0.009	4.609	0.132	2.851	0.171	2.712	0.202	145.7
3.600	1.503	0.169	0.283	0.010	4.427	0.156	2.609	0.201	2.559	0.238	133.8
4.200	1.521	0.198	0.271	0.012	4.273	0.185	2.380	0.235	2.430	0.275	123.2
4.800	1.555	0.227	0.263	0.014	4.166	0.213	2.182	0.271	2.312	0.315	114.4
5.400	1.582	0.257	0.254	0.016	4.084	0.244	2.017	0.307	2.201	0.357	106.9
6.272	1.566	0.215	0.244	0.014	3.955	0.206	1.823	0.257	2.056	0.298	97.5
7.476	1.479	0.266	0.229	0.017	3.665	0.259	1.609	0.317	1.956	0.366	87.7
8.945	1.328	0.278	0.215	0.018	3.408	0.273	1.418	0.328	2.016	0.376	76.2
11.272	0.966	0.306	0.199	0.019	3.512	0.295	0.896	0.358	1.681	0.413	73.0
15.037	1.258	0.378	0.183	0.024	3.497	0.368	1.080	0.439	1.043	0.527	67.9
22.443	1.217	0.514	0.184	0.033	2.568	0.536	1.168	0.607	0.205	0.726	57.9

Table C.27: NGC 5582 major

r	Hβ	δHβ	Mg$_2$	δMg$_2$	Mg$_b$	δMg$_b$	Fe5270	δFe5270	Fe5335	δFe5335	σ
-0.300	1.365	0.106	0.322	0.007	4.524	0.102	2.657	0.135	2.584	0.161	163.0
-0.600	1.405	0.109	0.320	0.007	4.512	0.104	2.655	0.138	2.613	0.164	161.3
-1.200	1.455	0.117	0.313	0.007	4.461	0.111	2.653	0.146	2.612	0.173	154.5
-1.800	1.493	0.130	0.301	0.008	4.379	0.123	2.651	0.160	2.580	0.190	144.4
-2.400	1.516	0.148	0.286	0.009	4.282	0.140	2.622	0.180	2.528	0.212	130.1
-3.000	1.529	0.170	0.274	0.011	4.205	0.162	2.579	0.206	2.462	0.240	117.2
-3.600	1.547	0.196	0.263	0.012	4.141	0.188	2.533	0.235	2.389	0.275	108.3
-4.200	1.575	0.223	0.256	0.014	4.093	0.214	2.486	0.269	2.309	0.314	102.6
-4.800	1.599	0.251	0.252	0.016	4.054	0.243	2.438	0.303	2.233	0.354	97.2
-5.675	1.607	0.208	0.248	0.013	4.017	0.202	2.381	0.251	2.184	0.292	93.3
-6.878	1.530	0.252	0.247	0.016	4.064	0.246	2.274	0.304	2.134	0.352	87.9
-8.353	1.584	0.251	0.248	0.016	4.147	0.249	2.062	0.305	1.979	0.354	81.2
-10.428	1.514	0.280	0.243	0.018	4.015	0.279	2.043	0.336	1.944	0.391	71.9
-13.364	1.108	0.313	0.234	0.020	3.766	0.316	1.889	0.371	1.929	0.426	58.7
-17.767	1.000	0.374	0.255	0.025	3.380	0.398	1.099	0.451	1.781	0.497	38.9
-24.997	2.330	0.429	0.239	0.029	2.607	0.500	0.820	0.546	1.541	0.594	6.3
0.600	1.355	0.110	0.319	0.007	4.508	0.104	2.681	0.138	2.545	0.164	163.7
1.200	1.359	0.117	0.313	0.007	4.460	0.111	2.693	0.147	2.478	0.176	158.0
1.800	1.373	0.131	0.302	0.008	4.389	0.123	2.677	0.160	2.390	0.191	146.6
2.400	1.395	0.148	0.289	0.009	4.300	0.141	2.627	0.180	2.277	0.213	131.2
3.000	1.424	0.171	0.279	0.011	4.196	0.163	2.562	0.207	2.154	0.243	119.8
3.600	1.459	0.196	0.269	0.012	4.073	0.189	2.498	0.237	2.003	0.279	110.7
4.200	1.479	0.223	0.262	0.014	3.952	0.216	2.452	0.270	1.841	0.318	103.4
4.800	1.468	0.251	0.258	0.016	3.870	0.246	2.431	0.304	1.713	0.359	96.4
5.674	1.411	0.208	0.252	0.013	3.854	0.205	2.422	0.251	1.595	0.297	90.0

Table C.27: NGC 5582 major

r	Hβ	δHβ	Mg_2	δMg_2	Mg_b	δMg_b	Fe5270	δFe5270	Fe5335	δFe5335	σ
6.878	1.330	0.252	0.243	0.016	3.913	0.249	2.369	0.303	1.509	0.358	81.1
8.353	1.084	0.255	0.231	0.016	3.895	0.250	2.305	0.304	1.645	0.357	78.0
10.427	1.001	0.285	0.227	0.018	3.804	0.281	1.964	0.342	1.739	0.395	74.8
13.363	1.091	0.317	0.231	0.021	3.831	0.316	1.868	0.384	1.135	0.448	70.4
17.773	1.747	0.372	0.223	0.025	3.339	0.388	0.659	0.475	0.475	0.549	63.6
25.015	0.416	0.458	0.215	0.029	3.671	0.459	1.704	0.548	0.575	0.646	52.6
39.573	-0.515	0.749	0.266	0.047	4.056	0.720	3.970	0.786	2.108	0.910	30.5

Table C.28: NGC 5582 minor

r	Hβ	δHβ	Mg_2	δMg_2	Mg_b	δMg_b	Fe5270	δFe5270	Fe5335	δFe5335	σ
-0.300	1.374	0.119	0.309	0.007	4.621	0.109	2.883	0.143	2.587	0.171	153.6
-0.600	1.400	0.121	0.307	0.007	4.609	0.112	2.885	0.147	2.600	0.175	153.2
-1.200	1.432	0.129	0.303	0.008	4.559	0.120	2.851	0.157	2.579	0.187	150.4
-1.800	1.466	0.142	0.296	0.009	4.470	0.134	2.786	0.174	2.530	0.207	145.8
-2.400	1.497	0.162	0.286	0.010	4.344	0.153	2.700	0.200	2.458	0.237	139.7
-3.000	1.518	0.189	0.275	0.012	4.204	0.182	2.605	0.235	2.374	0.279	132.4
-3.600	1.524	0.223	0.263	0.014	4.061	0.217	2.511	0.279	2.285	0.331	125.3
-4.460	1.507	0.201	0.245	0.013	3.865	0.198	2.386	0.252	2.154	0.297	115.4
-5.669	1.470	0.273	0.220	0.017	3.554	0.270	2.230	0.337	2.027	0.399	110.0
-7.388	1.590	0.275	0.204	0.017	3.255	0.271	1.916	0.337	2.053	0.393	108.7
-10.565	2.049	0.338	0.209	0.021	2.721	0.341	1.095	0.415	1.174	0.486	106.1
-16.563	1.254	0.441	0.241	0.028	2.309	0.453	0.746	0.541	-0.268	0.636	101.2
-30.880	0.851	0.738	0.276	0.045	2.090	0.754	1.140	0.899	0.832	0.926	89.7
0.600	1.356	0.121	0.308	0.007	4.595	0.112	2.850	0.147	2.547	0.175	152.7
1.200	1.349	0.129	0.303	0.008	4.537	0.120	2.787	0.157	2.473	0.187	149.6

Table C.28: NGC 5582 minor

r	Hβ	δHβ	Mg$_2$	δMg$_2$	Mg$_b$	δMg$_b$	Fe5270	δFe5270	Fe5335	δFe5335	σ
1.800	1.353	0.143	0.294	0.009	4.446	0.134	2.701	0.174	2.374	0.208	144.8
2.400	1.370	0.164	0.282	0.010	4.326	0.154	2.602	0.201	2.263	0.238	138.5
3.000	1.399	0.192	0.268	0.012	4.192	0.182	2.502	0.236	2.161	0.280	131.3
3.600	1.439	0.228	0.255	0.014	4.046	0.218	2.407	0.280	2.078	0.331	124.1
4.459	1.480	0.206	0.241	0.013	3.828	0.199	2.263	0.252	1.981	0.298	113.9
5.921	1.373	0.243	0.222	0.015	3.428	0.237	1.862	0.294	1.808	0.346	105.0
7.999	0.985	0.317	0.208	0.020	2.988	0.309	1.222	0.377	1.649	0.441	99.0
11.184	1.268	0.373	0.183	0.023	2.922	0.366	0.487	0.454	0.780	0.532	89.8
17.372	1.326	0.452	0.148	0.028	3.255	0.450	-0.954	0.588	0.770	0.661	71.9